Solid-State Transition Metal Dichalcogenide Electrocatalysts for the Hydrogen Evolution Reaction

University of Glasgow

Jessica C. McGlynn

Submitted in fulfilment of the requirements of the Degree of Doctor of Philosophy

School of Chemistry

College of Science and Engineering

February 2020

Abstract

This work seeks to understand the origins of catalytic behaviour in transition metal dichalcogenide electrocatalysts, which are currently convoluted by a variety of factors. To achieve this, a solid-state approach to molybdenum ditelluride ($MoTe_2$) is investigated, which allows for the synthesis of both semiconducting 2H- and metallic 1T'-phases in the bulk form. In doing so, not only is the effect of surface area excluded as the route to advanced activity, but also the role that lithium may play in altering the elemental composition. Therefore, the only factor remaining that may affect the electrocatalytic activity of $MoTe_2$ is the change in coordination geometry which governs the semiconducting / metallic character. As a result, one may confidently attribute the emergence of catalytic activity to the result of polymorphic transition.

Continuing with the quest of understanding the origins of catalytic behaviour, the metallic 1T'-$MoTe_2$ material is studied exclusively, with the effect of surface area now being considered. Again using a solid-state approach, thus removing external factors which may otherwise contaminate this study, a low temperature variant of 1T'-$MoTe_2$ is synthesised in order to explore the result of introducing a degree of disorder to the crystalline material. This method will then highlight the importance of intrinsic activity measurements when comparing HER electrocatalysts.

Upon fully characterising the 1T'-$MoTe_2$ materials, the phenomenon of activation is explored. With the aim of understanding the origins of catalytic enhancement in mind, efforts are turned towards determining the primary reason of activation, and excluding changes in structure and composition as the root cause of the improvement. Following *ex-situ* characterisation, intrinsic activity measurements coupled with computational studies such as Density Functional Theory (DFT) explore the possibility of an electrochemical activation, which may be inherent to 1T'-$MoTe_2$.

In a final endeavour to understand the mechanism behind electrochemical activation, attempts were made to scale up the working electrode to comply with *in operando* electrochemical cells. Additionally, alternative activation mechanisms are considered and confirmation of the catalytic sites at which activation takes place is revealed. Thus, this thesis aims to provide a coherent explanation for the observed catalytic activity in $MoTe_2$, which may also be applied to other members of the TMDC family.

Acknowledgements

Most of all, I would like to express my genuine gratitude to Dr. Alexey Ganin. I couldn't have asked for a better supervisor, and I appreciate everything you have done for me. I will genuinely miss working with you.

Throughout the course of my PhD, I have been fortunate to work with a variety of collaborators. In particular, I would like to thank Dr. Mark Symes, Dr. Harry Miras, Dr. Emma Gibson and Dr. Nuno Banderia for their help along the way.

I'd also like to acknowledge the following people:

Mairi – We've come a long way, my friend. I never thought we'd make it past your 20th birthday. Thanks for always being willing to give me a wee slap when needed, may both of us continue to become The Swan.

Karen (KTJ) – my chemistry mum. The solver of all my problems. I've enjoyed our chats almost as much as I enjoyed being the apprentice Janitor. Thanks for letting me vent all my problems (poor Finlay) and for providing a safe place to release my inner bitch (my true self).

Edu – I guess I can't acknowledge you without also thanking the people of Pret for funding our daily skives – good luck getting free coffee without me (25 and counting!). Gràcies Edu per fer-me veure que hi ha llum quan sóc al pou.

The Ganin group and occupants of C2-02 – I have no idea how you guys put up with my music box for so long. I guess you will have Aux Champs-Élysées imprinted in your minds forever. Thanks for making the office a fun place to work, and for accepting my craziness. Please take care of the cherubs. Little James (I really am sorry for calling you 'Little James'), Liudvika, Youyi and Friskey - I've enjoyed working with you all, and hope you keep me updated with Alexey's crazy antics once I'm gone. Long live Alexey's Angels. Jake, Cailean, Nicole, Ludo, - thanks for making every day in the office entertaining. In the words of Elle Woods, 'What, like it's hard?'

Mercè, Ross Winter, Lewis, Irene, Silke, – my time in the JBB would have been a lot less entertaining without you all.

The Dallas Cowboys – James and Alex, this Little Lady would like to thank you for turning a conference into a holiday. I don't think I'll ever be able to look at an electric scooter without being reminded of my near death experience or brisket.

If I were to thank everyone who helped me throughout this PhD or made my time in the JBB an enjoyable experience, this section would be longer than my thesis. So, to everyone; from, the academics to the students, technical staff, janitors and cleaners: thank you, it's been fun.

Lastly, to my family and friends in Ayrshire – The McGlynns, The McCallums, The One Legged Bitches and The Heroes of Olympus – thanks for keeping me sane, life would be very different without you all in it.

Abbreviations

R_{CT}	Charge Transfer Resistance
j	Current Density
CV	Cyclic Voltammetry
DFT	Density Functional Theory
C_{DL}	Double Layer Capacitance
ECSA	Electrochemically Active Surface Area
EDX	Energy Dispersive X-Ray Spectroscopy
EIS	Electrochemical Impedance Spectroscopy
ECPB	Electron-Coupled-Proton-Buffer
GC	Gas Chromatography
j_0	Exchange Current Density
HER	Hydrogen Evolution Reaction
ICP-OES	Inductively Couple Plasma – Optical Emission Spectroscopy
iR	Internal Resistance
IR	Infrared
LSV	Linear Sweep Voltammetry
n-BuLi	*n*-Butyllithium
NHE	Normal Hydrogen Electrode
OER	Oxygen Evolution Reaction
η	Overpotential
PND	Powder Neutron Diffraction
PEM	Proton Exchange Membrane
PXRD	Powder X-Ray Diffraction
SEM	Scanning Electron Microscopy

SXRD	Synchrotron Powder X-Ray diffraction
TEM	Transmission Electron Microscopy
TMDC	Transition Metal Dichalcogenide
XAS	X-Ray Adsorption Spectroscopy
XPS	X-Ray Photoelectron Spectroscopy

Thesis Contributions

Some of the work detailed in this thesis was performed in collaboration with others. Listed below are the details of collaboration.

- Synchrotron powder XRD data was collected by Dr. Irene Cascallana-Matías, and Le Bail refinement was performed by Dr. Alexey Ganin from the University of Glasgow.
- Dr. Torben Dankwort from the University of Kiel in Germany carried out TEM studies.
- ICP-OES was performed by Dr. Ross Winter from the University of Glasgow.
- IR measurements were performed by Prof. Katalin Kamaras at the Hungarian Academy of Sciences.
- *Ex-situ* XAS data was collected by Dr. Irene Cascallana-Matías while data analysis was performed by Dr. Emma Gibson from the University of Glasgow. Dr. Emma Gibson also collected and analysed *in operando* XAS data.
- Computational studies were carried out by Dr. Nuno Bandeira at the University of Lisbon in Portugal.

Author's Declaration

I declare that, except where explicit reference is made to the contribution of others, that this dissertation is the result of my own work and has not been submitted for any other degree at the University of Glasgow or any other institution.

Printed name: Jessica McGlynn

Signature:

Publications and Conferences

The following manuscripts were published as a result of work undertaken over the course of this PhD:

- **J.C. McGlynn**, T. Dankwort, L. Kienle, N.A.G. Bandeira, J.P. Fraser, E.K. Gibson, I. Cascallana-Matias, K. Kamaras, M.D. Symes, H.N. Miras and A.Y. Ganin., *Nat. Commun.,* 2019, **10**, 4916.
- J. McAllister, N.A.G. Bandeira, **J.C. McGlynn**, A.Y. Ganin, Y-F. Song, C. Bo and H.N. Miras, *Nat. Commun.*, 2019, **10,** 370.
- I. Koltsov, J. Smalc-Koziorowska, M. Prześniak-Welenc, M , Malysa, G. Kimmel, **J. McGlynn**, A. Ganin and S. Stelmakh, *Materials*, 2018, **11**, 829.
- K. Crawford, D. Qi, **J.C. McGlynn**, T. Ivanov, P. Shah, J. Weil, A. Tallaire, A.Y. Ganin and D. Moran, *Scientific Reports*, 2018, **8**, 3342.
- **J.C. McGlynn**, I. Cascallana-Matias, J.P. Fraser, I. Roger, J. McAllister, H.N. Miras, M.D. Symes and A.Y. Ganin, *Energy Technol.,* 2018, **6**, 345-350.
- L. MacDonald, **J.C. McGlynn**, N. Irvine, I. Alshibane, L.G. Bloor, B. Rausch, J.S.J. Hargreaves and L. Cronin, *Sustainable Energy Fuels,* 2017, **1**, 1782-1787.
- G. Sneddon, **J.C. McGlynn**, M.S. Neumann, H.M. Aydin, H.H.P, Yiu and A.Y. Ganin, *J. Mater. Chem. A.,* 2017, **5**, 11864-11872.

The following conferences were attended throughout the duration of this PhD:

- 235th ECS Meeting 2019 (Dallas, USA) – Oral Presentation.
- Materials Research Society Fall Meeting 2018 (Boston, USA) – Oral Presentation.
- 233rd ECS Meeting 2018 (Seattle, USA) – Oral Presentation.
- Solid State Chemistry Group Meeting 2017 (Reading, UK) – Oral Presentation.
- EMRS Fall Meeting 2017 (Warsaw, Poland) – Oral presentation.
- Faraday Joint Interest Group Conference 2017 (Warwick, UK) – Poster presentation.
- Scotland and North of England Electrochemistry Symposium 2017 (St. Andrews, UK) – Poster presentation.
- Solid State Chemistry Group Meeting 2016 (Loughborough, UK) – Poster presentation.

Table of Contents

1. Introduction

The world is currently mostly powered by fossil fuels such as coal, oil and natural gas.[1] Industrialisation of the western world has led to the irresponsible use of these carbon sources, and has continuously contributed to the irreversible environmental damage known as the Climate Crisis. Now, with the world finally recognising the importance of action, efforts are being made to turn away from carbon sources and towards a renewable energy future.

The consumption of fossil fuels is the primary contributor to the increasing release of greenhouse gases, namely carbon dioxide and nitrogen oxides. This, in tandem with the increasing number of natural disasters as a result of climate change, has resulted in a growing interest in developing a 'clean energy' alternative. Fossil fuels currently supply 83% of the world's annual energy usage, and with the growing population expected to consume increasingly more energy as demands rise, the need for alternative energy sources is a necessity.[2,3]

With public knowledge of the climate crisis growing, the pressure has since turned towards politicians and their historic backing of big oil companies rather than acknowledging and tackling the crisis in hand. In April 2019, Scotland became the first country in the world to declare a state of climate emergency. In doing so, the First Minister committed to a carbon neutral Scotland by 2045. Shortly after, declarations followed from the UK Parliament, European Union and the Pope, who stated 'fossil fuels should remain underground'. An illustration of the world map showing countries which have declared a state of climate emergency, or subdivisions which have done so, is depicted in Figure 1-1. Now, with the majority of scientists in agreement that human activity is the primary source of climate change, advances in technology are becoming more and more capable of making the renewable energy vision a reality.

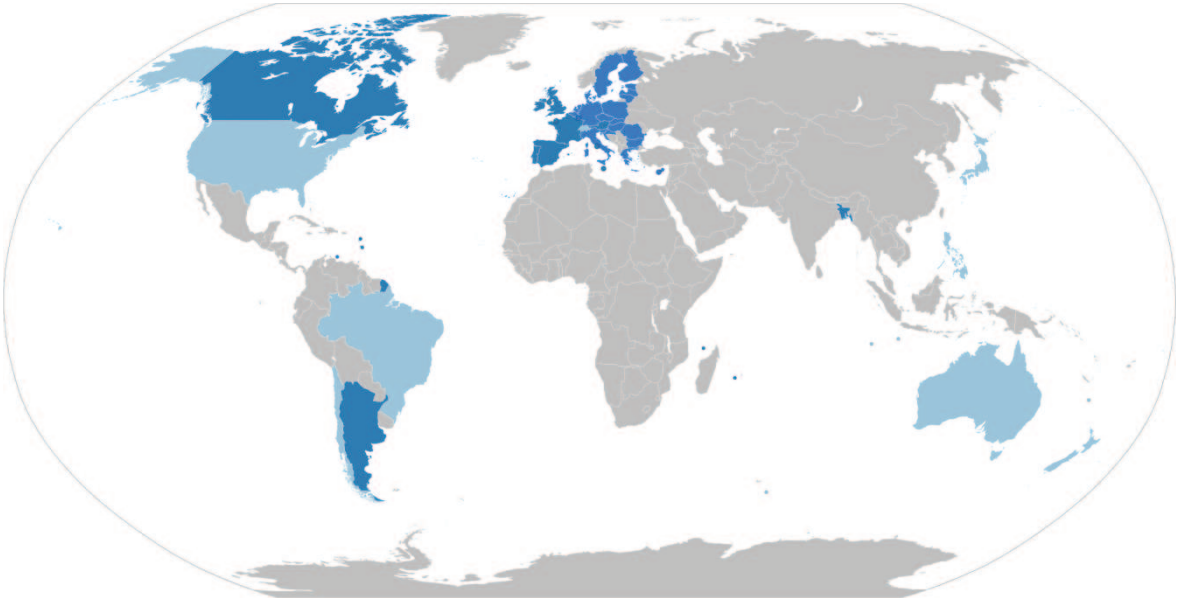

Figure 1-1: *World map illustrating countries in which a climate emergency has been declared (dark blue), declared only in some subdivisions (light blue) or countries in which a climate emergency has not been declared (grey) as of October 2019. This file was made available and is licensed under the Creative Commons CC0 1.0 Universal Public Domain Dedication.*

1.1. The Hydrogen Economy

Arguably, the most promising alternative to fossil fuels, particularly for a mobile society, is the use of molecular hydrogen as an energy vector.[4] The 'Hydrogen Economy' was coined by John Bockris in 1972, who envisaged a world where hydrogen would be the primary energy supply, powering homes, transport vehicles and industrial processes.[5] This idea was proposed to combat the predicted increase in energy demand and air pollution; however Bockris predicted several limiting factors which may hinder the transition towards a hydrogen economy. Namely, these were: conservatism, lack of knowledge and understanding in electrochemical engineering, and finally the widespread fear of hydrogen usage in the community. Now, in 2020, Bockris' apt predictions are slowly dissipating, with advancing technologies allowing for the realisation of hydrogen powered devices.[6]

Motorized traffic is a contributor to the release of harmful greenhouse gases, and is currently responsible for 20% of global CO_2 emissions.[7] The internal combustion engine can be replaced with hydrogen fuel cell technology, which burns hydrogen in oxygen to generate electricity to power a vehicle. The only by-product from this process is water, thus

eliminating the release of pollutants which would otherwise occur from the combustion of gas and oil. Figure 1-2 represents the setup of a typical proton exchange membrane (PEM) fuel cell. This comprises of two electrodes, an anode and cathode, and an electrolyte. Hydrogen (H_2) is split into protons (H^+) and electrons (e^-) at the anode. The electrons flow through the external circuit and, simultaneously, the protons pass through the membrane, typically Nafion™ (which will be discussed further in Section 1.2.2.4.), towards the cathode. These protons and electrons then combine with oxygen, producing water and heat as the only by-products. These half-reactions are summarised in Equations 1 and 2, and the overall reaction highlighting the absence of harmful by-products is shown in Equation 3.

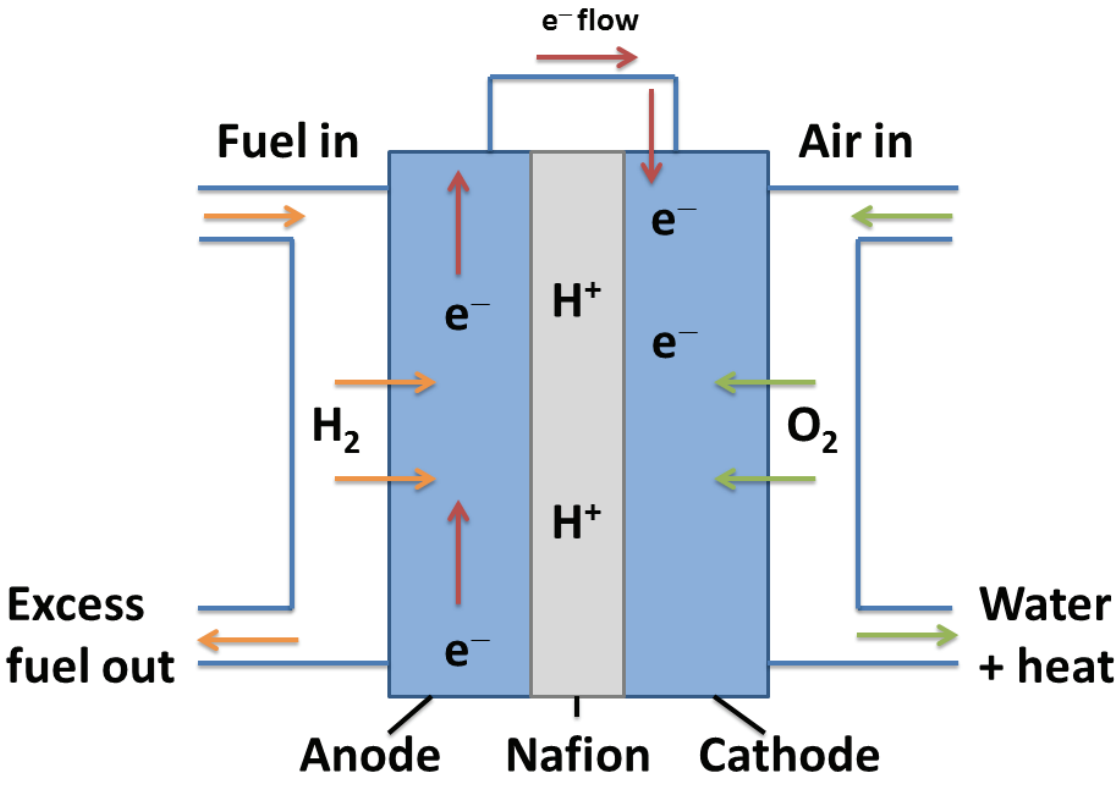

Figure 1-2: *Illustration of a typical PEM hydrogen fuel cell.*

$$2H_2 \rightarrow 4H^+ + 4e^- \quad (1)$$

$$O_2 + 4H^+ + 4e^- \rightarrow 2H_2O \quad (2)$$

$$2H_2 + O_2 \rightarrow 2H_2O \quad (3)$$

Unlike fossil fuels, hydrogen is an energy carrier rather than a primary energy source.[8] Rather than providing the fuel itself, hydrogen is an energy vector, meaning it is capable of transferring energy from one form into another. However, hydrogen must first be extracted from compounds such as water or hydrocarbons before it can be used in fuel cell devices. Provided the energy source is water, the closed system is considered a green process, as the water by-product can be recycled for further use and no greenhouse gases are released into the atmosphere. However, the splitting of water requires energy, and currently this energy is most commonly provided by fossil fuel sources. Therefore, despite eliminating the release of harmful pollutants in the fuel cell system, the overall process still releases greenhouse gases, albeit at an earlier stage.[9]

The primary goal of hydrogen fuel cell technology is to become independent from fossil fuels, and achieve the global target of reducing carbon dioxide emissions.[10] However, approximately 95% of hydrogen is produced *via* steam reforming of natural gas, while the remaining is produced by electrolysis of water (see Section 1.2).[11] The production of hydrogen itself is therefore a major contributor to the greenhouse gas effect. Hence, in order for a hydrogen economy to be truly green, the method of hydrogen production must stem from renewable energy resources.

1.2. Methods of Hydrogen Production

1.2.1. Steam Reforming of Natural Gas

Currently, commercial hydrogen is most commonly produced by the steam reforming of natural gas, the details of which are shown in Equation 4.[12] This process involves the high temperature reaction of methane with steam, producing a mixture of carbon monoxide and hydrogen, known as syngas. Increases in hydrogen yield can be achieved by reforming the CO product further with water vapour, known as the Water-Gas Shift Reaction (Equation 5).

$$CH_4 + H_2O \rightarrow CO + 3H_2 \quad (4)$$

$$CO + H_2O \leftrightarrow CO_2 + H_2 \quad (5)$$

These processes produce CO_2, which contributes to the greenhouse gas effect. This therefore makes the process of steam reforming unfeasible in the long term. Nevertheless, the production of hydrogen from carbon sources is a more economically attractive process than renewable alternatives at present.

In the near future, however, the complete transition away from fossil fuels remains unlikely. Rather, the incorporation of renewable methods of hydrogen production into existing infrastructure would provide a stepping stone into the ultimate hydrogen economy. Thus, existing processes such as steam reforming of natural gases to produce hydrogen can be utilised, while minimizing the emission of greenhouse gases until such point that the technology is advanced enough to phase in fuel cells completely (see Section 1.3.).

For example, the production and storage of methanol as an energy vector can be achieved by reaction of captured CO_2 and hydrogen produced *via* renewable means, *e.g.* water electrolysis. This hydrogen would be derived from the excess renewable energy which would otherwise be lost (see Section 1.3), while the CO_2 product of industrial processes (such as steam reforming) would be collected and used as the reactant.[13] This method would not only allow for the use of renewable energy surplus but also for the storage of a green fuel in the form of methanol. This methanol could then be delivered as fuel for a variety of energy requirements, ranging from public transport to powering homes and industrial processes.[14]

1.2.2. Water Electrolysis

1.2.2.1. Background

Water electrolysis is a promising method of producing hydrogen, however this method currently only produces around 5% of the world's hydrogen supply, as it is more cost demanding than steam reforming of fossil fuels.[11] Dating as far back as 1789, water electrolysis was first reported by Troostwijk and Deiman who observed the decomposition of water into its constituent elements by an electric discharge.[15] Water electrolysis is therefore defined as the splitting of water into hydrogen and oxygen using electricity.

Typically, water splitting proceeds in an electrolyser, consisting of positive and negative electrodes (anode and cathode, respectively). These electrodes are immersed in an electrolyte solution which is capable of generating anions and cations when an electric current is applied. PEM electrolysis operates in acidic conditions; therefore the two electrodes are separated by a Nafion™ membrane, which allows for the passage of protons from the anode to the cathode. An illustration of a typical water electrolyser conducted in acidic conditions is shown in Figure 1-3.

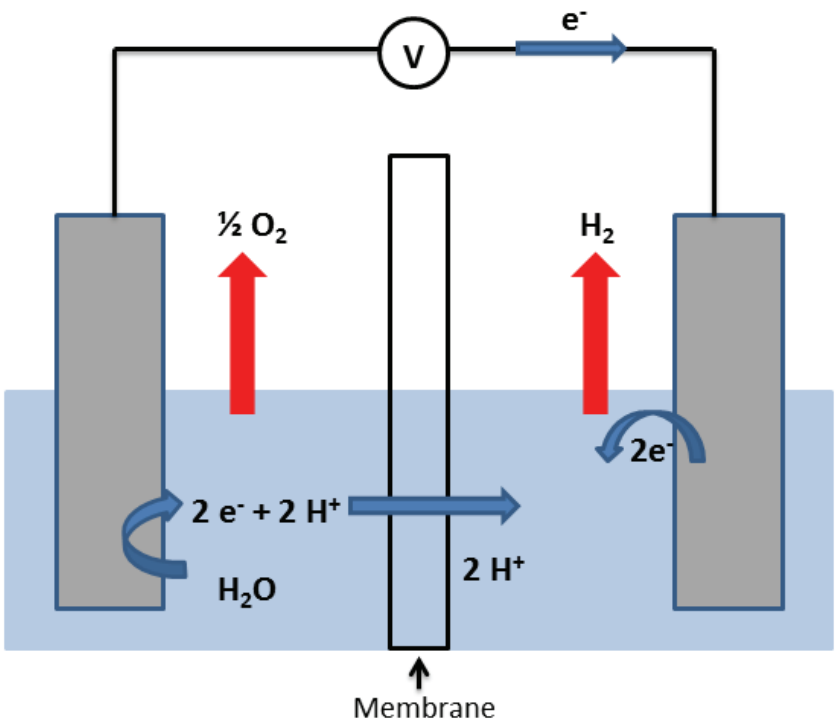

Figure 1-3: *General water electrolysis setup. The left hand side illustrates water oxidation at the anode, while the right hand side shows hydrogen evolution at the cathode.*

When a sufficient potential difference is applied, water oxidation takes place at the anode, where oxygen is evolved along with protons and electrons (Equation 6). This half reaction is known as the oxygen evolution reaction (OER). The protons then pass through the Nafion™ membrane towards the cathode, and the electrons flow through the external circuit where they then recombine with the protons to form hydrogen, otherwise known as the hydrogen evolution reaction (HER). Equation 7 summarises the half reaction for the HER. The cell potential (E^o_{cell}) is defined as the potential difference between the cathodic and anodic half-reactions (Equation 8). The overall process is shown in Equation 9 and emphasises that for every one mole of oxygen produced, two moles of hydrogen are produced. This process is split into two half reactions, the OER and the HER, as described above, with the rate of one reaction being dependent on the other. Since the rate of oxygen production is slower than that of hydrogen, the overall reaction is governed by the OER.

$$2H_2O \rightarrow O_2 + 4H^+ + 4e^- \qquad E^o_{anode} = 1.23\ V \qquad (6)$$

$$4H^+ + 4e^- \rightarrow 2H_2 \qquad E^o_{cathode} = 0.00\ V \qquad (7)$$

$$E^o_{cell} = E^o_{cathode} - E^o_{anode} \qquad E^o_{cell} = -1.23\ V \qquad (8)$$

$$2H_2O \rightarrow 2H_2 + O_2 \qquad E^o_{cell} = -1.23\ V \qquad (9)$$

The standard electrode potential (E^o) at which all redox couples are measured against is the Normal Hydrogen Electrode (NHE). The theoretical potential for the NHE, which is the potential capable of combining protons and electrons to form hydrogen gas, is defined as 0.00 V under standard temperature and pressure (298.15 K and 101.325 kPa, respectively). Simple addition of the standard electrode potentials of water oxidation and proton reduction allows for the calculation of the overall standard potential required for the water splitting reaction, and is determined to be 1.23 V (Equation 10).

$$E = E^o_{ox}(H_2O) + E^o_{red}(H^+) = 1.23\ V + 0.00\ V = 1.23\ V \qquad (10)$$

Therefore, for the overall water splitting reaction to occur, a minimum potential difference of 1.23 V must be applied between the anode and cathode. However, in reality, an excess of this energy is required (known as the overpotential) and will be discussed further in Section 1.2.2.3.

1.2.2.2. Thermodynamics

Water electrolysis is a non-spontaneous process, requiring a positive Gibbs free energy value of ΔG^o = +237.23 kJ mol^{-1}, as calculated by Equation 11.[16]

$$\Delta G^o = \Delta H^o - T\Delta S^o = -zFE^o_{cell} \quad (11)$$

where ΔG^o is the change in Gibbs free energy, ΔH^o is the change in enthalpy (285.8 kJ mol^{-1}), ΔS^o is the change in entropy (163 J K^{-1} mol^{-1}), T is the temperature (K), z is the stoichiometric number of moles of electrons involved in the reaction, F is the Faraday constant (96485 C mol^{-1}) and E^o_{cell} is the cell potential.

The minimum potential required for the overall water splitting reaction is governed by the conditions within the electrolyser itself, *e.g.* temperature and pH. For example, at 0 K, E^o_{cell} is equal to 1.48 V, while at room temperature (298.15 K) energy is acquired from the surroundings in the form of heat, and the minimum potential is lowered to 1.23 V. Therefore, the splitting of water becomes easier with increasing temperature.

Similarly, pH has a profound effect on the required potential. In accordance with moving away from standard conditions, the Nernst equation can be written as shown in Equation 12. Subsequently, the potential under non-standard conditions is defined by the Nernst Equation (Equation 13).

$$\Delta G = \Delta G^o + RTlnQ \quad (12)$$

$$E = E^o - \frac{RT}{zF} lnQ \quad (13)$$

where R is the gas constant, T is the absolute temperature and Q is the reaction quotient.

Q is defined as the ratio of activities of the oxidant and reductant species. Therefore, the effect of pH can be investigated by setting Q equal to the concentration of protons, $[H^+]$, and converting the natural log to $\log_{10}$. At standard temperature, Equation 11 can be rearranged into the following (Equation 14):

$$E = E^o - \frac{0.059}{z}\log[H^+] = E^o - \frac{0.059}{z}pH \quad (14)$$

Accordingly, for every 1 pH unit change, the potential shifts by 0.059 V. The potentials required for the OER and HER at varying pH values can therefore be written as Equations 15 and 16, respectively. Since, in acidic conditions, both OER and HER are proton-dependent, both reaction potentials shift by the same magnitude, meaning a constant cell potential of –1.23 V is required for the overall reaction, regardless of pH.

$$E = 1.23 - 0.059\,pH \quad (15)$$

$$E = 0.00 - 0.059\,pH \quad (16)$$

1.2.2.3. Overpotential

As mentioned in Section 1.2.2.1., the theoretical potential required for water electrolysis is 1.23 V. However, in reality, an excess of this value is required, known as the overpotential (η). The overpotential is the difference between the thermodynamically required potential and the experimentally observed potential, and arises due to several resistances within the system. Equation 17 highlights that the increased energy inputs arise from overpotentials associated with the anode and cathode, and the internal resistance of the cell (iR). Overpotentials arise due to energy being lost within the system; therefore, in order to drive the reaction, a higher voltage than theoretically calculated is required. These energy losses are a result of many resistances, primarily between the electrodes, the solvent and the membrane. The overpotential will be discussed further in Section 1.4.2.1.

$$E_{total} = 1.23 + \eta_{anode} + \eta_{cathode} + iR \quad (17)$$

Resistance associated with the solvent is related to the conductivity of the electrolyte solution. This can be minimised by decreasing the pH of the electrolyte, since protons possess the highest ionic conductivity. Hence, conductivity increases with decreasing pH, which lowers the resistance. The membrane can also have a profound effect on the resistance as charge transfer between compartments can be inhibited. Therefore the use of a thinner membrane (*i.e.* Nafion™) has a beneficial effect on lowering the internal resistance. Crucially, the electrodes play an important role in the setup of the electrochemical cell. The greater the distance between the anode and cathode, the greater the resistance. Therefore, the positioning of the electrodes within the cell is of utmost importance. Further, overpotentials arise due to electron transfer between the electrolyte and the electrode surface (η_{anode} and $\eta_{cathode}$). These overpotentials can be minimised by applying an electrocatalyst to the electrode, which is currently an area of extensive research (see Section 1.4).

1.2.2.4. PEM Electrolysis

Proton Exchange Membrane (PEM) electrolysis is an attractive area of research. In fact, PEM electrolysis is considered as the most promising method of hydrogen production for transport applications to date. This is due to the straightforward setup of the system, which is essentially the reverse of a fuel cell.[17] High energy densities are achieved at low operating temperatures of only 80 °C, making PEM electrolysis more efficient than its alkaline counterpart.[18]

In an identical manner as discussed previously, PEM electrolysis is conducted under acidic conditions, with a solid polymer electrolyte separating the anodic and cathodic compartments. The OER occurs at the anode, producing oxygen, protons and electrons. The protons and electrons then recombine at the cathode, where the protons are reduced to form hydrogen (HER). A schematic of a typical PEM electrolyser is shown in Figure 1-4.

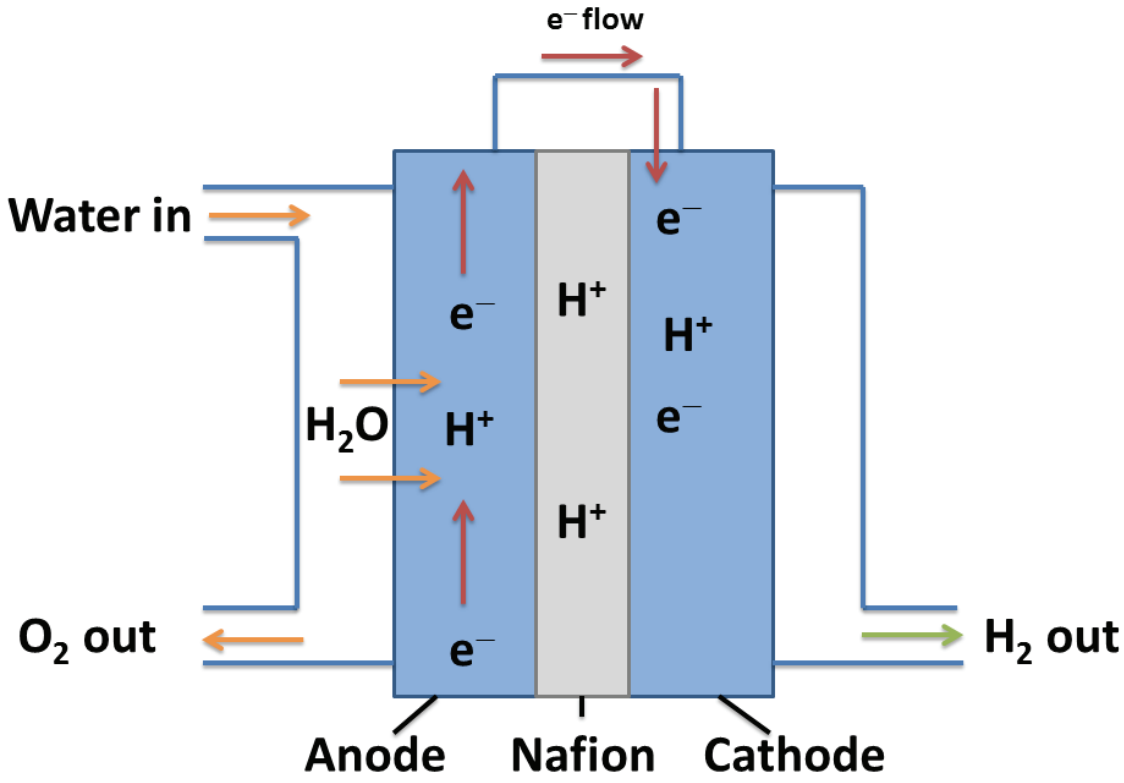

Figure 1-4: *Typical setup for a PEM electrolyser.*

The development of the Nafion™ membrane in the 1960s proved to be a turning point for research into PEM electrolysis. Currently the most popular proton exchange membrane used to date; Nafion™ is a sulphonated tetrafluoroethylene based fluoropolymer-copolymer. The membrane has demonstrated substantial durability under oxidizing environments, and is hence able to withstand the harsh acidic conditions required for use within a PEM electrolyser.[19] The structure of the Nafion™ membrane is shown in Figure 1-5.[20] The Nafion™ membrane has a particular advantage for PEM electrolysis due to its high proton conductivity and low gas permeability. This allows for membrane thicknesses as low as 0.2 mm, which in turn results in lower resistances and increased current densities being achieved.[21] Most importantly, the Nafion™ membrane allows for the isolation of gaseous products in their respective compartments. The negatively charged sulfonate groups allow for the movement of protons through the structure while repelling anions such as hydroxyl groups. Therefore, the mixing of electrolysis products is minimised. However, a small degree of gas crossover and resulting contamination is inevitable, which is a bottleneck for water electrolysis systems. This crossover results in a dangerous and explosive mixture of hydrogen and oxygen gases within the cell.[22] Within the electrolyser, a build-up of these

high pressure gases can result in the degradation of the Nafion membrane, which can reduce its lifespan significantly.[23]

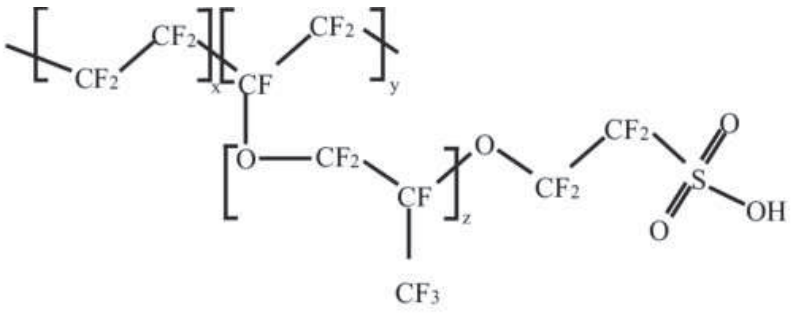

Figure 1-5: *The structure of the Nafion™ membrane.*[20]

The main disadvantage of PEM electrolysis is its expensive components which are required to withstand acidic conditions. In particular, the scarce noble metal platinum electrocatalyst significantly boosts the cost of the electrolyser, with further research required to develop a cheaper alternative capable of tolerating the highly acidic conditions. Additionally, the issue of gas crossover means that further purification, and hence an additional energy input, is required. Until these problems are addressed, steam reforming of natural gas remains as the most cost effective method of hydrogen production.

1.2.3. Electron-Coupled-Proton-Buffer Mediated Water Electrolysis

One possible solution to combating this bottleneck of gas crossover was proposed by Symes *et al.* who introduced the concept of Electron-Coupled-Proton-Buffer (ECPB) mediated water electrolysis.[24] This novel approach offers an alternative to the traditional process of water splitting, and allows for the OER and HER to be separated in space and time. As with typical water electrolysis, water oxidation occurs at the anode, with protons and electrons being produced. The electrons flow through the external circuit, and the protons pass through the membrane towards the cathode and the ECPB in the second compartment. However, rather than the protons and electrons recombining at the cathode to produce hydrogen, they are intercepted by the ECPB, typically a polyoxometalate (POM), forming a two-electron reduced ECPB species, as shown in Equation 18. Therefore, rather than forming hydrogen directly, the ECPB is capable of capturing the protons and electrons, thus allowing for storage and transport until such point that hydrogen is required. Subsequent re-oxidation of

the ECPB results in the release of protons and electrons, which again flow through the external circuit and pass through the membrane, respectively, where they recombine to produce hydrogen gas. Therefore, the reduced ECPB can be re-oxidised when required, releasing hydrogen on demand (Equation 19). The ECPB-mediated water electrolysis process is illustrated in Figure 1-6.[36] The decoupling of the OER and HER in space and time therefore minimises the effect of gas crossover. Additionally, the rate of the HER is no longer dependent on the OER.

$$ECPB + H_2O \rightarrow [ECPB]^{2-} + \frac{1}{2}O_2 \quad (18)$$

$$[ECPB]^{2-} + 2H^+ \rightarrow H_2 + ECPB \quad (19)$$

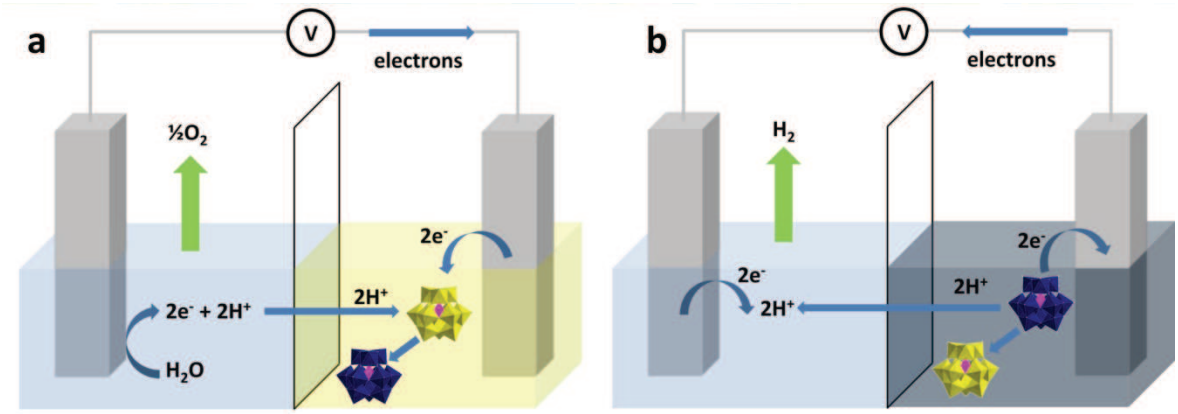

Figure 1-6: *Illustration of an ECPB-mediated water electrolysis system.* ***a)*** *water oxidation and ECPB reduction followed by* ***b)*** *ECPB oxidation and hydrogen generation.*[36] The reduction / oxidation reactions are visualised by a colour change, with the polyoxometalate undergoing a colour change from yellow to blue upon reduction, and from blue to yellow upon subsequent re-oxidation.

1.3. Renewables-to-fuels

Renewable energy sources, such as wind or solar power, are intermittent. This means that energy can only be provided when the wind is blowing or when the sun is shining. During times of abundant wind and sunshine, these renewable sources provide enough energy to power humanity's needs in excess. However, due to the intermittent nature of renewables, the energy must be used immediately; otherwise it is wasted.[25] Figure 1-7 shows a representation of the electrical grid demand in Ontario, Canada for a summer day compared to a winter day, and overlaid with the total wind generation for the summer day.[26] Clearly, the demand for electricity is not correlated with the generation of wind power, which is sporadic and hence unreliable. Therefore, storage of excess energy is imperative in order for the complete transition into a renewable energy infrastructure.

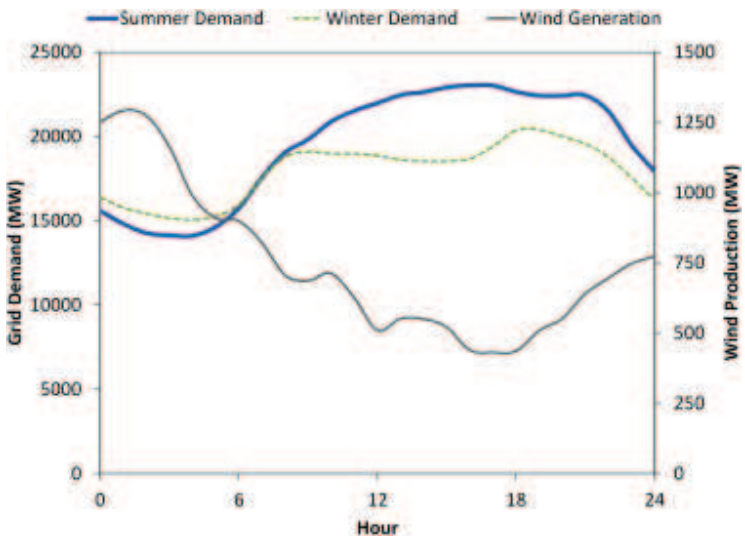

Figure 1-7: *Grid demand in Ontario, Canada for a summer and winter day overlaid with the total wind generation from the summer day.*[26] *Blue and dashed green lines show the summer and winter grid demands, respectively, while the solid grey line shows the wind generation for the summer day. The wind power generation is not related to changes in grid demand since large and rapid variations are observed.*

Coupling solar irradiation to electrochemical water splitting has attracted increased attention in recent years. However, to achieve this form of 'artificial photosynthesis', practical and scalable devices which consist of cheap and earth abundant materials are required. Combining solar power with water electrolysis allows for the excess energy to be stored in the form of hydrogen, which can then be fed into a PEM fuel cell to produce electricity. In

this way, the hydrogen produced for the fuel cell comes from renewable resources, thus removing the need for fossil fuels and making the overall process a green system.

Currently, conventional electrolysers operate using a noble metal platinum electrocatalyst, and generate current densities of approximately 0.5 - 2.0 A cm^{-2}.[21] In a typical direct solar-to-fuels device, the current densities will be limited by the power of incident sunlight, which is both diffuse and intermittent. Therefore, a benchmark current density of 10 mA cm^{-2} is considered a realistic quantity for artificial photosynthesis systems.[27] If comparable current densities, and hence gas production, were to be reached, the surface area of the solar-to-hydrogen device electrode would have to be scaled to around 50 – 200 times the size of that of a conventional electrolyser. Due to their cost and scarcity, noble metals are deemed impractical choices, hence efforts must be turned towards cheaper and earth abundant alternatives.

1.4. Hydrogen Evolution Reaction Electrocatalysts

1.4.1. Background

As discussed in Section 1.2.2.3., an excess of energy known as the overpotential (η) is required in order to drive the water splitting reaction. In order to reduce the overpotential to as close to the thermodynamically required energy input as possible (0 V (vs. NHE) in the case of the HER) an electrocatalyst is applied to the electrode. Typically, as mentioned above, overpotentials of HER electrocatalysts are measured at a current density (j) of $j = -10$ mA cm^{-2}, as this equates to a 12.3% efficient solar-to-fuels device.[28]

Platinum has historically been the electrocatalyst of choice for the hydrogen evolution reaction, owing to its high electronic conductivity which correlates with a low resistance, amongst other factors.[21] These include a high specific surface area and highly efficient charge transfer kinetics which result in an increased density and reactivity of active sites.[29] Additionally, the use of highly acidic conditions in PEM electrolysers limits the choice of electrocatalyst materials, with noble metals found to be the most stable. These factors, coupled with the large cathodic current densities achieved at a near-zero overpotential; provide platinum with an unrivalled electrocatalytic performance.

However, the high cost of platinum and its low abundance hinder its use not only for fuel cell systems, but also for a plethora of additional uses.[30] Platinum is an essential component

in the automotive industry, which accounts for over 60% of the global platinum supply. The replacement of platinum with other noble metals such as palladium, rhodium, ruthenium *etc.* demands a compromise in activity, and these platinum group metals are equally as scarce.[30]

In terms of the viability of fuel cell technologies, the only option is to replace platinum with an earth abundant alternative. Despite compromising on the activity, *i.e.* greater overpotentials being required, the development of cheap and earth abundant electrocatalysts for the HER has been a dominating field of research in recent years. Non-noble metals, namely molybdenum and nickel-based compounds in particular, have been increasing in interest as a potential replacement for platinum.

Several characteristics may be considered when evaluating electrocatalytic performance. However, a plethora of literature studies report varying methods of determining these performance parameters. Therefore, accurately comparing electrocatalytic materials has become somewhat difficult due to the lack of a uniform methodology. In this work, both total electrode and intrinsic activity measurements will be explored.

1.4.2. Total Electrode Activity Measurements

Total electrode activity measurements are currently the most relevant method of comparing HER electrocatalysts. These include metrics such as the overpotential, Tafel slope and exchange current density (j_0), all of which are related by the Tafel Equation (Equation 20). However, these methods are limited as the currents used to obtain these metrics are normalised to the geometric area of the electrode substrate, rather than the electrocatalyst itself. Thus, it follows that electrodes with high electrocatalyst loadings show the greatest total electrode activity, which can be misleading when comparing catalytic activities in the literature.

$$\eta = a + b \log j \tag{20}$$

where η is the overpotential, a is a constant, b is the Tafel slope and j is the current density.

Nonetheless, these measurements remain as the most commonly practised means of exploring the initial catalytic activity of electrocatalysts, and are frequently used to characterise catalytic activity in this work.

1.4.2.1. Overpotential Determination

When investigating an HER electrocatalyst, the initial test performed is that of overpotential determination. The electrocatalyst is supported on an inert and conducting substrate, most commonly glassy carbon, and characterisation is typically performed by cyclic voltammetry (CV) or linear sweep voltammetry (LSV). These methods allow for the current to be swept across a range of potentials, with a current being produced indicating a redox reaction taking place. From these current-potential graphs, the overpotential is chosen at a particular current density, achieved by normalising the observed current to the geometric surface area of the inert electrode substrate. In doing so, effective comparison can be achieved between a variety of electrocatalysts, provided all are reported at a particular current density.

A direct comparison, however, is somewhat difficult to achieve, as some reports compare the 'onset potential' of an electrocatalyst, otherwise known as the potential at which catalytic activity is initially observed. However, there is some ambiguity surrounding this concept. Primarily, there is no benchmark current at which this onset potential is required to be reported, thus leading to the overpotential being a product of the eye of the observer. Rather, reporting the overpotential at a specific current density is deemed to be a more reliable metric. As discussed earlier, a benchmark current density of $j = -10$ mA cm^{-2} is typically used to report overpotentials of HER electrocatalysts, as this relates to a 12.3% efficient solar-to-hydrogen device.[28]

1.4.2.2. Tafel Analysis

By definition, the Tafel slope represents the voltage required to increase the current density by an order of magnitude. Tafel plots can be obtained from LSV curves, and are presented in graphical form by the overpotential as a function of the logarithm of current density. From these plots, the exchange current density (j_0), *i.e.* the current density at $\eta = 0$ V, can be extrapolated.

The overpotential alone is not a reliable performance parameter since, as mentioned above, the currents are normalised to the geometric surface area of the electrode substrate, rather than the electrocatalyst itself. The Tafel slope, in tandem with the exchange current density (j_0), can provide detailed information about the electrocatalytic performance, with their product being the overpotential from Equation 20 above. Therefore, each parameter can either be calculated or observed experimentally from the current-potential curves.

The total electrode activities are most commonly analysed by their experimental overpotential at a given current density, which depends on the Tafel slope and onset potential. The onset potential governs the Tafel slope, *i.e.* the gradient of the overpotential plotted against the logarithm of current density. However, it is possible for differing Tafel slopes, and hence differing onset potentials, for given catalysts to reach the same overpotential for a given current density. For example, Figure 1-8 shows theoretical activities of two HER catalysts with differing onset potentials and Tafel slopes. Figure 1-8a shows the LSV and highlights two different onset potentials for each catalyst. Despite this, the overpotential at the benchmark current density of $j = -10$ mA cm^{-2} is achieved at an identical overpotential for each catalyst. Similarly, Figure 1-8b depicts representative Tafel slopes as a result of the LSV curves, and despite different slopes being calculated, the overpotential for $j = -10$ mA cm^{-2} is identical. The Tafel slope can also be an indicator of the HER reaction mechanism (as will be discussed in Section 1.4.5.) therefore the mechanism by which each catalyst reaches this current density is expected to be different.

Therefore, in terms of total electrode activity measurements, the most practical method of evaluating HER catalytic activity is by comparing the overpotential at a given current density. Comparing the overpotentials at $j = -10$ mA cm^{-2} provides an indication of the activity per geometric surface area of the electrode substrate, and therefore, however useful, must also be handled with caution when studying materials of varying surface areas.

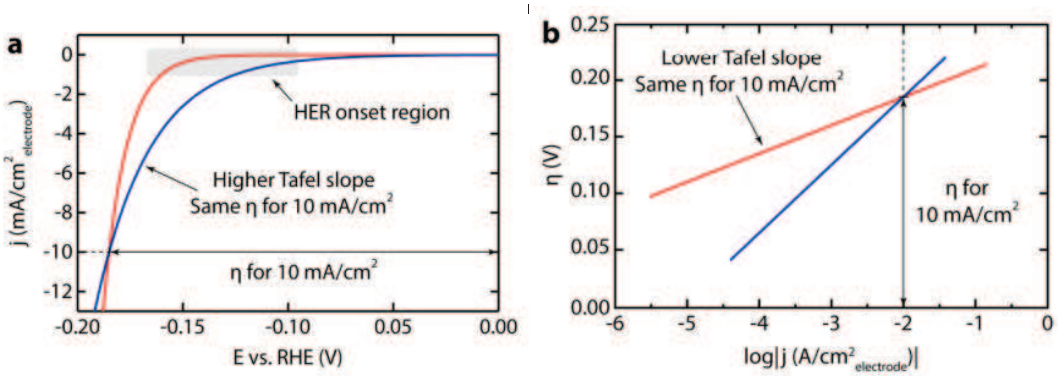

Figure 1-8: *Theoretical examples of HER activity adapted from a study by Benck et al.*[31] ***a)*** *Representative LSV showing current density as a function of potential and* ***b)*** *Representative Tafel plot illustrating that different Tafel slopes may reach the same overpotential for a specific current density.*

1.4.3. Intrinsic Activity Measurements

From a practical perspective, the total electrode activity is the most important metric, as this aids the development for device use. A more detailed insight into catalytic activity, however, is obtained post-total electrode activity measurements, and delves further into the realm of catalytic active sites. Intrinsic activity measurements allows for a fundamental understanding of the origins of catalytic activity which could aid material design.

These measurements, however, are more challenging experimentally than the total electrode metrics, and are therefore less commonly investigated for non-precious metal catalysts. Due to the presence of different active sites within materials, each with varying catalytic performances, methods of probing individual sites remains limited. Quantification of the active sites is the most sought after intrinsic activity metric, albeit in the majority of instances the numbers obtained are approximate rather than exact. A common method employed to generate an idea of the number of active sites, rather than the precise value, is the approximation of the electrochemically active surface area (ECSA). Since the number of catalytically active sites often scales with catalyst surface area, estimating the ECSA is widely used for intrinsic activity studies. This can be achieved by calculating the double layer capacitance of a material, C_{DL}, which is directly proportional to the ECSA.

As discussed in Section 1.4.2., total electrode activities are normalised to the surface area of the electrode substrate, rather than the electrocatalyst itself. This therefore leads to a dependence on catalyst loading, and does not provide any insight into the inherent activity

of the catalyst. For example, Figure 1-9 illustrates a representation of a 2D surface of 2H-MoS_2 (which will be discussed further in Section 1.4.6.). As can be seen, the geometric surface area does not take into account the catalyst morphology. In addition, the variation in site activity plays an important role. From Figure 1-9, the active edge sites (green dots) and inert basal plane (blue squares) can be visualised. Since the basal plane, in this case, is inert, higher catalytic activity will be associated with materials which have more accessible edge sites and fewer basal plane sites.[32,33] Therefore, the ECSA can vary greatly from the geometric surface area, which assumes all surfaces in contact with the electrolyte are active and that the surface is completely flat.

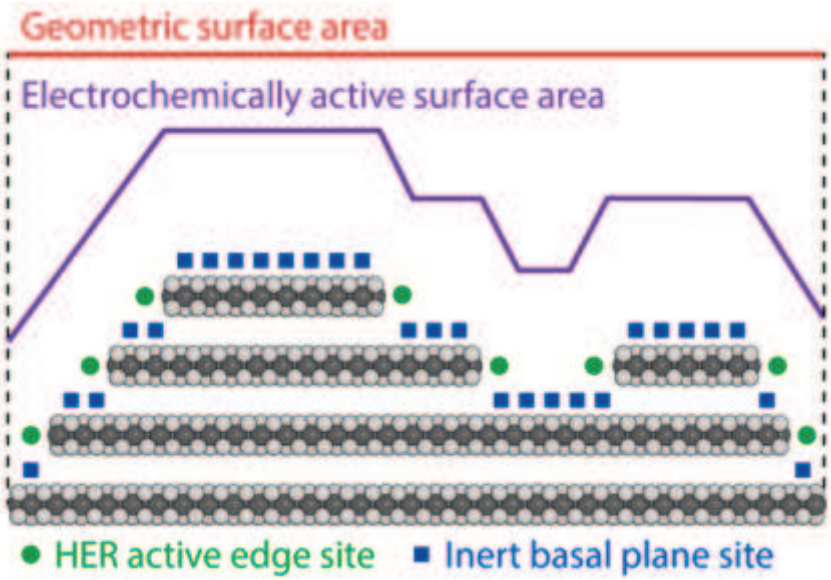

Figure 1-9: *Representation of the electrochemically active surface area (ECSA) of MoS_2 as depicted by Benck et al.*[31] *compared with the geometric surface area.*

1.4.4. Volcano Plot Analysis

From Sabatier's principle, it follows that the energy of hydrogen adsorption should neither be too high nor too low. At excessively endothermic (high) energies, adsorption of hydrogen on the catalyst substrate is slow; at particularly exothermic (low) energies, desorption is slow, thus the overall rate is limited in both cases. In other words, hydrogen must bind strongly enough to the catalyst surface in order for the reaction to take place, but if the binding energy is too strong, then the product cannot desorb. On the other hand, if the binding energy is too weak, then the hydrogen will be unable to bind to the catalyst surface, and no reaction will take place. For the HER, the maximum efficiency is achieved at the equilibrium potential when the free energy of hydrogen adsorption is close to zero.[34]

A trend which led to the identification of possible electrocatalysts for the HER was first identified by Trasatti[35] in 1971, who coined the 'Volcano plot' correlation of HER exchange current densities of various metals with their chemisorption energy of hydrogen. The exchange current density is unanimous with the reaction rate at the equilibrium potential, and is extrapolated from the Tafel slope at $\eta = 0$ V. Figure 1-10 illustrates Trasatti's Volcano plot, as recreated by Roger *et al.*[35,36]

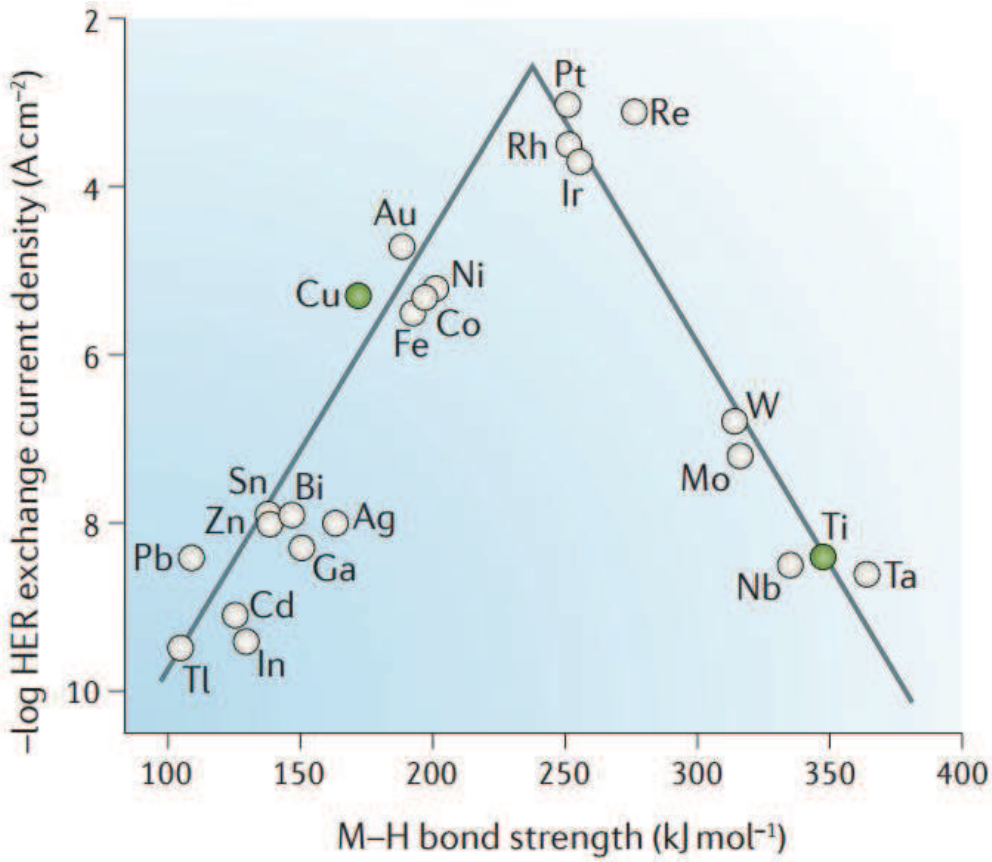

Figure 1-10: *Trasatti's HER Volcano plot as recreated by Roger et al.*[36] *using data obtained by Trasatti.*[35] *Exchange current densities for the HER are plotted as a function of the energy of the intermediate metal-hydrogen bond formed between adsorbed H and the electrode surface.*

Trasatti's Volcano plot follows Sabatier's principle, *i.e.* there is an optimum binding energy at which the maximum catalytic activity is achieved. In terms of this volcano plot, platinum unsurprisingly falls at the apex, thus indicating that the optimum catalytic activity is achieved by materials which bind hydrogen neither too strongly nor too weakly to the surface.[37]

1.4.5. Mechanism of Hydrogen Evolution

In order for hydrogen to be evolved, it must adsorb on to the surface of the electrocatalyst for the reaction to take place, and subsequently desorb, allowing for the release of the gaseous product. There are two possible mechanisms through which the evolution of hydrogen can occur in acidic media, namely the Volmer-Tafel and Volmer-Heyrovsky mechanisms.[38]

Both mechanisms involve the Volmer step (Equation 21), otherwise known as the discharge step. This involves the initial adsorption of protons from the acidic electrolyte on to the catalyst surface to form adsorbed H (H_{ad}). The Volmer step is usually considered to be fast, with the rate determining step being either of the two subsequent steps.[38] These two possible routes are the Tafel step (Equation 22) or the Heyrovsky step (Equation 23).[39]

$$H^+ + e^- \rightarrow H_{ads} \quad (21)$$

$$H_{ads} + H_{ads} \rightarrow H_2 \quad (22)$$

$$H_{ads} + H^+ + e^- \rightarrow H_2 \quad (23)$$

Platinum is known to occur *via* the Volmer-Tafel mechanism, with the Tafel step, also known as the recombination step, being rate-limiting. This step involves the combination of two adsorbed H_{ads} species and can be predicted to occur when a Tafel slope of ~30 mV dec^{-1} is obtained.

Alternatively, the Heyrovsky step involves ion-atom recombination during which a proton reacts with adsorbed hydrogen on the catalyst surface before producing hydrogen gas. Provided the Volmer reaction is fast, the Tafel slope for the Volmer-Heyrovsky reaction mechanism is approximately 40 mV dec^{-1}. In some instances, the Volmer step may be rate-limiting, in which case the Tafel slope is expected to be ~120 mV dec^{-1}.[40] The underlying electrochemical processes which described the mechanism of hydrogen evolution are illustrated in Figure 1-11.[41]

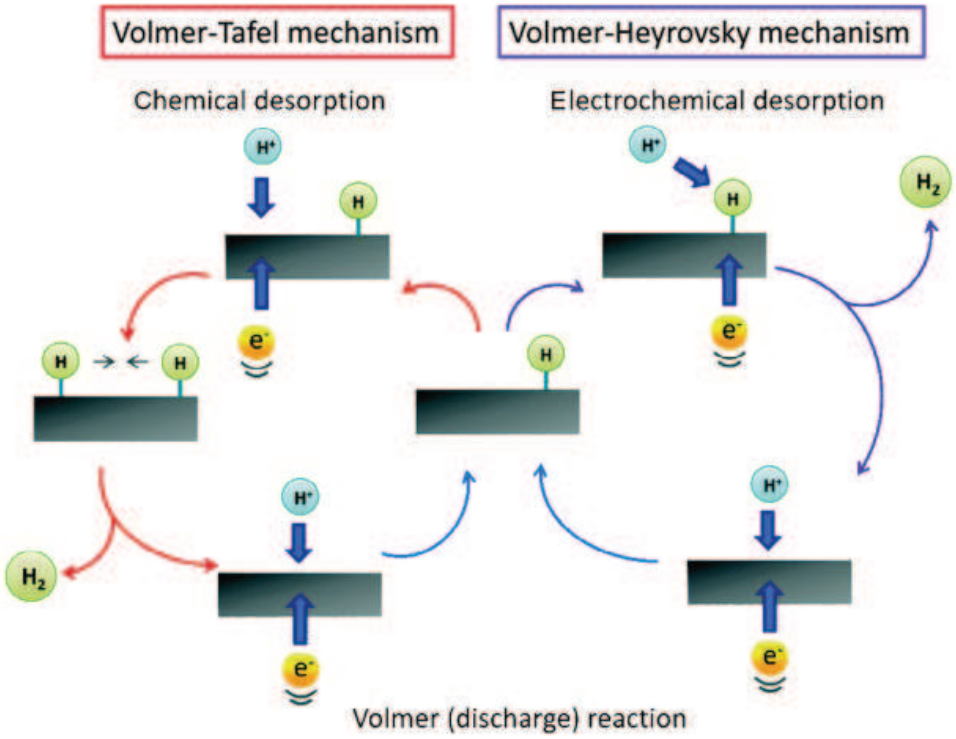

Figure 1-11: *Illustration of the Volmer-Tafel and Volmer-Heyrovsky mechanisms of hydrogen evolution reaction in acidic media.*[41]

1.4.6. Molybdenum Disulfide

Following the discussion on volcano plot analysis, Hinnemann *et al.*[42] expanded on this work several years later. The authors applied density functional theory (DFT) to uncover materials which encountered a free energy change, associated with the bonding of atomic hydrogen to the catalyst surface, close to zero. In doing so, they proposed that MoS_2 lies close to platinum on Trasatti's volcano plot (Figure 1-12), and hence predicted that it would be a promising catalytic material.

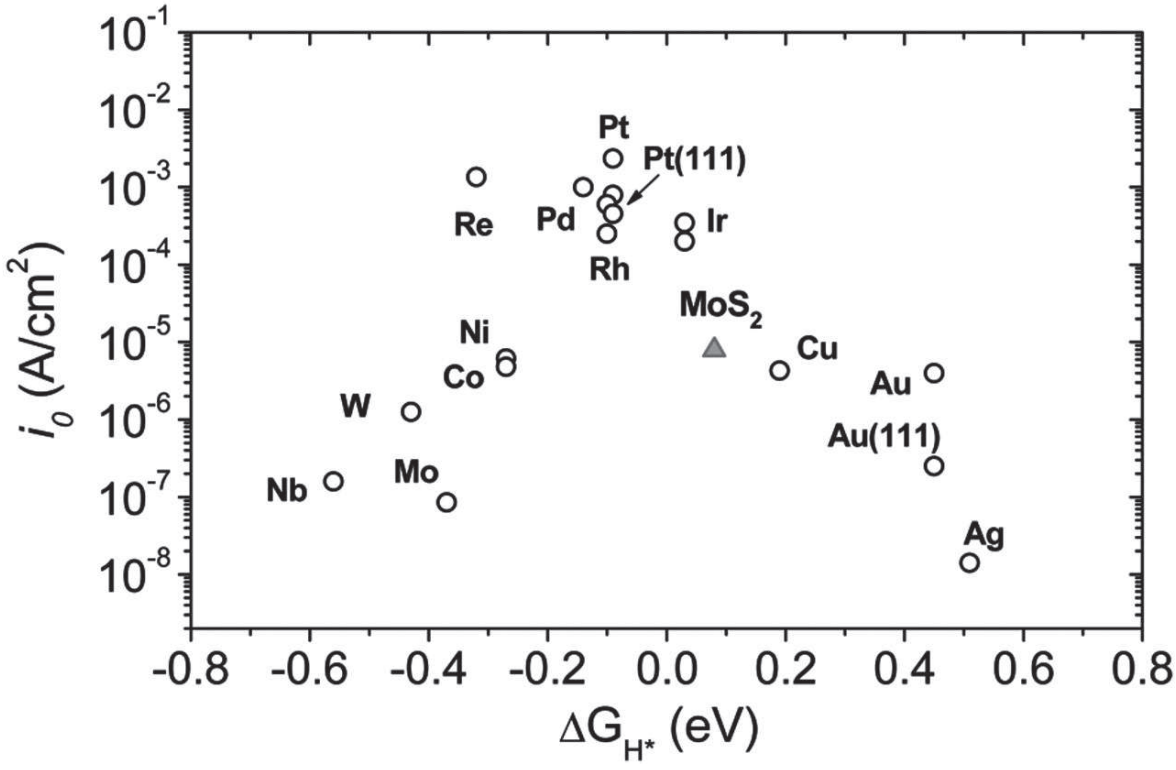

Figure 1-12: *Volcano plot of the exchange current densities as a function of the Gibbs free energy (as calculated by DFT) of adsorbed atomic hydrogen for MoS_2 nanoparticles compared with the pure metals.*[43]

MoS_2 exists naturally in the bulk form as the semiconducting hexagonal (2H) phase, with layers of S-Mo-S sandwiched together through weak van der Waals bonding. These layers consist of two possible active sites: edge sites and the basal plane. The proposal that MoS_2 would be a suitable candidate for the replacement of platinum was initially surprising, as bulk MoS_2 is known to be an inherently poor electrocatalyst for the HER.[44,45] However, the promising activity of MoS_2 was later confirmed experimentally by Jaramillo *et al.*[43] who identified the edge sites as being the active component of MoS_2. This study varied the fractions of active sites and found that the catalytic activity increased with increasing number

of edge sites. Therefore, the active component of MoS_2 has been widely acknowledged to be the edge site, while the basal plane is considered catalytically inert.[46] However, since the material consists largely of the inert basal plane, the activity of 2H-MoS_2 is limited by the density and reactivity of the edge sites.[47,48] The activity of the edge sites has been attributed to their favourable Gibbs free energy of hydrogen adsorption (ΔG_H = 0.08 eV), while the basal plane exhibits a ΔG_H value as high as 2 eV.[42,49] These findings indicate a site-dependency of the Gibbs free energy value, thus subsequent site engineering by nanostructuring is commonly used to increase the number of edge sites. Therefore, a plethora of studies have stemmed from this theory and has led to the exposure of the edges in a variety of catalytically active transition metal dichalcogenide (TMDC) materials.[32,50–53] In doing so, the electrocatalytic activity towards the HER has been found to substantially improve as the number of edge sites increases. Table 1-1 shows a comparison of the overpotentials and Tafel slopes of current state-of-the-art MoS_2 HER electrocatalysts. However, despite the promisingly low overpotentials required for $j = -10$ mA cm^{-2}, the activity of 2H-MoS_2 is still limited by the poor electrical transport associated with its semiconducting nature and inefficient electrical contact to the substrate.[48]

Table 1-1: *Comparison of HER activity in current state-of-the-art MoS_2 electrocatalysts.*

Catalyst	**V (vs. NHE) at j = 10 mA cm^{-2}**	**Tafel Slope (mV dec^{-1})**	**Reference**
Double gyroid MoS_2	0.28 V	50	[32]
MoS_2 Nanoparticles	0.17 V	55-60	[43]
Exfoliated 1T-MoS_2 Nanosheets	0.19 V	43	[29]
MoS_2/RGO	0.16 V	41	[51]
Amorphous MoS_2	0.20 V	60	[54]
$[Mo_3S_{13}]^{2-}$ nanoclusters on carbon supports	0.18 – 0.22 V	38-57	[55]
Cu_7S_4@MoS_2 Hetero-nanoframes	0.13 V	48	[56]
Defect-rich MoS_2 nanosheets	0.2 V	50	[57]

MoS_2 and several other TMDCs exist in a variety of polymorphs. As discussed above, early efforts into the initial use of MoS_2 as an HER electrocatalyst have focused on the edge-site exposure of the naturally occurring 2H-MoS_2. This hexagonal phase is semiconducting and is comprised of MoS_6 trigonal prisms. However, MoS_2 also exists as the 1T-MoS_2 polymorph, consisting of edge sharing MoS_6 octahedra.[58] A comparison of the crystal structure of the 2H and 1T polymorphs is shown in Figure 1-13. This 1T-MoS_2 polymorph is metastable and, due to the rearrangement of the crystal structure, is metallic in character, thus offering drastically different catalytic properties to its semiconducting counterpart.

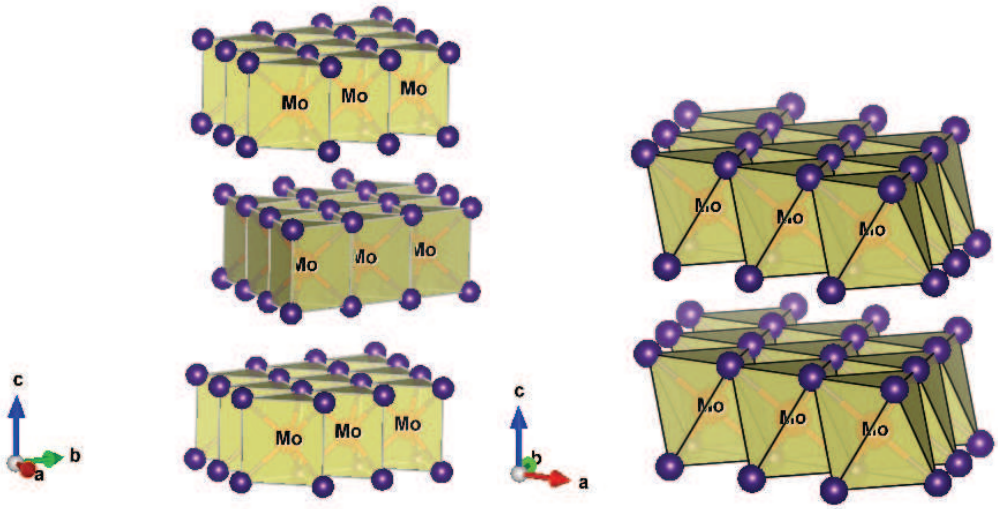

Figure 1-13: *Crystals structure of* ***left)*** *trigonal prismatically coordinated 2H-MoS_2 and* ***right)*** *octahedrally coordinated 1T-MoS_2.*

However, 1T-MoS_2 does not exist naturally, and often requires complex synthetic procedures in order to be obtained. Arguably the most common method of transitioning from 2H- to 1T-MoS_2 is chemical exfoliation *via* lithium intercalation. The transition is a result of an electron transfer from intercalated lithium, inducing a d^2 to d^3 transition, which in turn leads to the destabilisation of the thermodynamically favoured trigonal prismatic coordination.[59] Instead, the octahedrally coordinated 1T-MoS_2 is now favoured, with the emergence of a metallic character associated with the change in crystal symmetry (Figure 1-14).[60]

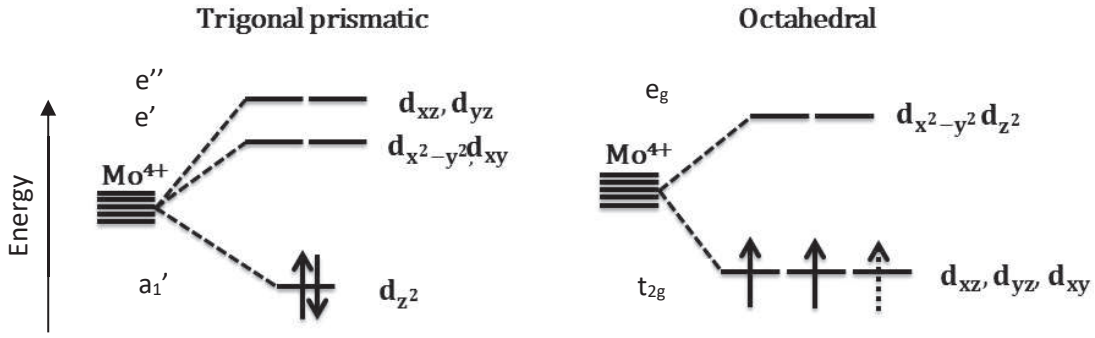

Figure 1-14: *d orbital splitting diagrams showing the trigonal prismatic coordination of 2H-MoS_2 resulting in semiconducting behaviour and the octahedral coordination of 1T-MoS_2 leading to metallic properties. The dashed arrow indicates the electron transfer from intercalated lithium which is the origin of the transition.*

This method of preparing 1T-MoS_2 also raises several concerns. In addition to the reverse transformation into the 2H phase, chemical exfoliation *via* lithium intercalation requires complex chemical procedures and may lead to a compromised chemical composition.[61] Likewise, due to the low thermodynamic stability, isolation of the phase pure metallic product remains a significant challenge.[58] These factors therefore make the origin of the catalytic activity difficult to fully comprehend. The activity may arise due to an increase in conductivity associated with the metallic phase; an increased surface area upon chemical exfoliation which renders the bulk material into a nanostructured catalyst; or due to compositional changes as a result of lithium intercalation. In order to understand the origin of the catalytic activity, which may then aid the development of future catalysts; the uncertainties surrounding MoS_2 need to be de-convoluted.

1.5. Aims

This thesis aims to understand the origin of catalytic activity in 2D transition metal dichalcogenides. To do this, a strategic investigation of the role of the active sites needs to be employed. Work in this study therefore seeks to identify and test an electrocatalytic material which can deliver selective control over morphology and structure. In this way, the electrocatalytic activity of differing polymorphs may be investigated, with the coordination geometry of the material being the sole source of varying activity. Further, gaining insight into the correlation between structure / morphology and electrochemical performance forms the basis of this research.

1.6. References

1. Olah, G. A. Beyond Oil and Gas: The Methanol Economy. *Angew. Chemie Int. Ed.* **44**, 2636–2639 (2005).

2. Schiffer, H. W. WEC energy policy scenarios to 2050. *Energy Policy* **36**, 2464-2474 (2008).

3. Turner, J. A realizable renewable energy future. *Science* **285**, 687–9 (1999).

4. Schultz, M. G., Diehl, T., Brasseur, G. P. & Zittel, W. Air Pollution and Climate-Forcing Impacts of a Global Hydrogen Economy. *Science* **302**, 624–627 (2003).

5. Bockris, J. O. M. A hydrogen economy. *Science* **176**, 1323 (1972).

6. Bahruji, H., Euiz Esquius, J., Bowker, M., Hutchings, G., Armstrong, R. D. & Jones, W. Solvent Free Synthesis of PdZn/TiO2 Catalysts for the Hydrogenation of CO2 to Methanol. *Top. Catal.* **61**, 144–153 (2018).

7. CO_2 emissions from cars: facts and figures (infographics): News: European Parliament. *CO_2 emissions from cars: facts and figures (infographics) | News | European Parliament* (2019). Available at: https://www.europarl.europa.eu/news/en/headlines/society/20190313STO31218/co2-emissions-from-cars-facts-and-figures-infographics. (Accessed: 7th April 2020).

8. Sakintuna, B., Lamari-Darkrim, F. & Hirscher, M. Metal hydride materials for solid hydrogen storage: A review. *Int. J. Hydrogen Energy* **32**, 1121–1140 (2007).

9. Graetz, J. New approaches to hydrogen storage. *Chem. Soc. Rev.* **38**, 73–82 (2009).

10. Neef, H. J. International overview of hydrogen and fuel cell research. *Energy* **34**, 327–333 (2009).

11. Chisholm, G. & Cronin, H. *Hydrogen from water electrolysis*. 441-457 (2017)

12. Liguras, D. K., Kondarides, D. I. & Verykios, X. E. Production of hydrogen for fuel cells by steam reforming of ethanol over supported noble metal catalysts. *Appl. Catal. B Environ.* **43**, 345-354 (2003).

13. Koytsoumpa, E. I., Bergins, C. & Kakaras, E. The CO_2 economy: Review of CO_2

capture and reuse technologies. *J. Supercrit. Fluids* **132**, 3–16 (2017).

14. Koytsoumpa, E. I., Bergins, C., Buddenberg, T., Wu, S., Sigurbjörnsson, Ó., Tran, K. C. & Kakaras, E. The Challenge of Energy Storage in Europe: Focus on Power to Fuel. *J. Energy Resour. Technol.* **138**, 042002 (2016).

15. Trasatti, S. Water electrolysis: Who first? *J. Electroanal. Chem.* **476**, 90–91 (1999).

16. Kelly, N. A. Hydrogen production by water electrolysis. *Adv. Hydrog. Prod. Storage Distrib.* 159–185 (2014).

17. Barbir, F. PEM electrolysis for production of hydrogen from renewable energy sources. *Sol. Energy* **78**, 661–669 (2005).

18. Broka, K. & Ekdunge, P. Oxygen and hydrogen permeation properties and water uptake of Nafion® 117 membrane and recast film for PEM fuel cell. *J. Appl. Electrochem.* **27**, 117–123 (1997).

19. Millet, P. in *Hydrogen Production: By Electrolysis* 63-116 (wiley, 2015).

20. Inamuddin, Mohammad, A. & Asiri, A. M. *Organic-inorganic composite polymer electrolyte membranes: Preparation, properties, and fuel cell applications.* 1–460 (Springer International Publishing, 2017).

21. Carmo, M., Fritz, D. L., Mergel, J. & Stolten, D. A comprehensive review on PEM water electrolysis. *Int. J. Hydrogen Energy* **38**, 4901–4934 (2013).

22. Schalenbach, M., Carmo, M., Fritz, D. L., Mergel, J. & Stolten, D. Pressurized PEM water electrolysis: Efficiency and gas crossover. *Int. J. Hydrogen Energy* **38**, 14921–14933 (2013).

23. Ghassemzadeh, L., Kreuer, K. D., Maier, J. & Müller, K. Chemical degradation of Nafion membranes under mimic fuel cell conditions as investigated by solid-state NMR spectroscopy. *J. Phys. Chem. C* **114**, 14635–14645 (2010).

24. Symes, M. D. & Cronin, L. Decoupling hydrogen and oxygen evolution during electrolytic water splitting using an electron-coupled-proton buffer. *Nat. Chem.* **5**, 403–409 (2013).

25. Yekini Suberu, M., Wazir Mustafa, M. & Bashir, N. Energy storage systems for renewable energy power sector integration and mitigation of intermittency. *Renew.*

Sustain. Energy Rev. **35**, 499–514 (2014).

26. Leadbetter, J. & Swan, L. Battery storage system for residential electricity peak demand shaving. *Energy Build.* **55**, 685–692 (2012).

27. McCrory, C. C. L., Jung, S., Ferrer, I. M., Chatman, S. M., Peters, J.C. & Jaramillo, T. F. Benchmarking Hydrogen Evolving Reaction and Oxygen Evolving Reaction Electrocatalysts for Solar Water Splitting Devices. *J. Am. Chem. Soc.* **137**, 4347–4357 (2015).

28. Luo, J., Im, J-H., Mayer, M. T., Schreier, M., Khaja Nazeeruddin, M., Park, N-G., Tilley, S. D., Jin Fan, H. & Grätzel, M. Water photolysis at 12.3% efficiency via perovskite photovoltaics and Earth-abundant catalysts. *Science* **345**, 1593–1596 (2014).

29. Lukowski, M. A., Daniel, A. S., Meng, F., Forticaux, A., Li, L. and Jin, S. Enhanced Hydrogen Evolution Catalysis from Chemically Exfoliated Metallic MoS_2 Nanosheets. *J. Am. Chem. Soc.* **135**, 10274-10277 (2013).

30. Yang, C. J. An impending platinum crisis and its implications for the future of the automobile. *Energy Policy* **37**, 1805–1808 (2009).

31. Benck, J. D., Hellstern, T. R., Kibsgaard, J., Chakthranont, P. & Jaramillo, T. F. Catalyzing the hydrogen evolution reaction (HER) with molybdenum sulfide nanomaterials. *ACS Catal.* **4**, 3957–3971 (2014).

32. Kibsgaard, J., Chen, Z., Reinecke, B. N. & Jaramillo, T. F. Engineering the surface structure of MoS_2 to preferentially expose active edge sites for electrocatalysis. *Nat. Mater.* **11**, 963–969 (2012).

33. Kong, D., Wang, H., Cha, J. J., Pasta, M., Koski, K. J., Yao, J. & Cui, Y. Synthesis of MoS_2 and $MoSe_2$ Films with Vertically Aligned Layers. *Nano Lett.* **13**, 1341-1347 (2013).

34. Quaino, P., Juarez, F., Santos, E. & Schmickler, W. Volcano plots in hydrogen electrocatalysis-uses and abuses. *Beilstein J. Nanotechnol.* **5**, 846–854 (2014).

35. Trasatti, S. Work function, electronegativity, and electrochemical behaviour of metals. II. Potentials of zero charge and 'electrochemical' work functions. *J. Electroanal. Chem.* **33**, 351–378 (1971).

36. Roger, I., Shipman, M. A. & Symes, M. D. Earth-abundant catalysts for electrochemical and photoelectrochemical water splitting. *Nat. Rev. Chem.* **1**, 3 (2017).

37. Laursen, A. B., Sofia Varela, A., Dionigi, F., Fanchiu, H., Miller, C., Trinhammer, O. L., Rossmeisl, J. & Dahl, S. Electrochemical Hydrogen Evolution: Sabatier's Principle and the Volcano Plot. *J. Chem. Educ.* **89**, 1595–1599 (2012).

38. Tang, Q. & Jiang, D. Mechanism of Hydrogen Evolution Reaction on 1T-MoS_2 from First Principles. *ACS Catal.* **6**, 4953-4961 (2016).

39. Skúlason, E., Karlberg, G. S., Rossmeisl, J., Bligaard, T., Greeley, J., Jónsson & Nørskov, J. K. Density functional theory calculations for the hydrogen evolution reaction in an electrochemical double layer on the Pt (111) electrode. *Phys. Chem. Chem. Phys.* **9**, 3241–3250 (2007).

40. Markovi, N. M., Grgur, B. N. & Ross, P. N. Temperature-Dependent Hydrogen Electrochemistry on Platinum Low-Index Single-Crystal Surfaces in Acid Solutions. *J. Phys. Chem. B* **101**, 5405-5413 (1997).

41. Morales-Guio, C. G., Stern, L. A. & Hu, X. Nanostructured hydrotreating catalysts for electrochemical hydrogen evolution. *Chem. Soc. Rev.* **43**, 6555–6569 (2014).

42. Hinnemann, B., Georg Moses, P., Bonde, J., Jørgensen, K. P., Nielsen, J. H., Horch, S., Chorkendorff, I. & Nørskov, J. K. Biomimetic Hydrogen Evolution: MoS_2 Nanoparticles as Catalyst for Hydrogen Evolution. *J. Am. Chem. Soc.* **127**, 5308–5309 (2005).

43. Jaramillo, T. F., Jørgensen, K. P., Bonde, J., Nielsen, J. H., Horch, S. & Chrokendorff, I. Identification of Active Edge Sites for Electrochemical H_2 Evolution from MoS_2 Nanocatalysts. *Science* **317**, 100–102 (2007).

44. Jaegermann, W. & Tributsch, H. Interfacial properties of semiconducting transition metal chalcogenides. *Progress in Surface Science* **29**, 1–167 (1988).

45. Merki, D., Fierro, S., Vrubel, H. & Hu, X. Amorphous molybdenum sulfide films as catalysts for electrochemical hydrogen production in water. *Chem. Sci.* **2**, 1262 (2011).

46. Greeley, J., Jaramillo, T. F., Bonde, J., Chorkendorff, I. & Norskov, J. K.

Computational high-throughput screening of electrocatalytic materials for hydrogen evolution. *Nat. Mater.* **5**, 909–913 (2006).

47. Albu-Yaron, A., Levy, M., Tenne, R., Popovitz-Biro, R., Weidenbach, M., Bar-Sadan, M., Houben, L., Enyashin, A. N., Seifert, G., Feuermann, D., Katz, E. A. & Gordon, J. M. MoS_2 Hybrid Nanostructures: From Octahedral to Quasi-Spherical Shells within Individual Nanoparticles. *Angew. Chem. Int. Ed.* **50**, 1810–1814 (2011).

48. Voiry, D., Yamaguchi, H., Li, J., Silva, R., Alves, D. C. B., Fujita, T., Chen, M., Asefa, T., shenoy, V. B., Eda, G. & Chhowalla, M. Enhanced catalytic activity in strained chemically exfoliated WS_2 nanosheets for hydrogen evolution. *Nat. Mater.* **12**, 850–855 (2013).

49. Tsai, C., Chan, K., Nørskov, J. K. & Abild-Pedersen, F. Theoretical insights into the hydrogen evolution activity of layered transition metal dichalcogenides. *Surf. Sci.* **640**, 133–140 (2015).

50. Vrubel, H., Merki, D. & Hu, X. Hydrogen evolution catalyzed by MoS_3 and MoS_2 particles. *Energy Environ. Sci.* **5**, 6136-6144 (2012).

51. Li, Y., Wang, H., Xie, L., Liang, Y., Hong, G. & Dai, H. MoS_2 Nanoparticles Grown on Graphene: An Advanced Catalyst for the Hydrogen Evolution Reaction. *J. Am. Chem. Soc.* **133**, 7296-7299 (2011).

52. Faber, M. S., Dziedzic, R., Lukowski, M. A., Kaiser, N. S., Ding, Q. & Jin, S. High-Performance Electrocatalysis Using Metallic Cobalt Pyrite (CoS_2) Micro- and Nanostructures. *J. Am. Chem. Soc.* **136**, 10053–10061 (2014).

53. Kiran, V., Mukherjee, D., Jenjeti, R. N. & Sampath, S. Active guests in the MoS_2/$MoSe_2$ host lattice: Efficient hydrogen evolution using few-layer alloys of MoS2(1-x)Se2x. *Nanoscale* **6**, 12856–12863 (2014).

54. Benck, J. D., Chen, Z., Kuritzky, L. Y., Forman, A. J. & Jaramillo, T. F. Amorphous Molybdenum Sulfide Catalysts for Electrochemical Hydrogen Production: Insights into the Origin of their Catalytic Activity. *ACS Catal.* **2**, 1916-1923 (2012).

55. Kibsgaard, J., Jaramillo, T. F. & Besenbacher, F. Building an appropriate active-site motif into a hydrogen-evolution catalyst with thiomolybdate $[Mo_3S_{13}]^{2-}$ clusters. *Nat. Chem.* **6**, 248–253 (2014).

56. Fominykh, K., Feckl, J. M., Döblinger, M., Böcklein, S., Ziegler, B., Peter, L., Rathousky, J., Scheidt, E-W., Bein, T. & Fattakhova-Rohlfing, D. Ultrasmall Dispersible Crystalline Nickel Oxide Nanoparticles as High-Performance Catalysts for Electrochemical Water Splitting. *Adv. Funct. Mater.* **24**, 3123–3129 (2014).

57. Yin, Y., Han, J., Zhang, Y., Zhang, X., Xu, P., Yuan, Q., Samad, L., Wang, X., Wang, Y., Zhang, Z., Zhang, P., Cao, X., Song, B. & Jin, S. Contributions of Phase, Sulfur Vacancies, and Edges to the Hydrogen Evolution Reaction Catalytic Activity of Porous Molybdenum Disulfide Nanosheets. *J. Am. Chem. Soc.* **138**, 7965–7972 (2016).

58. Fang, Y., Pan, J., He, J., Luo, R., Wang, D., Che, X., Bu, K., Zhao, W., Liu, P., Mu, G., Zhang, H., Lin, T. & Huang, F. Structure Re-determination and Superconductivity Observation of Bulk 1T MoS_2. *Angew. Chem. Int. Ed.* **57**, 1232–1235 (2018).

59. Py, M. A. & Haering, R. R. Structural destabilization induced by lithium intercalation in MoS_2 and related compounds. *Can. J . Phys* **61**, (1983).

60. Kertesz, M. & Hoffmann, R. Octahedral vs. Trigonal-Prismatic Coordination and Clustering in Transition-Metal Dichalcogenides. *J. Am. Chem. Soc.* **106**, 3453–3460 (1984).

61. Heising, J. & Kanatzidis, M. G. Exfoliated and Restacked MoS_2 and WS_2: Ionic or Neutral Species? Encapsulation and Ordering of Hard Electropositive Cations. *J. Am. Chem. Soc.* **121**, 11720–11732 (1999).

2. Experimental Methods

2.1. Synthesis of $MoTe_2$

All $MoTe_2$ materials were prepared using a stoichiometric mixture of elemental molybdenum (Sigma Aldrich, 99.95%) and tellurium (Alfa Aesar, 99.999%) unless otherwise stated. The powders were sealed under a vacuum pressure of 4.5×10^{-2} mbar in a quartz ampoule which was carefully shaken in order to homogenise the mixture.

2.1.1. Crystalline 1T'-$MoTe_2$

Preparation of crystalline 1T'-$MoTe_2$ consisted of heating the elemental powders at 900 °C with a heating rate of 5 °C min^{-1} for a total of 19 hours. After this time, the ampoule and its contents were quenched in water before being ground with a mortar and pestle.

2.1.2. Crystalline 2H-$MoTe_2$

2H-$MoTe_2$ was synthesized by subsequent reannealing of crystalline 1T'-$MoTe_2$ at 700 °C with a heating rate of 5 °C min^{-1} for 24 hours. The ampoule and its contents were then allowed to cool naturally to room temperature. After this time, the powders were ground in a mortar and pestle before analysis.

2.1.3. Nanocrystalline 1T'-$MoTe_2$

Nanocrystalline 1T'-$MoTe_2$ was prepared in a similar manner to the crystalline 1T'-$MoTe_2$ material, with the temperature being lowered to 400 °C (heating rate of 5 °C min^{-1}). After 16 hours of reaction at this temperature, the resulting powders were cooled to room temperature naturally and ground with a mortar and pestle. These powders were subsequently reannealed under identical conditions.

2.1.4. Nanocrystalline 2H-$MoTe_2$

A nanocrystalline variant of 2H-$MoTe_2$ was synthesized by reannealing nanocrystalline 1T'-$MoTe_2$. This involved heating the powders at 500 °C with a heating rate of 5 °C min^{-1} for a total of 72 hours to ensure the complete conversion from 1T'- to 2H-$MoTe_2$. The powders were subsequently ground by a mortar and pestle.

2.2. Characterisation

2.2.1. Powder X-Ray Diffraction (PXRD)

Powder X-Ray Diffraction (PXRD) was performed on a Panalytical Xpert-pro diffractometer with Cu K_α (λ = 1.54178 Å) operating in Bragg-Brentano geometry. The powdered sample was centered on a bracket and diffraction patterns were measured between 10 ° and 65 ° with a step size of 0.016 ° and time per step of 2 ° min^{-1} . PXRD was performed directly on the electrode surface for *ex-situ* stability studies using the fabricated bracket as depicted in Figure 2-1. In these measurements, the diffraction patterns were measured between 10 ° and 30 ° with a step size of 0.016 ° and time per step of 0.75 ° min^{-1}. The phase purity of the diffraction patterns were analysed by comparing the measured patterns with those calculated from the Inorganic Crystal Structure Database (ICSD).

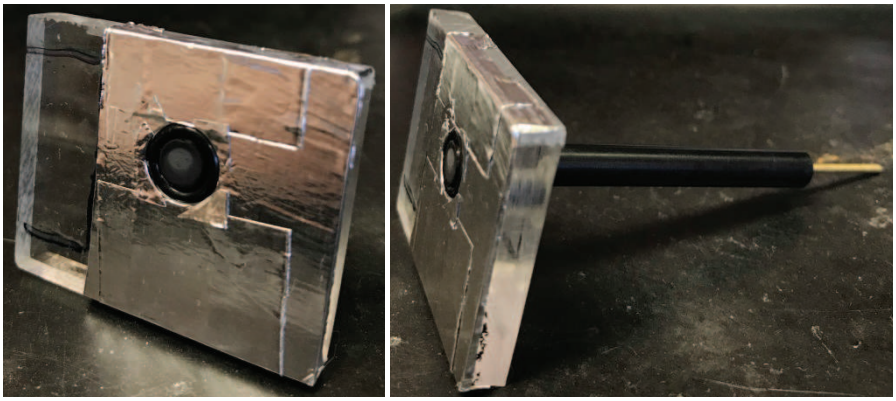

Figure 2-1: *Fabricated bracket designed for the ex-situ characterisation of the catalyst by PXRD directly on the electrode surface before and after electrochemical measurements.*

2.2.2. Synchrotron powder XRD

Synchrotron powder X-ray diffraction (SXRD) data were collected at ambient temperature from powder loaded into 0.3 mm capillaries using the ID22 beamline [λ=0.3998490(1) Å] at the European Synchrotron Radiation Facility (ESRF). Before the powder was loaded, it was reground with glass powder to minimize the adsorption and preferred orientation. However, despite all efforts to eliminate the preferred orientation, it still had a significant impact as revealed by high intensity of the associated peaks. Therefore, only LeBail refinements of the SXRD were performed by using the GSAS/ EXPGUI software package.[1] Experimental data was collected by Dr. Irene Cascallana-Matías and refinement was carried out by Dr. Alexey Ganin.

2.2.3. Powder Neutron Diffraction (PND)

Time-of-flight PND measurements were performed on the General Materials (GEM) diffractometer at the ISIS Facility of the Rutherford Appleton Laboratory, UK. Samples were loaded in 0.7 mm diameter quartz capillaries and data was collected at room temperature.

2.2.4. Raman Spectroscopy

Raman spectroscopy was performed using a Horiba Jobin-Yvon LabRam Raman HR800 operating with a 532 nm laser. An aperture size of 100 µm and a 1% filter was used in order to prevent sample degradation. Spectra were measured between the range of 50 and 1000 cm^{-1}. Measurements were taken directly on the electrode surface.

For *ex-situ* stability studies, *i.e.* Chapter 3, Section 3.3.2.4., Raman spectroscopy was performed directly on the electrode surface after electrochemical measurements. To do this, the catalyst ink was deposited on a glassy carbon electrode and inserted into a fabricated holder for the Raman spectrometer. This allowed for the electrode to be flush with the surface, and is depicted in Figure 2-2. *In operando* Raman measurements (Chapter 6, Section 6.3.2.) were performed using two cells (depending on electrode substrate) as depicted in Figure 2-3.

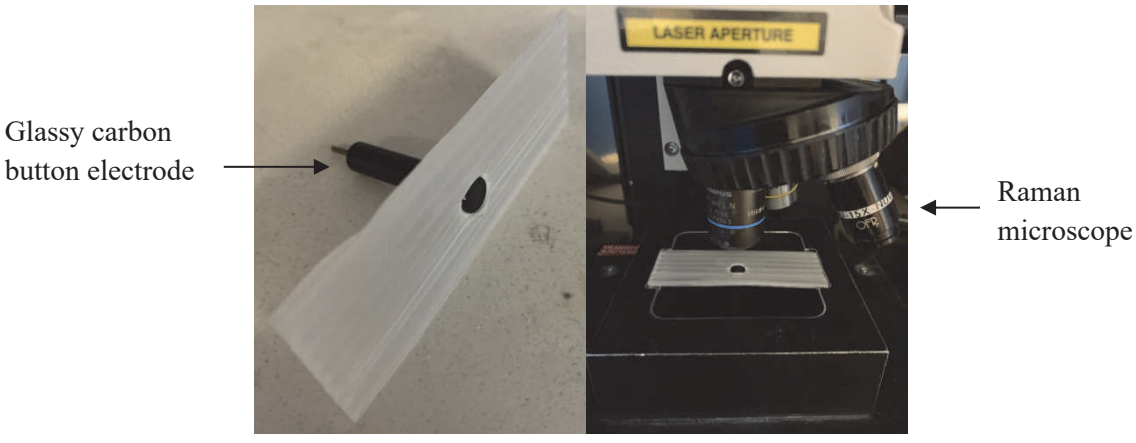

Figure 2-2: *Setup for ex-situ Raman spectroscopy measurements. Catalysts were studied directly on the electrode surface before and after electrochemical measurements.*

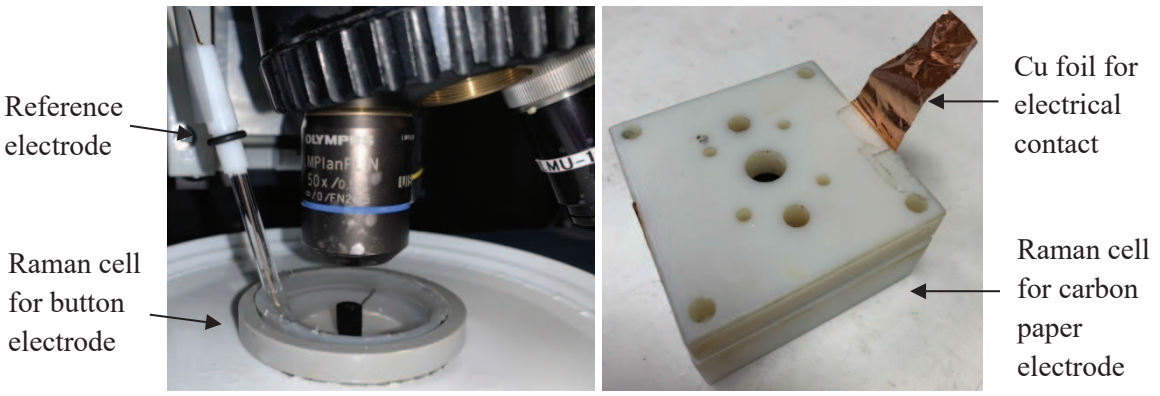

Figure 2-3: *Fabricated in operando Raman cells for use with* ***left)*** *glassy carbon working electrode and* ***right)*** *carbon paper working electrode.*

2.2.5. Scanning Electron Microscopy coupled with Energy Dispersive X-Ray Spectroscopy (SEM / EDX)

Scanning Electron Microscopy (SEM) images were obtained using a Phillips XL30 ESEM instrument coupled with an Oxford Instruments X-act spectrometer for Energy Dispersive X-Ray (EDX) measurements. The EDX was calibrated using the INCA software with Cu as the calibration standard.

For an accurate comparison of the samples before and after electrochemical measurements, the samples were prepared as catalyst inks and allowed to dry on the surface of the glassy carbon electrode. The material was then carefully scraped off the surface of the electrode for analysis of the material before electrochemical measurements and afterwards. These powders were dispersed in ethanol and deposited on copper foil for analysis by SEM / EDX. It should be noted that the materials studied were deemed as being stable in air.

2.2.6. Transmission Electron Microscopy (TEM)

Transmission electron microscopy micrographs were obtained using a FEI Tecnai G2 F30 S-twin equipped with a 300 kV field emission gun. Diffraction pattern simulations were performed using JEMS.[2] All TEM measurements were performed by Dr. Torben Dankwort at the University of Kiel in Germany.

2.2.7. Inductively Couple Plasma – Optical Emission Spectroscopy (ICP-OES)

ICP-OES was conducted using an Agilent 5100 ICP-OES instrument calibrated to a range of known-concentration (ppm) solutions of Mo and Te. Comparisons were made between activated and non-activated samples by preparing the catalysts directly on the electrode surface. The samples were carefully scraped off of the surface of the glassy carbon working electrode and digested in 0.5 mL concentrated nitric acid (ICP reagent grade) and made up to 10 mL with deionised water. All ICP-OES measurements were performed by Dr. Ross Winter at the University of Glasgow.

2.2.8. X-Ray Photoelectron Spectroscopy (XPS)

1T'-$MoTe_2$ samples were carefully packed and sent to the National EPSRC XPS Users' Service (NEXUS) at Newcastle University, UK. XPS spectra were acquired with a K-Alpha instrument (Thermo Scientific, East Grinstead, UK), using a micro-focused monochromatic AlKα source (X-ray energy 1486.6 eV, spot size 400 × 800 microns). The emission angle was zero degrees and the pass energy was 200 eV for surveys and 40 eV for high resolution. Charge neutralization was enabled. The resulting spectra were referenced to the adventitious C 1s peak (285.0 eV) and were analysed using the free-to-download CasaXPS software package. These measurements were carried out on samples which were dispersed in ethanol and deposited on copper foil.

Additional XPS data collection was performed at the EPSRC National Facility for XPS ("Harwell XPS") operated by Cardiff University and University College London, under contract no. PR16195. In this case, samples were prepared directly on the electrode surface and packed under inert atmosphere. In both non-activated and activated cases, the electrodes were subjected to four reductive potential cycles in 1 M H_2SO_4 (which was degassed under a flow of nitrogen) in order to remove the oxide layer from the surface. The electrodes were removed under nitrogen flow and packed under N_2 in the glove box. The samples were then sent directly on the electrodes sealed under nitrogen to avoid any oxidation in ambient conditions. The product was removed from the electrodes inside an Ar filled glove box and transferred into the XPS instrument directly from the glove box. At no point were the samples exposed to ambient conditions.

2.2.9. Infrared Spectroscopy (IR)

IR measurements (Chapter 4, Section 4.3.2.) were performed using a Bruker 66v Fourier transform instrument with a deuterated tryglicine sulfate (DTGS) detector in the far-infrared region, and a mercury cadmium telluride (MCT) detector in the mid-infrared region, with 2 cm^{-1} spectral resolution. Samples were ground and pressed into KBr pellets with 1 wt% concentration (~3 mg in 300 mg KBr) and measured in transmission mode. IR measurements were performed by Prof. Katalin Kamaras at the Hungarian Academy of Sciences.

2.2.10. X-Ray Adsorption Spectroscopy (XAS)

XAS measurements were performed at the Mo K-edge on the B18 beamline at the Diamond Light Source, Didcot, UK. Data was collected in transmission mode (to k_{max}=18) using a QEXAFS setup with a fast scanning Si(111) double crystal monochromator and ion chamber detectors, with a Mo foil placed between I_t and I_{ref}. XAS data processing was performed using IFEFFIT with the Horae package (Athena and Artemis).[3,4] The amplitude reduction factor, S_0^2 was derived from EXAFS data analysis of the Mo foil. Samples were prepared for measurement by pressing the powders mixed with cellulose into pellets; see Chapter 4, Section 4.3.1.2. Experimental data was collected by Dr. Irene Cascallana-Matías and data analysis was performed by Dr. Emma Gibson from the University of Glasgow. *In operando* XAS studies were investigated on catalyst-painted carbon paper (Chapter 6, Section 6.3.2.3.) using the electrochemical cell depicted in Figure 2-4. In this instance, experimental data was collected and analysed by Dr. Emma Gibson from the University of Glasgow.

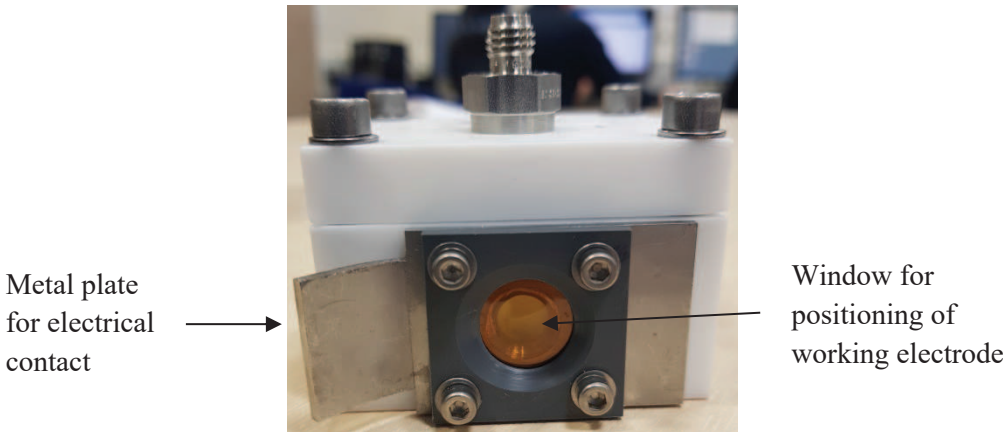

Figure 2-4: *In operando electrochemical cell available at Diamond Light Source.*

2.3. Electrochemical Measurements

2.3.1. Electrode Preparation

Electrocatalytic measurements were performed using a glassy carbon working electrode (IJ Cambria) with a surface area of 0.071 cm^2 unless otherwise stated. The glassy carbon electrode was cleaned prior to each measurement with diamond polish on an alumina pad (IJ Cambria), and electrochemically cycled in 1 M H_2SO_4 between the potential range of +1 V and −1.2 V (vs. NHE).

For electrochemical characterisation, the $MoTe_2$ samples were prepared as catalyst inks. This involved sonicating 10 mg catalyst powder in 1 mL of a 3:1 water/ethanol mixture with 80 μL Nafion™, which acts as the conductive binder to the substrate. 30 μL of this catalyst ink suspension was then drop-cast on to the surface of a glassy carbon electrode (surface area 0.071 cm^2) and left to dry overnight. This yielded a working electrode with a catalyst loading of 3.94 mg cm^{-2}.

2.3.2. Electrochemical Setup

All electrochemical measurements were performed using a Biologic SP-150 potentiostat with a single cell, three-electrode setup in 1 M H_2SO_4, unless otherwise stated. A typical three-electrode setup is shown in Figure 2-5. This involved a three-necked flask containing 1 M H_2SO_4 as the electrolyte, the catalyst-deposited glassy carbon as the working electrode, platinum wire or carbon felt (Alfa Aesar) as the counter electrode and Ag/AgCl in 3 M NaCl as the reference electrode (IJ Cambria). The electrode potentials were converted to NHE scale using:

$$E(\text{NHE}) = E(\text{Ag/AgCl}) + 0.209\ \text{V}$$

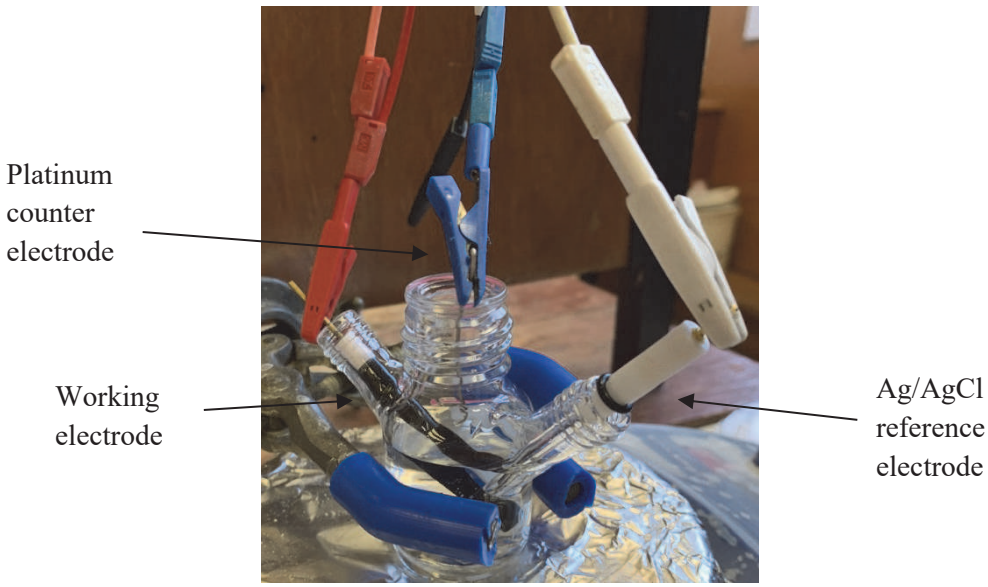

Figure 2-5: *Typical set up of the three-neck electrochemical cell used for catalytic measurements. Depicted are: glassy carbon working electrode, Ag/AgCl in 3 M NaCl reference electrode, and a platinum wire counter electrode. All electrodes are immersed in 1 M* H_2SO_4 *electrolyte.*

Identical experiments were also repeated with a saturated Hg/Hg_2SO_4 reference electrode in order to rule out leakage of silver as the source of any electrocatalytic activity. The electrode potentials were corrected to NHE scale accordingly using:

$$E(\text{NHE}) = E(Hg/Hg_2SO_4) + 0.658\ \text{V}$$

2.3.3. Voltammetry

Cyclic voltammetry (CV) is an electrochemical method used to determine the current at a working electrode over a fixed potential range. The voltage is swept in both reductive and oxidative directions between two fixed potentials. Upon initial application of potential, no flow of current is observed; however, as the potential is swept to more negative potentials, *i.e.* more reductive potentials, a current begins to flow as a species is being reduced. Once the potential reaches the fixed reductive voltage, the potential is swept in the positive direction, *i.e.* to more oxidative potentials, and a current is generated when a species is oxidized. Similarly, linear sweep voltammetry (LSV) involves the sweeping of potentials

between a fixed range; however this technique is applied in only one direction, *i.e.* towards reductive potentials. LSV also allows for the use of slower scan rates, which provides a more accurate reading of the currents achieved at a particular potential.

Typically, a three electrode set up is used for CV and LSV measurements. This consists of working, counter and reference electrodes immersed in an electrolyte. Oxidation / reduction reactions occur at the surface of the working electrode, and the charge that is generated is balanced by the counter electrode. The balancing of charge is controlled by the reference electrode, which has a known reduction potential.

CV and LSV measurements were carried out using a Biologic SP-150 potentiostat. Unless otherwise stated, glassy carbon was used as the working electrode substrate, carbon felt as the counter and Ag/AgCl in 3 M NaCl as the reference electrode. The electrolyte used was 1 M H_2SO_4 and measurements were performed with a scan rate of 100 mV s^{-1} for CV and 2 mV s^{-1} for LSV. The electrolyte was stirred to remove bubbles form the surface of the working electrode. Potentials were adjusted to NHE scale and resistance was compensated for using the iR compensation function on the potentiostat.

2.3.4. Tafel Analysis

Tafel plots were obtained directly from the linear sweep voltammograms with a scan rate of 2 mV s^{-1} by calculating the logarithm of the current density, which is plotted on the x-axis vs. the overpotential on the y-axis. The gradient of the resulting graph gives the Tafel slope, which is a measure of the voltage required to increase the current density by an order of magnitude, and is measured typically in mV per decade (mV dec^{-1}). Extrapolation to $\eta = 0$ mV gives the logarithm of the exchange current density.

2.3.5. Electrochemical Impedance Spectroscopy (EIS)

EIS was performed in an identical electrochemical cell as the voltammetry techniques, however the electrolyte remained static. A potential of –300 mV was applied in each case, and Nyquist plots were obtained with frequencies ranging between 200 kHz and 1 mHz. Fittings were obtained using the EC-Lab software.

2.3.6. Electrochemically Active Surface Area (ECSA)

The electrochemically active surface area was investigated using an analogous three-electrode setup up in 1 M H_2SO_4. The ECSA was obtained by sweeping the applied potential over a small potential range in the non-Faradaic region (in this case between +0.05 V and +0.25 V (vs. NHE)) at various scan rates (20, 40, 60, 80, 100, 120, 160, 200, 250 and 300 mV s^{-1}). Capacitive currents at +0.15 V (vs. NHE) were then plotted against scan rate, with the gradient being the double layer capacitance, C_{DL}. Due to their proportional relationship, ECSA can be estimated from the calculated C_{DL} values.

2.3.7. Chronoamperometry

For stability measurements, chronoamperometry was performed using a three-electrode set up in 1 M H_2SO_4. In order to investigate the stability of the catalyst, the potential required for $j = -10$ mA cm^{-2} (as determined by LSV) was chosen as the applied potential. The change in current could then be observed over set time periods.

2.3.8. Gas Chromatography (GC)

Gas chromatography (GC) was performed using an Agilent 7890 A Gas Chromatograph with a thermal conductivity detector. The GC system was calibrated using certified standards of hydrogen at various volume % in argon (CK Gas Product Limited (UK)) before use. Faradaic efficiency measurements were obtained in a single airtight cell (Figure 2-6) after being degassed under argon. A two electrode setup consisting of a carbon felt counter electrode attached to a silver wire and the catalyst-deposited glassy carbon working electrode was used for electrolysis. Galvanostatic electrolysis was then performed with a current density of $j = -3.4$ mA cm^{-2} being applied. 25 µL samples of the headspace were directly injected into the GC at various intervals. The Faradaic efficiency was then calculated as the ratio of expected H_2% in the headspace (as calculated from the charge passed) to the H_2% detected by GC measurements.

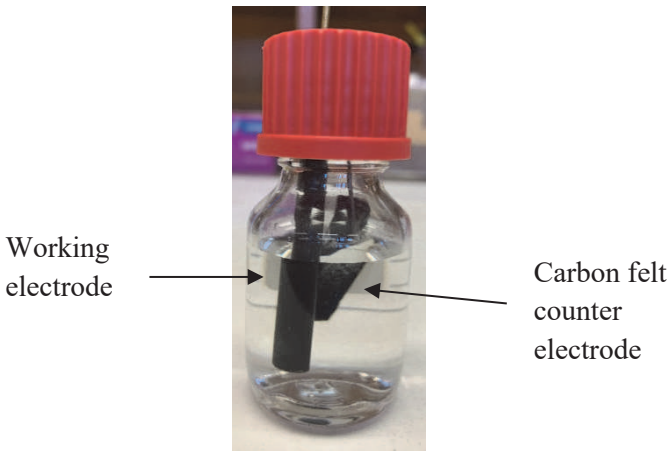

Figure 2-6: *Electrochemical cell used for Faradaic Efficiency measurements consisting of a two-electrode set up. Catalyst-deposited glassy carbon and carbon felt attached to silver wire were used as the working and counter electrodes, respectively.*

For analysis of hydrogen production during electrochemical activation, a different approach was used for gas chromatography. Rather than calculating the Faradaic Efficiency, the number of moles of hydrogen produced was calculated from the charge passed during chronoamperometry measurements in a three-electrode setup, as before. The applied potential was chosen as the potential which corresponded to $j = -10$ mA cm^{-2}.

2.4. Computational Studies

Computational studies, *i.e.* Density Functional Theory (DFT), are discussed in Chapter 5, Section 5.3.5. and were performed by Dr. Nuno Bandeira at the University of Lisbon in Portugal.

The ADF-Band version 2017.113 software package was used for the *in silico* analysis of the catalyst hydrogenation process. The Perdew, Burke and Ernzerhof[5] generalised gradient approximate density functional as revised by Zhang and Yang[6] was employed throughout the calculations with the addition of Grimme's third generation dispersion correction (rev-PBE-D3). A combination of Herman-Skillman numerical atomic orbitals (NAOs) with triple zeta polarised (TZP) Slater type orbitals[7] were used for all the heavy atoms, whereas for hydrogen a double zeta polarised (DZP) augmentation was used. The geometry optimisations[8] of both coordinates and unit cell parameters were carried out in a 2×2 unit cell of 1T'-$MoTe_2$ single layer slab using a regular 1×3 k point grid. A partial Hessian calculation (involving the vibrational modes of the Mo-H bonds) was computed for $^{2}_{\infty}[\eta\text{-}MoTe_2H_{0.125}]$ yielding only real wavenumbers (with a lower bound 156 cm^{-1} and upper bound 1291 cm^{-1}).

The hydrogen atom addition was calculated with reference to the standard hydrogen electrode such that $E(H_2) = E(H^+ + e^-)$; E symbolising electronic energies, thus hydrogenation reaction energies were determined with the following formula $\Delta E_H = E(^{2}_{\infty}[MoTe_2H_{0.125}]) - E(^{2}_{\infty}[MoTe_2]) - \frac{1}{2}E(H_2)$ where the last term is the electronic energy of hydrogen gas at the same level of theory.

2.5. References

1. Toby, B. H. EXPGUI, a graphical user interface for GSAS. *J. Appl. Crystallogr.* **34**, 210–213 (2001).

2. Winkler, F. *et al.* Quantitative measurement of mean inner potential and specimen thickness from high-resolution off-axis electron holograms of ultra-thin layered WSe_2. *Ultramicroscopy* **178,** 38–47 (2017).

3. Newville, M.J. IFEFFIT: interactive XAFS analysis and FEFF fitting. *Synchrot. Radiat.* **8,** 322-324 (2001).

4. Ravel, B. & Newville, M. ATHENA, ARTEMIS, HEPHAESTUS: Data analysis for X-ray absorption spectroscopy using IFEFFIT. *J. Synchrotron Radiat.* **12**, 537–541 (2005).

5. Perdew, J. P., Burke, K. & Ernzerhof, M. Generalized gradient approximation made simple. *Phys. Rev. Lett.* **77**, 3865–3868 (1996).

6. Zhang, Y. & Yang, W. Comment on "generalized gradient approximation made simple". *Phys. Rev. Lett.* **80**, 890 (1998).

7. Grimme, S., Antony, J., Ehrlich, S. & Krieg, H. A consistent and accurate ab initio parametrization of density functional dispersion correction (DFT-D) for the 94 elements H-Pu. *J. Chem. Phys.* **132**, (2010).

8. Te Velde, G. & Baerends, E. J. Precise density-functional method for periodic structures. *Phys. Rev. B* **44**, 7888–7903 (1991).

3. Polymorphic control of $MoTe_2$

As observed frequently in MoS_2, transitioning from the semiconducting to the metallic phase leads to a rise in catalytic performance towards the hydrogen evolution reaction. The change in crystal structure has therefore sparked interest in the role polymorphic control plays in tuning catalytic activity. However, for MoS_2, the origin of catalytic activity remains unclear due to the variety of factors arising from the need for chemical exfoliation. Turning our attention to $MoTe_2$ allows for the synthesis of both 2H and 1T' polymorphs in the bulk form, which in turn allows for the control of morphology and composition. In this way, the effect of the semiconductor-to-metal phase transition can be accurately investigated and the consequent effect on catalytic activity can be analysed. By fully characterising the structure of both polymorphs and measuring their respective catalytic activities, the 1T'-$MoTe_2$ phase was found to be the superior HER electrocatalyst due to the enhanced reaction kinetics associated with its metallic character.

3.1. Introduction

3.1.1. Polymorphism in MoS_2

Transition metal dichalcogenides (TMDCs) exist as a variety of polymorphs, consisting of the general formula MX_2 (M = metal, X = chalcogenide). Taking MoS_2 as an example, each 2D layer is formed of S-Mo-S sandwiches, with strong intralayer bonds connecting the metal and chalcogen atoms, and weak van der Waal's forces keeping the layers in contact. In this way, TMDCs form a characteristic layered structure.[1] The stacking of the chalcogenide layers around the metal can vary, leading to the formation of distinct polymorphs with differing properties including semiconducting and metallic behaviours.

If the chalcogen atoms are stacked directly above each other in the S-Mo-S sandwich, then a trigonal prismatic arrangement of S about Mo is formed, with the metal atom forming bonds to six chalcogens (Figure 3-1a), otherwise known as 2H-MoS_2. Conversely, if the chalcogen layers are staggered, the metal atom becomes octahedrally coordinated to six chalcogen atoms (Figure 3-1b) and the 1T-MoS_2 polymorph is formed. The crystal structures of both 2H- and 1T-MoS_2 are shown in Figure 3-2 which also illustrates the two distinct structural regions in TMDCs. These include the chalcogen-terminated surface of each layer, known as the 'basal plane', and the edge sites. The catalytic activities of these sites vary depending on the semiconducting / metallic nature of the polymorph in question, as

discussed in Chapter 1. Thus, the properties, and resulting catalytic activity, of each TMDC polymorph depends on its coordination environment, which is controlled by the ligand-field splitting of the metal *d* orbitals and *d* electron count.

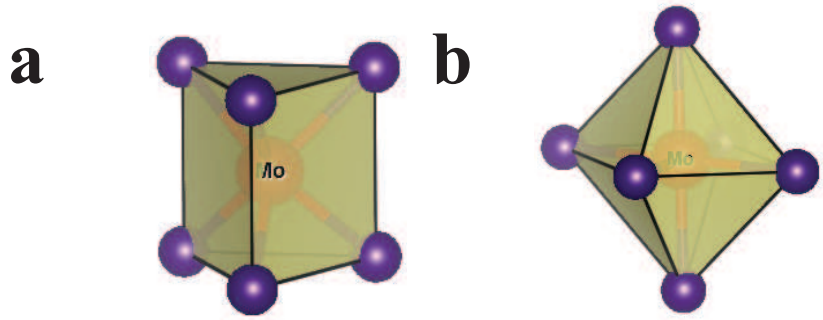

Figure 3-1: *{MoS_6} building blocks of* ***a)*** *trigonal prismatic arrangement and* ***b)*** *octahedral arrangement.*

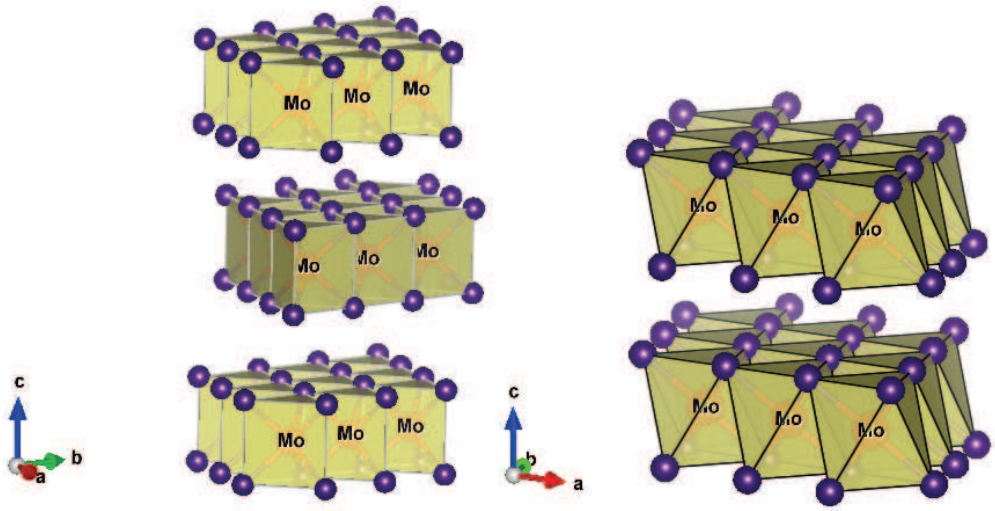

Figure 3-2: *Crystal structure and {MoS_6} polyhedra showing the building blocks of* ***a)*** *hexagonal 2H-MoS_2 and* ***(b)*** *orthorhombic 1T-MoS_2.*

Using the hydrogen evolution reaction activity of MoS_2 as an example, the varying properties of TMDC polymorphs become apparent. In its naturally occurring state, MoS_2 crystallises with the hexagonal crystal structure (Space group: $P6_3/mmc$),[2] in which Mo is coordinated by S in a trigonal prismatic arrangement, as described above. This 2H-MoS_2 polymorph is semiconducting due to its fully occupied valence band (Figure 3-3a)[3], meaning that electron transfer is significantly hindered, and the number of active edge sites is limited.

Therefore, bulk 2H-MoS_2 is a rather inefficient electrocatalyst for the HER.[4–6] The 1T-MoS_2 polymorph, however, crystallises within a trigonal lattice consisting of edge-sharing MoS_6 octahedra (Space group: P–3m1).[7] The transition from 2H- to 1T-MoS_2 results in a significant improvement in HER activity, and indicates that polymorphic control may be an important factor for designing electrocatalysts.[8,9]

However, 1T-MoS_2 does not exist naturally, and must therefore be synthesised from its 2H counterpart directly.[10] This procedure involves complex syntheses such as chemical exfoliation *via* lithium intercalation in order to destabilise the thermodynamically favoured trigonal prismatic arrangement.[11] The transition from 2H to 1T-MoS_2 is a result of an electron transfer from intercalated lithium which induces a d^2 to d^3 transition. As such, the octahedral coordination is now favoured, and the valence band is partially occupied (Figure 3-3b). Therefore, the emergence of metallic character is associated with the change in crystal symmetry.[12]

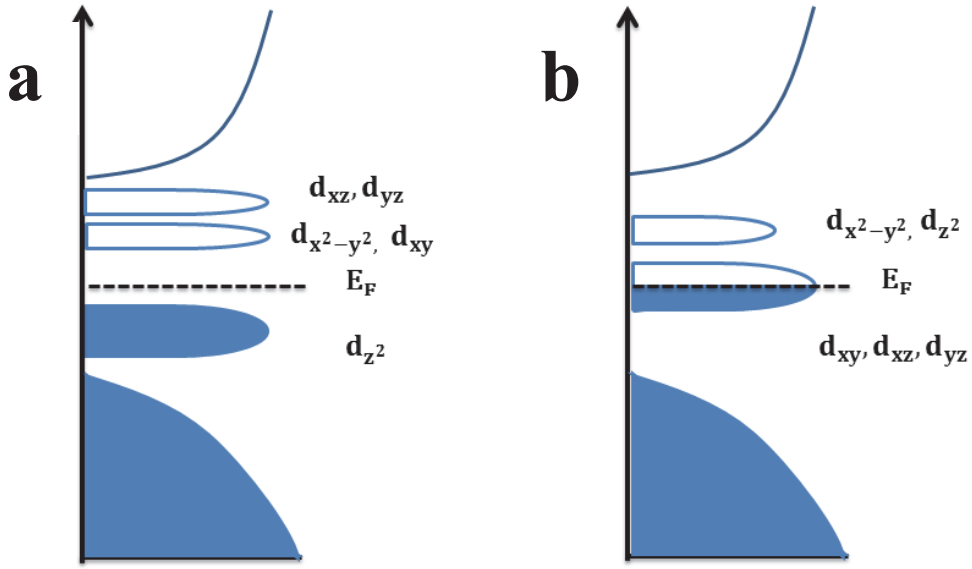

Figure 3-3: *d orbital splitting diagrams of* ***a)*** *2H-$MoTe_2$ with a trigonal prismatic coordination of Te around Mo and* ***b)*** *1T'-$MoTe_2$ with a distorted octahedral coordination of Te around Mo.*

3.1.2. Electrocatalytic Activity of MoS_2

As discussed in Chapter 1, Hinnemann *et al*.[13] first proposed MoS_2 to be a promising catalytic material, as DFT studies suggested it to possess a free energy change close to zero. In this study, the authors proposed that MoS_2 lies close to platinum at the apex of Trasatti's volcano plot, which illustrates that there is an optimum binding energy at which the maximum catalytic activity is obtained.[14] As mentioned in Section 3.1.1., TMDCs exist as layered materials consisting of basal planes and edge sites, with the basal plane comprising the majority of the bulk material due to their 2D nature. Jaramillo *et al*.[15] initially confirmed the promising activity of bulk MoS_2, which exists naturally as semiconducting 2H-MoS_2, and identified the activity to originate from the edge sites, while the basal plane was found to be inert. Despite extensive efforts to increase the number of edge sites in 2H-MoS_2, the catalytic activity of the 2H phase remains limited due to the semiconducting nature of the material. Thus, efforts were turned towards 1T-MoS_2, which exhibits enhanced conductivity owing to its metallic behaviour.

Lukowski *et al*.[9] initially studied the catalytic activity of the 1T-MoS_2 polymorph towards the HER, and found that this phase is amongst the best performing MoS_2 materials. This study therefore suggested that tailoring the number of edge sites is not the only prerequisite for improved catalytic activity, but rather proposed that crystal structure plays a pivotal role. For example, by measuring the charge transfer resistance, R_{CT}, it was evident that the reaction kinetics are much more efficient on the metallic 1T-MoS_2 than on 2H-MoS_2. However, this finding then raised the question of the origin of the enhanced activity: either 1T-MoS_2 is intrinsically more active or the catalytic properties are enhanced due to the increased number of active edges that result from chemical exfoliation. Further studies by Voiry *et al*.[16] sought to answer this question by exploring the nature of the basal plane in 1T-MoS_2. This was achieved by partially oxidizing the edge sites of both 2H- and 1T-MoS_2. In doing so, the catalytic activity of 2H-MoS_2 was lost, while that of 1T-MoS_2 was largely unaffected. This outcome was consistent with prior work by Bonde *et al*.[17] who suggested the active sites of metallic 1T-MoS_2 are mainly located on the basal plane.

Despite this discovery, most studies have focussed on maximising the number of edge sites, which is most commonly achieved by chemical exfoliation *via* lithium intercalation. This procedure not only results in the nanostructuring of the bulk material, but also induces the 2H- to 1T-MoS_2 phase transition.[8,18–21] This method of preparing 1T-MoS_2 also raises several concerns. In addition to the reverse transformation into the 2H phase, chemical

exfoliation *via* lithium intercalation requires complex chemical procedures and may lead to a compromised chemical composition.[22] Likewise, due to low thermodynamic stability, isolation of the phase pure metallic product remains a significant challenge.[7] Combined, these factors render the origin of the catalytic activity difficult to fully comprehend. The activity may arise due to an increase in conductivity associated with the metallic phase; an increased surface area upon chemical exfoliation which renders the bulk material into a nanostructured catalyst; or due to compositional changes as a result of lithium intercalation. In order to understand the origin of the catalytic activity, which may then aid the development of future catalysts; the uncertainties surrounding MoS_2 need to be de-convoluted.

3.1.3. Polymorphism in $MoTe_2$

Similar to MoS_2, $MoTe_2$ can be synthesised as both semiconducting and metallic polymorphs. Both materials exhibit drastically different properties due to the ligand-field splitting of the metal *d* orbitals. In both cases, strong intralayer bonds are present between the metal and chalcogen atoms, forming Te-Mo-Te sandwiches. Each sandwich is separated by weak van der Waal's forces resulting in a gap between each layer (Figure 3-4).

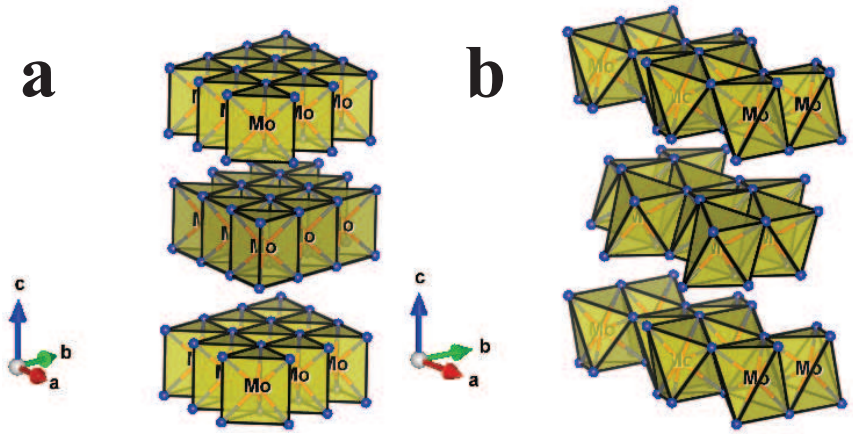

Figure 3-4: *Crystal structure and {$MoTe_6$} polyhedral showing the building blocks of* ***a)*** *hexagonal 2H-$MoTe_2$ and* ***(b)*** *monoclinic 1T'-$MoTe_2$.*

At temperatures below 850 °C, $MoTe_2$ crystallises as the thermodynamically favourable hexagonal 2H-phase, with a structure similar to that of MoS_2. In this way, each molybdenum atom is coordinated to six tellurium atoms in a trigonal prismatic arrangement. Infinite 2D layers of edge-sharing {$MoTe_6$} trigonal prisms are thus formed, with each layer consisting of hexagonally packed Te-Mo-Te sandwiches (Figure 3-4a). Within each prism, the Te atoms are stacked directly above each other, and the Mo atoms in successive layers are

shifted slightly, thus forming the 2H-$MoTe_2$ polymorph with flat Te terraces terminating each layer. The crystallographic data of 2H-$MoTe_2$ in comparison with 1T'-$MoTe_2$ is shown in Table 3-1.

In contrast to the disulfide and diselenide derivatives of molybdenum, $MoTe_2$ also crystallises as the monoclinic 1T'-phase in the bulk form. This can be achieved *via* a simple solid-state synthesis due to the significantly small difference in ground state energy between hexagonal and monoclinic $MoTe_2$ polymorphs.[23,24] By applying higher temperatures (>850 °C) the distorted octahedral coordination of $MoTe_2$ is now energetically favoured, whereby the Mo atoms are displaced from the centre of the {$MoTe_6$} octahedra and the tellurium sheets are now buckled (Figure 3-4b). As a result of this change in crystal symmetry, 1T'-$MoTe_2$ is metallic.[12,25]

Table 3-1: *Crystallographic data of 2H-$MoTe_2$ and 1T'-$MoTe_2$ according to literature reports.*[26,27]

	2H-$MoTe_2$	**1T'-$MoTe_2$**
Crystal system	Hexagonal	Monoclinic
Space group	$P6_3/mmc$	$P2_1/m$
Lattice parameters	a = 3.519, c = 13.97, α=β= 90°, γ= 120°	a = 6.330, b = 3.469, c = 13.86 Å, β = 93°
Z	2	4

3.1.4. Electrocatalytic Activity of $MoTe_2$

The phase transition from semiconducting 2H-$MoTe_2$ to metallic 1T'-$MoTe_2$ is an interesting observation from an electrochemistry point of view. Since both materials can be synthesised in the bulk form, with no changes in morphology or composition between the two polymorphs, the result of the phase transition towards the HER can be accurately investigated. This study was initially conducted by Seok *et al.*, who sought to understand the origin of catalytic activity in 1T'-$MoTe_2$.[28] In doing so, the authors predicted a behaviour which cannot be explained by the historical 'Volcano plot' analysis which allows for the prediction of electrocatalytic behaviour. By synthesising both 2H- and 1T'-$MoTe_2$ as single crystals, Seok *et al.* found that the semiconducting phase is catalytically inactive, while the metallic phase experiences an intrinsic activity similar to that of platinum. The reaction mechanism on 1T'-$MoTe_2$ was found to differ from previously investigated HER catalysts, with the Volmer reaction being the rate determining step rather than the Heyrovsky reaction. A summary of the possible reaction pathways occurring during H_2 evolution is given in Table 3-2.

Typical HER electrocatalysts have been proposed to operate *via* the Volmer-Heyrovsky mechanism of hydrogen evolution, with the electrochemical desorption step (Heyrovsky) known to be rate limiting. Electrocatalysts which follow this reaction mechanism typically show a Tafel slope of approximately 40 mV dec^{-1}, whereas catalysts with the Volmer reaction being rate limiting exhibit a Tafel slope of 120 mV dec^{-1}. In this regard, 1T'-$MoTe_2$ fits well with the discharge step (Volmer step) being slow, justified by its large Tafel slope of 127 mV dec^{-1}. However, Seok *et al*.[28] calculated 1T'-$MoTe_2$ to have a per-site turnover frequency similar to that of platinum, which would suggest the metallic phase of $MoTe_2$ is a highly active electrocatalyst. These contradicting analyses led to the conclusion that the typical Volcano plot analysis cannot be accurately applied to TMDCs, and instead suggest that the lattice and electronic structures of TMDCs need to be considered in more detail. A comparison of the catalytic activities obtained by Seok *et al.* is recreated in Table 3-3.

Electron doping and mechanical strain have both been proven to affect the lattice and electronic structures of TMDCs.[29,30] However, the structural change that these parameters induce has only recently been investigated by Seok *et al*. in 2017.[28] The authors found that as hydrogen is adsorbed onto the surface of metallic 1T'-$MoTe_2$ a spontaneous lattice distortion, arising from Fermi surface nesting on the basal plane, otherwise known as Peierls distortion, occurs which enhances the activity of 1T'-$MoTe_2$. This distortion is driven by

electron doping on the metallic 1T'-$MoTe_2$ basal plane, which alters the pristine lattice structure and improves the Gibbs free energy of hydrogen adsorption, ΔG_H.

Table 3-2: *Underlying electrochemical processes occurring during the H_2 evolution reaction.*

Volmer step	$H_3O^+ + e^- \rightarrow H_{ads} + H_2O$	Discharge step
Heyrovsky step	$H_{ads} + H_3O^+ + e^- \rightarrow H_2 + H_2O$	Electrochemical desorption step
Tafel step	$H_{ads} + H_{ads} \rightarrow H_2$	Recombination step

Table 3-3: *Comparison of the catalytic activities obtained by Seok et al. for 2H-$MoTe_2$, 1T'-$MoTe_2$ and platinum.*[28]

Catalyst	**Potential for $j = -10$ mA cm^{-2}**	**Tafel slope**	**Exchange current density**
2H-$MoTe_2$	–0.650 V (vs. NHE)	184 mV dec^{-1}	7.04 x 10^{-4} mA cm^{-2}
1T'-$MoTe_2$	–0.356 V (vs. NHE)	127 mV dec^{-1}	2.1 x 10^{-2} mA cm^{-2}
Platinum	–0.046 V (vs. NHE)	36 mV dec^{-1}	4.50 x 10^{-1} mA cm^{-2}

Despite the extensive literature which states that the active sites of metallic TMDCs are located on the basal plane, recent literature has also hinted that increasing the number of edge sites of 1T'-$MoTe_2$ may also enhance the HER.[31] A recent study by Zhuang *et al.*[31] proved that, by synthesising pristine edge free 1T'-$MoTe_2$ ultrathin films with a thickness of only 5.2 nm, the effect of increasing number of edge sites could be investigated. In this study, the authors found that the pristine edge free films were catalytically inactive towards the HER, indicating that the basal plane is not the main active site and directly contradicts the work by Seok *et al*.[28] However, it should be noted that firstly, the pristine edge free material was prepared and investigated directly on SiO_2/Si substrate, which is non-conductive and hence would inhibit charge transfer from the metallic active sites found on the basal plane; and secondly, the catalytic activity of thin films is known to increase with increasing film thickness.[32] As the thickness increases, the roughness factor also increases, providing a greater surface area and hence greater number of active sites. With these points in mind, it is unsurprising that the pristine, edge free film with a thickness of 5.2 nm exhibits a poor HER ability. Nonetheless, the inactivity of the basal plane in this study allows for an accurate

determination of the edge site contribution to the HER. Zhuang *et al.*[38] were able to control the generation of edge sites with a focused ion beam, thus patterning the 1T'-$MoTe_2$ films with various numbers of line defects ranging from 5 lines to 40 lines. In doing so, the catalytic activity of 1T'-$MoTe_2$ was found to increase with increasing number of line defects, *i.e.* the greater the number of edges sites, the greater the HER activity. Thus, from this study, it is apparent that the edge sites also contribute towards the catalytic activity.

In line with studies on MoS_2, attempts have been made to chemically exfoliate 2H-$MoTe_2$ *via* lithium intercalation in order to improve the electrocatalytic activity. In doing so, the bulk 2H-$MoTe_2$ is reacted with *n*-butyllithium intercalant and subsequently sonicated in water to separate the bulk material into monolayers. A study by Luxa *et al.*[33] reinforces the drastic change in sample morphology upon exfoliation, with a greater number of edge sites easily visualised. Luxa *et al.*[33] also note an enhancement of the HER activity, however, unlike the case of MoS_2, no phase transition to 1T'-$MoTe_2$ occurs. Therefore, it is deduced from this study that the number of edges plays a significant role in the HER activity of TMDCs. However, upon exfoliating 2H-$MoTe_2$, the authors note the emergence of MoO_3 and elemental Te, as evidenced by Raman spectroscopy, indicating the decomposition of the material. As such, several other factors may be contributing to the enhancement of the catalytic activity, rather than the edge sites being solely responsible.

3.2. Aims

Herein, we exploit a solid state route to $MoTe_2$ which allows for the interconversion between both semiconducting and metallic phases to be carried out in the bulk form. In this way, the effect of polymorphic control on catalytic activity can be accurately investigated without compromising the composition and / or morphology of the materials. Thus, this chapter aims to fully characterise 2H- and 1T'-$MoTe_2$ structurally and determine the electrocatalytic activity of both materials as a result of the semiconductor-to-metal phase transition.

3.3. Results and Discussion

3.3.1. Synthesis and characterisation of $MoTe_2$ Polymorphs

3.3.1.1. Synthesis of 2H-$MoTe_2$

Initially, the synthesis of 2H-$MoTe_2$ was performed following the procedure by MacDonald *et al*.,[34] which involved heating stoichiometric mixtures of elemental molybdenum and tellurium under vacuum. This process required heating the powders at 600 °C for 48 hours (heating rate of 5 °C min^{-1}), and involved an intermediate heating step at 480 °C for 16 hours. Following this route, the elemental powders were sealed in a quartz ampoule under a vacuum pressure of 4.5 x 10^{-2} mbar and shaken carefully to homogenize the mixture. PXRD was utilised to monitor the reaction progress, and Figure 3-5 illustrates the result of intermediate heating at 480 °C. By comparing the obtained PXRD pattern with those calculated from the ICSD database, the resulting intermediate powder was identified as being monoclinic 1T'-$MoTe_2$ with an elemental molybdenum impurity present at 40.5 °. However, it is surprising for the intermediate heating step to result in a powder which can be isolated and identified as monoclinic 1T'-$MoTe_2$ at this low temperature, as the formation of the thermodynamically favoured 2H phase would be expected. This intermediate product will be discussed further in Chapter 4. Following the protocol by MacDonald *et al.*, this powder was subsequently reannealed at 600 °C for 48 hours. However, this reaction produced a mixture of monoclinic 1T'- and hexagonal 2H-$MoTe_2$, with the molybdenum impurity still remaining (Figure 3-6). Due to this, the procedure by MacDonald *et al*.[34] was adapted, and the synthesis of 2H-$MoTe_2$ was carried out without the intermediate heating step. Instead, the elemental powders were annealed directly at 600 °C for 48 hours, with the resulting PXRD pattern proving the product to be phase pure 2H-$MoTe_2$ (Figure 3-7). Therefore, the intermediate heating step was deemed unnecessary.

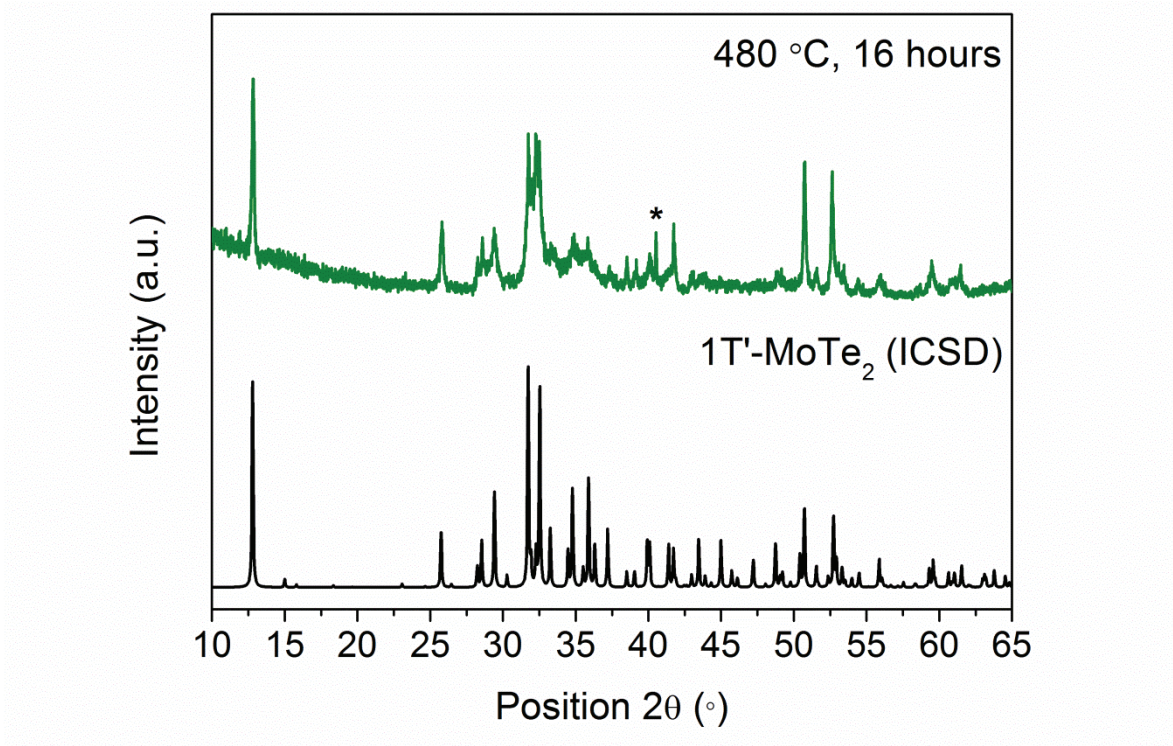

Figure 3-5: *PXRD patterns of the resulting powder obtained by heating elemental Mo and Te powders at 480 °C for 16 hours (top) in comparison with monoclinic 1T'-$MoTe_2$ as calculated from the ICSD database, card number 14349 (bottom). The elemental molybdenum impurity is represented by an asterisk (*).*

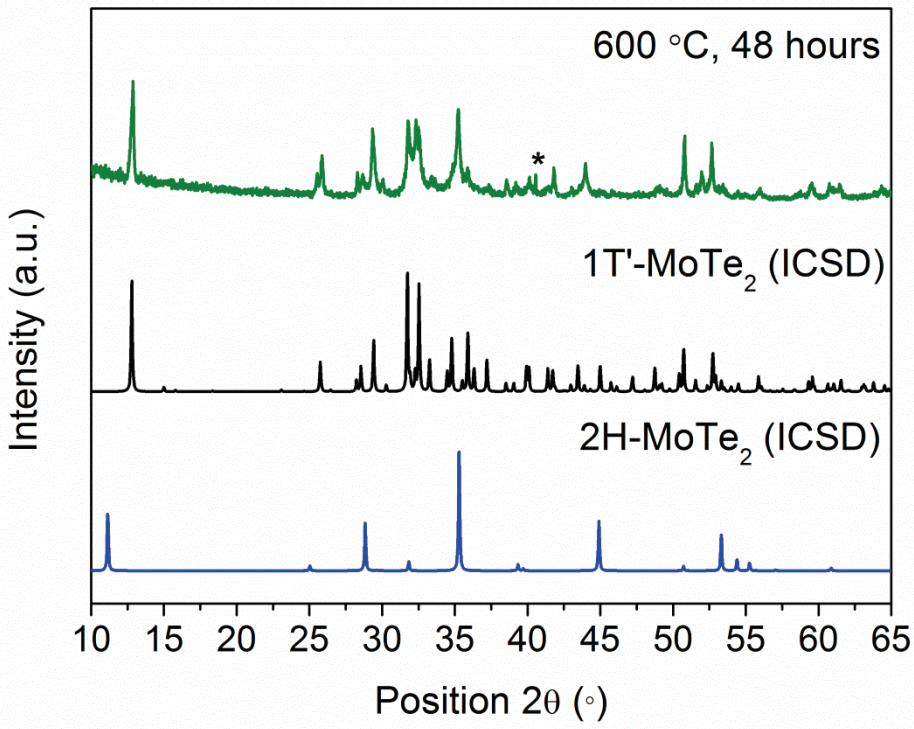

Figure 3-6: *PXRD patterns obtained after subsequent reannealing of the intermediate powders at 600 °C for 48 hours (top) in comparison with monoclinic 1T'-$MoTe_2$ as calculated from the ICSD database, card number 14349 (middle), and hexagonal 2H-$MoTe_2$ as calculated from the ICSD database, card number 15431 (bottom). The elemental molybdenum impurity is represented by an asterisk (*).*

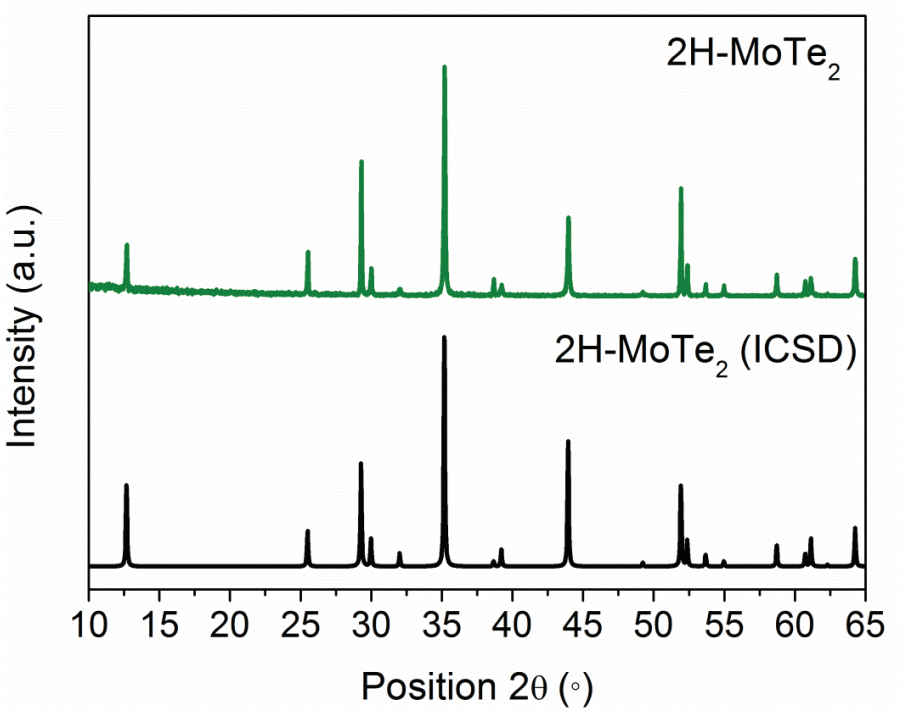

Figure 3-7: *PXRD patterns of 2H-$MoTe_2$ synthesised directly from the elements at 600 °C (top) compared with 2H-$MoTe_2$ as calculated from the ICSD, card number 15431 (bottom).*

3.3.1.2. Synthesis of 1T'-$MoTe_2$

According to the literature, hexagonal 2H-$MoTe_2$ experiences a phase transition into monoclinic 1T'-$MoTe_2$ at temperatures above 850 °C.[35] Therefore, the mixed phase powders discussed above were reannealed at 850 °C for 26 hours and quenched in water at 850 °C. The resulting PXRD pattern shows the crystallinity of the material to have improved, however hexagonal 2H-$MoTe_2$ remains as an impurity (Figure 3-8). In fact, reannealing the material for longer time periods in an attempt to remove this impurity had no impact on the phase transition. Instead, the reaction temperature was increased to 900 °C, at which the monoclinic 1T'-phase is known to be stable.[36] Simultaneously, a reaction mixture consisting of elemental Mo and Te was reacted under vacuum, in order to establish if an intermediate heating step was necessary for the formation of the 1T'-phase. Both mixtures were heated at 900 °C (heating rate of 5 °C min^{-1}) for 19 hours, and quenched in water at 900 °C. As a result, both reaction mixtures were identified as phase pure monoclinic 1T'-$MoTe_2$ by PXRD. Thus, an intermediate heating step is not required for the formation of 1T'-$MoTe_2$, and direct heating of elemental powders at 900 °C for 19 hours, followed by quenching in water, was used for all future syntheses of 1T'-$MoTe_2$. Figure 3-9 shows the PXRD pattern of the direct synthesis of 1T'-$MoTe_2$ at 900 °C, indicating the formation of a phase pure material. Quenching the powders at 900 °C is required since 1T'-$MoTe_2$ is metastable and, if allowed to cool naturally, would otherwise form the thermodynamically stable 2H-$MoTe_2$.[35]

PXRD identified the product of quenching the ampoule and its contents in water at 900 °C as single phase 1T'-$MoTe_2$ with no elemental Mo or Te present within the sample (Figure 3-9). The pattern is consistent with the monoclinic, distorted octahedral arrangement associated with the metallic phase, and matches well with that reported by Brown *et al.*[27] Further, Synchrotron XRD (I22) data was collected for 1T'-$MoTe_2$ at ambient temperature and confirmed the single phase nature of the sample. However, despite all efforts, the preferred orientation associated with the metallic phase could not be eliminated; therefore only LeBail refinements of the SXRD were performed using the GSAS/EXPGUI software package.[37] LeBail refinement (Figure 3-10) of the PXRD data was performed using a structural model reported previously,[27] and the unit cell was indexed to a monoclinic unit cell of dimensions: a = 6.32985(6) Å; b = 3.47827(2) Å; c = 13.8178(2) Å; β = 93.838(1) °. A comparison of the crystallographic data of synthesised 1T'-$MoTe_2$ with the literature data is reported in Table 3-4.

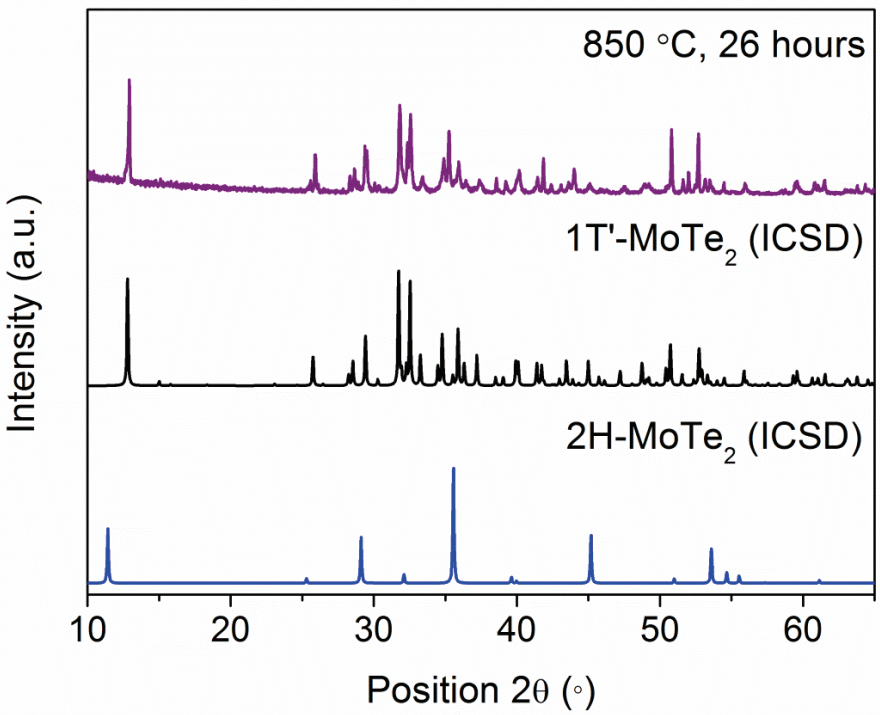

Figure 3-8: *PXRD patterns obtained after subsequent reannealing of the intermediate powders at 850 °C for 26 hours followed by quenching at 850 °C (top) in comparison with monoclinic 1T'-$MoTe_2$ as calculated from the ICSD database, card number 14349 (middle), and hexagonal 2H-$MoTe_2$ as calculated from the ICSD database, card number 15431 (bottom).*

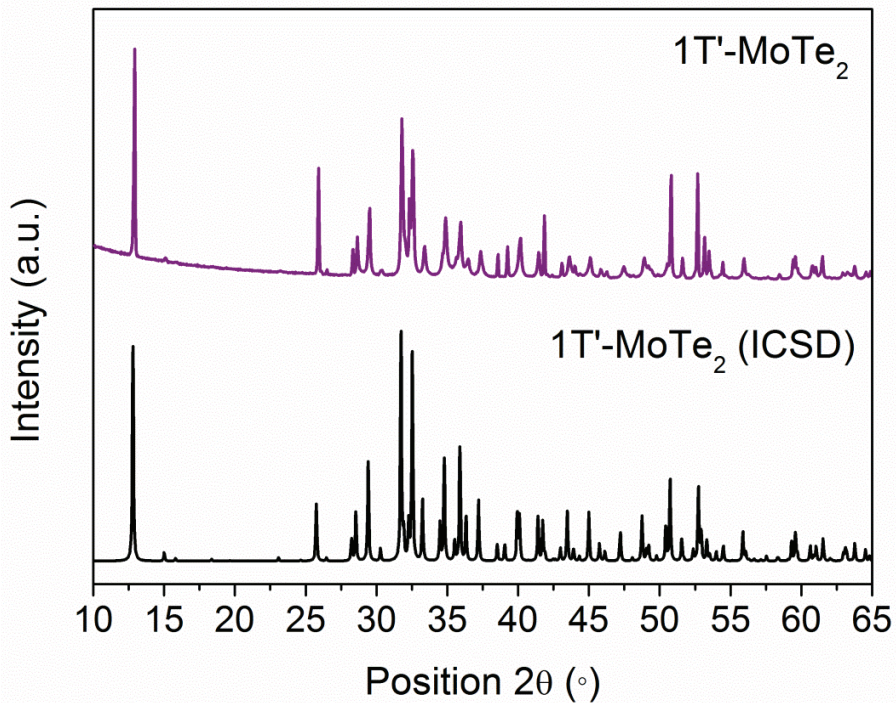

Figure 3-9: *PXRD patterns of 1T'-$MoTe_2$ synthesised directly from the elements at 900 °C for 24 hours followed by quenching at 900 °C (top) compared with 1T'-$MoTe_2$ as calculated from the ICSD, card number 14349 (bottom).*

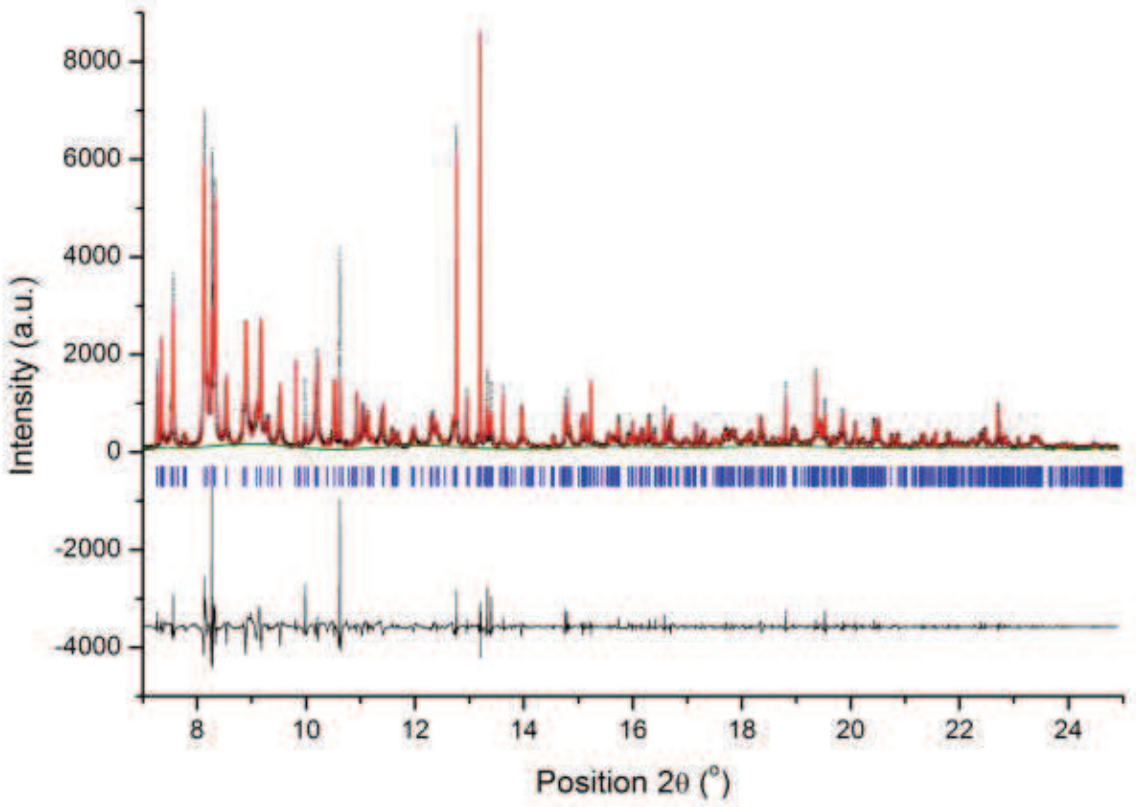

Figure 3-10: *Ambient temperature SXRD data from 1T'-$MoTe_2$ with observed (black), calculated (red), peak position (blue) and difference (grey) plots from Le Bail fit in $P2_1/m$. The unit cell parameters are in close agreement with the literature. The poorly fitted peaks consistently originated from 01l and 00l reflections.*

Table 3-4: *Crystallographic data of synthesised 1T'-$MoTe_2$ obtained by LeBail refinement in comparison to literature data by Brown et al.*[27]

	Le Bail refinement of synthesised 1T'-$MoTe_2$	**1T'-$MoTe_2$ (Brown *et al.*)**[27]
Crystal system	Monoclinic	Monoclinic
Space group	$P2_1/m$	$P2_1/m$
Lattice parameters	a = 6.32985(6), b = 3.47827 (2), c = 13.8178 (2), β = 93.838 (1)	a = 6.330, b = 3.469, c = 13.86 Å, β = 93°
Z	4	4

3.3.1.3. Morphology of $MoTe_2$

Morphology is another important parameter to consider: upon exfoliating 2H-MoS_2, the bulk material becomes nanostructured which leads to an increased surface area and an increased number of edge sites. Not only does this nanostructuring introduce additional variables which may contribute to the catalytic activity, it is also capable of the reverse transformation back into the 2H polymorph with time.[9] Applying a solid-state route to $MoTe_2$ allows for the morphology to be controlled, with both phases remaining in the bulk form, thus allowing for a direct comparison of activity. However, when considering the SEM images of 2H-$MoTe_2$ and 1T'-$MoTe_2$ (Figure 3-11a and b), the sample morphology of the two phases is not consistent. While the SEM image of 1T'-$MoTe_2$ shows large plate-like microcrystals, 2H-$MoTe_2$ is a more agglomerated material, with a greater number of edge sites clearly visible in addition to a smaller particle size. In order to determine the sole effect of the coordination geometry on catalytic activity, it is imperative that the morphology of both materials is similar. Therefore, in an attempt to maintain the same sample morphology as the monoclinic phase, a synthetic procedure employed by Jana *et al.* was adopted.[38] This involved reannealing powders of 1T'-$MoTe_2$ at 700 °C (5 °C min^{-1}) for 24 hours, followed by cooling to room temperature naturally. In this way, a complete transition from 1T'- to 2H-$MoTe_2$ took place, with the particle morphology being identical to that of 1T'-$MoTe_2$.

Now, the SEM images show both materials to be in the bulk form and consist of plate-like microcrystals, with the morphology being preserved upon transitioning from 1T'- to 2H-$MoTe_2$ (Figure 3-11b and c, respectively). It is important to note that, when performing SEM, the use of gold-coating was excluded due to the overlapping of gold and tellurium in the EDX spectra. This then led to the interesting observation of differing contrast between samples. Under the same magnification, images of 1T'-$MoTe_2$ are seen to have much sharper contrast than those of 2H-$MoTe_2$, which appear slightly blurry. This can be attributed to the increased conductivity associated with the metallic nature of the 1T'-phase, compared to its semiconducting 2H counterpart.

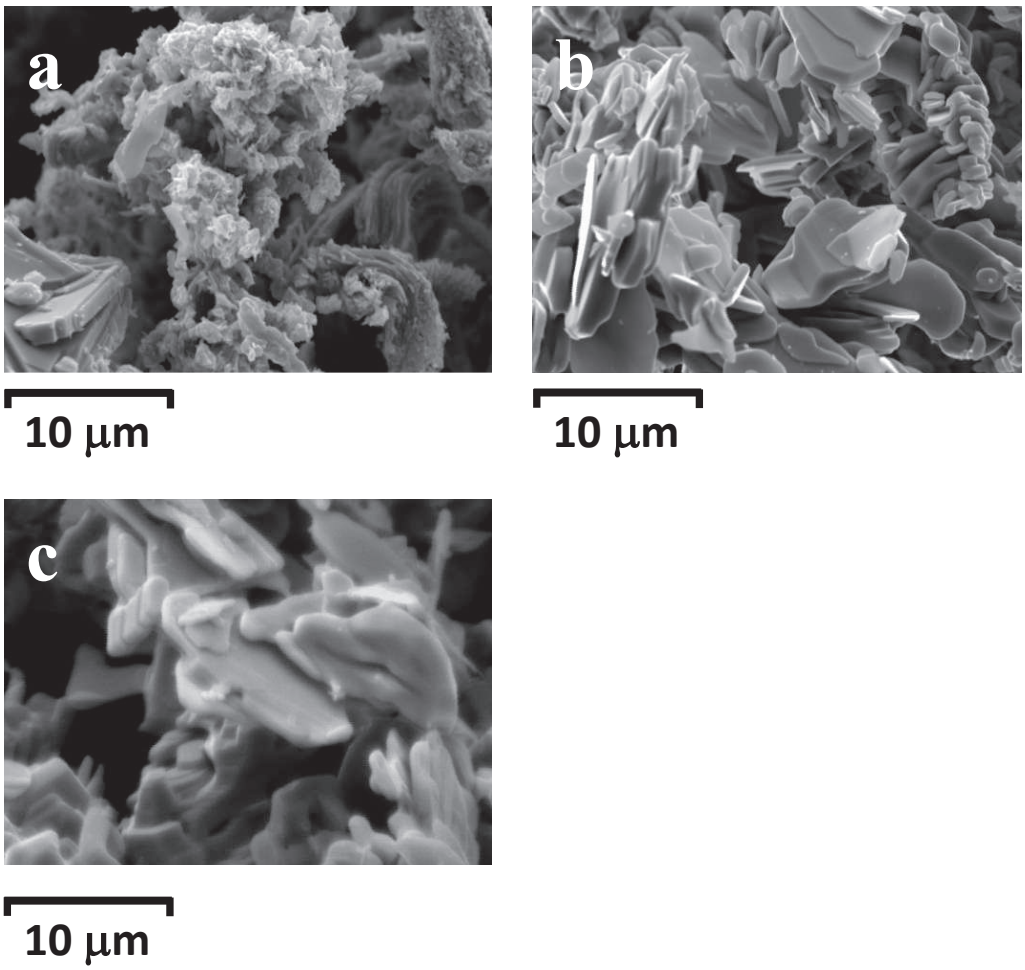

Figure 3-11: *SEM images of* ***(a)*** *2H-$MoTe_2$ synthesised from the elements at 600 °C,* ***(b)*** *1T'-$MoTe_2$ synthesised from the elements at 900 °C and* ***(c)*** *2H-$MoTe_2$ prepared by reannealing 1T'-$MoTe_2$ at 700 °C.*

3.3.1.4. Raman Spectroscopy of $MoTe_2$ Polymorphs

Further phase confirmation was performed by Raman spectroscopy. This measurement not only confirms the phase purity of both materials, but also the complete transformation from 1T'- to 2H-$MoTe_2$ by the simple annealing protocol. Figure 3-12 shows the Raman spectra of 1T'-$MoTe_2$ to be consistent with the {$MoTe_6$} distorted octahedra, which are the expected building blocks of the monoclinic phase. Several characteristic peaks are present within the Raman spectrum, with the main four highlighted in Figure 3-12. These peaks correspond to a B_g mode at ~107 cm^{-1} and A_g modes at ~128 cm^{-1}, ~161 cm^{-1} and ~255 cm^{-1}.[39] Likewise, the trigonal prismatic coordination of the hexagonal 2H-$MoTe_2$ is confirmed by the presence of the in-plane E^1_{2g} mode at ~234 cm^{-1} and out-of-plane A_{1g} mode at ~174 cm^{-1} (Figure 3-13).[40] Additionally, there is no evidence of either phase being present as impurities in each sample. In both cases, an extended range was employed for Raman spectroscopy in order to rule out the presence of MoO_2 and MoO_3, which would be seen at approximately $\tilde{\nu}$ = 750 cm^{-1} and $\tilde{\nu}$ = 800 cm^{-1}, respectively. The exclusion of these oxide impurities, and any other impurities, is crucial to ensure that any electrocatalytic activity associated with the studied catalyst is solely due to the material itself, rather than any other species present within the sample. Hence, by employing a solid-state route to $MoTe_2$, rather than chemical exfoliation *via* lithium intercalation, the electrocatalytic activity of the material itself can be confidently investigated.

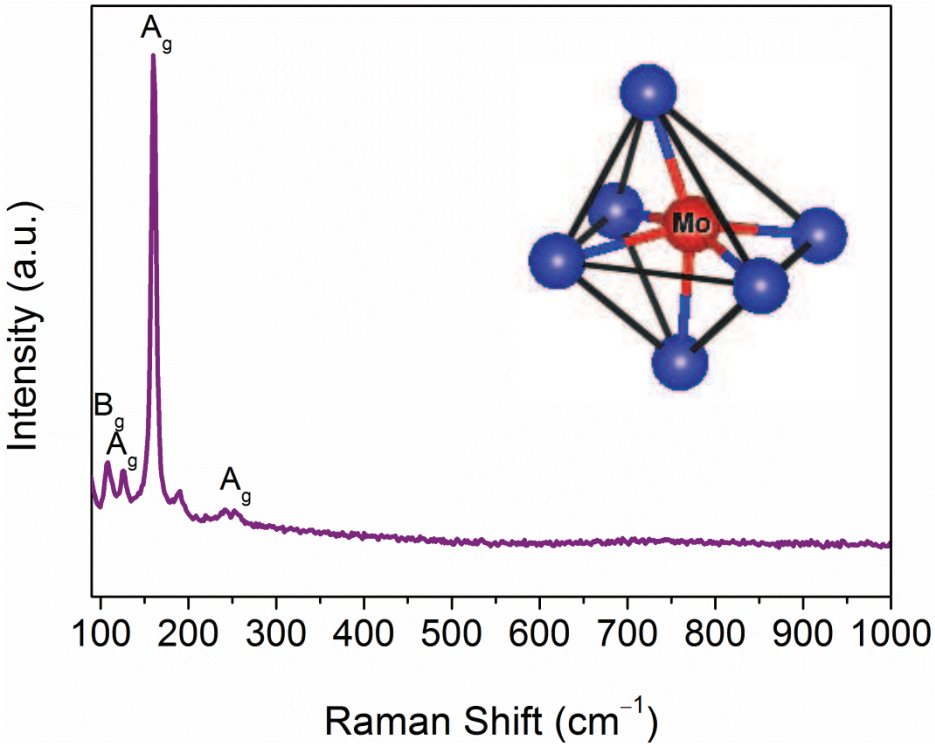

Figure 3-12: *Wide-range Raman spectrum of 1T'-$MoTe_2$ with four major vibrational modes highlighted. The inset shows the {$MoTe_6$} distorted octahedra which are the expected building blocks of the monoclinic phase.*

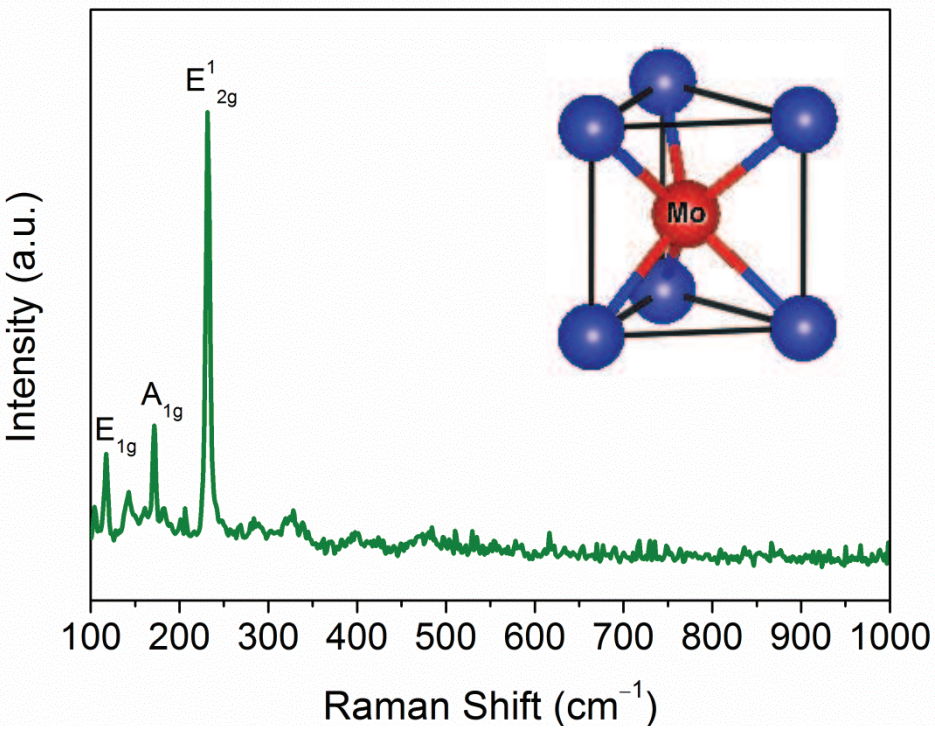

Figure 3-13: *Wide-range Raman spectrum of 2H-$MoTe_2$ with three major vibrational modes highlighted. The inset shows the {$MoTe_6$} trigonal prism which are the expected building blocks of the hexagonal phase.*

3.3.1.5. Composition of $MoTe_2$ Polymorphs

Additionally, energy-dispersive X-ray spectroscopy (EDX) was performed to analyse the elemental composition of both materials, with the weight and atomic compositions averaged over six areas of each sample. Accordingly, the elemental compositions were found to be identical within experimental error, with the stoichiometries being $Mo_{1.06(5)}Te_{1.94(5)}$ and $Mo_{1.00(9)}Te_{2.00(9)}$ for 1T'- and 2H-$MoTe_2$, respectively.

The composition of 1T'-$MoTe_2$ is particularly interesting as it indicates the material to be molybdenum-rich. Vellinga *et al.* reported the homogeneity region of the two $MoTe_2$ phases to be between $MoTe_{1.90}$ and $MoTe_{1.99}$, with the phase transition temperature varying depending on the resulting composition.[35] For Te-rich materials, the phase transition temperature was found to be 820 °C, while for Mo-rich samples a higher temperature of 880 °C is required. This then explains the incomplete formation of 1T'-$MoTe_2$ when powders were annealed at 850 °C during initial synthesis attempts.

The elemental compositions of both 1T'- and 2H-$MoTe_2$ were also found to be identical within experimental error by ICP-OES, which gave stoichiometric compositions of $Mo_{1.00}Te_{2.01(3)}$ and $Mo_{1.00}Te_{2.03(7)}$ for 1T'- and 2H-$MoTe_2$, respectively. From these analyses, the elemental composition shows negligible change upon transitioning from 1T'- to 2H-$MoTe_2$ using the simple annealing protocol, and hence compositional changes can be ruled out as a source of improved catalytic activity. Therefore, by a simple change in reaction temperature, both phases can be formed with an identical sample morphology and composition. This protocol removes the need for complex chemical exfoliation *via* lithium intercalation, as required for MoS_2. This thereby ensures that the only difference between the two phases is their coordination geometry. With this in mind, the catalytic activity of $MoTe_2$ can be accurately investigated with the only varying factor being the change in crystal structure and associated change in coordination geometry from 1T'- to 2H-$MoTe_2$.

3.3.2. Electrocatalytic Activity of $MoTe_2$ Polymorphs towards the HER

3.3.2.1. Electrode Preparation

Both $MoTe_2$ polymorphs were prepared for electrochemical testing by depositing the catalysts onto the surface of a glassy carbon electrode (surface area 0.071 cm^2). This involved preparing the materials as a catalyst ink according to a procedure reported by Gao *et al*.[41] In short, the ink was initially comprised of 1 mL water:ethanol (3:1), 40 µL Nafion™ and 10 mg catalyst. The mixture was then sonicated for 1 hour and 30 µL of this suspension was then drop-cast on to the surface of a glassy carbon working electrode. The Nafion™ content of the ink was later increased to 80 µL in order to aid the contact between catalyst and the glassy carbon electrode. Electrocatalytic measurements were then performed in a three-neck, single compartment cell using a three electrode set up in 1 M H_2SO_4. In addition to the catalyst-deposited glassy carbon working electrode, 3 M Ag/AgCl and carbon felt were used as the reference and counter electrodes, respectively.

An initial test was conducted on a bare glassy carbon working electrode to ensure that no catalytic activity arises from the use of carbon. Subsequently, the electrocatalytic activities of 2H-$MoTe_2$ and 1T'-$MoTe_2$ were tested by cyclic voltammetry, with the overpotential for hydrogen evolution being taken at a benchmark current density of $j = -10$ mA cm^{-2}, which corresponds to a 12.3% efficient solar-to-fuels device.[42] However, due to the presence of surface oxides as seen from XPS (Figure 3-14), both $MoTe_2$ materials require an initial oxide-layer-removal cycle. The presence of an oxide layer has been reported previously in the literature for $MoTe_2$ and other TMDCs, and can be simply removed upon application of potentiostatic bias.[32,43] It should also be noted that both MoO_2 and MoO_3 show no electrocatalytic properties towards the hydrogen evolution reaction.[44] Figure 3-15 highlights this removal of the oxide layer upon the first electrolytic cycle. Therefore, from herein, all polarisation curves, unless otherwise stated, have undergone a preliminary cycle to remove this oxide layer.

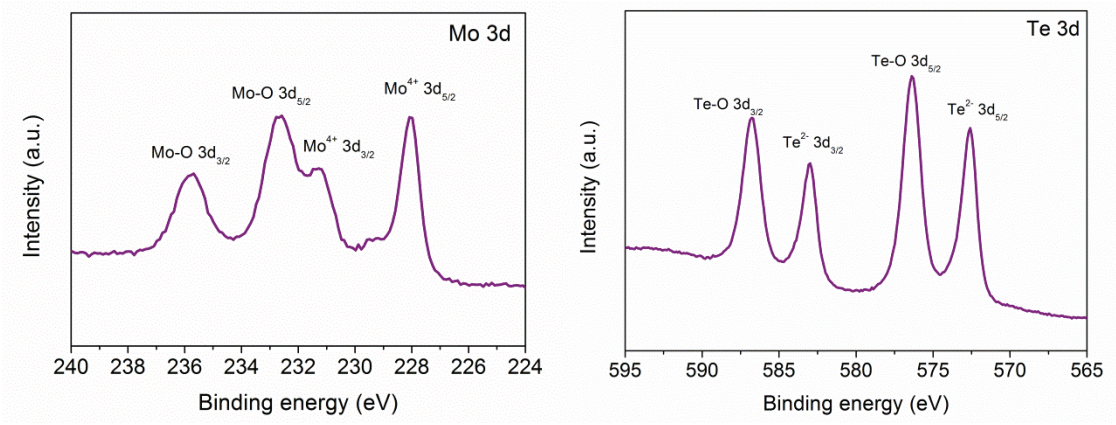

Figure 3-14: a) *3d Mo XPS spectra and* ***b)*** *3d Te XPS spectra of 1T'-$MoTe_2$ showing the presence of surface oxides.*

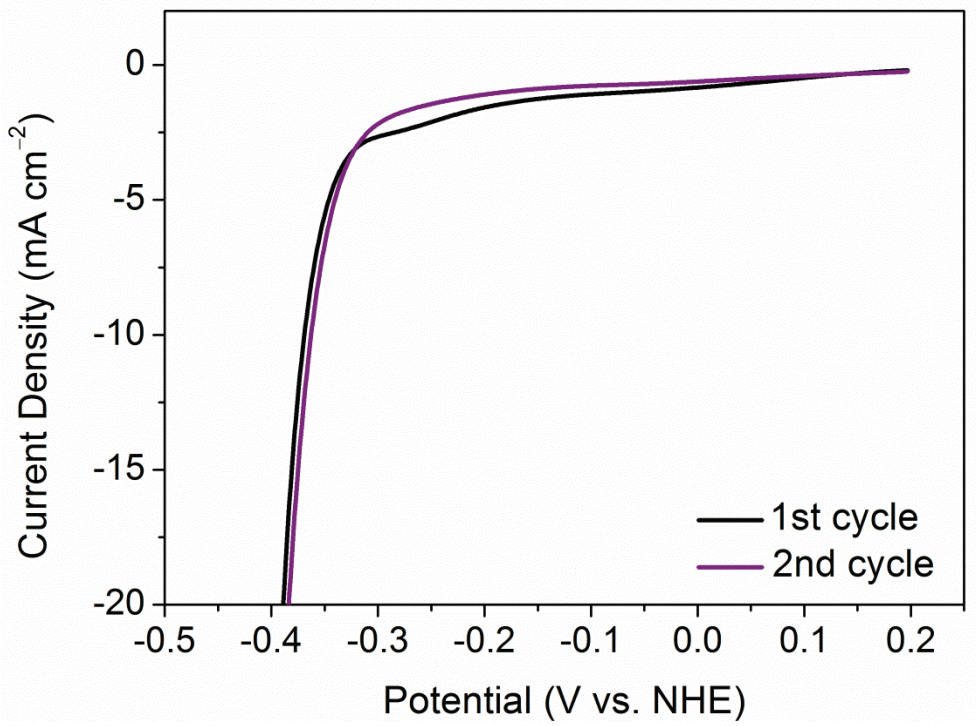

Figure 3-15: *Representative polarisation curves of 1T'-$MoTe_2$ highlighting the need for a preliminary oxide-layer-removal cycle.*

3.3.2.2. Overpotential Comparison

A comparison of the current densities achieved by each material is shown in Figure 3-16. Upon initial inspection of the overpotentials, the semiconducting 2H-$MoTe_2$ requires significantly greater cathodic potentials to reach a given current density than metallic 1T'-$MoTe_2$. In fact, the large overpotential of 650 mV associated with 2H-$MoTe_2$ is in line with that of 2H-MoS_2, which is considered to be catalytically inert.[45,46] Additionally, the overpotential of 2H-$MoTe_2$ is identical to that observed by Seok *et al*.[28] who also claim an inefficient catalytic activity of the semiconducting material. In contrast, 1T'-$MoTe_2$ requires significantly less energy to reduce protons to hydrogen than the 2H-phase, with the benchmark current density of $j = -10$ mA cm^{-2} being reached at an overpotential of 360 mV. This value is also on par with the results obtained by Seok *et al*.[28] with their single crystal 1T'-$MoTe_2$ requiring an overpotential of 356 mV for the same current density. The as-synthesised bulk $MoTe_2$ materials therefore exhibit an identical overpotential to the single crystals synthesised by the flux method.[47] However, following this work, several studies have reported varying overpotentials for $MoTe_2$, with the catalytic activities varying according to their method of preparation. Altering the route of preparation leads to a range of surface areas and morphologies. Therefore the drastic difference in overpotentials in the literature can be explained by the varying degree of active sites available within each material.[42] A summary of the literature reports on $MoTe_2$ is shown in Table 3-6.

Table 3-6: *Comparison of HER performances of $MoTe_2$.*

Sample	**Preparation method**	**Overpotential (vs. NHE) for $j = -10$ mA cm^{-2}**	**Tafel Slope (mV dec^{-1})**	**Ref.**
Single crystal 2H-$MoTe_2$	Flux Method	650 mV	184	[28]
Single crystal 1T'-$MoTe_2$	Flux Method	356 mV	127	[28]
Few-layer 1T'-$MoTe_2$ film	Precise defect adjusting	230 mV	44	[31]
1T'-$MoTe_2$ thin film	Thermally assisted conversion	481 mV	67	[32]
Bulk 2H-$MoTe_2$	Purchased from Lonjin Metal Material Co., Ltd	500 mV	120	[48]
1T'-$MoTe_2$ nanosheets	Liquid-exfoliation	309 mV	175	[48]
$MoTe_2$ - BuLi	Chemical Exfoliation	380 mV	57	[33]
Bulk 1T'-$MoTe_2$	Solid-state synthesis	360 mV	78	This work[49]
Bulk 2H-$MoTe_2$	Solid-state synthesis	650 mV	159	This work[49]

Since a solid-state route to $MoTe_2$ is applied in this work, and the phases can be interchanged simply by varying the reaction temperature, the sample morphology is consistent between both materials. This then means that the surface area and the number of edge sites of 2H and 1T'-$MoTe_2$ are similar, meaning the electrochemical performance can be accurately compared. In this way, the catalytic activity can be attributed to either the semiconducting or metallic nature of the $MoTe_2$ phase. Thus, from the LSV it is clear that the monoclinic arrangement of $\{MoTe_6\}$ octahedra results in an intrinsically more active material than the hexagonal phase. This is in line with recent work on 1T'-$MoTe_2$ single crystals which indicate that the basal plane is the major active site for hydrogen evolution in metallic materials.[28] From these initial tests, it is apparent that the transition from the monoclinic to

the hexagonal structure dramatically alters the catalytic properties of TMDCs towards the HER.

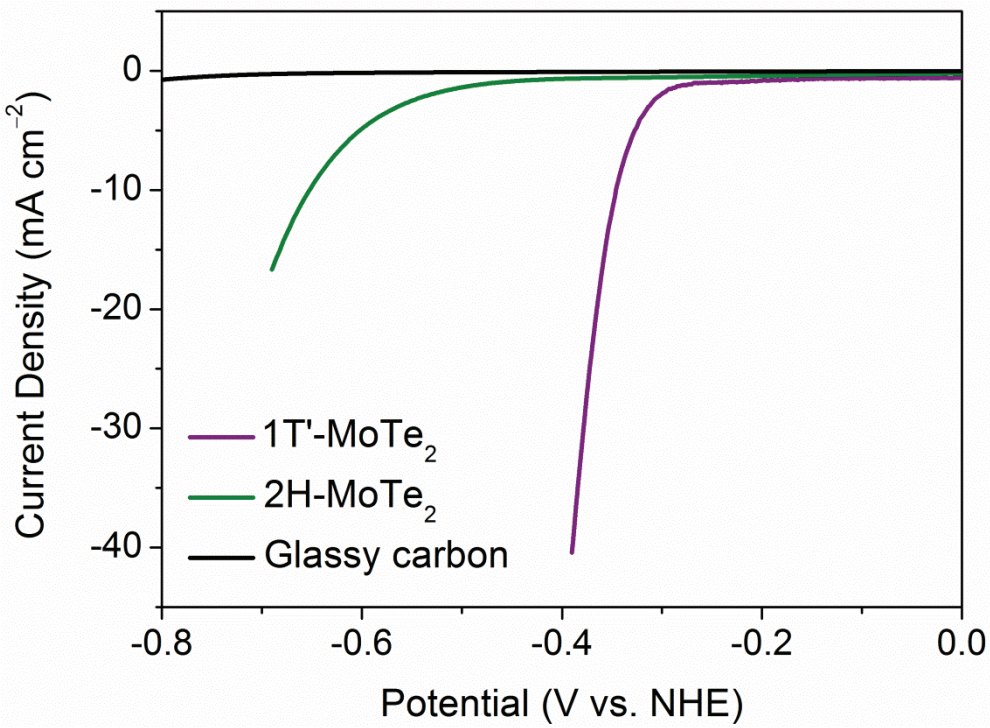

Figure 3-16: *Comparison of the current densities achieved by 1T'- and 2H-$MoTe_2$ in 1 M H_2SO_4 electrolyte. Bare glassy carbon is also included as a control measurement to ensure no contributing activity. Catalysts were prepared on a glassy carbon working electrode as described in the experimental chapter. A 3 M Ag/AgCl reference and carbon felt counter electrode were used. Curves were obtained using linear sweep voltammetry with a scan rate of 2 mV s^{-1} and all resistances were compensated for.*

3.3.2.3. Analysis of the Reaction Kinetics

Further insight into the catalytic activity is provided by Tafel analysis, which allows for a description of the reaction kinetics. Ideally, an efficient HER catalyst reaches the highest possible current density at the lowest possible overpotential. For example, the current state-of-the-art platinum electrocatalyst exhibits the lowest reported Tafel slope of 30 mV dec^{-1} due to the exceptionally efficient adsorption of hydrogen on the Pt (110) surface.[50] From the Tafel slope, the reaction mechanism can be interpreted, with hydrogen production on platinum known to proceed *via* the Volmer-Tafel mechanism.[51] This mechanism involves the initial adsorption of hydrogen onto the catalyst surface (Volmer) followed by the slow, *i.e.* rate-limiting, recombination step (Tafel). On the other hand, TMDC catalysts have been proposed to operate *via* the Volmer-Heyrovsky mechanism of hydrogen evolution, with the

electrochemical desorption step (Heyrovsky) known to be rate-limiting (see Table 3-2 in Section 3.1.4. for a description of electrochemical processes).[6,52] As such, Tafel analysis allows for an effective comparison between the activities of 1T'- and 2H-$MoTe_2$. Figure 3-17 shows the Tafel plots, and corresponding Tafel slopes, of both catalysts and reiterates the improved performance of the metallic phase. In the case of 2H-$MoTe_2$, a Tafel slope of 159 ± 6 mV dec^{-1} was obtained, which indicates that the reaction kinetics of the HER are limited due to the inefficient adsorption of hydrogen on the catalyst surface. This is perfectly in line with earlier studies which explain that inefficient hydrogen adsorption occurs on bulk 2H-MoS_2 due to the material being comprised primarily of inert basal plane sites rather than catalytically active edge sites.[52] By transitioning to the metallic 1T'-phase, however, the predominately active site is the basal plane, which therefore results in improved reaction kinetics, as evidenced by the reduced Tafel slope of 78 ± 4 mV dec^{-1}. This is then indicative of hydrogen adsorption on metallic active sites being much more efficient than on semiconducting sites.[4]

As mentioned above, TMDCs have been proposed to operate *via* the Volmer-Heyrovsky mechanism of hydrogen evolution, with a Tafel slope of 40 mV dec^{-1} being expected.[52] However, Seok *et al.* suggest that the traditional volcano plot analysis for determining the reaction mechanism may not be applicable in the case of 1T-$MoTe_2$, and report a Tafel slope as high as 127 mV dec^{-1}.[28] The authors propose that this is due to a spontaneous Peierls-type lattice distortion that occurs with hydrogen adsorption, and improves the HER as a result. Hydrogen adsorption is therefore the rate determining step in the reaction mechanism, thus explaining the large Tafel slope. However, despite obtaining identical overpotentials for 2H- and 1T'-$MoTe_2$ as Seok *et al.*,[28] the Tafel slopes derived in this work vary significantly. Since the reaction kinetics depend on the density of active sites, it is possible that the variation between reports is due to the preparation route, *i.e.* single crystals *via* the flux method in the case of work by Seok *et al.* in contrast to drop-casting bulk materials on to a glassy carbon electrode (this work). Nonetheless, the general trend of the metallic phase exhibiting lower Tafel slopes than the semiconducting phase is consistent for both studies.

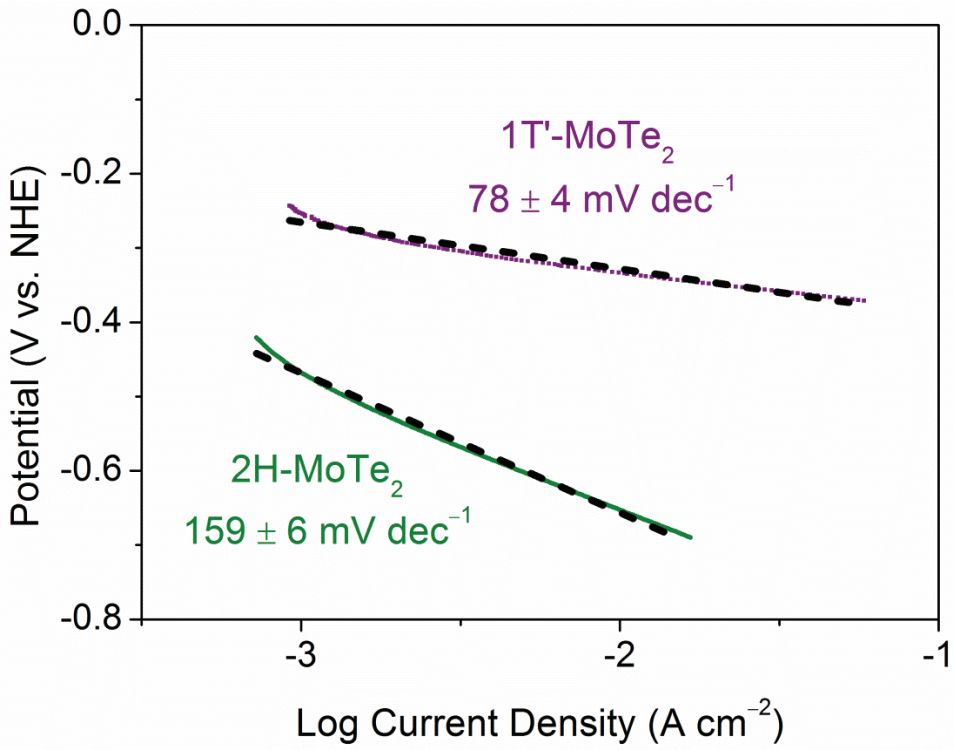

Figure 3-17: *Tafel plots and corresponding Tafel slopes of 1T'-$MoTe_2$ and 2H-$MoTe_2$ in 1 M H_2SO_4. Slopes were obtained by linear sweep voltammetry with a scan rate of 2 mV s^{-1}. Dashed lines are provided as a guide to the eye. All current densities have been compensated for resistance.*

To probe the reaction kinetics further, electrochemical impedance spectroscopy (EIS) was investigated to observe the change in charge transfer resistance, R_{CT}, upon transitioning between polymorphs. Obtaining Nyquist plots allows for the elucidation of R_{CT} at a given potential, in this case –300 mV (vs. NHE), which can be extrapolated as the diameter of the semi-circle. Figure 3-18 illustrates the Nyquist plots obtained for 1T'- and 2H-$MoTe_2$, and extrapolation gives their respective charge transfer resistances of 740 and 8300 Ω. This dramatic difference in charge transfer resistance between polymorphs is attributed to the conductive properties of metallic 1T'-$MoTe_2$ compared to the semiconducting 2H-$MoTe_2$. The metallic nature of the 1T'-phase leads to more efficient charge transfer kinetics, as evidenced by the lower R_{CT} value and also by Tafel analysis as discussed previously. This increased activity in charge transfer is associated with an increased activity for the HER, as reported previously for metallic 1T-MoS_2 nanosheets.[9,16] As a result, significantly higher current densities can be achieved at considerably lower overpotentials. Thus, since changes in composition and morphology have been ruled out, it is clear that the catalytic activity of

1T'-$MoTe_2$ arises from the polymorphic transition, meaning the coordination geometry is key for the development of active hydrogen evolution electrocatalysts.

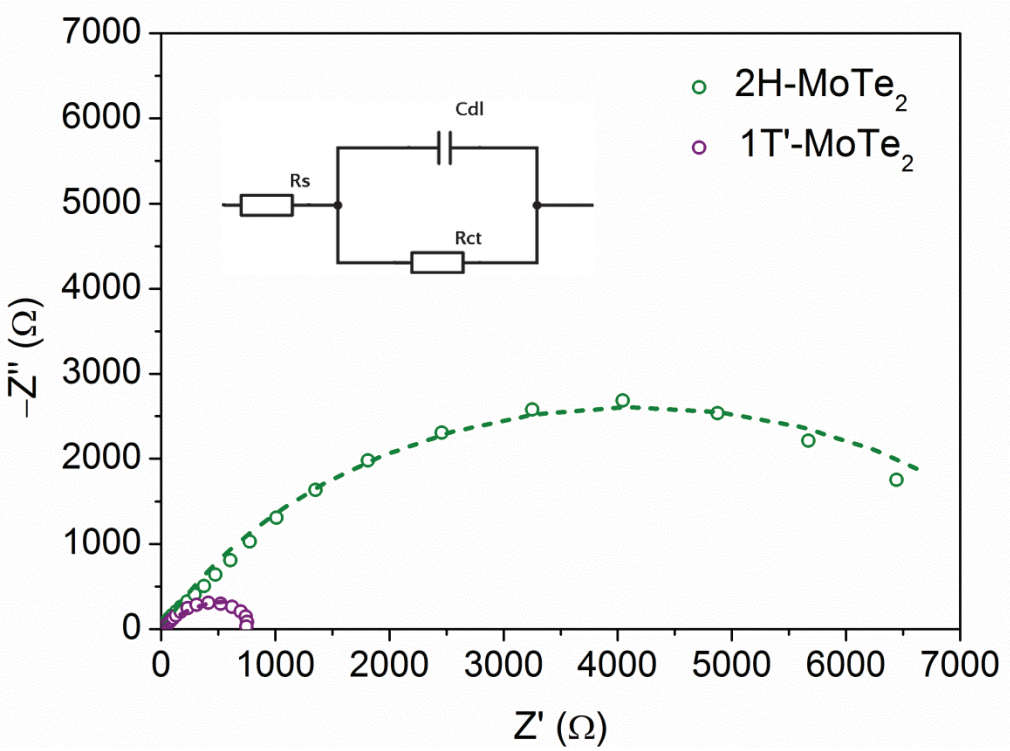

Figure 3-18: *Nyquist plots showing electrochemical impedance spectroscopy on 2H-$MoTe_2$ and 1T'-$MoTe_2$ in 1 M H_2SO_4 electrolyte at a potential of –300 mV (vs. NHE). Uncompensated resistances were calculated as R_u = 8.4 and 8.0 Ω, respectively, which are in close agreement with the iR compensation function on the potentiostat. Dashed lines represent the equivalent circuit fitting, obtained using Randles circuit model.*

The origin of the catalytic activity in 1T'-$MoTe_2$ can therefore be attributed solely to the change in crystal structure. The distorted octahedral coordination gives rise to a partially filled valence band, meaning electron density can be accepted. On the contrary, the trigonal prismatic coordination of 2H-$MoTe_2$ leads to a fully occupied valence band, thus limiting electron transfer on the catalyst surface. In the case of 1T'-$MoTe_2$, protons are free to adsorb onto the surface of the catalyst, and are then reduced to hydrogen upon application of a sufficient overpotential. Since changes in composition and morphology have been discarded, the generation of catalytic activity in 1T'-$MoTe_2$, and similarly other TMDCs, has been de-convoluted.

3.3.2.4. Electrochemical Stability of $MoTe_2$ Catalysts

A limitation for current 'state-of-the-art' nanostructured catalysts is their stability, with 1T-MoS_2 shown to exhibit a reverse transformation into the catalytically unfavourable 2H phase. Hence, in this regard, bulk materials show considerable promise. The electrochemical stability of both $MoTe_2$ polymorphs was investigated using cyclic voltammetry. This involved sweeping the applied potential for 1000 cycles in 1 M H_2SO_4. A comparison of the current densities achieved during the initial cycle and 1000th cycle of 1T'-$MoTe_2$ is shown in Figure 3-19. After 1000 cycles, although there appears to be a very minor difference in the onset of hydrogen evolution, the catalytic activity remains stable, *i.e.* the current densities achieved before and after 1000 cycles are identical at a given potential. Likewise, the activity of 2H-$MoTe_2$ also remains constant, with no changes in current density observed after 1000 cycles (Figure 3-20). Additionally, after cycling, the Raman spectra of both materials were obtained in order to observe any changes related to the crystal structure. As can be seen in Figures 3-21 and 3-22, which show the Raman spectra of 1T'- and 2H-$MoTe_2$ before and after 1000 cycles, respectively, there are no obvious structural changes. Therefore, unlike 1T-MoS_2 which shows the reverse transformation from 1T- to 2H-MoS_2, both materials remain phase pure and show no sign of degradation.

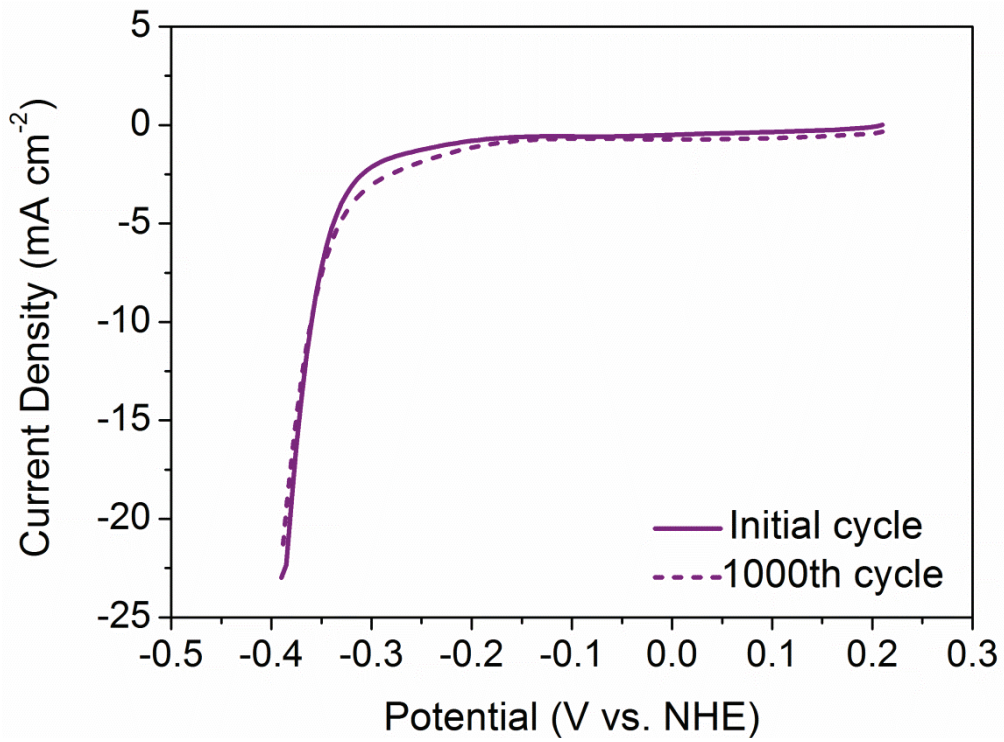

Figure 3-19: *Comparison of the current densities achieved by 1T'-$MoTe_2$ before and after 1000 cycles in 1 M H_2SO_4. Dashed lines represent the 1000th cycle. Catalysts were prepared on a glassy carbon working electrode as described in the experimental chapter. A 3 M Ag/AgCl reference and carbon felt counter electrode were used. Curves were obtained using linear sweep voltammetry at a scan rate of 100 mV s^{-1} and all resistances were compensated for.*

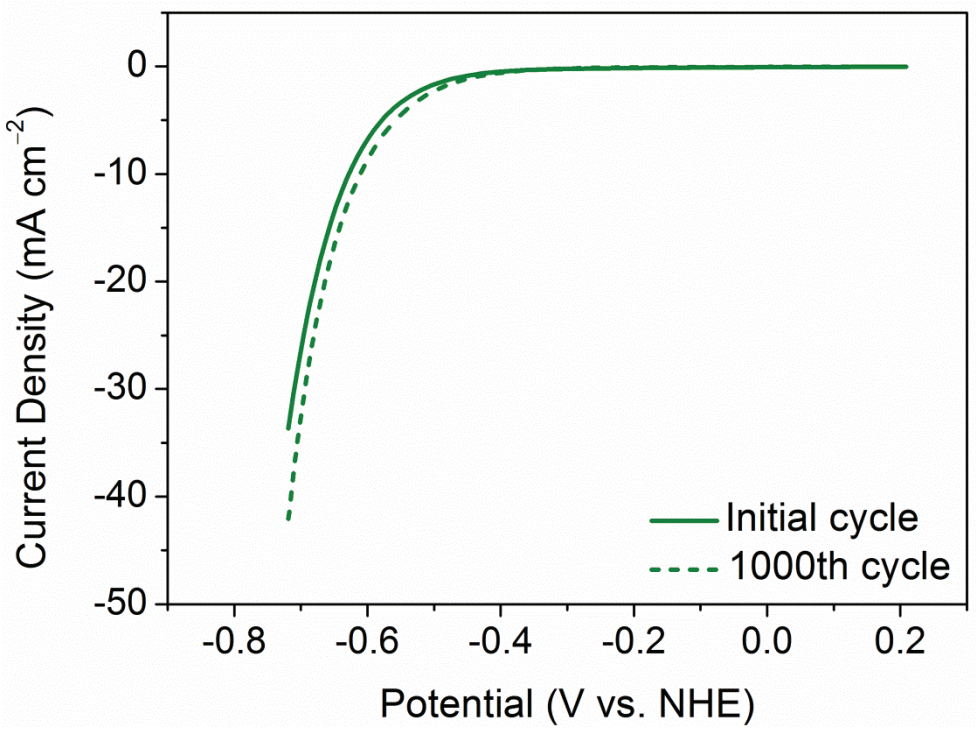

Figure 3-20: *Comparison of the current densities achieved by 2H-$MoTe_2$ before and after 1000 cycles in 1 M H_2SO_4. Dashed lines represent the 1000th cycle. Catalysts were prepared on a glassy carbon working electrode as described in the experimental chapter. A 3 M Ag/AgCl reference and carbon felt counter electrode were used. Curves were obtained using linear sweep voltammetry at a scan rate of 100 mV s^{-1} and all resistances were compensated for.*

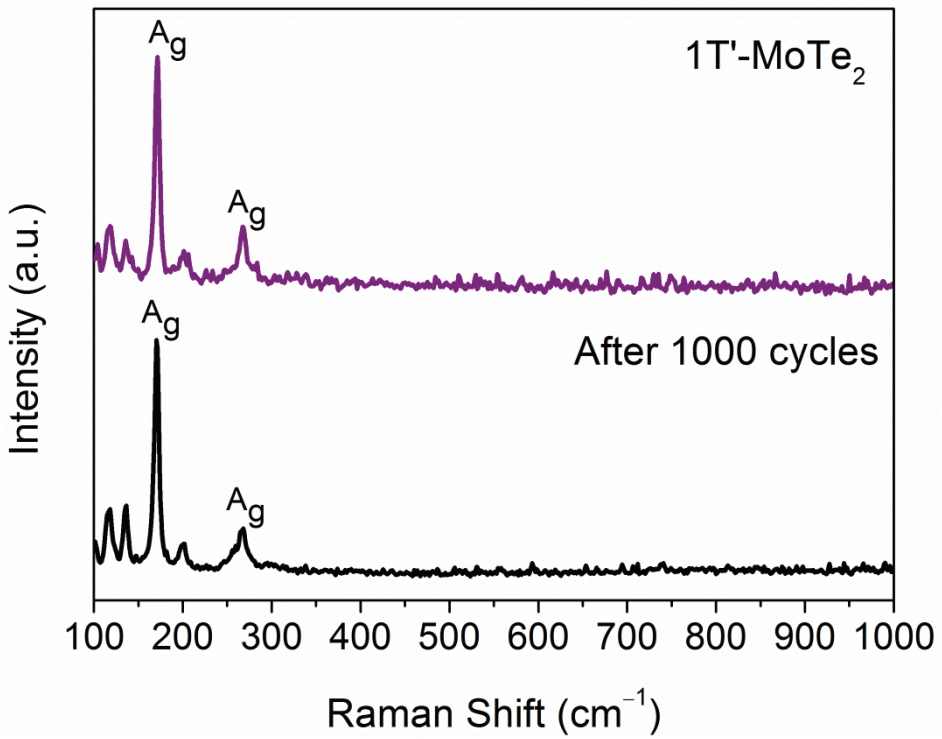

Figure 3-21: *Comparison of the Raman spectra of 1T'-$MoTe_2$ obtained before and after the 1000 cycle stability test.*

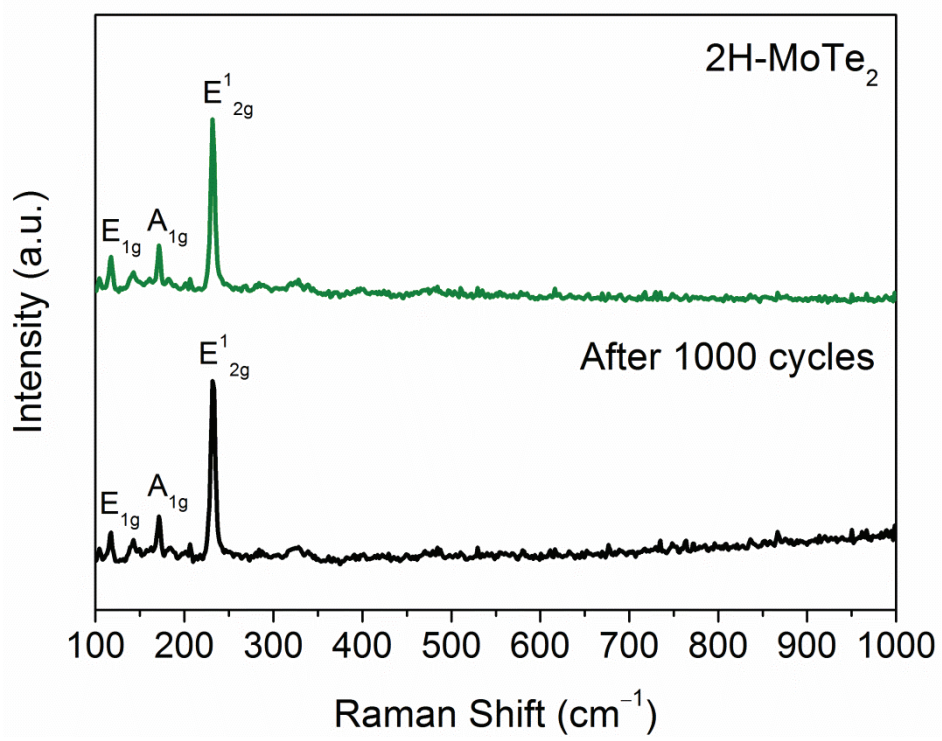

Figure 3-22: *Comparison of the Raman spectra of 2H-$MoTe_2$ obtained before and after the 1000 cycle stability test.*

3.3.2.5. Confirmation of Hydrogen Production

One of the most important, and often overlooked, experiments in the development of electrocatalysts for the HER is the confirmation of hydrogen production by gas chromatography. In this way, the reduction observed by linear sweep voltammetry is attributed categorically to the production of hydrogen, rather than to the reduction of any other species present in the system. Accordingly, the Faradaic efficiency, which relates the experimentally determined percentage of hydrogen produced to the theoretical value calculated from the charge passed, can also be determined.

Gas chromatography measurements were conducted in an airtight single cell with a two-electrode setup that consisted of the catalyst-deposited glassy carbon working electrode and carbon felt attached to a silver wire as the counter electrode. Before investigation of the catalysts, the experiment was performed using platinum as the working electrode to ensure the cell was airtight. Galvanostatic electrolysis was performed with an applied current density of $j = -3.4$ mA cm^{-2}. The headspace was sampled (25 µL) and injected directly into the GC at set time intervals throughout the course of the reaction. The Faradaic efficiencies were then calculated as the ratio of expected H_2 (%) in the headspace (as calculated from the charge passed) to the H_2 (%) detected using the GC.

In both cases, 1T'- and 2H-$MoTe_2$ were shown to produce hydrogen, thus confirming their ability to act as hydrogen evolution catalysts. The Faradaic efficiencies were then determined to be 95 ± 8% and 82 ± 14% for 1T'-$MoTe_2$ and 2H-$MoTe_2$, respectively. Figures 3-23 and 3-24 illustrate a representative trace of the GC analysis of the headspaces in each airtight cell.

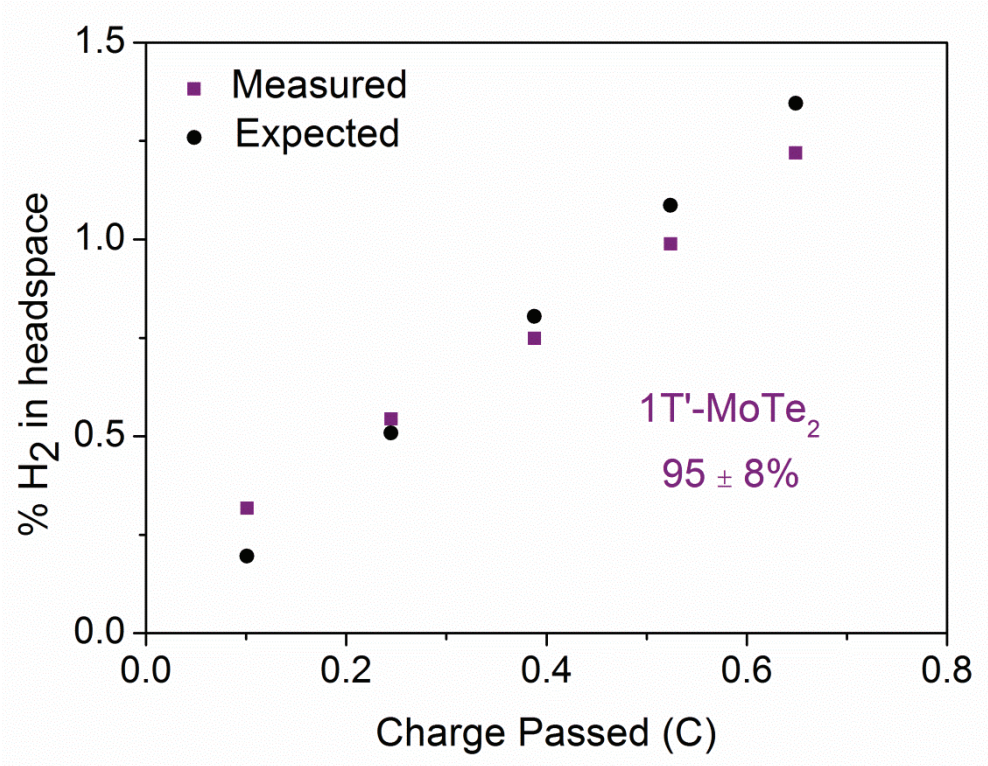

Figure 3-23: *A representative trace of the gas chromatographic analysis of the single-cell headspace during electrolysis of 1T'-$MoTe_2$ during which a constant current density of j = –3.4 mA cm^{-2} was applied in 1 M H_2SO_4. The expected proportion (%) of H_2 in the headspace was calculated from the charge passed, and the proportion (%) of H_2 measured experimentally was determined using gas chromatography.*

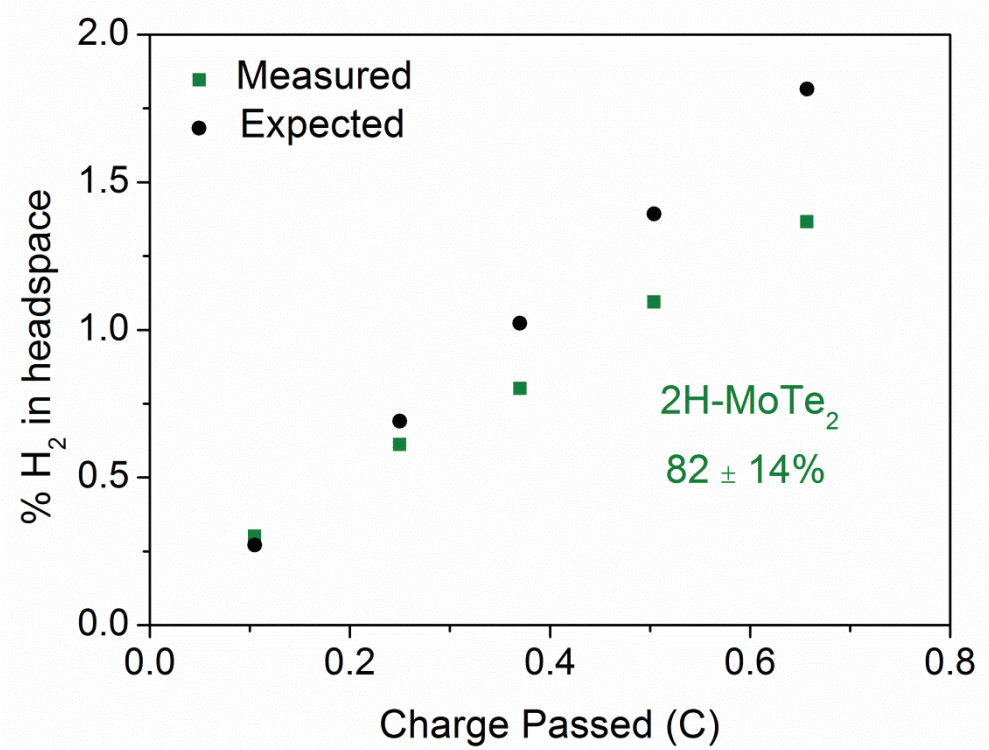

Figure 3-24: *A representative trace of the gas chromatographic analysis of the single-cell headspace during electrolysis of 2H-$MoTe_2$ during which a constant current density of –3.4 mA cm^{-2} was applied in 1 M H_2SO_4. The expected proportion (%) of H_2 in the headspace was calculated from the charge passed, and the proportion (%) of H_2 measured experimentally was determined using gas chromatography.*

3.4. Conclusions

In summary, this chapter has focused on understanding the origin of the enhanced catalytic activity in TMDCs. By applying a solid-state route to $MoTe_2$, both semiconducting and metallic polymorphs could be synthesised in the bulk form, thus ruling out the effect of nanostructuring as the source of improved performance. Upon polymorphic transition between 1T'- and 2H-$MoTe_2$ the morphology is retained, meaning that the catalytic activity can be investigated and compared in the bulk form with both materials exhibiting identical plate-like microcrystals. This is in contrast to the synthesis of MoS_2 polymorphs, which require chemical exfoliation in order to induce the transition between phases. This chemical exfoliation results in the formation of a nanostructured 1T-MoS_2 material, and introduces a variety of factors which may affect catalytic activity. Consequently, since the need for chemical exfoliation *via* lithium intercalation has been excluded in the case of $MoTe_2$, the stoichiometry of both 2H- and 1T'-$MoTe_2$ is identical within experimental error, meaning that any compositional changes in the form of defects / vacancies can also be disregarded. In this way, the electrocatalytic performance of both $MoTe_2$ polymorphs can be accurately investigated with the change in coordination geometry being the sole difference between materials. Thus, the superior performance of 1T'-$MoTe_2$ is attributed to the phase transition which gives rise to metallic conductivity. This in turn results in more efficient reaction kinetics associated with the reduced charge transfer resistance of the metallic phase. In contrast to 1T-MoS_2, 1T'-$MoTe_2$ remains stable after 1000 cycles in 1 M H_2SO_4, with no obvious structural transformation into the inferior 2H-phase occurring. Finally, gas chromatography confirms a full Faradaic Efficiency for 1T'-$MoTe_2$, thus confirming that polymorphic control allows for the access of a highly efficient and stable electrocatalyst in the bulk form, which would otherwise be considered catalytically inert.

3.5. References

1. Kertesz, M. & Hoffmann, R. Octahedral vs. trigonal-prismatic coordination and clustering in transition-metal dichalcogenides. *J. Am. Chem. Soc.* **106**, 3453–3460 (1984).

2. Bronsema, K. D., De Boer, J. L. & Jellinek, F. On the structure of molybdenum diselenide and disulfide. *ZAAC J. Inorg. Gen. Chem.* **540**, 15–17 (1986).

3. Tang, Q. & Jiang, D. Stabilization and Band-Gap Tuning of the 1T-MoS_2 Monolayer by Covalent Functionalization. *Chem. Mater.* **27**, 3743-3748 (2015).

4. Voiry, D., Salehi, M., Silva, R., Fujita, T., Chen, M., Asefa, T., Shenoy, V. B., Eda, G. & Chhowalla, M. Conducting MoS_2 Nanosheets as Catalysts for Hydrogen Evolution Reaction. *Nano Lett.* **13**, 6222-6227 (2013).

5. Ge, P., Scanlon, M. D., Peljo, P., Bian, X., Vubrel, H., O'Neill, A., Coleman, J. N., Cantoni, M., Hu, X., Konturri, K., Liu, B & Girault, H. H. Hydrogen evolution across nano-Schottky junctions at carbon supported MoS_2 catalysts in biphasic liquid systems. *Chem. Commun.* **48**, 6484–6486 (2012).

6. Tang, Q. & Jiang, D. Mechanism of Hydrogen Evolution Reaction on 1T-MoS_2 from First Principles. *ACS Catal.* **6**, 4953-4961 (2016).

7. Fang, Y., Pan, J., He, J., Luo. R., Wang, D., Che, X., Bu, K., Zhao, W., Liu, P., Mu, G., Zhnag, H., Lin, T. & Huang, F. Structure Re-determination and Superconductivity Observation of Bulk 1T MoS_2. *Angew. Chem. Int. Ed.* **57**, 1232–1235 (2018).

8. Chhowalla, M., Suk Shin, H., Eda,G., Li, L-J., Ping Loh, K. & Zhnag, H. The chemistry of two-dimensional layered transition metal dichalcogenide nanosheets. *Nature Chem.* **5**, 263-275 (2013).

9. Lukowski, M. A., Daniel, A. S., Meng, F., Forticaux, A., Li, L. & Jin, S. Enhanced Hydrogen Evolution Catalysis from Chemically Exfoliated Metallic MoS_2 Nanosheets. *J. Am. Chem. Soc.* **135**, 10274-10277 (2013).

10. Eda, G., Yamaguchi, H., Voiry, D., Fujita, T., Chen, M. and Chhowalla, M. Photoluminescence from Chemically Exfoliated MoS_2. *Nano Lett.* **12**, 526 (2012).

11. Py, M. A. & Haering, R. R. Structural destabilization induced by lithium intercalation

in MoS_2 and related compounds. *Can. J . Phys* **61**, (1983).

12. Dawson, W. G. & Bullett, D. W. Electronic structure and crystallography of $MoTe_2$ and WTe_2. *J. Phys. C Solid State Phys.* **20**, 6159–6174 (1987).

13. Hinnemann, B., Georg Moses, P., Bonde, J., Jórgensen, K. P., Nielsen, J. H., Horch, S., Chorkendorff, I. & Nørskov, J. K. Biomimetic Hydrogen Evolution: MoS_2 Nanoparticles as Catalyst for Hydrogen Evolution. *J. Am. Chem. Soc.* **127**, 5308–5309 (2005).

14. Trasatti, S. Work function, electronegativity, and electrochemical behaviour of metals. II. Potentials of zero charge and 'electrochemical' work functions. *J. Electroanal. Chem.* **33**, 351–378 (1971).

15. Jaramillo, T. F., Jørgensen, K. P., Bonde, J., Nielsen, J. H., Horch, S. & Chorkendorff, I. Identification of Active Edge Sites for Electrochemical H_2 Evolution from MoS_2 Nanocatalysts. *Science* **317**, 100–102 (2007).

16. Voiry, D., Salehi, M., Silva, R., Fujita, T., Chen, M., Asefa, T., Shenoy, V. B., Eda, G. & Chhowalla, M. Conducting MoS_2 Nanosheets as Catalysts for Hydrogen Evolution Reaction. *Nano Lett.* **13**, 6222–6227 (2013).

17. Bonde, J., Moses, P. G., Jaramillo, T. F., Nørskov, J. K. & Chorkendorff, I. Hydrogen evolution on nano-particulate transition metal sulfides. *Faraday Discuss.* **140**, 219-231 (2008).

18. Ejigu, A., Kinloch, I. A., Prestat, E. & Dryfe, R. A. W. A simple electrochemical route to metallic phase trilayer MoS_2 : evaluation as electrocatalysts and supercapacitors. *J. Mater. Chem. A* **5**, 11316–11330 (2017).

19. Xiong, F., Wang, H., Liu, X., Sun, J., Brongersma, M., Pop, E. & Cui, Y. Li Intercalation in MoS_2: In Situ Observation of Its Dynamics and Tuning Optical and Electrical Properties. *Nano Lett.* **15**, 6777–6784 (2015).

20. Xia, J., Wang, J., Chao, D., Chen, Z., Liu, Z., Kuo, J-L., Yan, J. & Xiang Shen, Z. Phase evolution of lithium intercalation dynamics in 2H-MoS_2. *Nanoscale* **9**, 7533–7540 (2017).

21. Kan, M., Wang, J. Y. Li, X. W., Zhang, S. H., Li, Y. W., Kawazoe, Y., Sun, Q. & Jena, P. Structures and Phase Transition of a MoS_2 Monolayer. *J. Phys. Chem. C* **118**,

1515–1522 (2014).

22. Heising, J. & Kanatzidis, M. G. Exfoliated and Restacked MoS_2 and WS_2: Ionic or Neutral Species? Encapsulation and Ordering of Hard Electropositive Cations. *J. Am. Chem. Soc.* **121**, 11720–11732 (1999).

23. Sung, J. H., Heo, H., Si, S., Hyeon Kim, Y., Rae Noh, H., Song, K., Kim, J., Lee, C-S., Seo, S-Y., Kim, D-H., Kug Kim, H., Woong Yeom, H., Kim, T-H., Choi, S-Y., Sung Kim, J. & Jo, M-H. Coplanar semiconductor-metal circuitry defined on few-layer $MoTe_2$ via polymorphic heteroepitaxy. *Nat. Nanotechnol.* **12**, 1064–1070 (2017).

24. Kumar, A. & Ahluwalia, P. K. Electronic structure of transition metal dichalcogenides monolayers 1H-MX_2 (M = Mo, W; X = S, Se, Te) from ab-initio theory: new direct band gap semiconductors. *Eur. Phys. J. B* **85**, (2012).

25. Vellinga, M. B., de Jonge, R. & Haas, C. Semiconductor to metal transition in $MoTe_2$. *J. Solid State Chem.* **2**, 299–302 (1970).

26. Puotinen, D. & Newnham, R. E. The crystal structure of $MoTe_2$. *Acta Crystallogr.* **14**, 691–692 (1961).

27. Brown, B. E. The Crystal Structures of WTe_2 and High-Temperature $MoTe_2$. *Acta Cryst* **20**, (1966).

28. Seok, J., lee, J-H., Cho, S., Ji, B., Won Kim, H., Kwon, M., Kim, D., Kim, Y-M., Ho Oh, S., Wng Kim, S., Hee Lee, Y., Son, Y-W. & Yang, H. Active hydrogen evolution through lattice distortion in metallic $MoTe_2$. *2D Mater.* **4**, 25061 (2017).

29. Keum, D. H., Cho, S., Ho Kim, J., Choe, D-H., Sung, H-J., Kan, M., Kang, H., Hwang, J-Y., Wng Kim, S., Yang, H. Chang, K. J. & Hee Lee, Y. Bandgap opening in few-layered monoclinic $MoTe_2$. *Nature Physics* **11**, 482-486 (2015).

30. Song, S., Keum, D. H., Cho, S., Perello, D., Kim, Y. & Hee Lee, Y. Room Temperature Semiconductor-Metal Transition of $MoTe_2$ Thin Films Engineered by Strain. *Nano Lett.* **16**, 188-193 (2016).

31. Zhuang, P., Sun, Y., Dong, P., Smith, W., Sun, Z., Ge, Y., Pei, Y., Cao, Z., Ajayan, P. M., Shen, J. & Ye, M. Revisiting the Role of Active Sites for Hydrogen Evolution Reaction through Precise Defect Adjusting. *Adv. Funct. Mater.* **29**, 1901290 (2019).

32. McManus, J. B., Cunningham, G., McEvoy, N., Cullen, C. P., Gity, F., Schmidt, M., McAteer, D., Mullarkey, D., Shvets, I. V., Hurley, P. K., Hallam, T. & Duesberg, G. S. Growth of 1T′-$MoTe_2$ by Thermally Assisted Conversion of Electrodeposited Tellurium Films. *ACS Appl. Energy Mater.* **2**, 521–530 (2019).

33. Luxa, J., Vosecky, P., Mazánek, V., Sedmidubsky, D., Pumera, M., Lazar, P & Sofer, Z. Layered Transition-Metal Ditellurides in Electrocatalytic Applications - Contrasting Properties. *ACS Catal.* **7**, 5706–5716 (2017).

34. Knop, O. & MacDonald, R. D. Chalkogenides of the Transition Elements. *Can. J. Chem.* **39**, 897-904 (1961).

35. Vellinga, M. B., de Jonge, R. & Haas, C. Semiconductor to metal transition in $MoTe_2$. *J. Solid State Chem.* **2**, 299-302 (1970).

36. Revolinsky, E. & Beerntsen, D. J. Electrical Properties of α- and β-$MoTe_2$ as Affected by Stoichiometry and Preparation Temperature. *J. Phys. Chem. Solids Pergamon Press* **27**, 523–526 (1966).

37. Toby, B. H. EXPGUI, a graphical user interface for GSAS. *J. Appl. Crystallogr.* **34**, 210–213 (2001).

38. Jana, M. K., Singh, A., Sampath, A., Rao, C. N. R. & Waghmare, U. V. Structure and Electron-Transport Properties of Anion-Deficient $MoTe_2$: A Combined Experimental and Theoretical Study. *Zeitschrift für Anorg. und Allg. Chemie* **642**, 1386–1396 (2016).

39. Zhou, L., Zubair, A., Wang, Z., Zhang, X., Ouyang, F., Xu, K., Fang, W., Ueno, K., Li, J., Palacios, T., Kong, J. & Dresselhaus, M. S. Synthesis of High-Quality Large-Area Homogenous 1T′ $MoTe_2$ from Chemical Vapor Deposition. *Adv. Mater.* **28**, 9526–9531 (2016).

40. Guo, H., Yang, T., Yamamoto, M., Zhou, L., Ishikawa, R., Ueno, K., Tsukagoshi, K., Zhnag, Z., Dresselhaus, M. S. & Saito, R. Double resonance Raman modes in monolayer and few-layer $MoTe_2$. *Phys. Rev. B - Condens. Matter Mater. Phys.* **91**, 205415 (2015).

41. Gao, S., Lin, Y., Jiao, X., Sun, Y., Luo, Q., Zhang, W., Li, D., Yang, J. & Xie, Y. Partially oxidized atomic cobalt layers for carbon dioxide electroreduction to liquid fuel. *Nature* **529**, 68–71 (2016).

42. Voiry, D., Chhowalla, M., Gogotsi, Y., Kotov, N. A., Li, Y., Penner, R. M. Schaak, R. E. & Weiss, P. S. Best Practices for Reporting Electrocatalytic Performance of Nanomaterials. *ACS Nano* **12**, 9635–9638 (2018).

43. Oshikawa, K., Nagai, M. & Omi, S. Characterization of molybdenum carbides for methane reforming by TPR, XRD, and XPS. *J. Phys. Chem. B* **105**, 9124–9131 (2001).

44. Vrubel, H. & Hu, X. Molybdenum Boride and Carbide Catalyze Hydrogen Evolution in both Acidic and Basic Solutions. *Angew. Chem. Int. Ed.* **51**, 12703-12706 (2012).

45. Merki, D., Fierro, S., Vrubel, H. & Hu, X. Amorphous molybdenum sulfide films as catalysts for electrochemical hydrogen production in water. *Chem. Sci.* **2**, 1262 (2011).

46. Jaegermann, W. & Tributsch, H. Interfacial properties of semiconducting transition metal chalcogenides. *Progress in Surface Science* **29**, 1–167 (1988).

47. Keum, D. H., cho, S., Ho Kim, J., Choe, D-H., Sung, H-J., Kan, M., Kang, H., Hwang, J-Y., Wng Kim, S., Yang, H, Chang, K. J. & Hee Lee, Y. Bandgap opening in few-layered monoclinic $MoTe_2$. *Nature Phys.* **11**, 482–486 (2015).

48. Qiao, H., Huang, Z., Liu, S., Liu, Y., Li, J. & Qi, X. Liquid-exfoliated molybdenum telluride nanosheets with superior electrocatalytic hydrogen evolution performances. *Ceram. Int.* **44**, 21205–21209 (2018).

49. McGlynn, J. C., Cascallana-Matías, I., Fraser, J. P., Roger, I., McAllister, J., Miras, H. N., Symes, M. D. & Ganin, A. Y. Molybdenum Ditelluride Rendered into an Efficient and Stable Electrocatalyst for the Hydrogen Evolution Reaction by Polymorphic Control. *Energy Technol.* **6**, 345–350 (2018).

50. Gómez, R., Fernández-Vega, A., Feliu, J. M. & Aldaz, A. Hydrogen evolution on Pt single crystal surfaces. Effects of irreversibly adsorbed bismuth and antimony on hydrogen adsorption and evolution on Pt (100). *J. Phys. Chem.* **97**, 4769–4776 (1993).

51. Marković, N. M., Grgur, B. N. & Ross, P. N. Temperature-Dependent Hydrogen Electrochemistry on Platinum Low-Index Single-Crystal Surfaces in Acid Solutions. *J. Phys. Chem. B* **101**, 5405–5413 (1997).

52. Tsai, C., Chan, K., Nørskov, J. K. & Abild-Pedersen, F. Theoretical insights into the

hydrogen evolution activity of layered transition metal dichalcogenides. *Surf. Sci.* **640**, 133–140 (2015).

4. Nanocrystalline morphology of 1T'-$MoTe_2$

Continuing with the solid-state route to $MoTe_2$, our efforts are now turned towards the metallic 1T'-$MoTe_2$ exclusively, and focus on investigating the effect of morphology on catalytic activity. Few reports have investigated the effect of nanostructuring $MoTe_2$; however evidence of their electrocatalytic performance towards the HER is limited. In this chapter, a nanocrystalline variant of 1T'-$MoTe_2$ is synthesised *via* a solid-state method at a remarkably low temperature of 400 °C, at which 2H-$MoTe_2$ would be thermodynamically expected. As such, this new nanocrystalline 1T'-$MoTe_2$ is fully characterised to confirm the monoclinic structure, and its catalytic activity compared with its high temperature crystalline counterpart.

4.1. Introduction

4.1.1. Synthetic routes to 1T'-$MoTe_2$

The phase pure synthesis of 1T'-$MoTe_2$ is synthetically challenging due to the small energy difference between the 2H and 1T' phases.[1,2] Synthetic routes are also sensitive to subtle changes in experimental parameters, *i.e.* elemental composition and temperature.[3] In addition, 1T'-$MoTe_2$ is metastable, and has historically required high temperatures (>850 °C) in order to generate the single phase material.[4] The solid-state synthesis of bulk 1T'-$MoTe_2$ resulted in a stable and phase pure material capable of evolving hydrogen, however its activity towards the HER is not on par with typical state-of-the-art TMDC electrocatalysts (Table 4-1). The reason for this is most likely due to the bulk nature of the solid-state material, which means the density of catalytically available active sites is limited due to low surface area. The catalysts depicted in Table 4-1, however, are either nanostructured (which increases the number of catalytically active sites) or are supported on materials such as reduced graphene oxide (RGO), which are capable of increasing conductivity through doping. This gives rise to considerably lower overpotentials when compared with solid-state bulk 1T'-$MoTe_2$ and the single crystalline 1T'-$MoTe_2$ studied by Seok *et al*.[5]

Table 4-1: *Comparison of HER activity in state-of-the-art TMDC electrocatalysts.*

Catalyst	**V (vs. NHE) at j = 10 mA cm^{-2}**	**Tafel Slope (mV dec^{-1})**	**Reference**
Bulk 1T'-$MoTe_2$	360 mV	78	Chapter 3 and [6]
Single crystal 1T'-$MoTe_2$	356 mV	127	[5]
Double gyroid MoS_2	280 mV	50	[7]
MoS_2 Nanoparticles	170 mV	55-60	[8]
Exfoliated 1T-MoS_2 Nanosheets	190 mV	43	[9]
MoS_2/RGO	160 mV	41	[10]
Amorphous MoS_2	200 mV	60	[11]
$[Mo_3S_{13}]^{2-}$ nanoclusters on carbon supports	180 - 220 mV	38-57	[12]
Cu_7S_4@MoS_2 Hetero-nanoframes	130 mV	48	[13]
Defect-rich MoS_2 nanosheets	200 mV	50	[14]
T-WS_2 nanosheets	230 mV	60	[15]
WS_2/RGO	260 mV	58	[16]

Studies into the application of nanostructured 1T'-$MoTe_2$ as an electrocatalyst have been limited thus far. [17–19] Most commonly, nanostructured $MoTe_2$ is achieved through chemical exfoliation of bulk powders or by chemical vapour deposition. A recent study by Qiao *et al.* developed liquid-exfoliated 1T'-$MoTe_2$ nanosheets from bulk 2H-$MoTe_2$.[17] In this study, the authors aim to increase the number of active sites by exfoliating bulk 2H-$MoTe_2$ into mono- or few-layered nanosheets. A significant enhancement in overpotential from ~500 mV to 360 mV at j = –10 mA cm^{-2} is observed in 1 M H_2SO_4. The authors therefore claim an identical performance to the bulk 1T'-$MoTe_2$ reported in Chapter 3,[6] and attribute the improved performance to the increased number of active sites. However, the authors fail to take the 2H to 1T' phase transition into consideration, thus making the impact of the change in morphology on the activity rather unclear. In fact, the similarity of the nanosheets with the bulk 1T'-$MoTe_2$ in Chapter 3 would instead suggest that increasing the surface area by nanostructuring has no effect on the catalytic activity, since the performance is identical for both morphologies. Additionally, as reported by Luxa *et al.*, chemical exfoliation of bulk

2H-$MoTe_2$ using *n*-butyllithium (*n*-BuLi) results in an improvement in catalytic activity.[18] However, in contrast to the report by Qiao *et al.,*[17] exfoliation using *n*-BuLi does not induce a phase transition from 2H- to 1T'-$MoTe_2$. Therefore, in this case, it is unsurprising that the change in morphology from bulk to few-layered nanosheets has a significant impact on catalytic activity, as the edges of the 2H material are catalytically active.

Therefore, the effect of nanostructuring on the catalytic activity of 1T'-$MoTe_2$ has not yet been accurately investigated. This is primarily due to the challenging synthetic conditions required to isolate phase pure metastable 1T'-$MoTe_2$ which generally focus on the 'top-down' exfoliation of bulk powders. Analogous to MoS_2, these routes are often complex and involve a variety of factors which may compromise the catalytic activity. Hence, direct methods of obtaining nanostructured 1T'-$MoTe_2$ are needed in order to accurately investigate the intrinsic activity of the 1T' phase.

4.1.2. Low Temperature 1T'-$MoTe_2$

Nanostructures of $MoTe_2$ are considered more synthetically challenging than those of MoS_2 and $MoSe_2$. This is in part due to the tendency of $MoTe_2$ to be more readily oxidised than the sulfide or selenide derivatives. For example, reaction of tellurium with oxygen readily produces TeO_2 species, whereas sulfur and selenium require additional steps and reactants in order to be oxidised.[20] Similarly, the bonding energy of Mo-Te is much weaker than that of Mo-S and Mo-Se, which tends to result in a Te deficiency as tellurium is lost as a vapour at high temperatures due to the decomposition of $MoTe_2$.[2] These factors contribute to the difficulty in selectively targeting a single phase of $MoTe_2$, with a mixture of 2H and 1T' commonly observed.

Sun *et al*.[21] and subsequently Liu *et al*.[22] reported the direct solution synthesis of nanostructured 1T'-$MoTe_2$ at a remarkably low temperature of 300 °C. The formation of the metastable 1T'-$MoTe_2$ at such a low temperature is surprising, since the thermodynamically stable 2H phase would be expected. In both cases, 1T'-$MoTe_2$ is presented as uniform flower-like nanostructures made up of few-layer nanosheets. However, neither of these materials have been tested for the hydrogen evolution reaction. The nanostructured material produces a PXRD pattern with substantially broader peaks consistent with the disordered nature of the nanostructures. Sun *et al*. suggested that the formation of the high temperature monoclinic phase was due to grain boundary pinning, which, according to DFT studies, prevents the transformation into 2H-$MoTe_2$. The 1T' phase

is therefore stabilised by its small grain sizes and polycrystallinity.[21,23] The direct synthesis of a stable nanostructured variant of 1T'-$MoTe_2$ would allow for a reliable comparison of catalytic activities with bulk 1T'-$MoTe_2$. Hence, the effect of morphology and varying active sites may be considered.

4.1.3. Edge Sites vs. Basal Plane

As discussed in Chapter 3, previous studies have reported that in the metallic phase, the basal plane is the main active site, which is considered catalytically inert in the semiconducting form. Work in the previous chapter has shown that the origin of catalytic activity is due to the emergence of metallic conductivity which is associated with the phase transition from 2H to 1T, rather than due to changes in morphology and / or composition.[6]

In the case of semiconducting TMDCs, *i.e.* 2H-MoS_2, 2H-$MoTe_2$, *etc.,* the basal plane is considered catalytically inert, whereas the edge sites display an activity close to platinum.[8] Upon transitioning from semiconducting 2H- to metallic 1T'- phases, however, the basal plane has been proven to be catalytically active due to the emergence of metallic conductivity. In the case of $MoTe_2$, the metallic properties arise due to the distortion of the {$MoTe_6$} octahedra, which displaces the Mo atom from the centre of the octahedra. The Mo atom then comes into close contact with its neighbouring Mo atom, and forms Mo-Mo metal bonds (Figure 4-1).

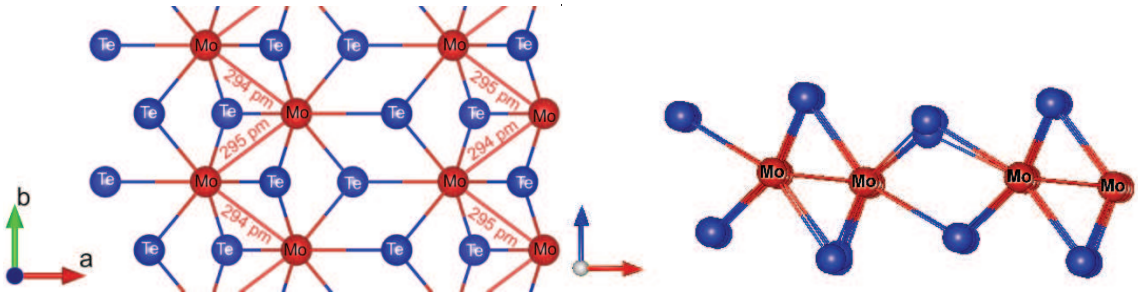

Figure 4-1: *Lattice structures of 1T'-$MoTe_2$ highlighting the presence of Mo-Mo bonds. Red spheres are Mo atoms and blue spheres are Te atoms.*

Chhowalla *et al.* sought to investigate the contribution of the edge and basal plane active sites to the catalytic activity of 2H- and 1T-MoS_2 nanosheets.[24] To do this, both materials were partially oxidised, with the edge sites being known to be more readily oxidised than the basal plane.[25] As a result, the electrocatalytic performance of the edge oxidised 2H-MoS_2 nanosheets was found to decrease, while that of the edge oxidized 1T-MoS_2 nanosheets remained unaffected. Since oxidation of the 1T-MoS_2 edges has no effect on the catalytic activity, it was concluded that the edge sites are not involved in the reaction. Rather, this result indicates that the reaction occurs on the basal plane. Whereas for 2H-MoS_2, the loss of catalytic activity proves that hydrogen evolution occurs on the edges.

Now, in an attempt to improve the catalytic activity, we investigate solely the effect of nanostructuring on 1T'-$MoTe_2$. In this way, the intrinsic activity of the metallic 1T'-$MoTe_2$ phase can be further investigated.

4.2. Aims

To date, there is no accurate investigation which reliably compares the electrocatalytic activity of bulk 1T'-$MoTe_2$ and a nanostructured variant of this metallic phase. Therefore, this chapter focuses on the synthesis and characterisation of a nanocrystalline variant of 1T'-$MoTe_2$ *via* a solid-state route. In this way, the coordination environment, which gives rise to the metallic nature of the material, is maintained. Accordingly, the effect of morphology on the electrocatalytic activity of 1T'-$MoTe_2$ can be determined.

4.3. Results and Discussion

4.3.1. Synthesis and Characterisation of Nanocrystalline 1T'-$MoTe_2$

4.3.1.1. Synthesis of Nanocrystalline 1T'-$MoTe_2$

As mentioned in Chapter 3, Section 3.3.1.1., an intermediate heating step was employed when attempting to synthesise 2H-$MoTe_2$ at 600 °C. This step involved heating elemental Mo and Te powders at 480 °C before grinding and reannealing the material at 600 °C to produce 2H-$MoTe_2$. PXRD of the intermediate powder revealed a diffraction pattern which resembled 1T'-$MoTe_2$ (Figure 4-2). This result was surprising, as the thermodynamically favoured 2H-$MoTe_2$ would be expected at such a low temperature. The synthesis was therefore repeated at 480 °C to see if this result could be reproduced. However, the resulting PXRD pattern showed the majority of the material to be 2H-$MoTe_2$, while a small impurity of the 1T'-phase was present.

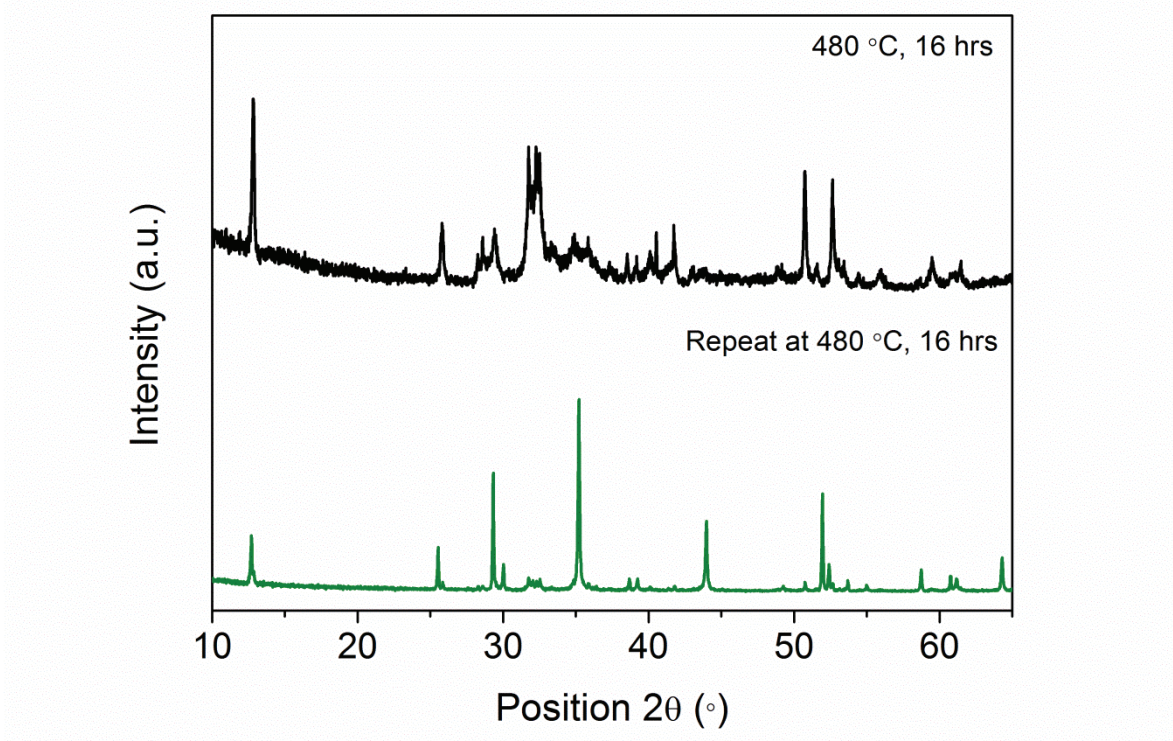

Figure 4-2: *PXRD patterns of the product of intermediate heating of elemental Mo and Te at 480 °C for 16 hours (top) and a repeat reaction procedure under identical conditions (bottom).*

Intrigued by this, the reaction temperature was lowered and the elemental powders were reacted at 400 °C for 16 hours. As a result, the more disordered pattern resembling 1T'-$MoTe_2$ was obtained with a slight elemental Mo impurity. Further annealing at 400 °C for 16 hours removed this Mo impurity and the 'low temperature' 1T'-$MoTe_2$ phase was obtained. Herein, the metallic 1T'-$MoTe_2$ material discussed in previous chapters will now be referred to as *crystalline* 1T'-$MoTe_2$, while the newly synthesised 'low temperature' variant will be described as *nanocrystalline* 1T'-$MoTe_2$. Figure 4-3 illustrates the PXRD patterns of nanocrystalline 1T'-$MoTe_2$ in comparison to crystalline 1T'-$MoTe_2$.

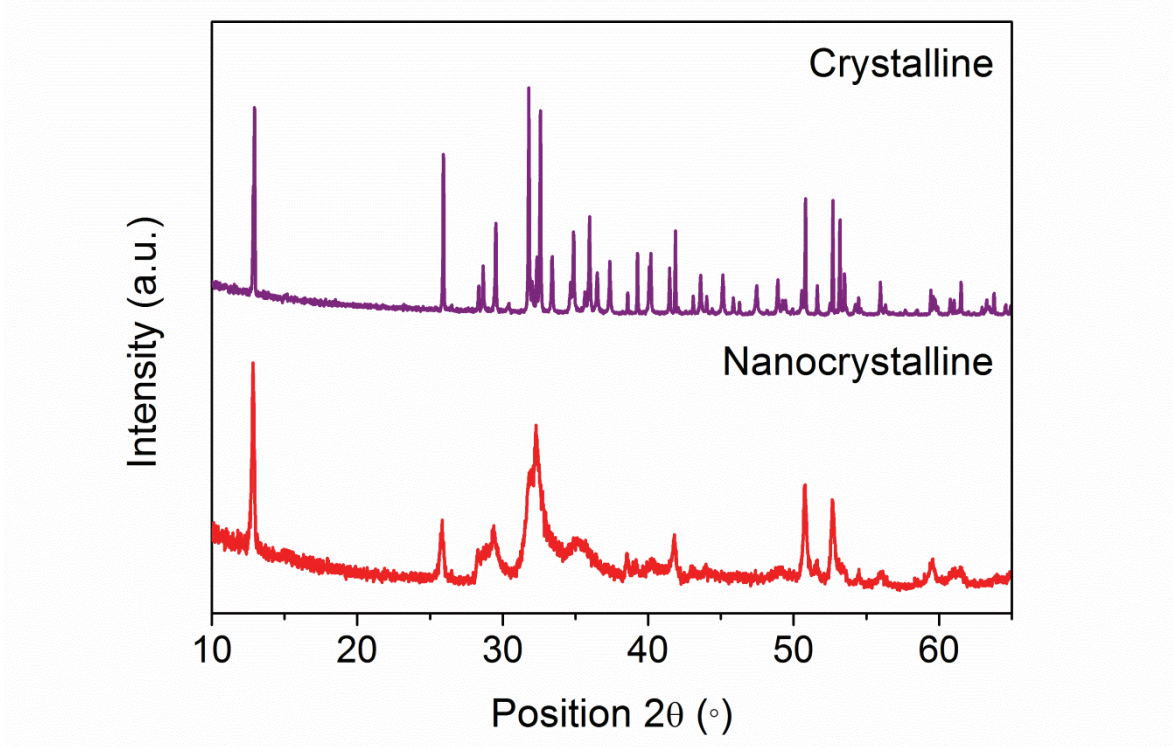

Figure 4-3: *Powder X-Ray Diffraction patterns of crystalline 1T'-$MoTe_2$ (top) and nanocrystalline 1T'-$MoTe_2$ (bottom).*

The two monoclinic 1T'-$MoTe_2$ materials can be easily distinguished between by the substantially broader peaks of the nanocrystalline material, which are also consistent with the $MoTe_2$ products synthesised *via* a solution-based route by Sun *et al.*[21] Despite this material being previously reported in the literature, the formation of this nanocrystalline material *via* a solid-state approach at such a low temperature is surprising. As discussed in Chapter 3, the semiconducting 2H-$MoTe_2$ phase with the hexagonal structure is thermodynamically stable, and hence one would expect its formation over the metastable 1T' material at low temperatures. Additionally, due to the small energy difference of only 35 meV between the 2H and 1T' polymorphs, the synthesis of phase pure $MoTe_2$ materials is generally considered to be synthetically challenging, with subtle changes in parameters

resulting in the unexpected formation of a given polymorph.[2] Sun *et al*. report the phase pure solution-synthesis of 1T'-$MoTe_2$ at only 300 °C, and propose that the monoclinic phase is stabilised by small grain sizes associated with flower-like nanostructures.[21,23] This, coupled with polycrystallinity of the material, prevents the transformation into the more stable 2H phase through grain boundary pinning, thus making the simultaneous changes of *a* and *b* lattice constants required for transformation into the hexagonal phase more challenging.[19,21]

In an attempt to recreate the results of the solution based synthesis route at 300 °C, this temperature was applied to the solid-state route described above. However, no reaction between the elemental Mo and Te powders was observed until a minimum temperature of 375 °C, at which the majority of the material presented as nanocrystalline 1T'-$MoTe_2$. However, despite an extended reaction time (up to 48 hours), impurities of elemental Mo and Te remained (Figure 4-4). Therefore, all future syntheses of nanocrystalline 1T'-$MoTe_2$ were carried out at 400 °C (5 °C min^{-1} heating rate) for 16 hours, before being ground and reannealed under the same conditions. Using this methodology, the product was consistently identified as phase pure nanocrystalline 1T'-$MoTe_2$ with no visible impurities or unreacted powders being observed (Figure 4-3).

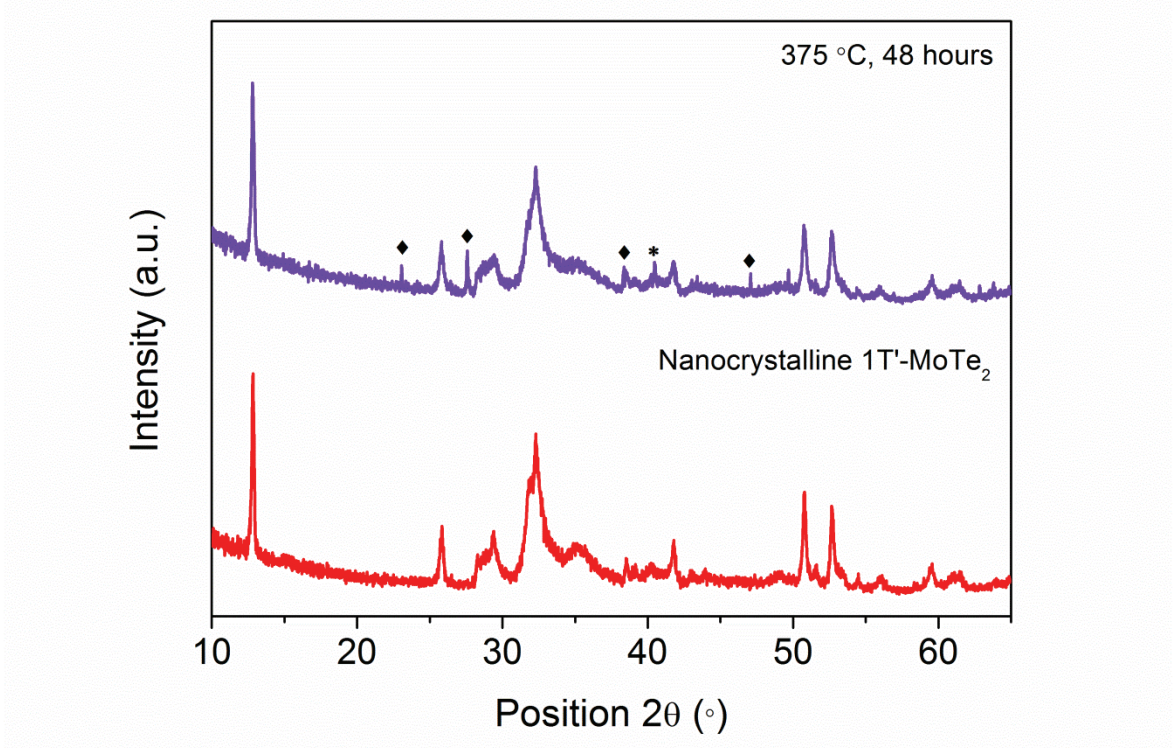

Figure 4-4: *PXRD patterns of the powders obtained after reaction of elemental Mo and Te at 375 °C for a total of 48 hours (top) in comparison to phase pure nanocrystalline 1T'-$MoTe_2$ obtained by reaction at 400 °C for a total of 32 hours. Elemental Mo and Te impurities are denoted as ✱ and ♦, respectively.*

The solid-state synthesis of nanocrystalline 1T'-$MoTe_2$ also offers the advantage of stability, as Sun *et al.* report their low temperature phase to rapidly oxidise in air, with substantial degradation being visible by PXRD after only one week.[21] Solid-state nanocrystalline 1T'-$MoTe_2$ shows no such degradation in air, despite a similar oxide layer removal being required as with crystalline 1T'-$MoTe_2$ during electrocatalytic measurements (as discussed in Chapter 3, Section 3.3.2.1).[26] TMDC tellurides are widely accepted to oxidise more easily than their sulfide or selenide counterparts,[19] and in the case of Sun *et al*. this would likely hinder the electrocatalytic performance of the material. Therefore, it is noteworthy that the solid-state material in this work does not degrade as a result of oxidation in air. The effect of oxidation will be discussed further in Chapter 6.

4.3.1.2. Structural Characterisation of Nanocrystalline 1T'-$MoTe_2$

Despite computational studies by Sun *et al.*[21] which explain the formation of 1T'-$MoTe_2$ at low temperatures, thorough characterisation was carried out on solid-state nanocrystalline 1T'-$MoTe_2$. This was required due to the broad nature of the observed PXRD peaks associated with the nanocrystalline material, which therefore makes confidently assigning the crystal system more difficult. Most importantly, in terms of comparing electrocatalytic performance, fully characterising the material to ensure that the coordination geometry is identical to crystalline 1T'-$MoTe_2$ is key. As such, Raman spectroscopy was also used to confirm that the coordination environment of the nanocrystalline material was consistent with the distorted {$MoTe_6$} octahedra, which are the expected building blocks of the monoclinic phase (Figure 4-5). The Raman peaks of both crystalline and nanocrystalline 1T'-$MoTe_2$ are observed at 110, 127, 163 and 256 cm^{-1}, which correspond to the A_g and B_g modes, and are in very close agreement with the literature data.[27,28] The wide range spectra also highlights the absence of MoO_2 and MoO_3, thus confirming that both materials are free from oxide impurities in the bulk.[29,30]

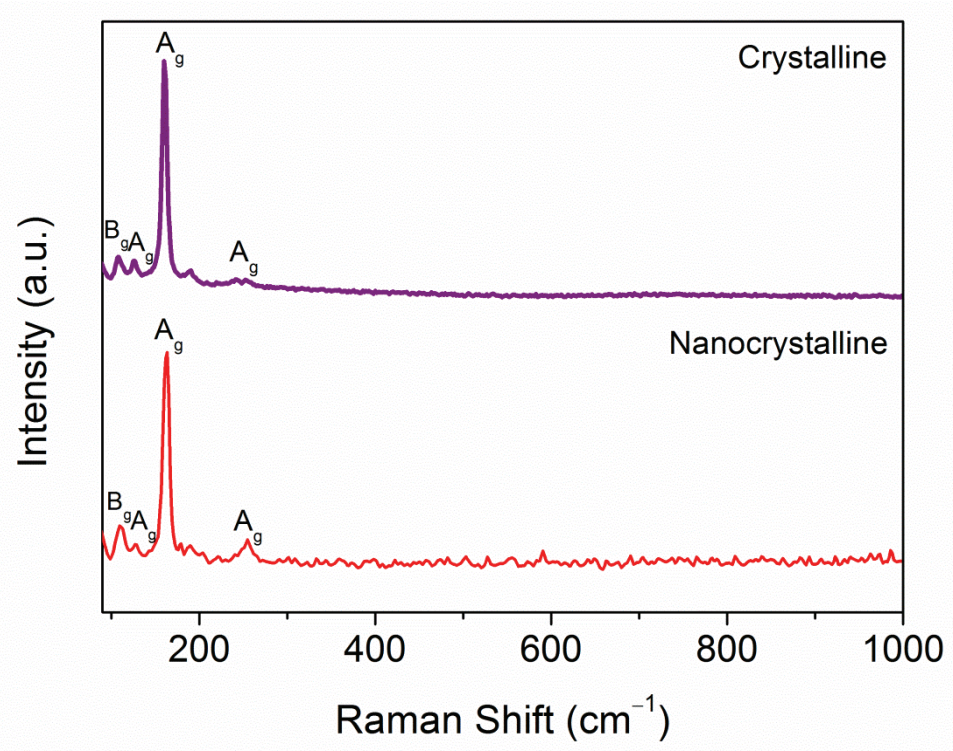

Figure 4-5: *Wide-range Raman spectra of crystalline and nanocrystalline materials with the four main vibrational modes of 1T'-$MoTe_2$ highlighted.*

Figure 4-6 shows a comparison of the low and high resolution TEM images of nanocrystalline 1T'-$MoTe_2$ and allows for closer inspection of the particle morphology. From these images, it is evident that the nanocrystalline material consists of an agglomeration of nanoplatelets around 20 nm in size. The electron diffraction images also confirm the validity of the proposed model, *i.e.* the material is consistent with the monoclinic distortion of 1T'-$MoTe_2$. Thus, the formation of the 1T'-$MoTe_2$ is confirmed and is in good agreement with the data reported by Sun *et al.*[21] In comparison, crystalline 1T'-$MoTe_2$ (Figure 4-7) consists of substantially larger crystallites, evident as platelets in the size range of several micrometers. Again, the expected monoclinic structure is confirmed by the electron diffraction images, which consist of discrete spots indicating the crystalline nature of the sample.

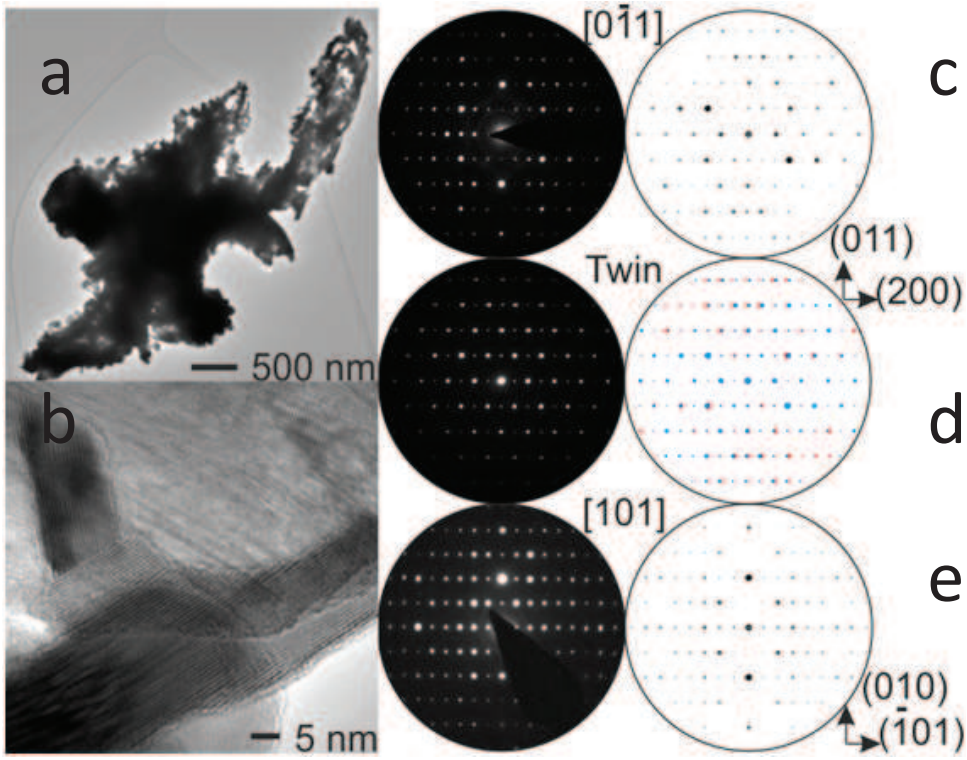

Figure 4-6: *TEM studies of nanocrystalline 1T'-$MoTe_2$. Representative* ***a)*** *low and* ***b****) high magnification TEM images of nanocrystalline 1T'-$MoTe_2$. The corresponding electron diffraction patterns along different directions of crystal orientation are shown in* ***c-e.***

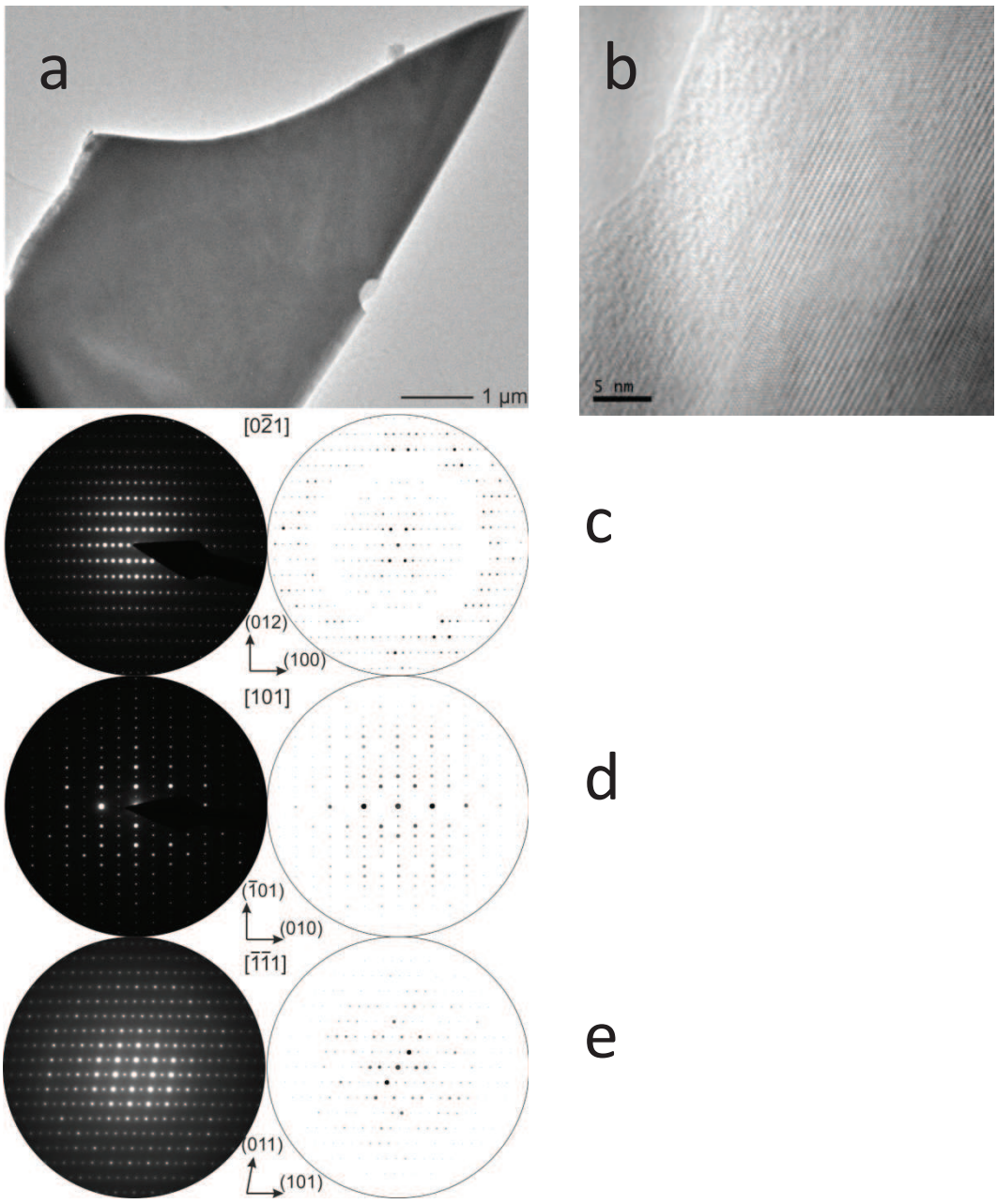

Figure 4-7: *TEM studies of crystalline 1T'-$MoTe_2$. Representative* ***a)*** *low and* ***b)*** *high magnification TEM image of crystalline 1T'-$MoTe_2$ and the corresponding electron diffraction images for different crystal orientations are shown in c-**e**.*

The normalised XANES spectra (Figure 4-8) of both crystalline and nanocrystalline 1T'-$MoTe_2$ resemble the literature spectra of MoS_2, with the main edge at 20006 eV, consistent with the Mo^{4+} oxidation state and a sharp feature at 20015 eV.[31] From the EXAFS data, there is a slight decrease in intensity of the oscillations of nanocrystalline 1T'-$MoTe_2$ compared with crystalline 1T'-$MoTe_2$, which could indicate a slight decrease in number of neighbours. This is evident from the feature at approximately 2.5 Å in the non-phase corrected plot of the k^2-weighted Fourier Transform of the EXAFS data (Figure 4-8). The EXAFS data can be fitted using two Mo-Te paths at 2.7 Å and 2.8 Å and a Mo-Mo path at 3.46 Å. The

magnitude and imaginary components of the k^2-weighted Fourier transform data and fits of crystalline and nanocrystalline 1T'-$MoTe_2$ are shown in Figure 4-9, with the imaginary components of each scattering path used. Despite the subtle differences observed in the EXAFS data, no statistically significant difference can be observed between the two samples, with the Mo-Te coordination numbers and distances being within error. Therefore, by fully characterising the nanocrystalline material, we can confirm that the coordination geometry and crystal structure are identical to that of the crystalline phase. Hence the sole difference between the two phases is the increased surface area as a result of the lower synthetic temperature.

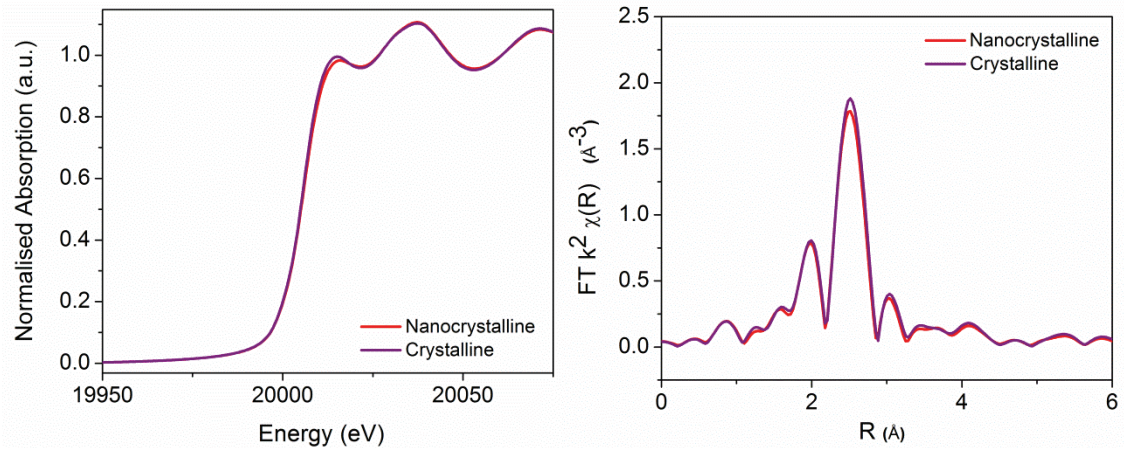

Figure 4-8: *Comparison of the EXAFS data collected for nanocrystalline and crystalline 1T'-$MoTe_2$. k^2-weighted Fourier Transform data of crystalline and nanocrystalline 1T'-$MoTe_2$ (left). Comparison of the normalised XANES spectra of crystalline and nanocrystalline 1T'-$MoTe_2$ (right).*

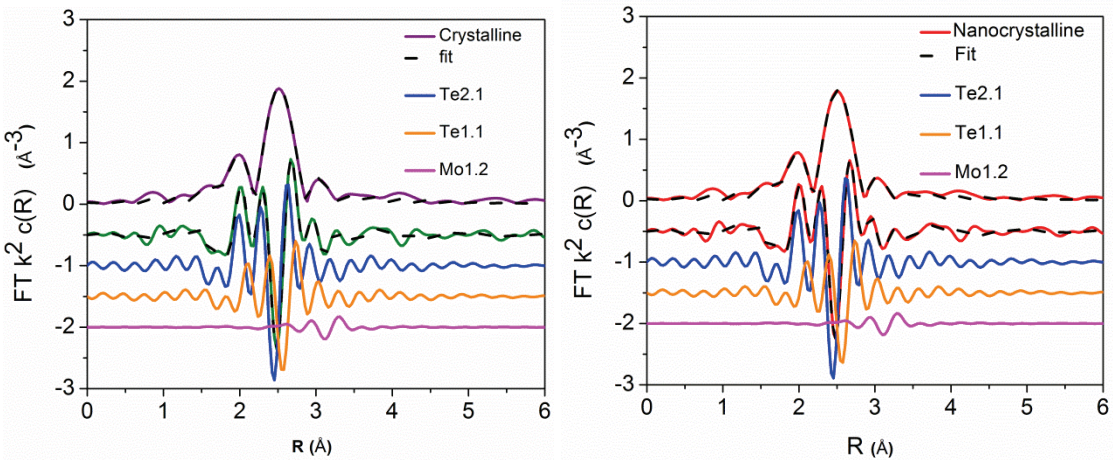

Figure 4-9: *Fourier transform data for crystalline (left) and nanocrystalline (right). The magnitude and imaginary components of the non-phase corrected k^2-weighted Fourier transform data and fits of the respective 1T'-$MoTe_2$ phase and the imaginary components of each scattering path used.*

4.3.1.3. Morphology of Nanocrystalline 1T'-$MoTe_2$

Clearly, the considerably lower temperature of 400 °C results in a more disordered material, which is also evidenced by SEM. Figure 4-10 shows the contrasting sample morphologies of the crystalline and nanocrystalline 1T'-$MoTe_2$ materials, with the low temperature phase expected to exhibit a larger surface area. These randomly agglomerated nanocrystallites are in contrast to the nanoflowers observed by Sun *et al.*[21] which are formed of few-layer nanosheets and are commonly obtained *via* solution based routes to TMDCs.[32,33] There have been few studies on the synthesis of 1T'-$MoTe_2$ nanostructures, with few-layered nanosheets developed by Qiao *et al.*[17] and nanoflakes in the form of thin films by McManus *et al.*[19] The work reported in this chapter therefore varies significantly as the low temperature 1T'-$MoTe_2$ material, despite being named 'nanocrystalline', is more bulk-like in nature than those reported in the literature.

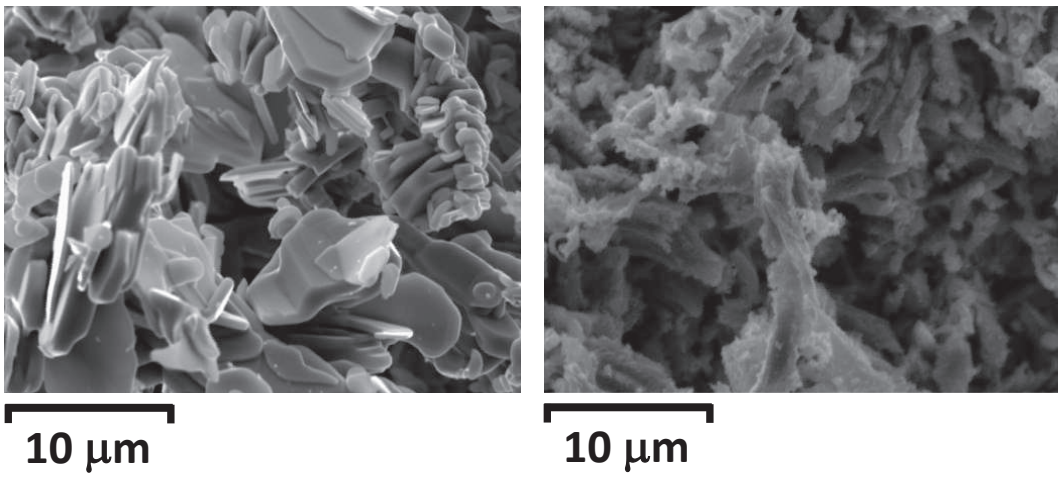

Figure 4-10: *SEM images of crystalline (left) and nanocrystalline (right) 1T'-$MoTe_2$, clearly showing the formation of bulk materials.*

Comparison of the elemental composition by ICP-OES also provides valuable insight into the formation of 1T'-$MoTe_2$ at such low temperatures. When compared with crystalline 1T'-$MoTe_2$, the nanocrystalline phase is slightly Te deficient, which is known to be a stabilising factor for the formation of the monoclinic phase over the hexagonal.[34] The compositions of the crystalline and nanocrystalline phases were determined to be $MoTe_{2.01(3)}$ and $MoTe_{1.97(5)}$, respectively, and averaged over three samples. Despite being within experimental error, the compositions of nanocrystalline 1T'-$MoTe_2$ calculated over the repeated measurements consistently show a lower Te content than the crystalline phase, as can be seen in Table 4-2.

Table 4-2: *Summary of the elemental compositions as obtained by ICP-OES.*

Sample	Crystalline 1T'-$MoTe_2$	Nanocrystalline 1T'-$MoTe_2$
1	$MoTe_{2.023}$	$MoTe_{1.912}$
2	$MoTe_{2.042}$	$MoTe_{1.993}$
3	$MoTe_{2.052}$	$MoTe_{2.002}$
Average	$MoTe_{2.01(3)}$	$MoTe_{1.97(5)}$

4.3.2. Electrocatalytic Activity of Crystalline vs. Nanocrystalline 1T'-$MoTe_2$

By confirming the distorted {$MoTe_6$} octahedral arrangement of the nanocrystalline phase, the effect of morphology on electrocatalytic activity can now be considered. Since crystalline 1T'-$MoTe_2$ has been shown to be active towards the HER, it is probable that the nanocrystalline material will also exhibit a good electrocatalytic performance. Therefore, the activity of nanocrystalline 1T'-$MoTe_2$ was assessed and compared directly with that of the crystalline phase.

Upon initial inspection of the electrocatalytic performance, the nanocrystalline phase proved to be similar to the crystalline material, with an overpotential of 320 mV being required for a benchmark current density of $j = -10$ mA cm^{-2}. Hence, at low current densities, the performance of nanocrystalline 1T'-$MoTe_2$ is essentially identical; with the crystalline phase only requiring a marginally larger value of 360 mV at the same current density (Figure 4-11). Additionally, there is only a minor difference in Tafel analysis, with the Tafel slope of nanocrystalline 1T'-$MoTe_2$ being calculated as 68 ± 4 mV dec^{-1}. This represents marginally improved electron transfer when compared with the Tafel slope of crystalline 1T'-$MoTe_2$ (78 ± 4 mV dec^{-1}). The comparison of the Tafel plots and their corresponding Tafel slopes can be seen in Figure 4-12. Therefore, due to the similarity in overpotentials and reaction kinetics at $j = -10$ mA cm^{-2}, the increased surface area (associated with the more disordered nature of the nanocrystalline material) does not appear to greatly improve the performance. This finding supports previous studies by Chhowalla *et al.*[35] and Bonde *et al*.[36] which prove the edge sites are not the main active site of metallic TMDCs.

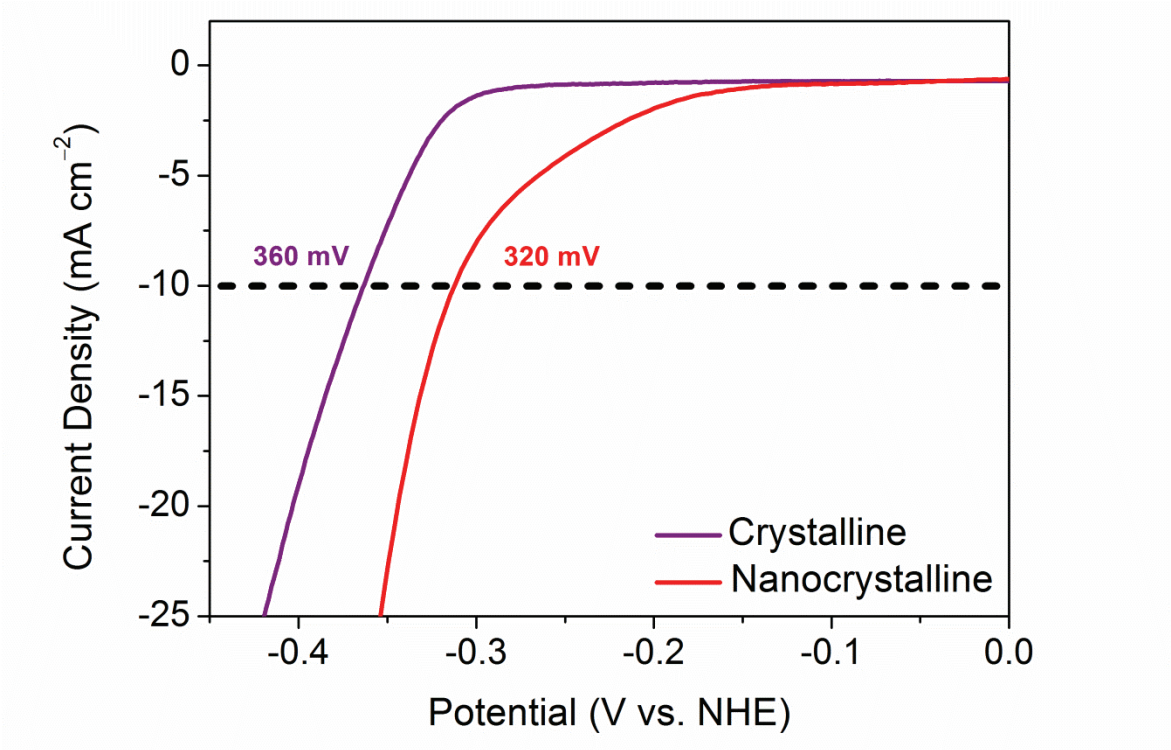

Figure 4-11: *Comparison of the current densities achieved by crystalline and nanocrystalline 1T'-$MoTe_2$ in 1 M H_2SO_4. Catalysts were prepared on a glassy carbon working electrode as described in the experimental section. Carbon felt and 3 M Ag/AgCl were used as the counter and reference electrodes, respectively.*

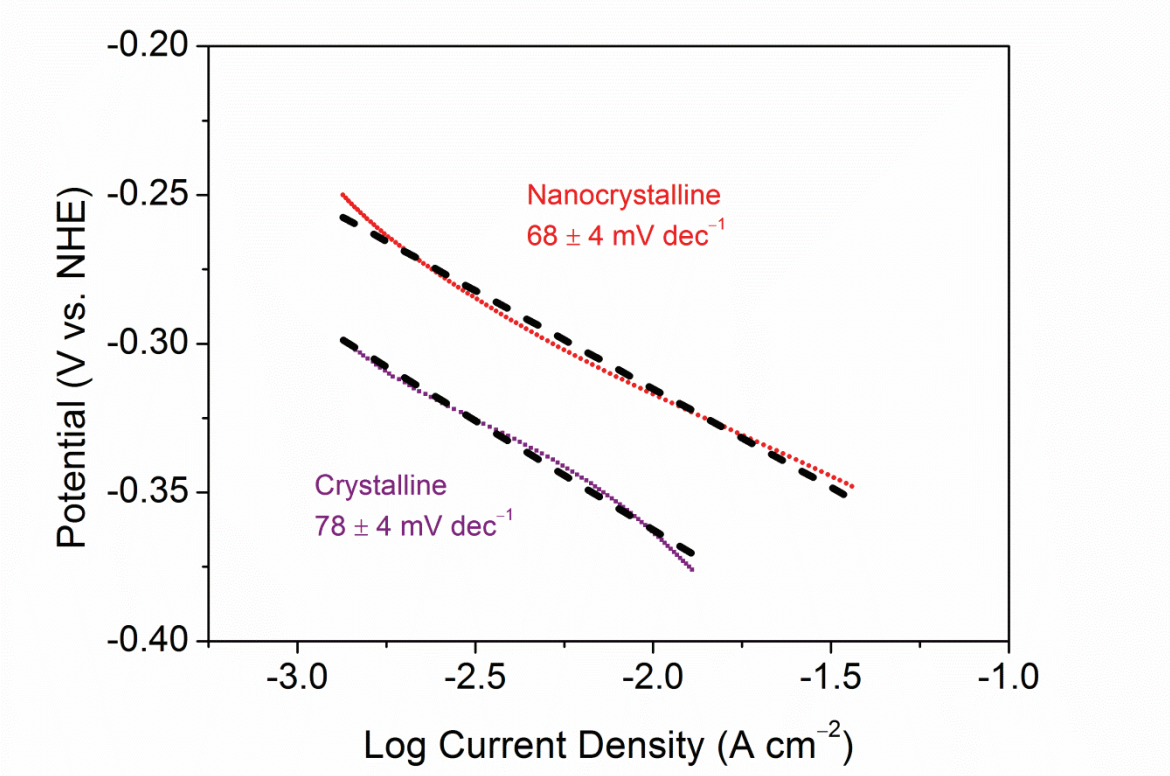

Figure 4-12: *Tafel plots and corresponding Tafel slopes of nanocrystalline and crystalline 1T'-$MoTe_2$. Dashed lines are provided as a guide to the eye. All current densities have been corrected for resistance.*

However, applying greater reductive potentials results in a significant difference in the current densities achieved between the two materials. For example, at a potential of –500 mV (vs. NHE), the crystalline phase reaches a current density of j = –50 mA cm^{-2}, while the nanocrystalline material soars to j = –250 mA cm^{-2} at the same potential (Figure 4-13). Given that the same catalyst loading is used per geometric surface area, it is reasonable to conclude that the enhanced performance is due to the greater surface area of the nanocrystalline phase. Experimental evidence therefore suggests that the increased surface area aids the reaction kinetics. Accordingly, by measuring the double layer capacitance (C_{DL}) of both crystalline and nanocrystalline materials, the electrochemical active surface area (ECSA) can be compared, since ECSA is directly proportional to C_{DL}. Figure 4-14 illustrates the calculation of C_{DL}, and hence proves that the ECSA of nanocrystalline 1T'-$MoTe_2$ is greater than that of the crystalline material by a factor of 20.

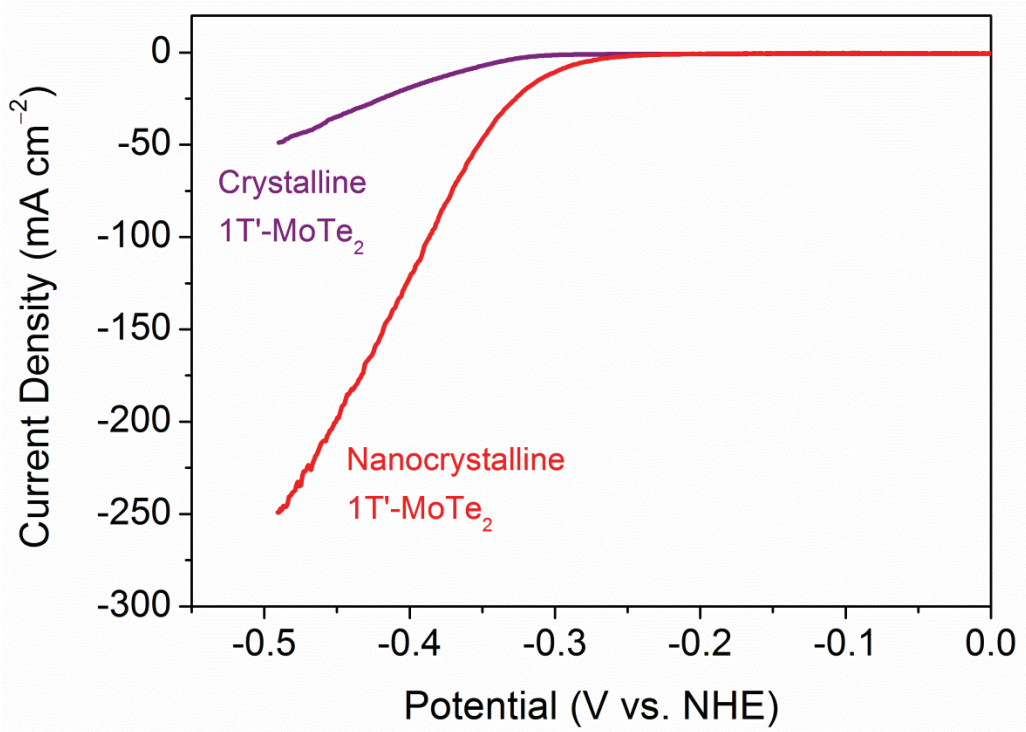

Figure 4-13: *Comparison of the current densities achieved by crystalline and nanocrystalline 1T'-$MoTe_2$ catalysts in 1 M H_2SO_4. Catalysts were prepared on a glassy carbon working electrode as described in the experimental section. Carbon felt and 3 M Ag/AgCl were used as the counter and reference electrodes, respectively.*

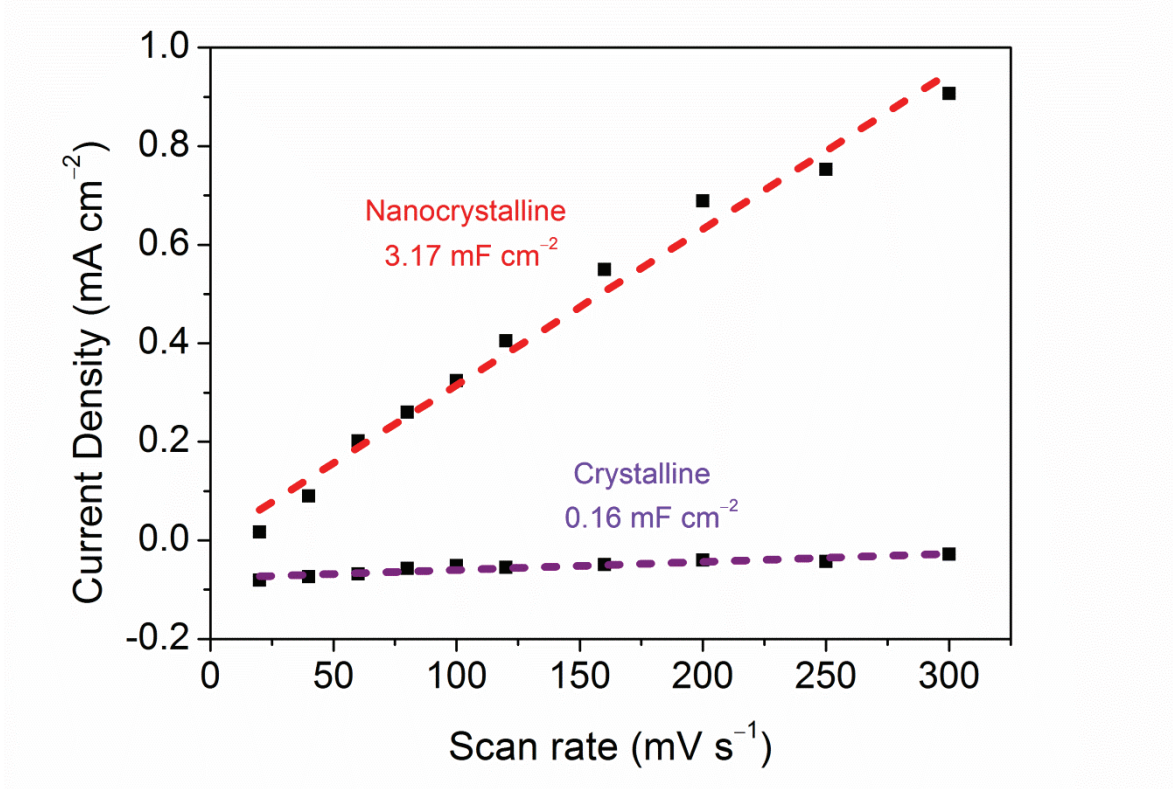

Figure 4-14: *Current density differences of nanocrystalline and crystalline 1T'-$MoTe_2$ plotted against scan rates. The capacitance currents were measured at 150 mV (vs. NHE) in 1 M H_2SO_4.*

Further, EIS indicates nanocrystalline 1T'-$MoTe_2$ is more conductive than the crystalline phase, with the charge transfer resistance, R_{CT}, dropping substantially upon increasing the surface area (Figure 4-15). An increase in surface area would provide a greater contact between the catalytically active sites and the electrolyte, thus promoting charge transfer.[22] This is also in line with optical spectroscopy absorbance values (Figure 4-16), which are proportional to the optical conductivity and thus indicate a conductivity increase when going from crystalline to the nanocrystalline morphology. As such, electron transport is different between the two phases, likely due to the shorter interlayer pathways associated with the disordered nature of the nanocrystalline 1T'-$MoTe_2$ morphology.[37] Thus, the greater electrocatalytic activity of nanocrystalline 1T'-$MoTe_2$ is attributed to its greater surface area, thus allowing access to an enhanced number of active sites and consequently a more efficient charge transfer.

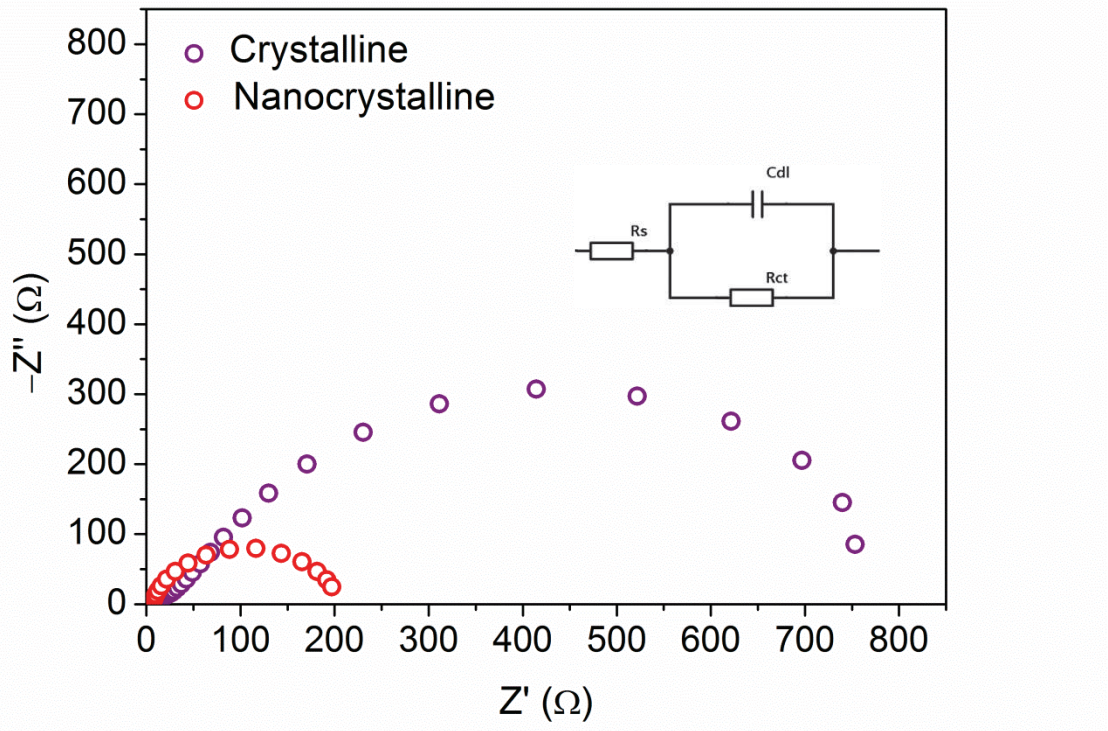

Figure 4-15: *Nyquist plots showing electrochemical impedance spectroscopy on nanocrystalline and crystalline 1T'-$MoTe_2$ at –300 mV (vs. NHE). Uncompensated resistances were calculated as 8.9 and 8.1 Ω for the crystalline and nanocrystalline materials, respectively. This corresponds well with the iR compensation function on the potentiostat which gave values of 9.0 and 9.8 Ω.*

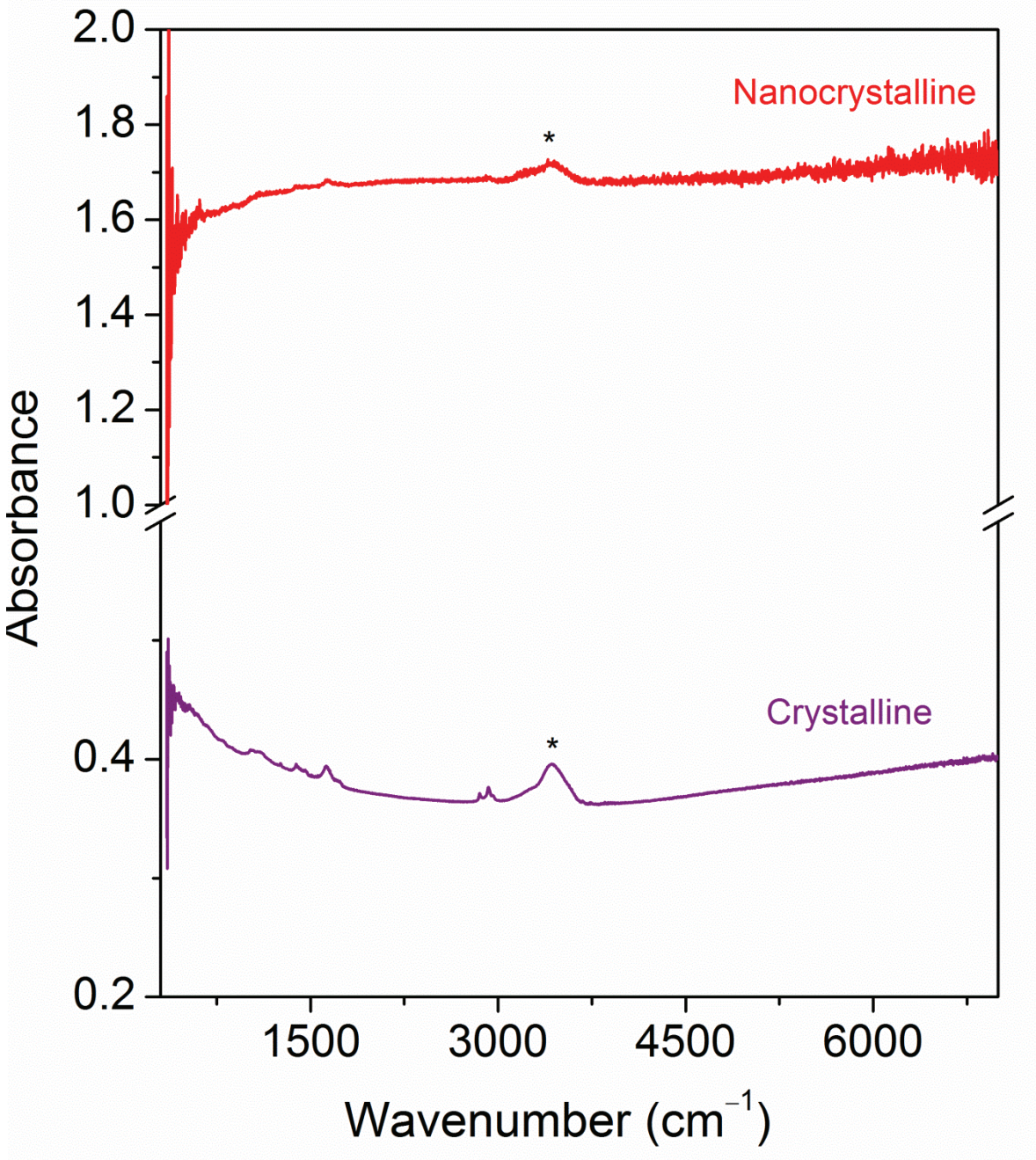

Figure 4-16: *Infrared spectra of the nanocrystalline and crystalline 1T'-$MoTe_2$ phases, respectively. The features denoted by asterisks indicate atmospheric water peaks.*

4.4. Conclusions

This chapter has focused on the synthesis and characterisation of a nanocrystalline variant of 1T'-$MoTe_2$. An identical solid-state route to $MoTe_2$ as used in Chapter 3 was applied, with the reaction temperature lowered to only 400 °C. This temperature was found to be the minimum required for the successful reaction of elemental Mo and Te powders, and resulted in the formation of an agglomerated and disordered 'nanocrystalline' 1T'-$MoTe_2$. Since the 2H phase would be thermodynamically more favourable at this low temperature, the material was fully characterised to confirm phase purity (PXRD, Raman spectroscopy, HRTEM/SAED, EXAFS, ICP-OES). This ensured that the coordination geometry was consistent with the {$MoTe_6$} distorted octahedra which are the building blocks associated with the monoclinic 1T'-$MoTe_2$ material. As such, the catalytic activity of the new nanocrystalline 1T'-$MoTe_2$ could be compared with its crystalline counterpart, with the only difference between the materials being the surface area.

Accordingly, at low current densities, *i.e.* the benchmark current density of $j = -10$ mA cm^{-2}, the overpotential of the nanocrystalline 1T'-$MoTe_2$ material is only marginally improved when compared with crystalline 1T'-$MoTe_2$ (320 mV and 360 mV, respectively). However, at more reductive potentials, nanocrystalline 1T'-$MoTe_2$ reaches much greater current densities. Given that an identical catalyst loading per geometrical surface area is used for both nanocrystalline and crystalline materials, it is apparent that the sample morphology plays a significant role in the electrocatalytic activity. The increase in surface area results in increased contact between the catalyst and electrolyte and aids charge transfer kinetics. This is corroborated by electrochemical impedance spectroscopy, which shows a reduction in charge transfer resistance upon nanostructuring 1T'-$MoTe_2$.

Therefore, this chapter concludes that, in contrast to 2H-$MoTe_2$, nanostructuring of 1T'-$MoTe_2$ to expose a greater number of edge sites does not substantially improve the catalytic activity. Rather, experimental evidence suggests that the increase in surface area provides a greater contact with the electrolyte, thus allowing charge transfer throughout the metallic material to occur more efficiently.

4.5. References

1. Keum, D. H., Cho, S., Ho Kim, J., Choe, D-H., Sung, H-J., Kan, M., Kang, H., Hwang, J-Y., Wng Kim, S., Yang, H. Chang, K. J. & Hee Lee, Y. Bandgap opening in few-layered monoclinic $MoTe_2$. *Nature Physics* **11**, 482-486 (2015).

2. Zhou, L., Xu, K., Zubair, A., Liao, A. D., Fang, W., Ouyang, F., Lee, Y-H., Ueno, K., Saito, R., Palacios, T., Kong, J. & Dresselhaus, M. S. Large-Area Synthesis of High-Quality Uniform Few-Layer $MoTe_2$. *J. Am. Chem. Soc.* **137**, 11892–11895 (2015).

3. Vellinga, M. B., de Jonge, R. & Haas, C. Semiconductor to metal transition in $MoTe_2$. *J. Solid State Chem.* **2**, 299–302 (1970).

4. Brown, B. E. The Crystal Structures of WTe_2 and High-Temperature $MoTe_2$. *Acta Cryst* **20**, (1966).

5. Seok, J., lee, J-H., Cho, S., Ji, B., Won Kim, H., Kwon, M., Kim, D., Kim, Y-M., Ho Oh, S., Wng Kim, S., Hee Lee, Y., Son, Y-W. & Yang, H. Active hydrogen evolution through lattice distortion in metallic $MoTe_2$. *2D Mater.* **4**, 25061 (2017).

6. McGlynn, J. C., Cascallana-Matías, I., Fraser, J. P., Roger, I., McAllister, J., Miras, H. N., Symes, M. D. & Ganin, A. Y. Molybdenum Ditelluride Rendered into an Efficient and Stable Electrocatalyst for the Hydrogen Evolution Reaction by Polymorphic Control. *Energy Technol.* **6**, 345–350 (2018).

7. Kibsgaard, J., Chen, Z., Reinecke, B. N. & Jaramillo, T. F. Engineering the surface structure of MoS_2 to preferentially expose active edge sites for electrocatalysis. *Nat Mater* **11**, 963–969 (2012).

8. Jaramillo, T. F., Jørgensen, K. P., Bonde, J., Nielsen, J. H., Horch, S. & Chrokendorff, I. Identification of Active Edge Sites for Electrochemical H_2 Evolution from MoS_2 Nanocatalysts. *Science* **317**, 100–102 (2007).

9. Lukowski, M. A., Daniel, A. S., meng, F., Forticaux, A., Li, L. & Jin, S. Enhanced Hydrogen Evolution Catalysis from Chemically Exfoliated Metallic MoS_2 Nanosheets. *J. Am. Chem. Soc.* **135**, 10274-10277 (2013).

10. Li, Y., Wang, H., Xie, L., Liang, Y., Hong, G. & Dai, H. MoS_2 Nanoparticles Grown on Graphene: An Advanced Catalyst for the Hydrogen Evolution Reaction. *J. Am. Chem. Soc.* **133**, 7296-7299 (2011).

11. Benck, J. D., Chen, Z., Kuritzky, L. Y., Forman, A. J. & Jaramillo, T. F. Amorphous Molybdenum Sulfide Catalysts for Electrochemical Hydrogen Production: Insights into the Origin of their Catalytic Activity. *ACS Catal.* **2**, 1916-1923 (2012).

12. Kibsgaard, J., Jaramillo, T. F. & Besenbacher, F. Building an appropriate active-site motif into a hydrogen-evolution catalyst with thiomolybdate $[Mo_3S_{13}]^{2-}$ clusters. *Nat. Chem.* **6**, 248–253 (2014).

13. Xu, J., Cui, J., Guo, C., Zhao, Z., Jiang, R., Xu, S., Zhuang, Z., Huang, Y., Wang, L. & Li, Y. Ultrasmall Cu_7S_4@MoS_2 Hetero-Nanoframes with Abundant Active Edge Sites for Ultrahigh-Performance Hydrogen Evolution. *Angew. Chem. Int. Ed.* **55**, 6502–6505 (2016).

14. Yin, Y., Han, J., Zhang, Y., Zhang, X., Xu, P., Yuan, Q., Samad, L., Wang, X., Wang, Y., Zhang, Z., Zhang, P., Cao, X., Song, B. & Jin, S. Contributions of Phase, Sulfur Vacancies, and Edges to the Hydrogen Evolution Reaction Catalytic Activity of Porous Molybdenum Disulfide Nanosheets. *J. Am. Chem. Soc.* **138**, 7965–7972 (2016).

15. Voiry, D., Yamaguchi, H., Li, J., Silva, R., Alves, D. C. B., Fujita, T., Chen, M., Asefa, T., shenoy, V. B., Eda, G. & Chhowalla, M. Enhanced catalytic activity in strained chemically exfoliated WS_2 nanosheets for hydrogen evolution. *Nat. Mater.* **12**, 850–855 (2013).

16. Yang, J., Voiry, D., Ahn, S. J., Kang, D., Kim, A. Y., Chhowalla, M. & Shin, H. S. Two-Dimensional Hybrid Nanosheets of Tungsten Disulfide and Reduced Graphene Oxide as Catalysts for Enhanced Hydrogen Evolution. *Angew. ChemInt. Ed.* **52**, 13751–13754 (2013).

17. Qiao, H., Huang, Z., Liu, S., Liu, Y., Li, J. & Qi, X. Liquid-exfoliated molybdenum telluride nanosheets with superior electrocatalytic hydrogen evolution performances. *Ceram. Int.* **44**, 21205–21209 (2018).

18. Luxa, J., Vosecky, P., Mazánek, V., Sedmidubsky, D., Pumera, M., Lazar, P & Sofer, Z. Layered Transition-Metal Ditellurides in Electrocatalytic Applications - Contrasting Properties. *ACS Catal.* **7**, 5706–5716 (2017).

19. McManus, J. B., Cunningham, G., McEvoy, N., Cullen, C. P., Gity, F., Schmidt, M., McAteer, D., Mullarkey, D., Shvets, I. V., Hurley, P. K., Hallam, T. & Duesberg, G.

S. Growth of 1T′-$MoTe_2$ by Thermally Assisted Conversion of Electrodeposited Tellurium Films. *ACS Appl. Energy Mater.* **2**, 521–530 (2019).

20. Chen, B., Sahin, H., Suslu, A., Ding, L., Bertoni, M. I., Peeters, F. M. & Tongay, S. Environmental Changes in $MoTe_2$ Excitonic Dynamics by Defects-Activated Molecular Interaction. *ACS Nano* **9**, 5326–5332 (2015).

21. Sun, Y., Wang, Y., Sun, D., Carvalho, B. R. Read, C. G., Lee, C-H., Lin, Z., Fujisawa, K., Robinson, J. A., Crespi, V. H., Terrones, M. & Schaak, R. E. Low-Temperature Solution Synthesis of Few-Layer 1T'-$MoTe_2$ Nanostructures Exhibiting Lattice Compression. *Angew. Chem. Int. Ed.* **55**, 2830–2834 (2016).

22. Liu, M., Wang, Z., Liu, J., Wei, G., du, J., Li, Y., An, C. & Zhang, J. Synthesis of few-layer 1T′-$MoTe_2$ ultrathin nanosheets for high-performance pseudocapacitors. *J. Mater. Chem. A* **5**, 1035–1042 (2017).

23. Qiu, L., Pol, V. G., Wei, Y. & Gedanken, A. A two-step process for the synthesis of MoTe2 nanotubes: Combining a sonochemical technique with heat treatment. *J. Mater. Chem.* **13**, 2985–2988 (2003).

24. Voiry, D., Salehi, M., Silva, R., Fujita, T., Chen, M., Asefa, T., Shenoy, V. B., Eda, G. & Chhowalla, M. Conducting MoS_2 Nanosheets as Catalysts for Hydrogen Evolution Reaction. *Nano Lett.* **13**, 6222-6227 (2013).

25. Chianelli, R. R., Ruppert, A. F., Behal, S. K., Kear, B. H., Wold, A. & Kershaw, R. The reactivity of MoS_2 single crystal edge planes. *J. Catal.* **92**, 56–63 (1985).

26. Vrubel, H. & Hu, X. Molybdenum Boride and Carbide Catalyze Hydrogen Evolution in both Acidic and Basic Solutions. *Angew. Chem. Int. Ed.* **51**, 12703-12706 (2012).

27. Jana, M. K., Singh, A., Sampath, A., Rao, C. N. R. & Waghmare, U. V. Structure and Electron-Transport Properties of Anion-Deficient $MoTe_2$: A Combined Experimental and Theoretical Study. *Zeitschrift für Anorg. und Allg. Chemie* **642**, 1386–1396 (2016).

28. Zhou, L. *et al.* Sensitive Phonon-Based Probe for Structure Identification of 1T′-$MoTe_2$. *J. Am. Chem. Soc.* **139**, 8396–8399 (2017).

29. Pine, A. S. & Dresselhaus, G. Raman Spectra and Lattice Dynamics of Tellurium. *Phys. Rev. B* **4**, 356–371 (1971).

30. Zhou, L., Zubair, A., Wang, Z., Zhang, X., Ouyang, F., Xu, K., Fang, W., Ueno, K., Li, J., Palacios, T., Kong, J. & Dresselhaus, M. S. Synthesis of High-Quality Large-Area Homogenous 1T′ $MoTe_2$ from Chemical Vapor Deposition. *Adv. Mater.* **28**, 9526–9531 (2016).

31. Cesano, F., Bertarione, S., Piovano, A., Agostini, G., Rahman, M. M., Groppo, E., Bonino, F., Scarano, D., Lamberti, C., Bordiga, S., Montanari, L., Bonoldi, L., Millini, R. & Zecchina, A. Model oxide supported MoS_2 HDS catalysts: Structure and surface properties. *Catal. Sci. Technol.* **1**, 123–136 (2011).

32. Hu, Z., Wang, L., Zhang, K., Wang, J., Cheng, F., Tao, Z. & Chen, J. MoS_2 Nanoflowers with Expanded Interlayers as High-Performance Anodes for Sodium-Ion Batteries. *Angew. Chem. Int. Ed.* **53**, 12794–12798 (2014).

33. Lu, Y., Yao, X., Yin, J., Peng, G., Cui, P. & Xu, X. MoS_2 nanoflowers consisting of nanosheets with a controllable interlayer distance as high-performance lithium ion battery anodes. *RSC Adv.* **5**, 7938–7943 (2015).

34. Cho, S., Kim, S., Kim, J. H., Zhao, J., Seok, J., Keum, D. H., Baik, J., Choe, D-H., Chang, K. J., Suenaga, K., Kim, S. W., Lee, Y. H. & Yang, H. Phase patterning for ohmic homojunction contact in $MoTe_2$. *Science* **349**, 625-628 (2015).

35. Voiry, D., Salehi, M., Silva, R., Fujita, T., Chen, M., Asefa, T., Shenoy, V. B., Eda, G. & Chhowalla, M. Conducting MoS_2 Nanosheets as Catalysts for Hydrogen Evolution Reaction. *Nano Lett.* **13**, 6222-6227 (2013).

36. Bonde, J., Moses, P. G., Jaramillo, T. F., Nørskov, J. K. & Chorkendorff, I. Hydrogen evolution on nano-particulate transition metal sulfides. *Faraday Discuss.* **140**, 219-231 (2008).

37. Liu, Y., Wu, J., Hackenberg, K. P., Zhang, J., Wang, Y. M., Yang, Y., Keyshar, K., Gu, J., Ogitsu, T., Vajtai, R., Lou, J., Ajayan, P. M., Wood, B. C. & Yakobson, B. I. Self-optimizing, highly surface-active layered metal dichalcogenide catalysts for hydrogen evolution. *Nat. Energy* **2** (2017).

5. Electrochemical Activation of Nanocrystalline 1T'-$MoTe_2$

Following on from the characterisation of nanocrystalline 1T'-$MoTe_2$, a remarkable improvement in catalytic activity was observed with continuous reductive potential cycling. By cycling nanocrystalline 1T'-$MoTe_2$ between the potential range of +0.2 V and –0.5 V (vs. NHE) the overpotential at $j = -10$ mA cm^{-2} was found to gradually improve from 320 ± 12 mV to 178 ± 8 mV after only 100 cycles. This enhancement of catalytic activity could be due to a variety of factors such as changes in structure, morphology and / or composition with continuous cycling. This chapter is hence dedicated to excluding these possibilities by discussing the experiments performed using a variety of characterisation techniques (PXRD, Raman spectroscopy, SEM, ICP-OES, ECSA, EIS) directly after the electrochemical reaction. Therefore, the improvement is proposed to be due to electron doping of the catalyst surface which results in the activation of the basal plane. Additionally, electrocatalytic measurements combined with gas chromatography confirm that the rate of hydrogen evolution increases as the reaction progresses, thus confirming the observed redox wave corresponds to the improved activity of nanocrystalline 1T'-$MoTe_2$. This phenomenon has been reported before but a clear understanding is yet to be obtained other than simply describing the observation as an 'activation'.

5.1. Introduction

5.1.1. Literature Reports of Electrochemical Activation

Electrochemical activation has recently emerged as a viable route for producing HER electrocatalysts *in operando*. However, the underlying mechanism of activation is not fully understood, with varying origins for the enhanced activity being reported. Application of continuous reductive potential cycling has led to a variety of 'activated' TMDC electrocatalysts, with changes in morphology, composition and electronic structure being proposed as the source of improved performance.[1–3]

5.1.1.1. Changes in Morphology

Previous work by Liu *et al*. demonstrates the electrochemical activation of metallic TaS_2 and NbS_2 with continuous reductive cycling.[1] In both cases, the initial overpotentials are in excess of 500 mV, and are therefore regarded as rather inefficient HER electrocatalysts. However, by cycling TaS_2 in acidic media, in the potential range of +0.2 V and –0.6 V (vs.

NHE) the overpotential was found to gradually improve. For TaS_2, the overpotential improved to only 60 mV after 5000 cycles, and the Tafel slope decreased from 282 mV dec^{-1} to 37 mV dec^{-1}. This change in Tafel slope is indicative of a change in reaction mechanism, with the rate determining step becoming the Heyrovsky reaction rather than the Volmer reaction. These electrochemical reaction processes are discussed in the Chapter 1, Section 1.4.5.; however Table 5-1 has been included for clarity.

Table 5-1: *Summary of the possible reaction pathways occurring during the hydrogen evolution reaction.*

Volmer step	$H_3O^+ + e^- \rightarrow H_{ads} + H_2O$	Discharge step
Heyrovsky step	$H_{ads} + H_3O^+ + e^- \rightarrow H_2 + H_2O$	Electrochemical desorption step
Tafel step	$H_{ads} + H_{ads} \rightarrow H_2$	Recombination step

As a result of the reductive potential cycling, the authors note a change in catalyst morphology and deem the process a 'self-optimising' behaviour. With increasing number of cycles, the platelets become thinner and more dispersed. As a result, the charge transfer resistance was found to improve, with the enhancement being attributed to the shorter interlayer pathways between particles of smaller size. Additionally, Liu *et al.*[1] note an increase in the effective active surface area, which is directly proportional to the double layer capacitance, C_{DL}. This increase in surface area indicates that new active sites are being produced with continuous cycling as a result of the change in sample morphology. This mechanism of activation is similar to that of chemical exfoliation *via* lithium intercalation, as both methods result in a morphology change which enhances the HER. Liu *et al*. attribute their morphology change to hydrogen becoming trapped between the layers of TaS_2, which results in the 'peeling away' of layers in order to free the hydrogen. However, this mechanism of activation offers the benefit of an *in operando* activation, without the need for any additional complex chemical procedures. A similar activation mechanism is also reported for metallic NbS_2, with the overpotential reaching 50 mV after 12000 cycles.[1]

5.1.1.2. Proton Intercalation

In contrast to the work on TaS_2 by Liu *et al.*[1] which generates additional active sites by altering the catalyst morphology with continuous reductive cycling, a study on 2H-MoS_2 by Li *et al.*[3] reported the electrochemical activation of the already present active sites. The authors report that cycling 2H-MoS_2 between 0 V and −0.5 V (vs. NHE) leads to an enhancement in catalytic activity without any changes to the structure, morphology or composition.

The study by Li *et al.*[3] excludes the generation of new active sites by initially examining the catalyst morphology and composition. Since the edge sites are the active component of the 2H-phase of MoS_2, the generation of new active sites would be visualised in the SEM images, however no change in morphology was observed. Likewise, a change in composition would be expected if the enhanced activity were due to an increase in sulfur vacancies, yet the authors exclude this. Rather, the authors claim that intercalation of protons between the MoS_2 layers results in an increase in electronic conductivity, which aids charge transfer and thus improves the catalytic performance. Additionally, the energy of hydrogen adsorption was calculated to become more favourable with protons intercalated between the layers, thus indicating an improvement in activity. Therefore, the catalytic enhancement was attributed to the enhancement of the 'as-grown' sites.

5.1.1.3. Platinum Deposition in 1T'-$MoTe_2$

In a follow up paper by Seok *et al.*,[2] whose original work was discussed in Chapter 3,[4] the authors report an electrochemical activation of metallic 1T'-$MoTe_2$ single crystals. This study proves that the enhanced catalytic activity is due to surface engineering on the metallic basal plane surface by electrochemical deposition of platinum on 1T'-$MoTe_2$. The result is a new hybrid Pt/$MoTe_2$ electrocatalyst which out performs current TMDC electrocatalysts. By poising the working electrode at reductive potentials (*i.e.* cycling between +0.2 V and −1.0 V (vs. NHE)), dissolution of the platinum counter electrode in the acidic electrolyte leads to the growth of a thin Pt layer on the metallic 1T'-$MoTe_2$ surface. This process has been observed before when explaining the surprising improvement of carbon-based HER catalysts.[5,6] As such, the catalytic activity was dramatically improved, with a comparison of the catalytic activities summarised in Table 5-2.

The authors note an improvement in overpotential from 356 mV to only 23 mV after 21 hours of reductive potential cycling. Interestingly, a progressive improvement in overpotential is observed, indicating the catalytic activity improves with increasing coverage of platinum. Hence, in this case, the electrochemical activation is attributed to the addition of the noble metal platinum, rather than the intrinsic activity of 1T'-$MoTe_2$ itself.

Table 5-2: *Summary of the catalytic performances of single crystal 1T'-$MoTe_2$ and Pt-deposited on 1T'-$MoTe_2$ as obtained by Seok et a.l*[2,4]

Catalyst	Potential for $j = -10$ mA cm^{-2} (V vs. NHE)	Tafel slope (mV dec^{-1})	Exchange current density (mA cm^{-2})	Ref.
1T'-$MoTe_2$	–0.356	127	2.1 x 10^{-2}	4
Pt/1T'-$MoTe_2$	–0.023	22	1.0	2

5.1.2. Intrinsic Activity of 1T'-$MoTe_2$

5.1.2.1. Lattice Distortion in 1T'-$MoTe_2$

In their original paper (as discussed in Chapter 3), Seok *et al.*[4] predicted an unusual catalytic enhancement of 1T'-$MoTe_2$ due to a spontaneous lattice distortion. This Peierls-type distortion is driven by hydrogen adsorption (and consequently electron doping) on the surface of the metallic basal plane. As a result, the authors suggest that the surprising performance of 1T'-$MoTe_2$ cannot be explained by the conventional volcano plot. The volcano plot allows for the identification of potential HER electrocatalysts by plotting the exchange current density against the free energy of hydrogen adsorption (see Chapter 1, Section 1.4.4.). Seok *et al.* claim that 1T'-$MoTe_2$ lies out with the conventional volcano plot, as its rather high ΔG_H value contradicts its promising exchange current density.

TMDC electrocatalysts typically follow the Volmer-Heyrovsky reaction mechanism of hydrogen evolution; with the Heyrovsky step being rate limiting and therefore a Tafel slope of ~40 mV dec^{-1} is obtained. In the case of 1T'-$MoTe_2$, Seok *et al.*[4] determine the Tafel slope of 1T'-$MoTe_2$ to be 127 mV dec^{-1}, hence the Volmer reaction (hydrogen adsorption) is the rate determining step. Therefore, as hydrogen is adsorbed on the basal plane surface, electron doping and consequently Peierls distortion occurs, thus altering the lattice structure away from that of the pristine 1T'-$MoTe_2$.

As discussed in Chapter 4,[7] the Tafel slope of nanocrystalline 1T'-$MoTe_2$ was determined to be 68 ± 4 mV dec^{-1}, which indicates that hydrogen adsorption is not the rate determining step, but rather it is the electrochemical desorption step (Heyrovsky) which is rate limiting. Thus, it is plausible that with increased hydrogen adsorption on nanocrystalline 1T'-$MoTe_2$, the effect of electron doping and lattice distortion may be further enhanced, resulting in additional improvement in catalytic activity.

5.1.2.2. Atomic-Site Dependency in 1T'-$MoTe_2$

The adsorption of hydrogen on the surface of 1T'-$MoTe_2$ is dependent on the atomic-site, as initially calculated by Seok *et al.*[4] These sites and their adsorption energies are summarised in Table 5-3 and can be visualised in Figure 5-1, which illustrates the adsorption of H on the most favourable Te site, the 'α-site'. The Mo active site, labelled 'β-site' revealed a significantly more positive ΔE_H value of 0.82 eV, compared to the lowest value of 0.55 eV for the Te α-site. Thus, hydrogen adsorption was deemed to occur on Te active sites. Additionally, Peierls distortion results in two-inequivalent surface Te sites: the 'low' Te α-site and the 'high' Te ε-site, which are located on the terraced surface. However, the 'low' Te α-site shows the lowest ΔE_H value; hence hydrogen adsorption mainly occurs on the α-sites. There are a further two crystallographically independent Te sites labelled γ and σ, however, due to their high hydrogen adsorption energies, are disregarded as being the primary active site.

Table 5-3: *Summary of the hydrogen adsorption energies of each atomic-site as calculated by Seok et al. It should be noted that the atomic site terminology is taken directly from work by Seok et al.*[4]

Atomic-site	ΔE_H (eV)
α	0.55
β	0.82
γ	1.05
ε	1.43
σ	1.52

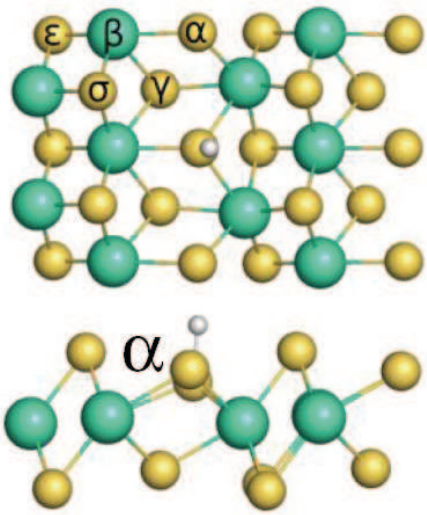

Figure 5-1: *Reaction sites of HER on 1T'-$MoTe_2$. Top and side lattice structures of hydrogen adsorbed at an 'α-site'. Blue spheres represent Mo atoms, yellow spheres represent Te atoms and white spheres represent adsorbed hydrogen. Figure has been adapted from the original work by Seok et al.*[4]

Further, the energy of hydrogen adsorption was found to decrease as hydrogen is adsorbed on to the α-site and the pristine lattice becomes distorted. This indicates that further adsorption of hydrogen on the basal plane surface may have a profound effect on the catalytic activity, and perhaps the electrochemical activation as discussed above in Section 5.1.1.3 may have been overlooked due to the deposition of platinum.

5.2. Aims

This chapter is dedicated to the first report of a reversible electrochemical activation of a TMDC electrocatalyst. Currently, the mechanism behind the electrochemical activation remains unclear in the literature, with several plausible routes of activation being reported. Hence, this study seeks to understand the origin of activation in the case of nanocrystalline 1T'-$MoTe_2$. To do this, a variety of structural characterisation and electrochemical techniques are required to analyse the activated material. In doing so, a viable explanation for the electrochemical activation of 1T'-$MoTe_2$ is proposed.

5.3. Results and Discussion

5.3.1. Overpotential Improvement of Nanocrystalline 1T'-$MoTe_2$

Continuing with metallic 1T'-$MoTe_2$, this chapter now focuses solely on nanocrystalline 1T'-$MoTe_2$. As discussed in Chapter 4, the change in morphology from crystalline to nanocrystalline 1T'-$MoTe_2$ results in significantly greater current densities being achieved, owing to its increased surface area and reduced charge transfer resistance. Further studies into the stability of this novel material led to the realisation of an interesting electrochemical phenomenon.

Upon continuous reductive potential cycling of nanocrystalline 1T'-$MoTe_2$ over the range +0.2 V to –0.5 V (vs. NHE) with a scan rate of 100 mV s^{-1}, a substantial improvement in the overpotential required for j = –10 mA cm^{-2} was observed. After 100 cycles, the overpotential at this current density becomes more favourable, improving from 320 ± 12 mV to 178 ± 8 mV, at which point the overpotential remains stable for at least 1000 cycles. Figure 5-2 highlights this dramatic improvement in overpotential by comparing the initial LSV with that of the 100th reductive sweep.

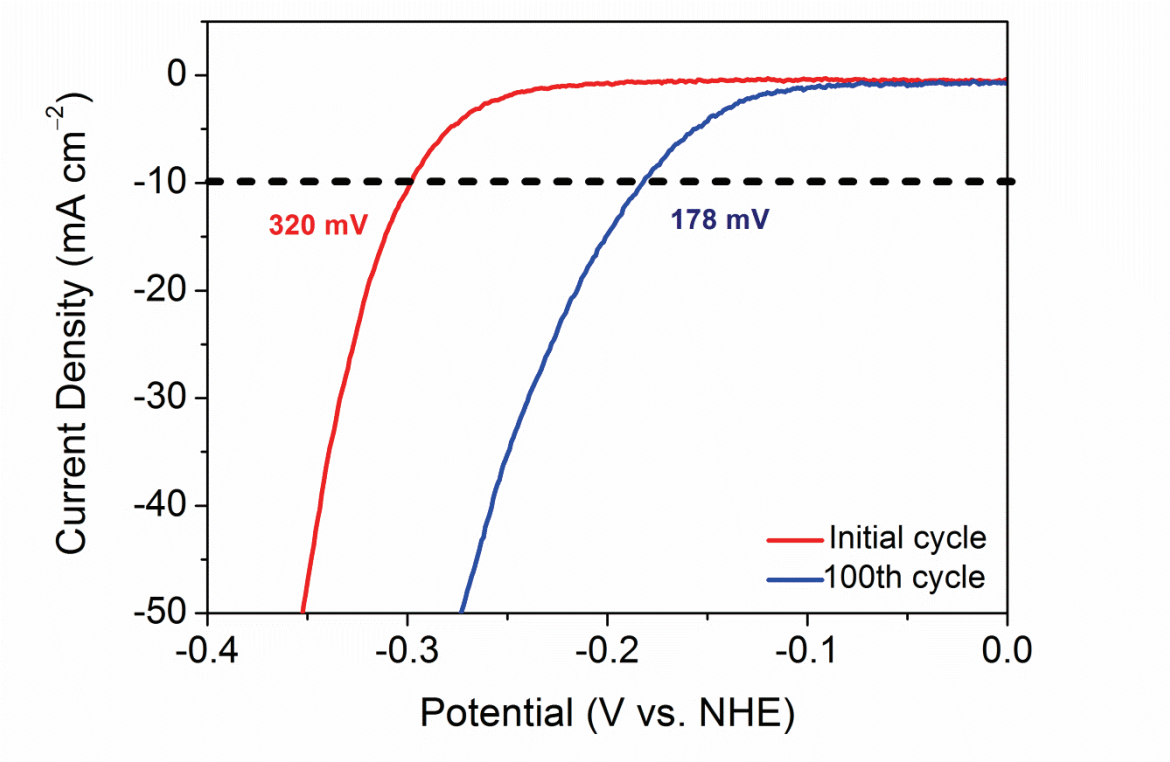

Figure 5-2: *Comparison of the current densities achieved by nanocrystalline 1T'-$MoTe_2$ before and after 100 cycles in 1 M H_2SO_4. Catalysts were prepared on a glassy carbon working electrode as described in the experimental section. Carbon felt and 3 M Ag/AgCl were used as the counter and reference electrodes, respectively.*

Originally, this experiment was performed using platinum as the counter electrode. However, in order to confirm that the dissolution of Pt and its deposition on to the surface of 1T'-$MoTe_2$ was not the cause for enhancement; the Pt counter electrode was replaced with carbon felt. As a result, an identical overpotential improvement was observed, thus proving that neither Pt nor carbon particles were the cause of the activation. Contrastingly, work by Seok *et al*. found that continuous reductive cycling resulted in the growth of platinum on the basal plane of 1T'-$MoTe_2$.[2] However, it should be noted that the authors applied much larger reductive potentials (+0.2 V to −1 V (vs. NHE)). This resulted in a gradual overpotential improvement from 356 mV to only 23 mV after 21 hours of cycling, and their new catalytic material was dubbed 'Pt/$MoTe_2$'. Since, in this work, nanocrystalline 1T'-$MoTe_2$ was cycled to much less reductive potentials than in the case of Seok *et al.*, coupled with the change in counter electrode, the deposition of Pt as the reason for the improvement was ruled out. Interestingly, in contrast to that reported by Seok *et al.*,[2] it was found that when the potential range was extended to –0.6 V (vs. NHE) rather than –0.5 V (vs. NHE), the catalyst lost contact with the glassy carbon substrate. As such, a complete

100 cycle scan was not achieved. Therefore, all subsequent scans were obtained by cycling between +0.2 V and –0.5 V (vs. NHE) unless otherwise stated.

Leakage of silver from the Ag/AgCl reference electrode is a possible reason for the enhanced activity. As proven by Symes *et al.,* silver ions can leak from the reference electrode and deposit on the catalyst surface, thus generating greater current densities than would otherwise be observed.[8] Therefore, the Ag/AgCl reference electrode was subsequently replaced with a saturated Hg/Hg_2SO_4 reference electrode. Figure 5-3 shows the result of cycling nanocrystalline 1T'-$MoTe_2$ 100 times using this alternative reference, and shows a similar activation. Thus, the deposition of silver on to the catalyst surface was also excluded as a possible source of improved performance.

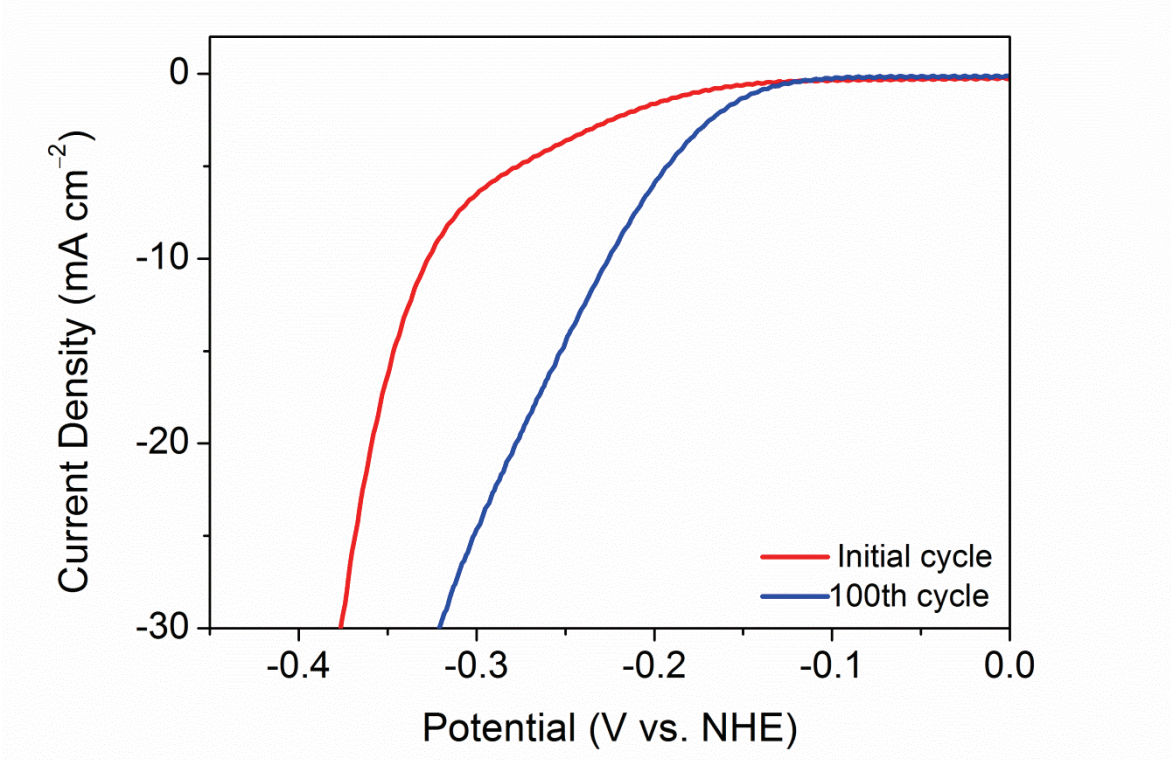

Figure 5-3: *Comparison of the current densities achieved by nanocrystalline 1T'-$MoTe_2$ before and after 100 cycles in 1 M H_2SO_4 using saturated Hg/Hg_2SO_4 as the reference electrode. The use of saturated $Hg/HgSO_4$ as the reference electrode rules out leakage of silver from the Ag/AgCl reference electrode as the source of improved performance.*

It should also be noted that a similar activation is observed for crystalline 1T'-$MoTe_2$, albeit to a lesser extent. Figure 5-4 shows the overpotential required for j = –10 mA cm^{-2} to improve from 360 mV to only 261 mV. The reason for this is most likely due to the larger crystallite size of the 1T'-$MoTe_2$ phase, and its less efficient charger transfer kinetics, as

discussed in Chapter 4. This is also corroborated by studies on MoS_2 by Li *et al.*[3] who found that more cycles were required for the activation of larger flakes than for flakes of a smaller size. From herein, only the activation of the nanocrystalline 1T'-$MoTe_2$ phase will be investigated.

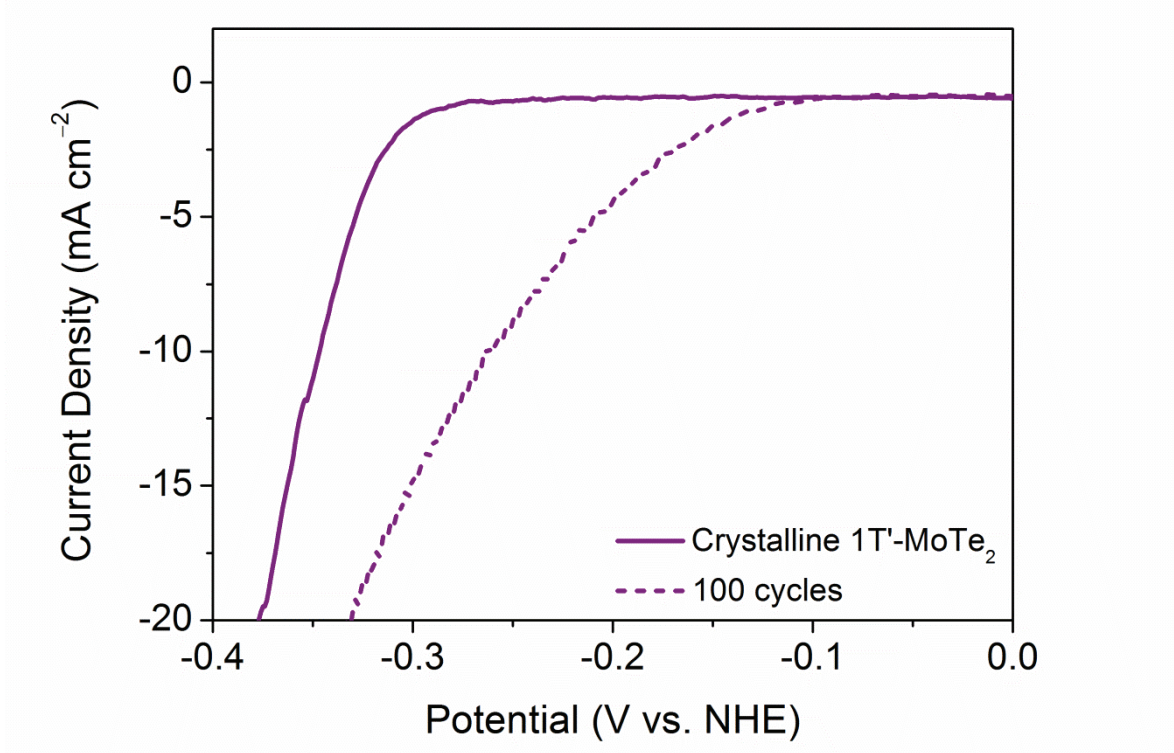

Figure 5-4: *Comparison of the current densities achieved by crystalline 1T'-$MoTe_2$ before and after 100 cycles in 1 M H_2SO_4. Catalysts were prepared on a glassy carbon working electrode as describe in the experimental section. Carbon felt and 3 M Ag/AgCl were used as the counter and reference electrodes, respectively.*

5.3.2. Hydrogen Production

Alternatively, it is possible that the lower overpotential is due to the reduction of some other species that may have formed upon cycling, rather than the reduction of protons to hydrogen. To investigate this, chronoamperometry coupled with gas chromatography was employed. Further to the previous findings, a similar enhancement was observed by chronoamperometry (Figure 5-5). A constant potential of –320 mV (vs. NHE) was applied (corresponding to the overpotential required for j = –10 mA cm^{-2}). Under normal circumstances, *i.e.* ones in which no electrochemical activation occurs, when a constant potential is applied, the current density would remain stable (as is depicted by the dashed line in Figure 5-5) or rather decrease if the catalyst degrades with time. Contrastingly, in the case of nanocrystalline 1T'-$MoTe_2$, the current density was found to gradually increase as the reaction progressed. This is indicative of the evolution of hydrogen becoming easier as the reaction proceeds.

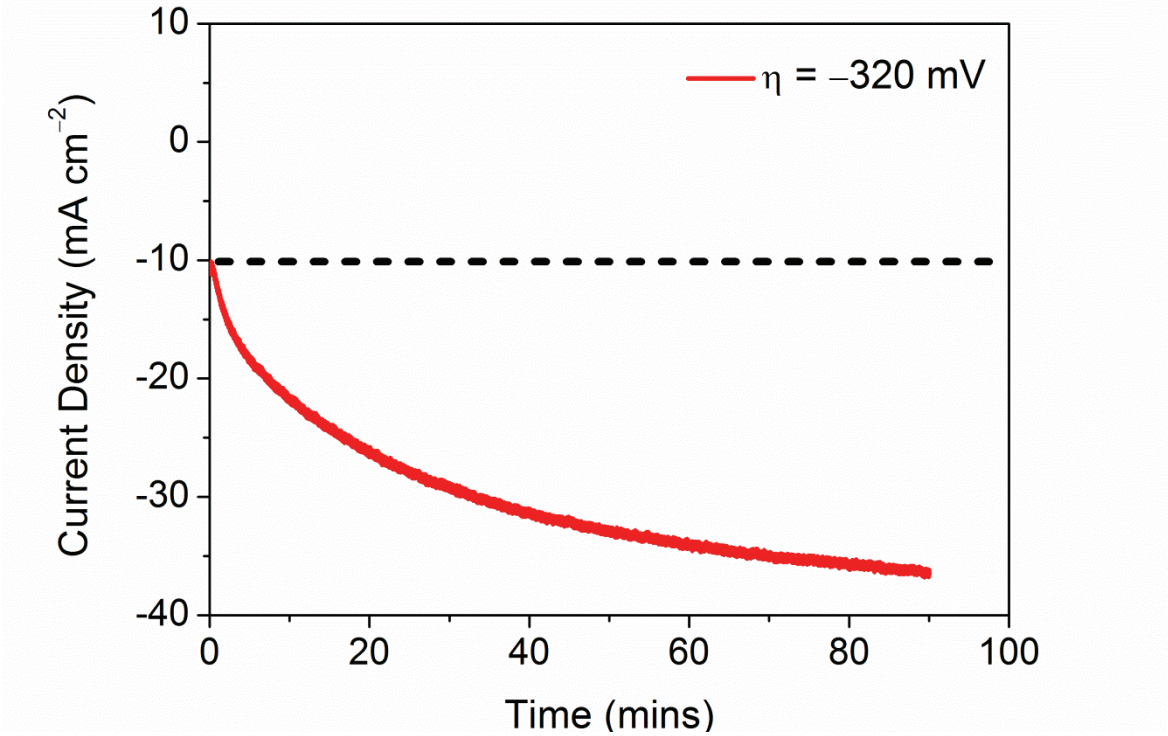

Figure 5-5: *Chronoamperometry profile of nanocrystalline 1T'-$MoTe_2$ in 1 M H_2SO_4. The applied potential was chosen as the value corresponding to j = –10 mA cm^{-2}. Experiments were performed using a three-electrode step, with catalyst-deposited glassy carbon as the working electrode, 3 M Ag/AgCl as the reference and carbon felt as the counter electrode. The dashed line represents the expected behaviour of a stable catalyst which does not undergo activation.*

Simultaneously, gas chromatography was performed which allowed for the identification of hydrogen as the gaseous product. The headspace of the cell was sampled at set time intervals, and it was found that as the current density increases, rather than the expected linear increase in hydrogen production with time, the rate of hydrogen evolution increases as the HER progresses (Figure 5-6).

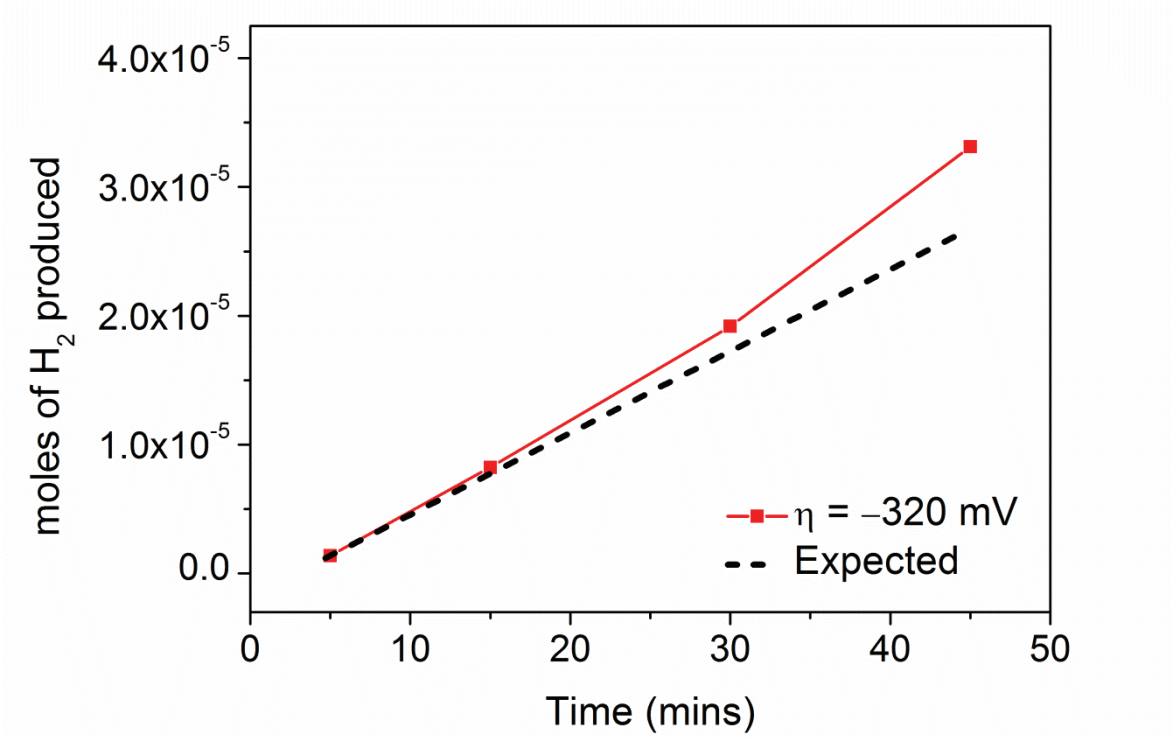

Figure 5-6: *Representative trace of the number of moles of hydrogen produced with time as a constant potential of –320 mV (vs. NHE) is applied. Solid line indicates the experimentally determined value of hydrogen yield from gas chromatography for the activated sample, while the dashed line represents the theoretically calculated value without activation.*

5.3.3. Stability Studies of Activated Nanocrystalline 1T'-$MoTe_2$

5.3.3.1. *Ex-situ* PXRD

Due to the small sample size required for electrochemical reactions, whereby the catalyst is made into an ink and deposited on to the surface of a glassy carbon electrode (Area = 0.071 cm^2) very little powder was available for analysis by PXRD after activation. To combat this, an *ex-situ* PXRD bracket was designed to fit the glassy carbon electrode, thus allowing for direct analysis of the catalyst on the electrode surface immediately after electrochemical treatment. Figure 5-7 shows an image of the bracket, with the surface of the electrode being flush with the surface. The bracket was made of acrylic, with aluminium tape used to cover this in order to remove any background diffraction from the acrylic. It should be noted that the range was limited to 10 - 40 °, since Al shows a diffraction peak at ~38 °. However, since the most prominent peaks of nanocrystalline 1T'-$MoTe_2$ occur below 30 °, the use of aluminium was deemed acceptable. Additionally, since the height of the electrode can be easily adjusted, a small amount of Si powder was added to the surface of the electrode prior to any measurements. In this way, silicon acts as an internal standard, meaning any shift in peak position can be attributed to the material itself rather than a difference in height between sample measurements.

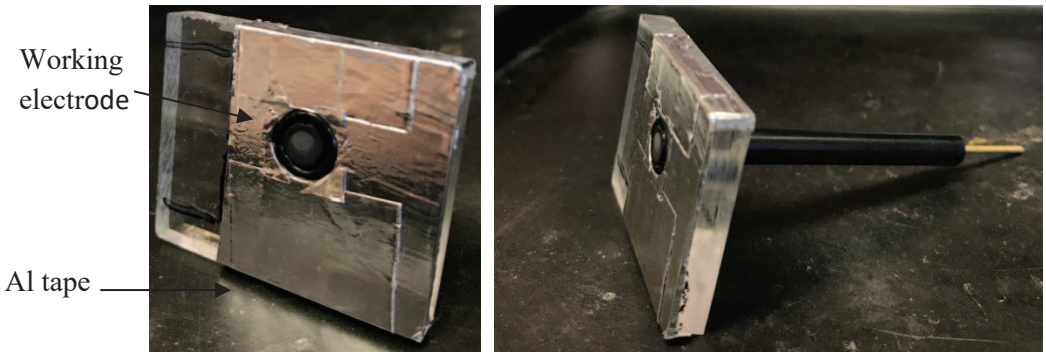

Figure 5-7: *Photographs of the ex-situ bracket designed for PXRD analysis of the catalyst directly on the electrode surface. Aluminium tape covers the acrylic, and the o-ring holds the glassy carbon electrode in place.*

Now, PXRD can be used to investigate the stability of nanocrystalline 1T'-$MoTe_2$ under electrochemical cycling conditions. As such, the catalyst-deposited glassy carbon electrode was cycled 1000 times between +0.2 V and –0.5 V (vs. NHE) and PXRD was performed immediately after cycling. The post cycling diffraction pattern was then compared with that of the electrode prior to cycling, and the patterns were adjusted according to the position of the silicon internal standard. It should be noted that since the PXRD pattern obtained after electrocatalytic measurements was performed directly on the electrode surface, a layer of H_2SO_4 electrolyte is present and may result in weaker Bragg reflections.

Figure 5-8 compares the PXRD patterns of nanocrystalline 1T'-$MoTe_2$ before and after 1000 CV cycles, and shows no obvious structural changes. Some literature studies point towards proton intercalation as a possibility for the electrochemical activation of TMDCs, however the lack of shift in the (001) peak position suggests no lattice expansion occurs. Hence, PXRD does not provide evidence of proton intercalation between the layers of nanocrystalline 1T'-$MoTe_2$.

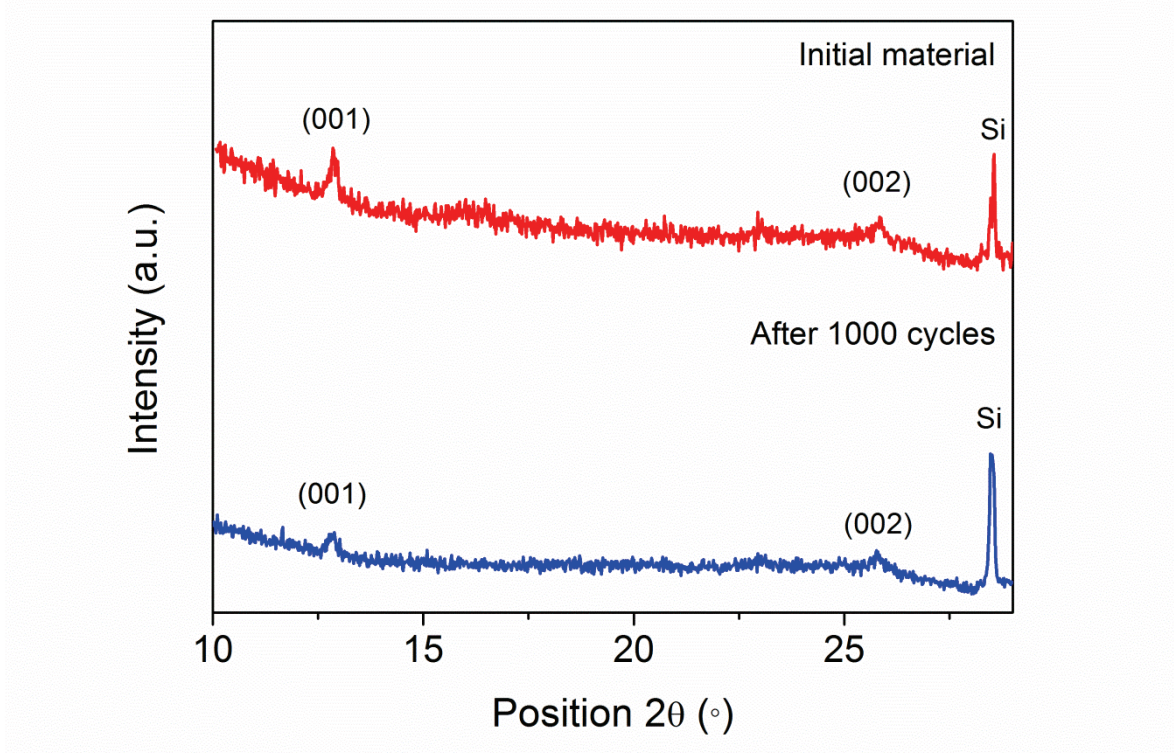

Figure 5-8: *PXRD patterns of nanocrystalline 1T'-$MoTe_2$ before and after 1000 cycles. Patterns were measured directly on the surface of the glassy carbon working electrode on which the catalyst ink was deposited. A small amount of silicon powder was placed on the surface to act as an internal standard.*

Continuing with the idea of proton intercalation, the material was then cycled 100 times in an identical manner with 1 M D_2SO_4 being used as the electrolyte in an attempt to observe a lattice expansion. The resulting powders were analysed by powder neutron diffraction (PND). Figure 5-9 shows the neutron scattering data from the nanocrystalline 1T'-$MoTe_2$ sample before and after activation in D_2SO_4. Again, no sign of lattice expansion or evidence of intercalation is observed which would lead to the substantial change in intensity of selected peaks. Therefore, *ex-situ* analysis by PXRD and PND exclude the intercalation of protons between the layers of 1T'-$MoTe_2$ as being the reason behind the activation process. However, since both of these techniques are performed *ex-situ*, they do not rule out the possibility of an *in operando* proton intercalation mechanism of activation. This will be discussed further in Chapter 6.

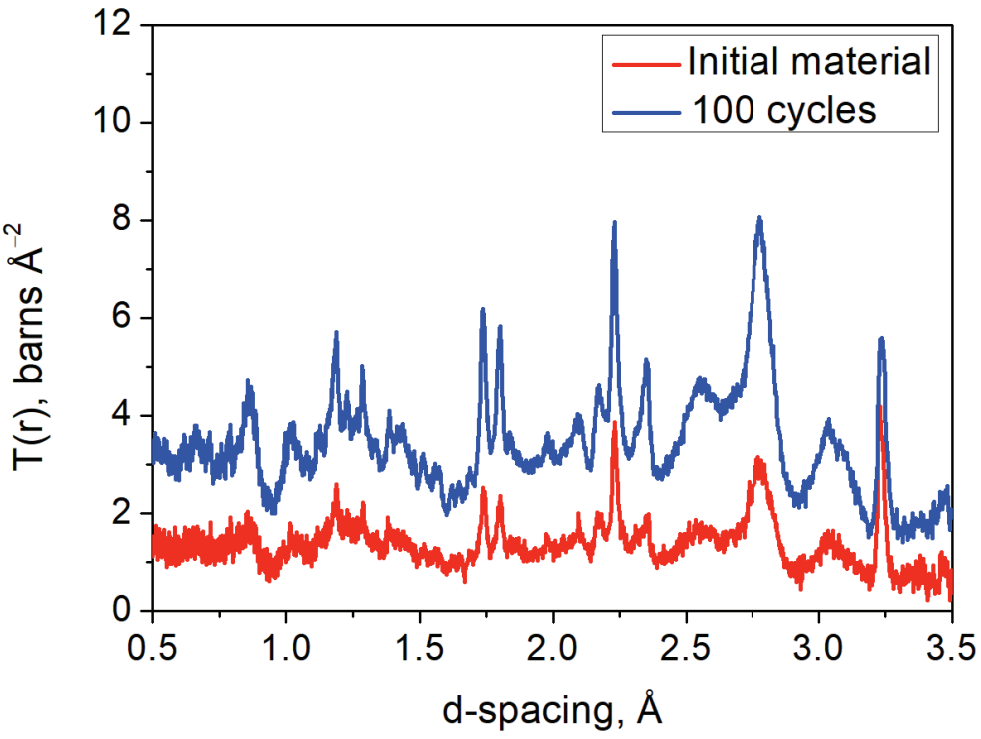

Figure 5-9: *Neutron scattering data collected in bank 4 of GEM from nanocrystalline 1T'-$MoTe_2$ before and after activation by 100 cycles in 1 M D_2SO_4 electrolyte. The difference in intensity between the two samples is due to the difference in collection time. The initial material was collected over approximately 1 hour while the activated material was collected overnight.*

5.3.3.2. *Ex-situ* Raman Spectroscopy

In a similar manner to PXRD, Raman spectroscopy was performed directly on the electrode surface after reductive potential cycling. This allowed for further confirmation of the phase purity. As can be seen in Figure 5-10, after 1000 cycles between +0.2 V and –0.5 V (vs. NHE) in 1 M H_2SO_4, the Raman spectra of both the initial material and the activated material post 1000 cycles are identical. Both spectra show the four main vibrational modes at ~107 cm^{-1}, ~128 cm^{-1}, ~161 cm^{-1} and ~255 cm^{-1}, which correspond to the B_g and A_g modes.[9] Therefore, combining the results obtained from PXRD and Raman Spectroscopy, structural changes can be eliminated as the cause of the enhanced activity.

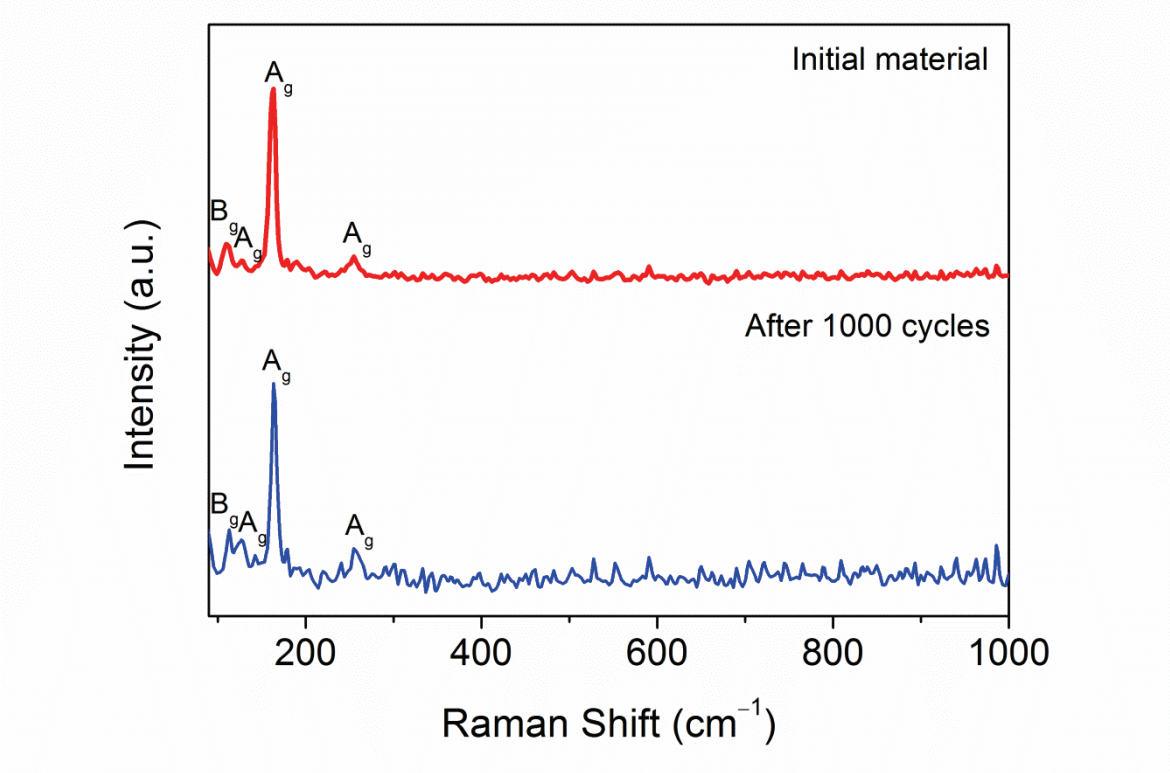

Figure 5-10: *Wide-range Raman spectra of nanocrystalline 1T'-$MoTe_2$ measured before (top) and after 1000 cycles (bottom). Raman spectra obtained after electrochemical measurements were performed directly on the electrode surface; therefore a layer of H_2SO_4 electrolyte is present thus resulting in an increased background after 1000 cycles.*

Contrastingly, looking at the Raman spectra of nanocrystalline 1T'-$MoTe_2$ when the potential range is extended to a more reductive potential of –0.6 V (vs. NHE), it was found that the activated material had decomposed into elemental tellurium. Figure 5-11 shows Raman spectra taken over three areas of the sample post cycling between +0.2 V and –0.6 V (vs. NHE). Elemental tellurium is observed at ~120 cm^{-1} and 140 cm^{-1} and the most

prominent A_g band of 1T'-$MoTe_2$ at ~161 cm^{-1} is less intense after only 50 cycles. This is in line with the electrochemical studies discussed above which showed the material to lose contact with the electrode surface at such reductive potentials. Contrastingly, Seok *et al.*[2] show no such degradation, possibly due to the more stable nature of their single crystal electrode rather than the preparation of a catalyst ink as reported here.

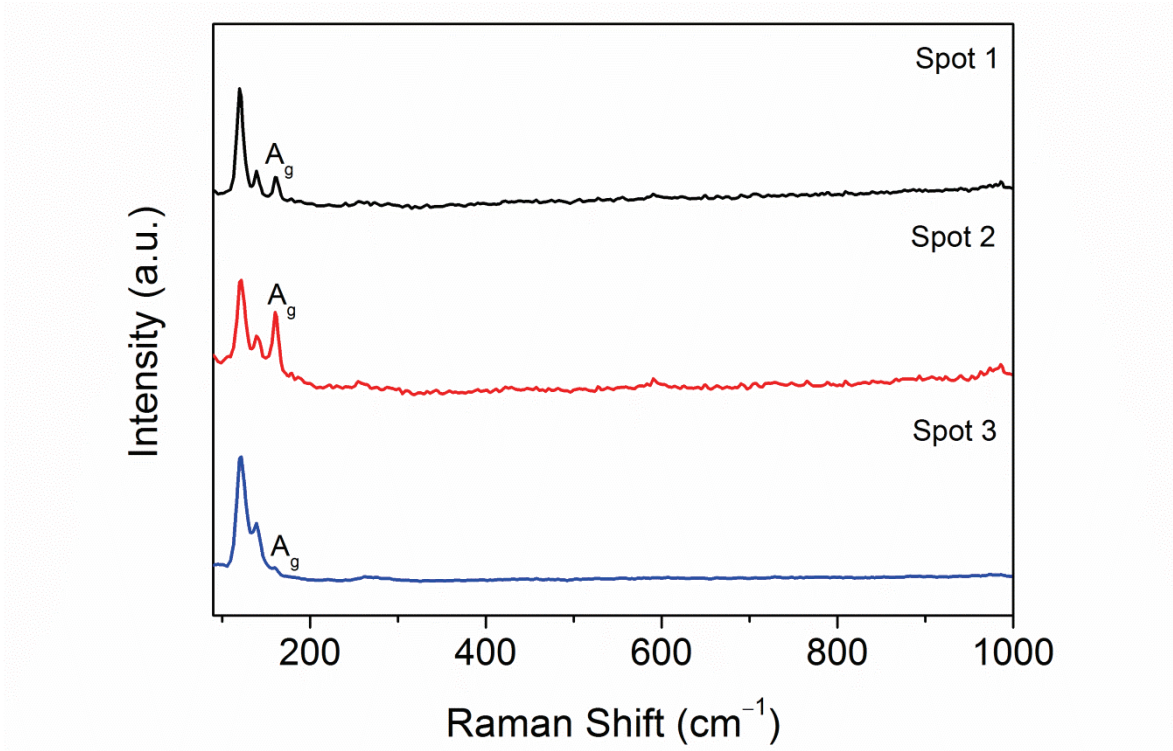

Figure 5-11: *Wide-range Raman spectra of nanocrystalline 1T'-$MoTe_2$ measured after 50 cycles ranging between +0.2 V and –0.6 V (vs. NHE). The A_g band of 1T'-$MoTe_2$ is highlighted for clarity. Spots 1,2 and 3 indicate three separate areas of the sample.*

5.3.3.3. Morphology and Composition

Previous studies by Liu *et al*. have attributed the electrochemical activation of TaS_2 and NbS_2 to sample thinning with cycling.[1] The change in morphology is easily seen by the appearance of smaller platelets after cycling. The authors report their improvement in catalytic activity to be due to the resulting shortened interlayer pathways, which aids electron transport between the catalyst and the electrolyte. Indeed, analysis of the electrochemical impedance spectroscopy showed that, in the case of both TaS_2 and NbS_2, the charge transfer resistance, R_{CT} decreased, thus indicating improved charge transfer kinetics.

However, looking at the morphology of 1T'-$MoTe_2$ after 100 cycles, *i.e.* after activation, no change in morphology was observed. Figure 5-12 shows a comparison of the SEM images of nanocrystalline 1T'-$MoTe_2$ samples before and after activation, and show that the morphology is maintained. Likewise, EDX mapping shows that both Mo and Te are well distributed throughout the activated material. Therefore, in combination with the *ex-situ* PXRD, PND and Raman spectroscopy results, the activation of nanocrystalline 1T'-$MoTe_2$ does not appear to be due to any structural or morphological changes to the sample.

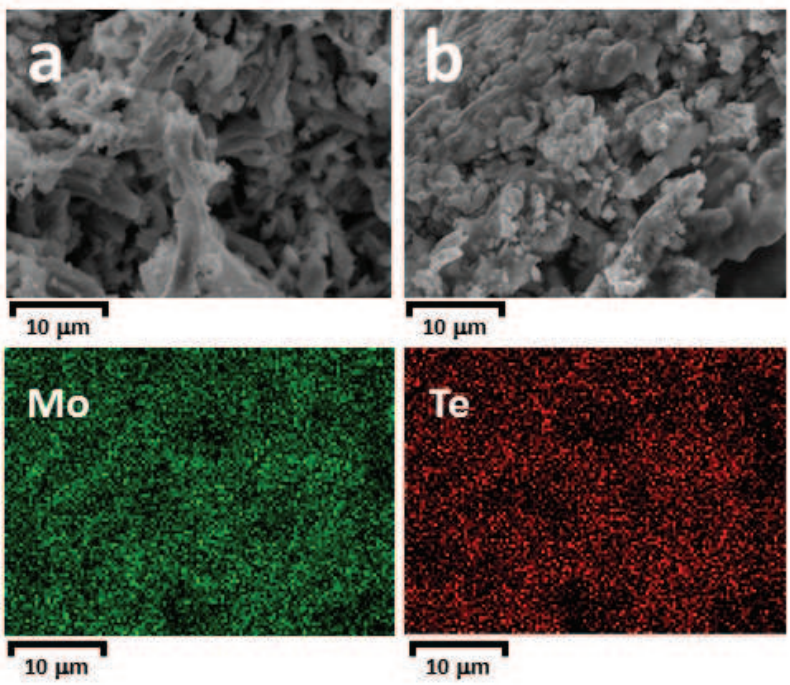

Figure 5-12: *SEM images of* ***a)*** *nanocrystalline 1T'-$MoTe_2$ before and* ***b)*** *after 100 cycles between +0.2 V and –0.5 V (vs. NHE). The EDX mapping images of the activated sample shows Mo (green) and Te (red) are well distributed throughout the material.*

5.3.3.4. Reversible Activation

As discussed above, application of reductive potential cycling for a total of 1000 cycles maintains the overpotential at 178 mV. Most interestingly, it was discovered that when the reductive potential is removed, the enhanced catalytic activity is lost and the overpotential required for $j = -10$ mA cm^{-2} reverts back to its original value of 320 mV. The catalyst must then be re-activated following the same procedure, thus resulting in a reversible activation mechanism. This phenomenon has not been reported elsewhere in the literature, with similar activation studies showing no experimental evidence of reversibility. Figure 5-13 shows the polarisation curves of nanocrystalline 1T'-$MoTe_2$ before and after 100 cycles between +0.2 V and –0.5 V (vs. NHE) and the dashed line indicates the LSV obtained immediately after the potential bias is removed.

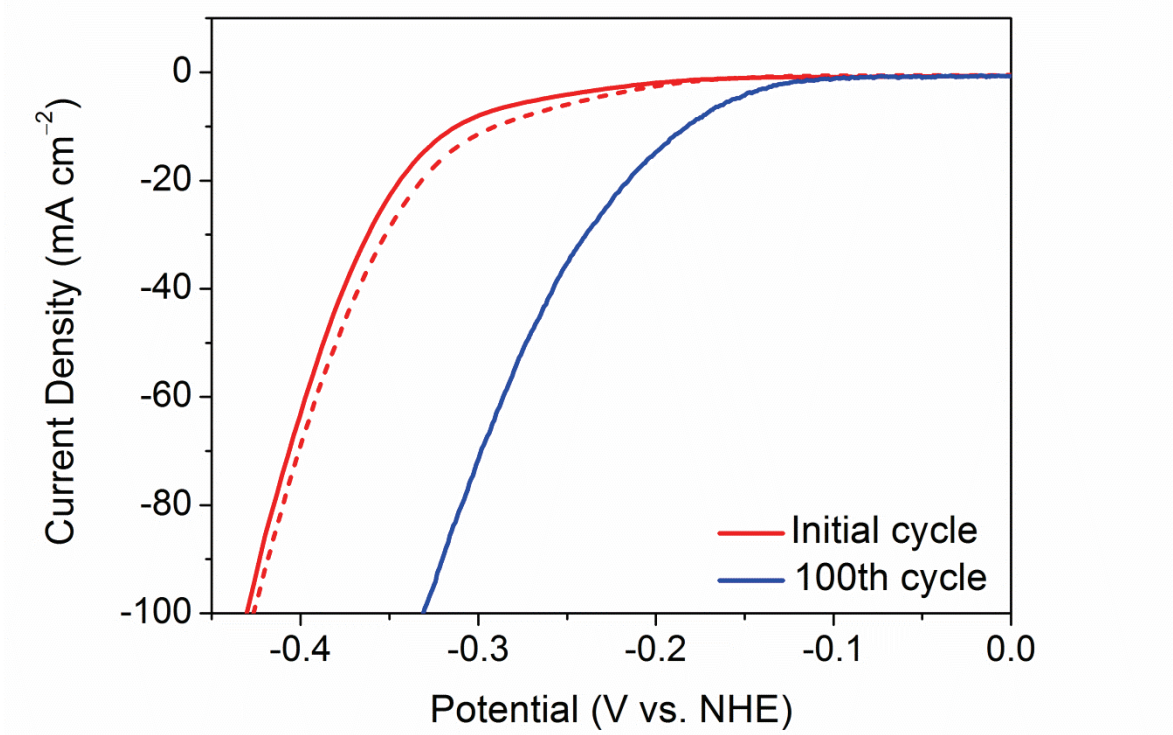

Figure 5-13: *Comparison of the current densities achieved by nanocrystalline 1T'-$MoTe_2$ before and after 100 cycles in 1 M H_2SO_4. The red dashed line illustrates the current densities achieved immediately after the 100 cycle scan, and shows the overpotential to return to its original value as the application of continuous cycling under reducing potentials is stopped.*

Due to this reversible shift in overpotential, the lack of changes in structure and morphology become obvious. Indeed, if any irreversible changes were to occur then the original overpotential would not be expected to be regenerated after the electrochemical reaction. Instead, the reversibility of the overpotential improvement implies that the activation is electronic in nature. Several studies have shown that 1T'-$MoTe_2$ displays a high susceptibility towards electron doping on the basal plane surface, and suggest that excess electron density can be accommodated at the Fermi level.[10–12] Therefore, it is possible that the partially filled *d* bands associated with the metallic character of 1T'-$MoTe_2$ are capable of accepting electron density during reductive potential cycling. This electron 'doping' may give rise to the enhanced catalytic performance.

To investigate this further, 2H-$MoTe_2$ was cycled 100 times under identical conditions to that conducted for 1T'-$MoTe_2$. Due to the semiconducting nature of 2H-$MoTe_2$, which exhibits poor charge transfer kinetics due to its fully occupied *d* bands, the material is an ideal candidate to test the theory of electron doping. As expected, Figure 5-14 shows that no such activation occurs in the case of 2H-$MoTe_2$. This finding reinforces the idea of electron doping as the cause of the enhanced activity, and will be discussed further in Section 5.3.5.

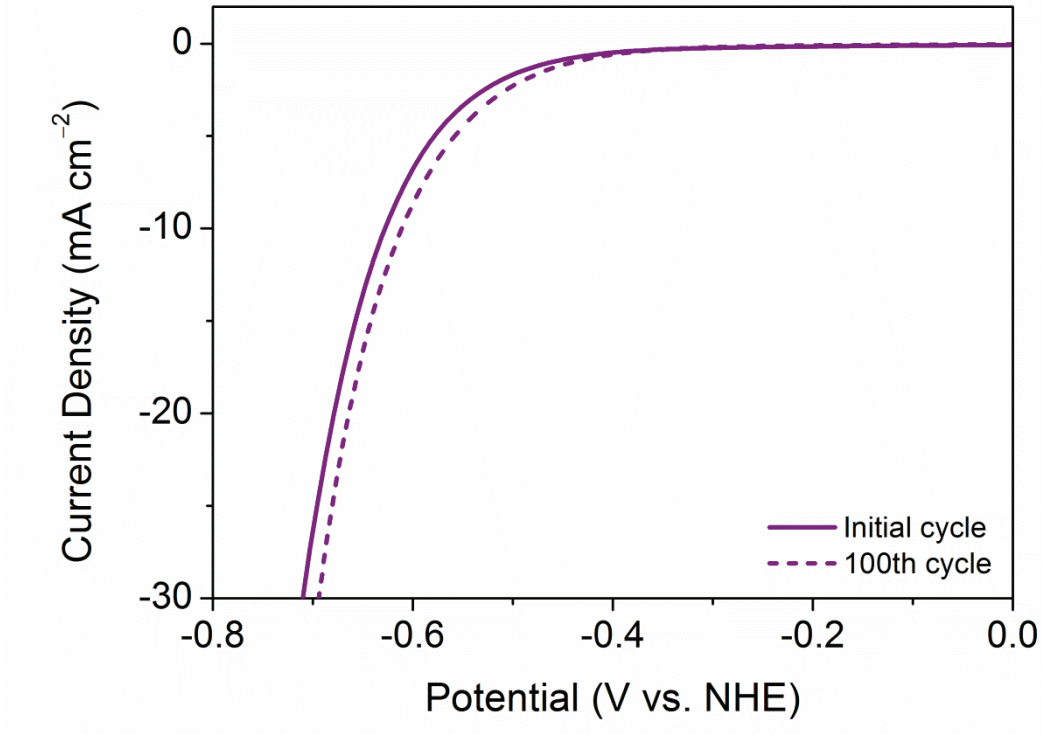

Figure 5-14: *Comparison of the current densities achieved by semiconducting 2H-$MoTe_2$ before and after 100 cycles in 1 M H_2SO_4.*

5.3.4. Electrochemical Activation

Since structural changes have been excluded as the origin of the enhanced activity, efforts were subsequently turned to investigating the electrochemical activation of the basal plane. As discussed in Chapter 4, the basal plane is considered as being the primary active site for metallic TMDCs. One possibility for the enhanced performance is that there is an increase in the number of active sites as the material becomes activated. The electrochemically active surface area (ECSA) was therefore investigated after 100 cycles. Figure 5-15 shows the double layer capacitance (C_{DL}) to remain identical within experimental error before and after 100 reductive cycles. This implies that the ECSA also remains identical with cycling, and no new active sites are generated. Additionally, ICP-OES reveals that the stoichiometry of the nanocrystalline 1T'-$MoTe_2$ remains unchanged after cycling, with the stoichiometries being $MoTe_{1.97(5)}$ and $MoTe_{1.98(2)}$, respectively. Hence, if any new active sites were generated, a change in composition would be expected due to the emergence of Te vacancies. Therefore, since there is no change in stoichiometry or ECSA, it appears that no new active sites are being created with cycling. This is also in line with the reversible nature of the activation process.

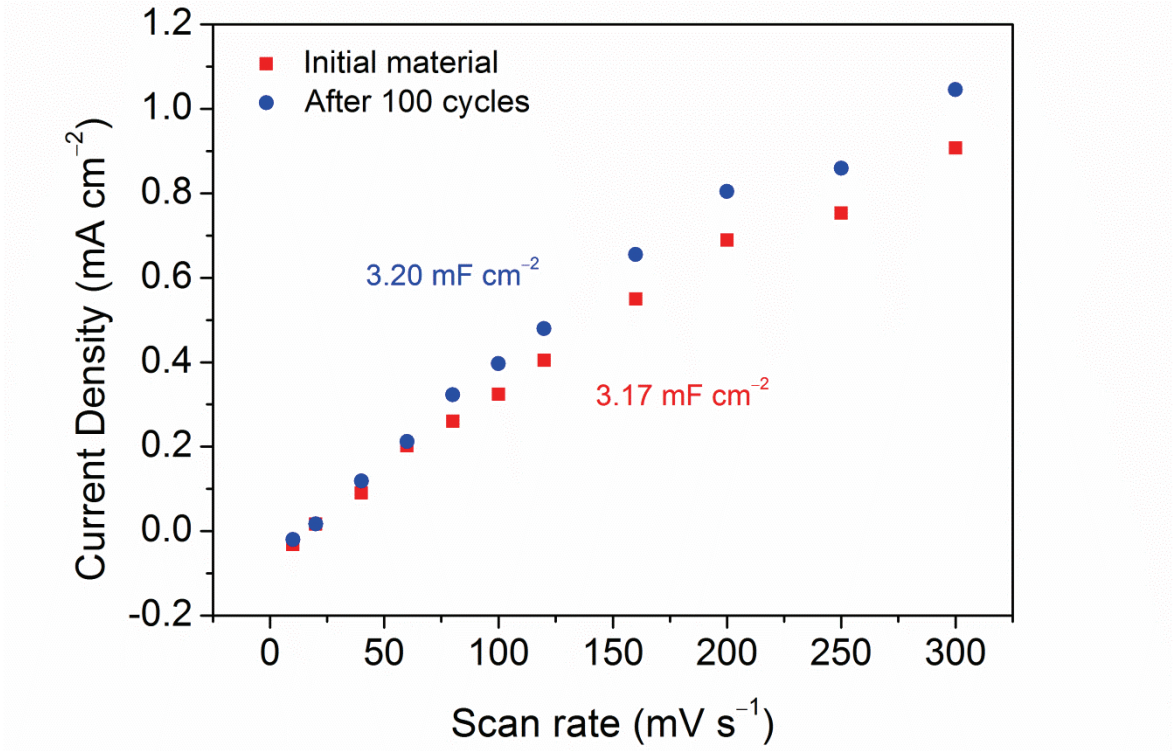

Figure 5-15: *Current density differences of nanocrystalline 1T'-$MoTe_2$ before and after 100 cycles plotted against scan rates. The capacitance currents were measured at 150 mV (vs. NHE).*

Following on from this, electrochemical impedance spectroscopy (EIS) was performed after 100 cycles at a potential of −300 mV (vs. NHE). In doing so, the charge transfer resistance, R_{CT}, was found to reduce by half (Figure 5-16). A reduction in charge transfer resistance implies that electron transfer is more efficient on the active sites. This, coupled with analysis of ECSA, suggests that rather than generating new active sites upon reductive cycling, the sites that are already present are becoming activated. It is therefore possible that with continuous reductive potential cycling the basal plane becomes 'activated', *i.e.* the reaction kinetics are enhanced on the active sites.

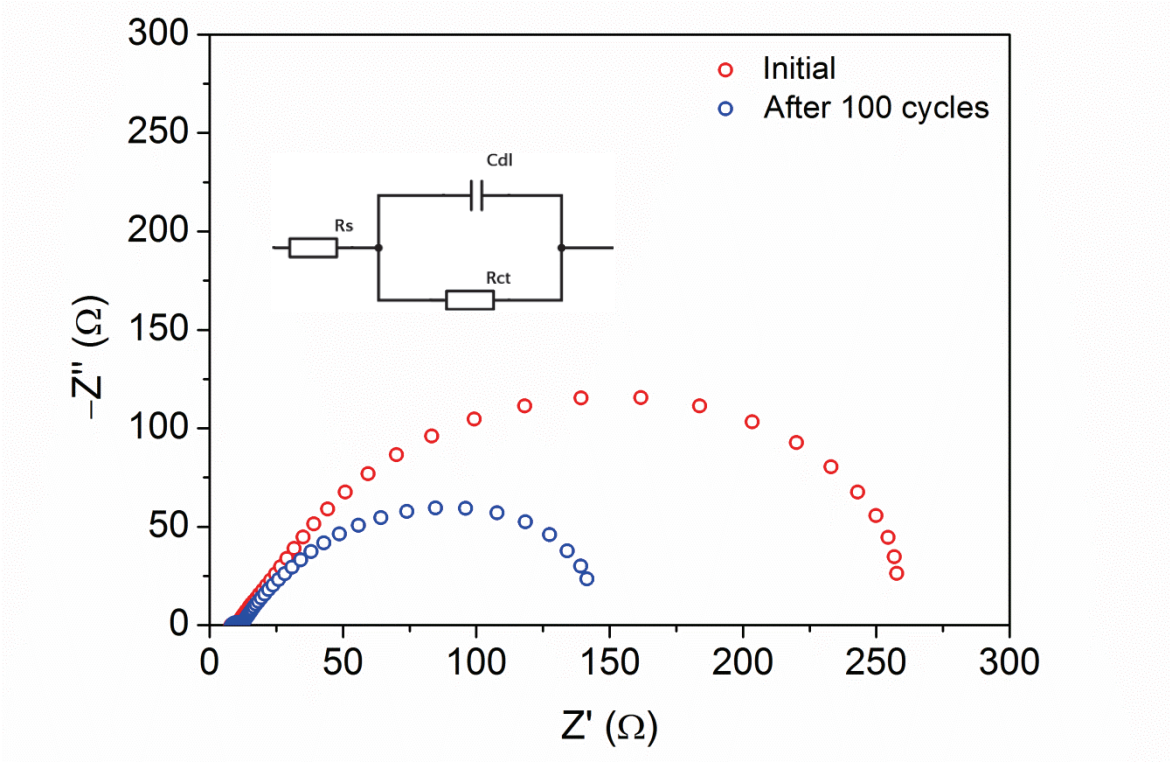

Figure 5-16: *Nyquist plots showing electrochemical impedance spectroscopy on nanocrystalline 1T'-$MoTe_2$ before and after 100 cycles. Uncompensated resistances were calculated as 8.1 and 8.3 Ω before and after 100 cycles, respectively. This corresponds well with the iR compensation function on the potentiostat which gave values of 9.8 and 10.1 Ω. The inset shows the equivalent circuit model.*

Seok *et al*. report an improvement in the Gibbs' free energy of hydrogen adsorption, ΔG_H, as hydrogen adsorption occurs on the basal plane of 1T'-$MoTe_2$.[4] Hydrogen adsorption induces electron doping and a Peierls-type lattice distortion that enhances the HER. Therefore, it is possible that reductive potential cycling is the driving force which induces further distortion, thus lowering ΔG_H to a more favourable value. This will be discussed further in Section 5.3.5.

As a result of this spontaneous lattice distortion, Seok *et al.* also propose that the traditional volcano plot analysis cannot explain the unexpected catalytic performance of 1T'-$MoTe_2$.[4] In contrast to previously reported TMDC electrocatalysts, the rate determining step of 1T'-$MoTe_2$ in the study by Seok *et al*. is the Volmer reaction, *i.e.* the electrochemical hydrogen adsorption step. A summary of the possible reaction pathways is recreated in Table 5-4. Interestingly, upon cycling nanocrystalline 1T'-$MoTe_2$, the Tafel slope increases from 68 ± 4 mV dec^{-1} to 116 ± 17 mV dec^{-1} (Figure 5-17). The activated nanocrystalline material therefore exhibits a Tafel slope similar to that obtained by Seok *et al*., thus suggesting that with continuous reductive cycling, hydrogen adsorption is becoming the rate determining step of the HER. It is therefore possible that Seok *et al.*[4] may have activated their single crystal 1T'-$MoTe_2$, however this may have been overlooked due to the deposition of platinum at such reductive potentials.[2] A comparison of the Tafel slopes obtained in this work in comparison to Seok *et al*. is shown in Table 5-5.

Table 5-4: *Summary of the possible reaction pathways occurring during the hydrogen evolution reaction.*

Volmer step	$H_3O^+ + e^- \rightarrow H_{ads} + H_2O$	Discharge step
Heyrovsky step	$H_{ads} + H_3O^+ + e^- \rightarrow H_2 + H_2O$	Electrochemical desorption step
Tafel step	$H_{ads} + H_{ads} \rightarrow H_2$	Recombination step

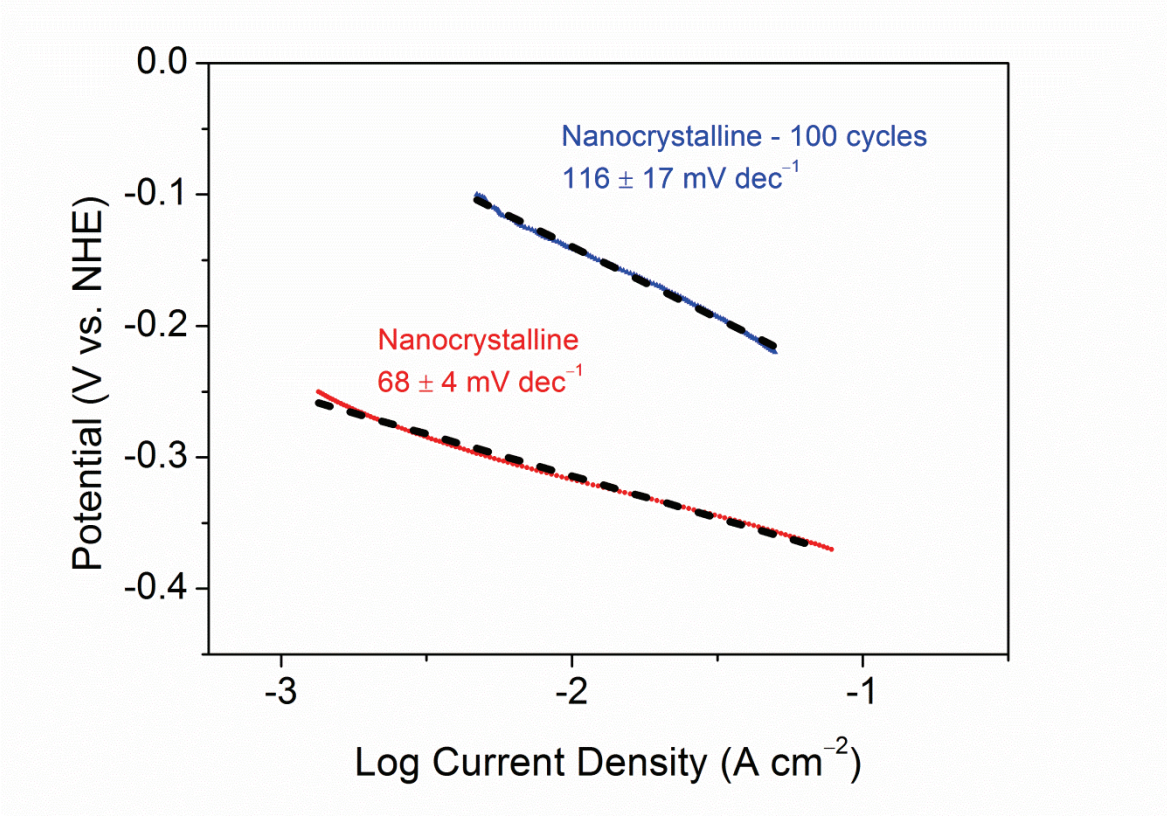

Figure 5-17: *Tafel plots and corresponding Tafel slopes of nanocrystalline 1T'-$MoTe_2$ before and after 100 cycles. Dashed lines are provided as a guide to the eye. All current densities have been corrected for resistance.*

Table 5-5: *Comparison of the Tafel slopes of 1T'-$MoTe_2$ obtained in this work and by Seok et al.*[4]

Catalyst	Tafel slope
Single crystal 1T'-$MoTe_2$ (Seok *et al.*[4])	127 mV dec^{-1}
Nanocrystalline 1T'-$MoTe_2$	68 ± 4 mV dec^{-1}
Nanocrystalline 1T'-$MoTe_2$ – 100 cycles	116 ± 17 mV dec^{-1}

This change in Tafel slope also highlights the difference in activation mechanism between 1T'-$MoTe_2$ in this work and that of TaS_2 and NbS_2 in the study by Liu *et al.*[1] In the case of TaS_2, the Tafel slope was found to decrease from 282 mV dec^{-1} to 37 mV dec^{-1} after 5000 cycles. The authors draw the conclusion that the rate determining step changes from the Volmer reaction to the Heyrovsky step as charge transfer becomes more efficient. However, as discussed above, the authors also note a thinning in sample morphology, which aids electron transfer. In the case of nanocrystalline 1T'-$MoTe_2$, the opposite effect is observed,

with the Tafel slope found to increase as the reaction progresses, and no change in morphology is observed.

In summary, as nanocrystalline 1T'-$MoTe_2$ is cycled 100 times, the overpotential improves from 320 mV to 178 mV and the charge transfer also halves in value, thus indicating more efficient reaction kinetics and an improved electrocatalytic performance. However, the Tafel slope increases with cycling, from 68 ± 4 mV dec^{-1} to 116 ± 17 mV dec^{-1} after 100 cycles. This indicates a change in the reaction mechanism, with the rate determining step of the activated material becoming the Volmer reaction *i.e.* hydrogen adsorption. As hydrogen adsorption occurs on the basal plane of 1T'-$MoTe_2$, electron doping and a spontaneous lattice distortion occurs which reportedly lowers ΔG_H to a more favourable value. Therefore, in this work, electron doping is proposed as the reason for the improved catalytic performance upon cycling nanocrystalline 1T'-$MoTe_2$.

5.3.5. Computational studies of potential reaction pathways

5.3.5.1. Hydrogen Surface Coverage

Continuing with the theory of electron doping, the effect of hydrogen surface coverage on the basal plane was explored. As reported by Seok *et al*.[4] hydrogen adsorption drives electron doping and a Peierls-type lattice distortion. With increasing number of cycles, the Tafel slope changes from 68 ± 4 mV dec^{-1} to 116 ± 17 mV dec^{-1}, thus indicating a change in the reaction mechanism from the Heyrovsky step being slow to the Volmer step (hydrogen adsorption) being rate limiting. This indicates that, as the hydrogen evolution reaction progresses, the adsorption of hydrogen on the basal plane surface becomes more difficult. Seok *et al*. calculated that hydrogen adsorption occurs on the Te α-site, and a similar approach was used in this work (see Section 5.3.5.2. for an explanation of the site-dependency). The authors also found that electron doping (through hydrogen adsorption) resulted in Peierls-type lattice distortion which improved ΔG_H by 0.16 eV. Hence, all surface coverage calculations were performed on the α-site.

In the case of nanocrystalline 1T'-$MoTe_2$, this model was extended by proposing that the distortion could be further enhanced through hydrogen adsorption on the α-site by reductive potential cycling. DFT calculations were performed to study how the amount of adsorbed hydrogen on the α-isomer would change the energy of hydrogen adsorption for the adjacent α-site as the surface coverage increases. Table 5-6 shows the energy of H_{ads} required for adsorption on the first (12.5% surface coverage), second (25% surface coverage) and third (37.5% surface coverage) α-site, respectively. Contrary to expectation (at higher coverage H-H becomes a repulsive interaction causing the energy of adsorption to increase) H_{ads} was found to decrease, *i.e.* become more favourable, until reaching a minimum at ca. 25%, at which point every other α-site is covered.

As can be seen in Figure 5-18, calculations show that once H is adsorbed on to an α-site, the ΔE_H value of the neighbouring α-site becomes more favourable. This also corroborates well with the reduction in charge transfer resistance after 100 cycles as discussed above. However, once this limiting level of hydrogen adsorption is reached, H_{ads} begins to increase, thus indicating the Volmer step (hydrogen adsorption) has become rate limiting, in line with the increase in Tafel slope.

Table 5-6: *Summary of the calculated hydrogen adsorption energies with increasing surface coverage.*

1T'-$MoTe_2$ surface coverage	**ΔE_H (eV)**
12.5%	+0.67
25%	+0.56
37.5%	+0.60

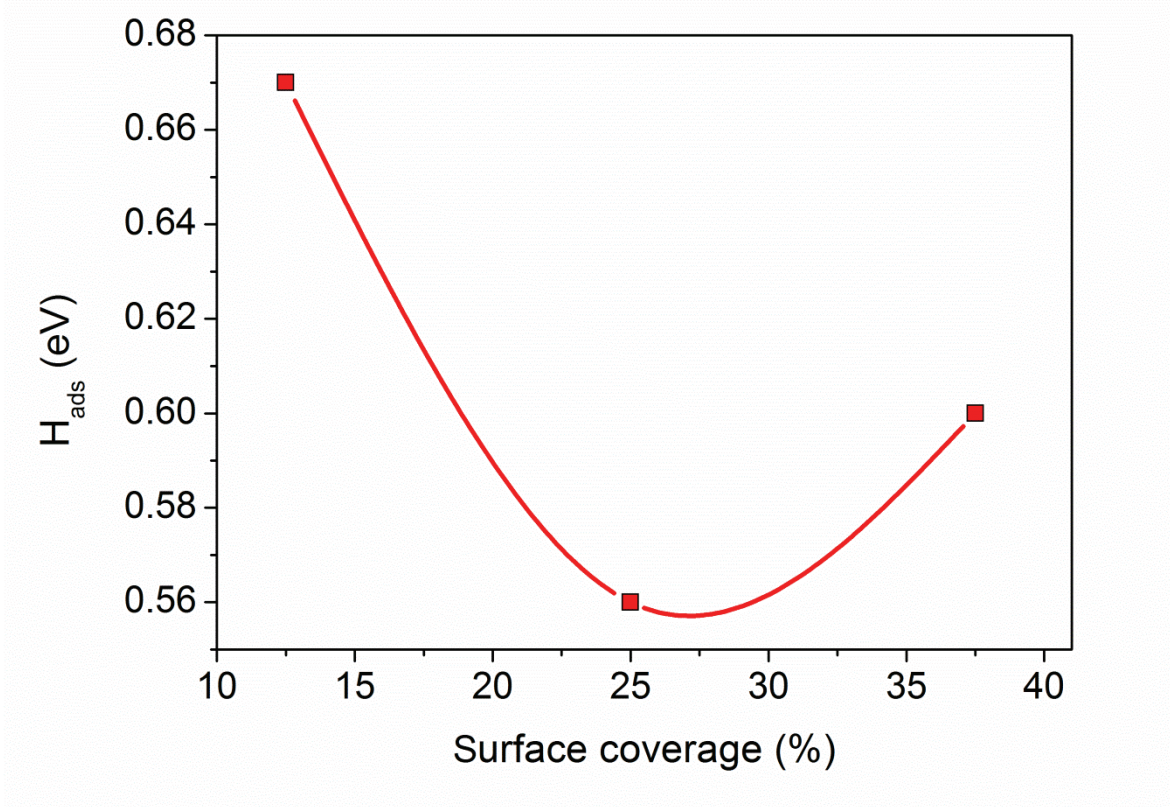

Figure 5-18: *The hydrogen adsorption energy on the α-site as a function of $MoTe_2$ surface coverage.*

5.3.5.2. Atomic-Site Dependency

Seok *et al*.[4] suggested that hydrogen adsorption (which drives electron doping) on to the Te active sites was the cause of spontaneous lattice distortion. Further, the authors calculated that the α-site, *i.e.* the low Te atomic site, showed the most favourable ΔG_H out of five possible atomic sites. In an attempt to explain the nature of the adsorption process in terms of activation in nanocrystalline 1T'-$MoTe_2$, a 2x2 supercell of a monolayer slab was adapted as the working model of 1T'-$MoTe_2$ (Figure 5-19). The α, β and ε-sites, as proposed by Seok *et al*.,[4] were investigated in addition to a new tri-haptic metal hydride 'η-site' (Figure 5-20). All of the regioisomers were investigated at a surface coverage of 12.5%. The energies of hydrogen adsorption (ΔE_H) calculated for each site is summarised in Table 5-7 and illustrated in Figure 5-21.

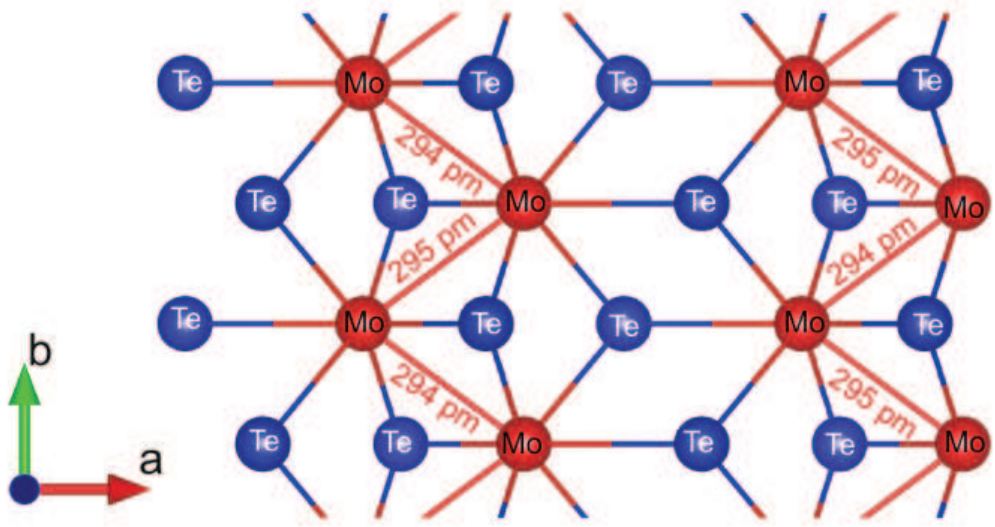

Figure 5-19: *The ab-plane projection of the optimised 2x2 unit cell of 1T'-$MoTe_2$ monolayer slab with selected calculated bond distances in pm (rev-PBE-D3/DZP + NO). The ADF-Band version 2017.113 software package was used for the in silico analysis of the catalyst hydrogenation process. The Perdew, Burke and Ernzerhof generalised gradient approximate density functional was employed throughout the calculations with the addition of Grimme's third generation dispersion correction (rev-PBE-D3). A combination of Herman-Skillman numerical atomic orbitals (NAOs) with triple zeta polarised (TZP) Slater type orbitals were used for all the heavy atoms, whereas for hydrogen a double zeta polarised (DZP) augmentation was used. Further details of computational studies are discussed in Chapter 2.*

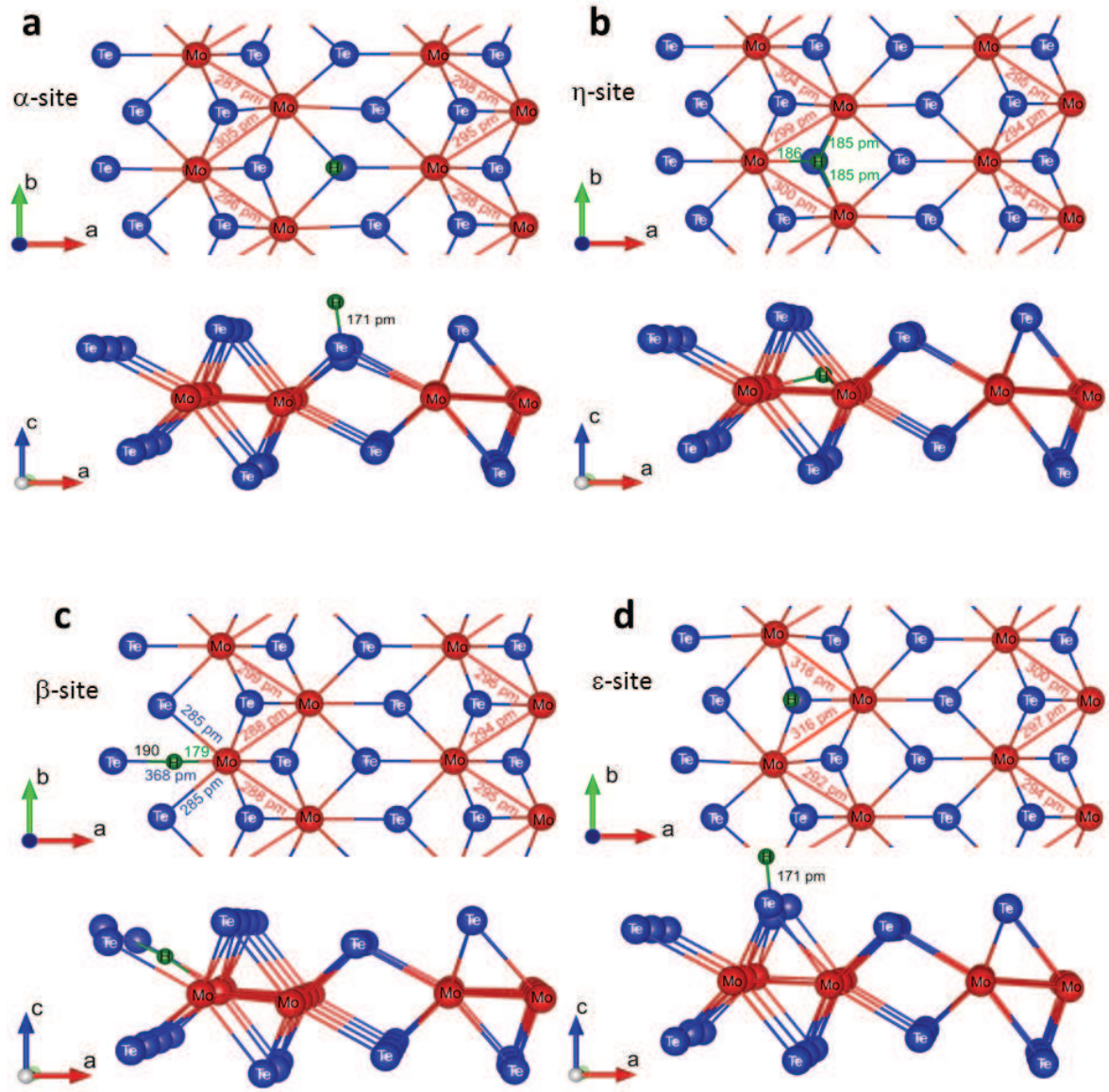

Figure 5-20: *Optimised structures and bond distances (pm) of the regioisomers of* $^{2}_{\infty}[MoTe_2H_{0.125}]$ *(2x2 unit cell) with hydrogen adsorbed at* ***(a)*** *α-site,* ***(b)*** *η-site,* ***(c)*** *β-site and* ***(d)*** *ε-site. Mo atoms are shown in red, Te atoms in blue and H atoms in green.*

Table 5-7: *Hydrogen adsorption energies of various atomic sites.*

Surface	ΔE_H (eV)	Reference
α-$MoTe_2H_{0.125}$	+0.67	This work[14]
α-$MoTe_2H_{0.250}$	+0.56	This work[14]
β-$MoTe_2H_{0.125}$	+0.92	This work[14]
ε-$MoTe_2H_{0.125}$	+1.73	This work[14]
η-$MoTe_2H_{0.125}$	+0.58	This work[14]
α-$MoS_2H_{0.125}$	–0.13	[15]
Pt_3H	–0.40	[16]

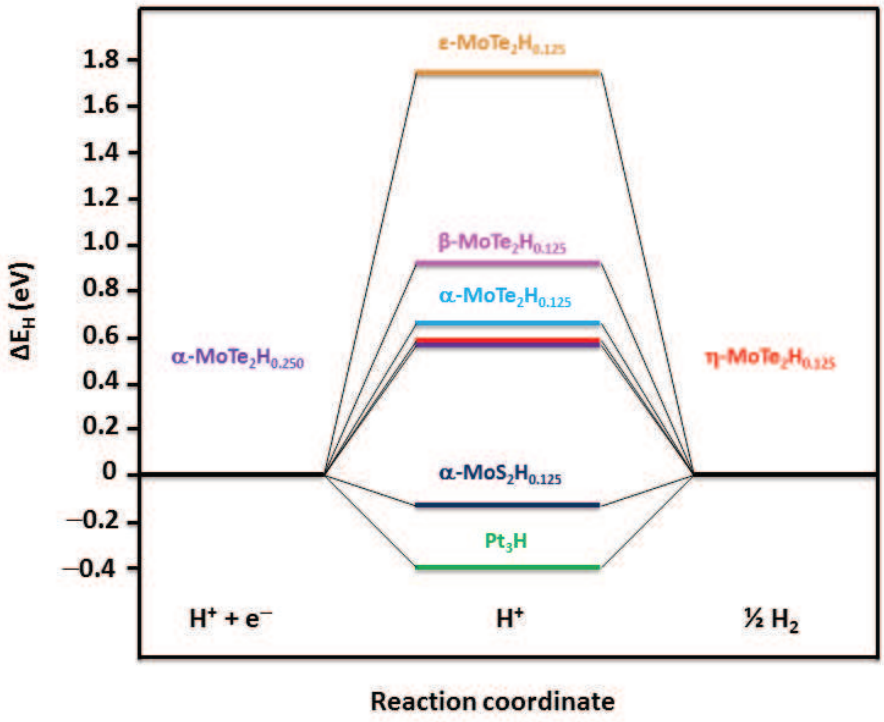

Figure 5-21: *Comparison of ΔE_H (eV) values at various H-bonding sites.*

In agreement with Seok *et al.*,[4] the much higher adsorption energies of the β- and ε-sites mean that these sites can be excluded as being the main catalytically active sites of nanocrystalline 1T'-$MoTe_2$. The η-site shows the most favourable hydrogen adsorption energy of ΔE_H = +0.58 eV, thus implying that the η-site is the primary active site. However, this contradicts experimental evidence. As the η-site involves the formation of a tri-haptic metal hydride, adsorption of hydrogen would thus occur on Mo active sites. Therefore, one would expect an improvement in catalytic performance in a Te-deficient 1T'-$MoTe_2$ when

additional Te vacancies are created, similar to the mechanism proposed for the 1T-MoS_2 analogue.[15] To test this hypothesis, a Te-deficient nanocrystalline 1T'-$MoTe_2$ was synthesised using an identical procedure to that of the stoichiometric material, with a 10% decrease in number of moles of Te used. Figure 5-22 shows the PXRD pattern of this Te-deficient material to be identical to that of stoichiometric nanocrystalline 1T'-$MoTe_2$. It should be noted that no elemental analysis was performed on this Te-deficient material, and is therefore only speculatively labelled 1T'-$MoTe_{1.8}$. Upon electrochemical cycling, the Te-deficient material does indeed show an overpotential improvement, however, the extent to which it improves is limited. As can be seen in Figure 5-23, the $MoTe_{1.8}$ material only improves from –320 mV to –230 mV. Therefore, hydrogen adsorption appears to occur on Te sites, thus the α-site was deemed the active site for nanocrystalline 1T'-$MoTe_2$.

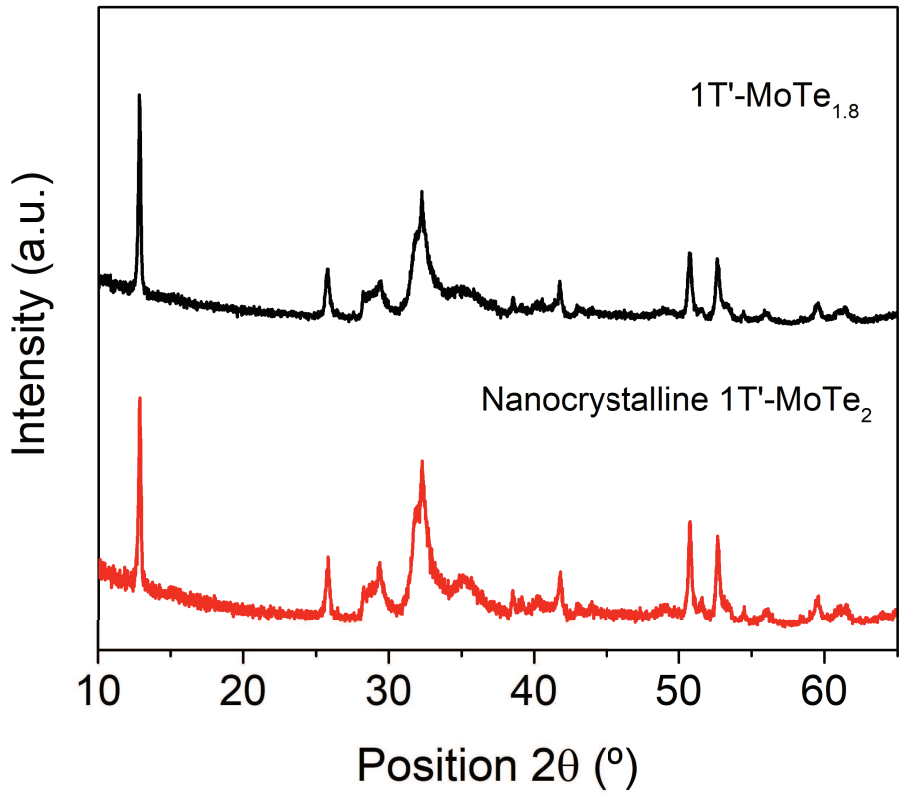

Figure 5-22: *PXRD patterns of stoichiometric nanocrystalline 1T'-$MoTe_2$ (bottom) and Te-deficient '1T'-$MoTe_{1.8}$' (top).*

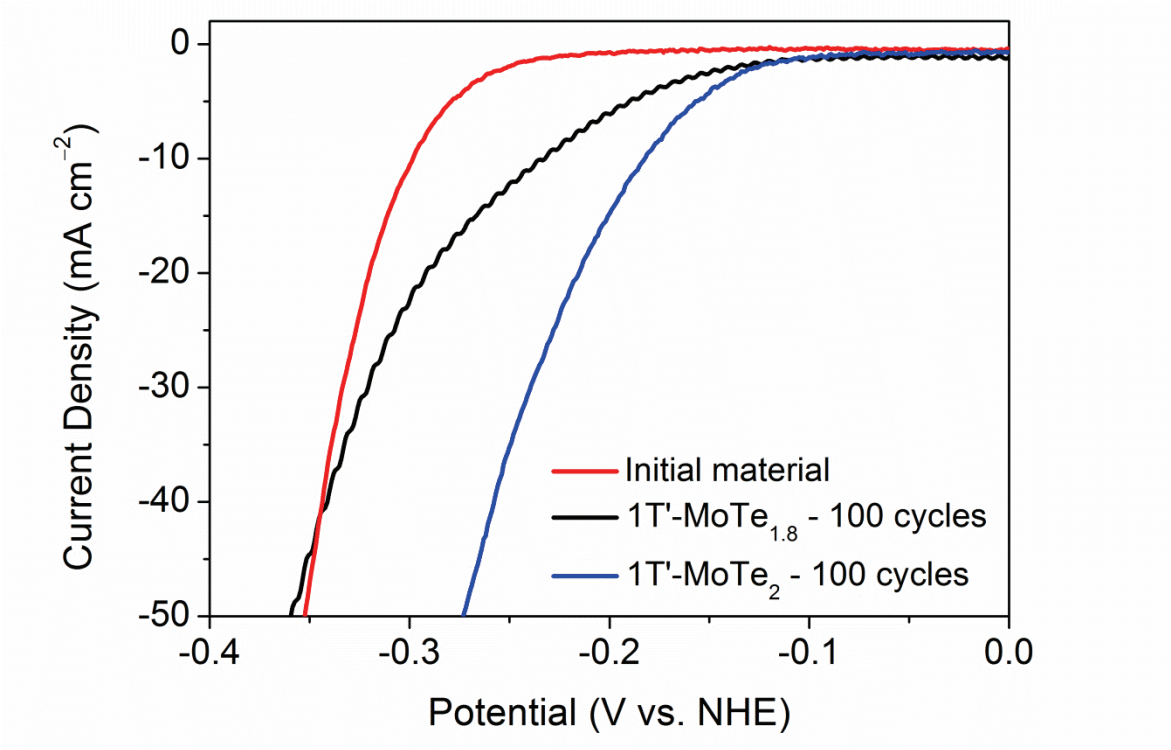

Figure 5-23: *Comparison of the current densities achieved by stoichiometric nanocrystalline 1T'-$MoTe_2$ before (red) and after 100 cycles (blue) and Te-deficient $MoTe_{1.8}$ after 100 reductive cycles (black).*

5.3.5.3. Limits of the Conventional Volcano Plot

The exchange current density is the current density measured at 0 mV (vs. NHE), *i.e.* when the hydrogen evolution reaction is at equilibrium. Trasatti's volcano plot correlates the exchange current density with the chemisorption energy of hydrogen, thus allowing for the identification of possible HER electrocatalysts.[17] The ascending slope of the volcano plot, *i.e.* $\Delta G_H < 0$ eV, represents metals which bond to hydrogen too strongly, thus the exchange current decreases with decreasing ΔG_H due to a lack of H recombination. The descending slope, *i.e.* $\Delta G_H > 0$ eV, represents metals which bond hydrogen too weakly, thus proton transfer is limited. In this case, the exchange current decreases with increasing ΔG_H. Platinum lies at the apex of the volcano, the point at which the reaction steps (Volmer and Heyrovsky or Tafel reactions) are thermo-neutral, *i.e.* hydrogen is neither bonded too strongly nor too weakly.[16] As such, platinum is currently the best performing HER electrocatalyst. Thus, one would expect a catalyst with a similar exchange current density to platinum to also be close to thermo-neutral. In this context, the closer the H adsorption energy is to zero, the greater the activity of the catalyst.

However, computational data obtained for activated nanocrystalline 1T'-$MoTe_2$ (after 100 cycles) contradicts this. In the case of nanocrystalline 1T'-$MoTe_2$, the exchange current density was obtained by extrapolation of the Tafel slope to 0 mV and shows a substantial improvement upon cycling. In fact, the exchange current density of the activated sample shows a value similar to that of platinum, although the Tafel slope indicates that a different reaction mechanism takes place. Despite having an exchange current density similar to platinum, the energy of hydrogen adsorption is rather high (+0.56 eV). The values of the initial and activated 1T'-$MoTe_2$ materials are summarised in Table 5-8 and are compared with calculated values for 1T-MoS_2 and Pt (111). The value of ΔE_H for activated 1T'-$MoTe_2$ is in line with that of the α-site obtained by Seok *et al*., as the authors noted a high positive energy of $\Delta E_H = +0.55$ eV.[4] The authors also noted a high exchange current density of –4.67 A cm^{-2}, which would place the catalytic activity of 1T'-$MoTe_2$ out with the conventional volcano plot. Their explanation was that Peierls-type lattice distortion (driven by hydrogen adsorption and consequently electron doping) leads to more favourable HER kinetics, and that the conventional volcano plot does not take structural distortions into account. This theory was extended for nanocrystalline 1T'-$MoTe_2$ by proposing that the distortion could be further enhanced through adsorption of hydrogen on the α-site by reductive potential cycling. Thus, the conventional volcano plot cannot explain the high experimental exchange

current density values of 1T'-$MoTe_2$, and is thus limited for TMDCs.

Table 5-8: *Hydrogen adsorption energy relationship to the logarithm of exchange current density.*

Surface	ΔE_H (eV)	Log i_0 (A cm^{-2})	Tafel slope (mV dec^{-1})	Ref.
Nano 1T'-$MoTe_2$	+0.67	–6.99	68	This work[14]
Nano 1T'-$MoTe_2$ – 100 cycles	+0.56	–3.30	116	This work[14]
Single crystal 1T'-$MoTe_2$	+0.55	–4.67	127	[13]
1T-MoS_2	–0.13	–4.90	48	[15]
Pt_3H	–0.40	–3.34	30	[16]

5.4. Conclusions

In conclusion, this chapter has focused on the dramatic enhancement of catalytic activity of nanocrystalline 1T'-$MoTe_2$, and sought to explore the origin of this activation. Upon reductive potential cycling, the overpotential required for $j = -10$ mA cm^{-2} was found to improve from 320 ± 12 mV to 178 ± 8 mV after 100 cycles. This lower overpotential remained stable for as long as the cathodic bias was maintained (1000 cycles). Once the application of potential was stopped, the overpotential was found to revert back to its original value of 320 mV. This work therefore demonstrates the first reversible activation of a TMDC electrocatalyst for the HER.

In an attempt to understand this enhanced catalytic activity, several characterisation techniques have shown that the improved performance is not structural or morphological in origin. Instead, the enhancement is proposed to be due to the activation of the basal plane sites with continuous potential cycling. Computational studies suggest that the activation is electronic in nature, and is a result of electron doping under an applied reductive bias which drives lattice distortion thus resulting in a more favourable energy of hydrogen adsorption. This is corroborated by DFT calculations which show that hydrogen adsorption on a Te α-site lowers the ΔE_H value of the neighbouring α-site. Thus, activation of the basal plane has been shown to substantially improve the electrocatalytic performance of nanocrystalline 1T'-$MoTe_2$. Thus, this study provides the ground work for optimising the HER activity of $MoTe_2$, which may also be applicable to other metallic TMDCs.

5.5. References

1. Liu, Y., Wu, J., Hackenberg, K. P., Zhang, J., Wang, Y. M., Yang, Y., Keyshar, K., Gu, J., Ogitsu, T., Vajtai, R., Lou, J., Ajayan, P. M., Wood, B. C. & Yakobson, B. I. Self-optimizing, highly surface-active layered metal dichalcogenide catalysts for hydrogen evolution. *Nat. Energy* **2** (2017).

2. Seok, J., Lee, J-H., Bae, D., Ji, B., Son, Y-W., Lee, Y. H., Yang, H. & Cho, S. Hybrid catalyst with monoclinic $MoTe_2$ and platinum for efficient hydrogen evolution. *APL Mater.* **7**, (2019).

3. Li, G., Zhang, D., Yu, Y., Huang, S., Yang, W. & Cao, L. Activating MoS_2 for pH-Universal Hydrogen Evolution Catalysis. *J. Am. Chem. Soc.* **139**, 16194-16200 (2017).

4. Seok, J., lee, J-H., Cho, S., Ji, B., Won Kim, H., Kwon, M., Kim, D., Kim, Y-M., Ho Oh, S., Wng Kim, S., Hee Lee, Y., Son, Y-W. & Yang, H. Active hydrogen evolution through lattice distortion in metallic $MoTe_2$. *2D Mater.* **4**, 25061 (2017).

5. Dong, G., Fang, M., Wang, H., Yip, S., Cheung, H-Y., Wang, F., Wong, C-Y., Chu, S. T. & Ho, J. C. Insight into the electrochemical activation of carbon-based cathodes for hydrogen evolution reaction. *J. Mater. Chem. A* **3**, 13080–13086 (2015).

6. Tavakkoli, M., Holmberg, N., Kronberg, R., Jiang, H., Sainio, J., Kauppinen, E. I., Kallio, T. & Laasonen, K. Electrochemical Activation of Single-Walled Carbon Nanotubes with Pseudo-Atomic-Scale Platinum for the Hydrogen Evolution Reaction. *ACS Catal.* **7**, 3121–3130 (2017).

7. McGlynn, J. C., Cascallana-Matías, I., Fraser, J. P., Roger, I., McAllister, J., Miras, H. N., Symes, M. D. & Ganin, A. Y. Molybdenum Ditelluride Rendered into an Efficient and Stable Electrocatalyst for the Hydrogen Evolution Reaction by Polymorphic Control. *Energy Technol.* **6**, 345–350 (2018).

8. Roger, I. & Symes, M. D. Silver Leakage from Ag/AgCl Reference Electrodes as a Potential Cause of Interference in the Electrocatalytic Hydrogen Evolution Reaction. *ACS Appl. Mater. Interfaces* **9**, 472–478 (2017).

9. Zhou, L., Zubair, A., Wang, Z., Zhang, X., Ouyang, F., Xu, K., Fang, W., Ueno, K., Li, J., Palacios, T., Kong, J. & Dresselhaus, M. S. Synthesis of High-Quality Large-

Area Homogenous 1T′-$MoTe_2$ from Chemical Vapor Deposition. *Adv. Mater.* **28**, 9526–9531 (2016).

10. Li, Y., Duerloo, K. A. N., Wauson, K. & Reed, E. J. Structural semiconductor-to-semimetal phase transition in two-dimensional materials induced by electrostatic gating. *Nat. Commun.* **7**, 10671 (2016).

11. Zhang, C., KC, S., nie, Y., Liang, C., Vandenberghe, W. G., Longo, R. C., Zheng, Y., Kong, F., Hong, S., Wallace, R. M. & Cho, K. Charge Mediated Reversible Metal−Insulator Transition in Monolayer $MoTe_2$ and $W_xMo_{1-x}Te_2$ Alloy. *ACS Nano* **10**, 7370-7375 (2016).

12. Wang, Y., Xiao, J., Zhu, H., Li, Y., Alsaid, Y., Fong, K. Y., Zhou, Y., Wang, S., Shi, W., Wang, Y., Zettle, A., Reed, E. J. & zhang, X. Structural phase transition in monolayer $MoTe_2$ driven by electrostatic doping. *Nature* **550**, 487–491 (2017).

13. Seok, J., lee, J-H., Cho, S., Ji, B., Won Kim, H., Kwon, M., Kim, D., Kim, Y-M., Ho Oh, S., Wng Kim, S., Hee Lee, Y., Son, Y-W. & Yang, H. Active hydrogen evolution through lattice distortion in metallic $MoTe_2$. *2D Mater.* **4**, 25061 (2017).

14. McGlynn, J. C., Dankwort, T., Kienle, L., Bandeira, N. A. G., Fraser, J. P., Gibson, E. K., Cascallana-Matías, Kamarás, K., Symes, M. D., Miras, H. N. & Ganin, A. Y. The rapid electrochemical activation of $MoTe_2$ for the hydrogen evolution reaction. *Nat. Commun.* **10**, 4916 (2019).

15. Yin, Y., Han, J., Zhang, Y., Zhang, X., Xu, P., Yuan, Q., Samad, L., Wang, X., Wang, Y., Zhang, Z., Zhang, P., Cao, X., Song, B. & Jin, S. Contributions of Phase, Sulfur Vacancies, and Edges to the Hydrogen Evolution Reaction Catalytic Activity of Porous Molybdenum Disulfide Nanosheets. *J. Am. Chem. Soc.* **138**, 7965–7972 (2016).

16. Nørskov, J. K., Bligaard, T., Logadottir, A., Kitchin, J. R., Chen, J. G., Pandelov, S. & Stimming, U. Trends in the Exchange Current for Hydrogen Evolution. *J. Electrochem. Soc.* **152**, J23–J26 (2005).

17. Trasatti, S. Work function, electronegativity, and electrochemical behaviour of metals. II. Potentials of zero charge and ‘electrochemical’ work functions. *J. Electroanal. Chem.* **33**, 351–378 (1971).

6. Exploration of the Activation Mechanism

In previous chapters, investigations indicated that the electrochemical activation of nanocrystalline 1T'-$MoTe_2$ is electronic in origin. Further, DFT suggests that electron doping, driven by hydrogen adsorption, resulting in a lattice distortion is the origin of the improved electrocatalytic activity. In this chapter further investigation into the nature of the activation is presented. Thus, this chapter seeks to delve deeper into the activation mechanism, by initially explaining the gradual nature of the enhancement, followed by *in operando* Raman and XAS studies in attempt to detect any structural changes that may not be observed *ex-situ*. Subsequently, alternative theories for gradual enhancement such as the removal of oxide layer species and re-oxidation of the sample are explored. Ultimately, experimental evidence supports that the activation mechanism occurs on the basal plane of nanocrystalline 1T'-$MoTe_2$.

6.1. Introduction

6.1.1. Methods of Activation

Expanding on the literature discussion presented in Chapter 5, several studies report differing electrochemical activation mechanisms, although none appear to apply to nanocrystalline 1T'-$MoTe_2$. In the case of TaS_2 and NbS_2, Liu *et al.*[1] report a change in catalyst morphology as the reason for enhanced activity. However, the reversible nature of nanocrystalline 1T'-$MoTe_2$, which is the first of its kind to be reported,[2] rules out changes in morphology and composition as the source of activation.

On the other hand, Li *et al.*[3] evidence the p-doping of 2H-MoS_2 by Raman spectroscopy and PXRD. The authors observe a shift in Raman peak which indicates the intercalation of protons between the interlayer spacing of MoS_2. This is further confirmed by PXRD which shows a slight shift in *d* spacing, therefore indicating a lattice expansion. These results are obtained *ex-situ*, meaning that the protons remain intercalated between the layers for a period of time, and indicates that the activation of 2H-MoS_2 is irreversible. Contrastingly, no such shifts are observed in the case of nanocrystalline 1T'-$MoTe_2$ when measured *ex-situ*.[2] Moreover, it is important to note that in the study by Li *et al.*, an internal standard is not used, hence any observable shifts may be deceiving.[3] The reversible nature of this activation, however, may imply that structural changes only occur *in operando*. Thus, in order to gain

a clear understanding of the activation of nanocrystalline 1T'-$MoTe_2$, electrochemical studies must be conducted *in operando*.

While the study by Li *et al.*[3] provides an interesting theory, it should be noted that their activation occurs in the semiconducting 2H-phase of MoS_2. No such activation is observed in the case of semiconducting 2H-$MoTe_2$, further validating the hypothesis that the activation of $MoTe_2$ is electronic in origin.[2] Nonetheless, the activation of nanocrystalline 1T'-$MoTe_2$ displays one similar quality to the two mechanisms described above: the activation is a gradual process. Li *et al*.[3] attribute the gradual nature of the activation process to be due to the sample morphology, with samples films requiring more cycles than flakes. Additionally, flakes of a larger size required more cycles than those of smaller size, thus confirming that the morphology plays an important role in the activation. Similar studies have also shown that the number of layers have a profound effect on the catalytic activity of MoS_2, with the activity increasing with decreasing number of layers.[4] Therefore, from these studies, it is likely that the number of cycles required for activation is dependent on the sample morphology.

6.1.2. The Role of Oxygen

As discussed in Chapter 3, the $MoTe_2$ materials are covered by a layer of surface oxides, as evidenced by XPS. These oxides are commonly observed in TMDC electrocatalysts, and are removed by performing cyclic voltammetry under reducing conditions in acidic media.[5] However, a possible theory for the electrochemical activation of nanocrystalline 1T'-$MoTe_2$ is that the surface oxides are gradually removed with increasing cycle number, thus revealing the true catalytic material. A similar theory has been proposed in the literature for amorphous molybdenum sulfide, whereby MoS_3 is a 'pre-catalyst' and is reduced to the active component by electrochemical cycling.[6–8]

In the same vein, one may argue that the presence of oxygen on the surface of 1T'-$MoTe_2$, as evidenced by XPS, may mask the true catalytic activity of the nanocrystalline material. Surface oxides have been previously reported to inhibit the catalytic activity of TMDC catalysts, and tellurides are known to be oxidised more readily than other TMDCs.[9,10] Thus, the role of oxygen needs to be studied in order to determine its effect (or lack of) on the electrocatalytic activity.

6.2. Aims

The reversible nature of the electrochemical activation of nanocrystalline 1T'-$MoTe_2$ has thus far been attributed to electron doping as a result of hydrogen adsorption. However, in order to confirm this theory as the most plausible explanation, several alternative means of activation must be considered. As such, this chapter seeks to explain the gradual nature of electrochemical activation, and further investigates possible alternative routes to the activated material.

6.3. Results and Discussion

6.3.1. Gradual Activation

The previous chapter proposed that the electrochemical activation of nanocrystalline 1T'-$MoTe_2$ is due to electron doping as a result of hydrogen adsorption on the basal plane surface, which in turn induces a Peierls-type lattice distortion. Despite literature reports requiring an excess of 5000 cycles in order to reach the limit of their activation,[1,3,11] these studies offer alternative explanations for their activation mechanisms, *e.g.* morphological changes. Accordingly, the authors show no evidence of a reversible activation. The reversible nature of the activation of nanocrystalline 1T'-$MoTe_2$ suggests a different mechanism entirely, with electron doping being the proposed method. However, if electron doping is indeed the reason for the activation then the process appears to be rather slow, with 100 cycles being required in order to reach the improved overpotential of 178 mV.

In the case of molecular materials, the effect of electron doping would be instantaneous; hence the improved overpotential would be obtained immediately upon cycling. Thus, the slow cathodic response is initially surprising. However, nanocrystalline 1T'-$MoTe_2$ is a bulk freestanding material, which raises issues of limitation by electrochemical processes such as diffusion and double layer formation. This is perhaps most notably evidenced by the activation of crystalline 1T'-$MoTe_2$ (as discussed in Chapter 5) which is hindered due to its considerably lower surface area. These electrochemical processes must be overcome in order to drive hydrogen adsorption; therefore a sufficient energy input must be applied. Upon application of a sufficiently large potential, the catalyst will indeed be 'activated' quickly. For example, chronoamperometry measurements at a large reductive potential for a short period of time would result in a faster activation. However, when a constant potential of –500 mV (vs. NHE) was applied to nanocrystalline 1T'-$MoTe_2$ (*i.e.* the most reductive potential used when electrochemically cycling) the catalyst lost contact with the glassy carbon substrate. Hence, this potential was found to be too reductive for prolonged periods of time.

Instead, a potential of –400 mV (vs. NHE) was applied. However, this potential could only be held for approximately one minute before the catalyst began to flake off of the electrode. Regardless, comparing the polarisation curves before and after chronoamperometry at –400 mV (vs. NHE) for one minute resulted in an overpotential improvement from 320 mV to 220 mV at $j = -10$ mA cm^{-2} (Figure 6-1). At these reductive potentials of –500 mV and –400

mV (vs. NHE) an increasingly large volume of hydrogen bubbles are produced with time, most likely causing the catalyst to lose contact with the glassy carbon substrate.

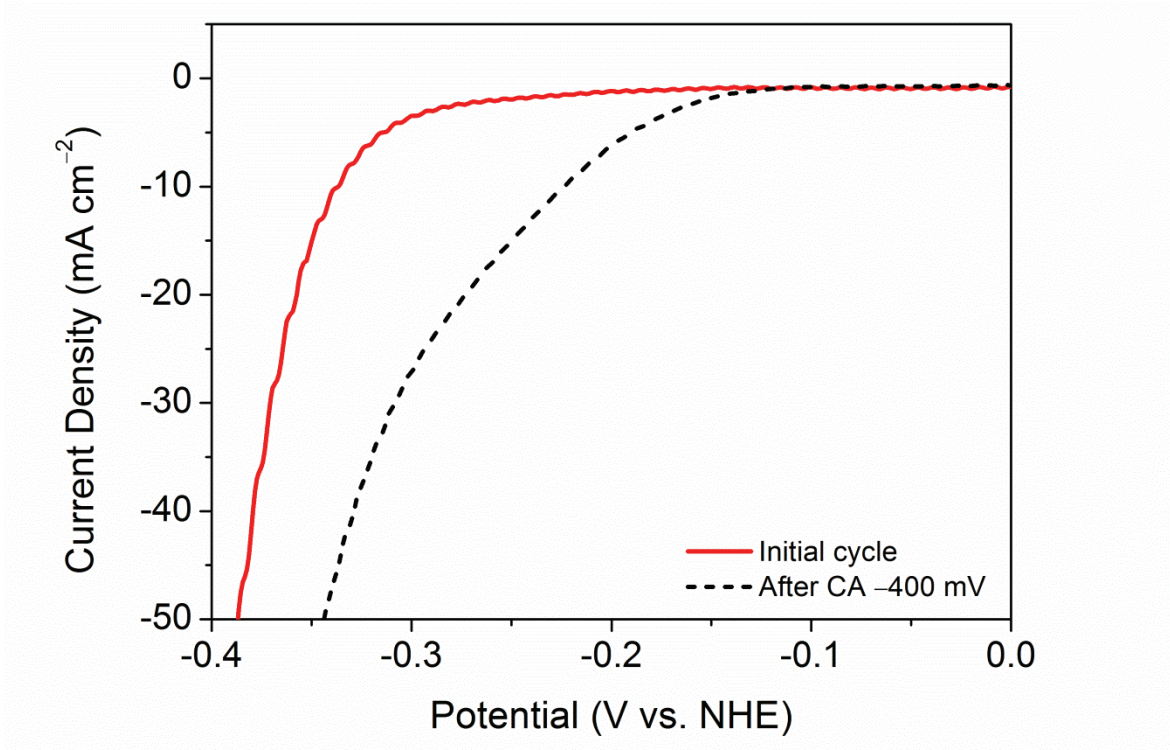

Figure 6-1: *Comparison of the current densities achieved by nanocrystalline 1T'-$MoTe_2$ before and after chronoamperometry (CA) measurements with an applied potential of –400 mV (vs. NHE) for one minute in 1 M H_2SO_4.*

To combat this, cyclic voltammetry can strategically be used in place of chronoamperometry. Sweeping the voltage to sufficiently more reductive potentials enables high current densities to be reached in a pulsing manner, and hence diffusion-limitations can be overcome, all the while maintaining contact between the catalyst and substrate. In this manner, a compromise is reached between the speed of activation and the energy input applied. Thus, due to the sweeping nature of cyclic voltammetry, the slow cathodic response is unsurprising.

Therefore, the optimum conditions of activation were found to be 100 cycles in the potential range of +0.2 V and –0.5 V (vs. NHE). In support of the gradual activation process, the improvement in overpotential can be visualised with increasing number of cycles. Figure 6-2 shows the polarisation curves of nanocrystalline 1T'-$MoTe_2$ after 25, 50 and 100 cycles, and the overpotential required for $j = -10$ mA cm^{-2} can be seen to improve with each interval. Likewise, the Tafel slope was also found to gradually increase with cycle number, thus

highlighting the change in reaction mechanism from Heyrovsky-limiting to Volmer-limiting (Figure 6-3).

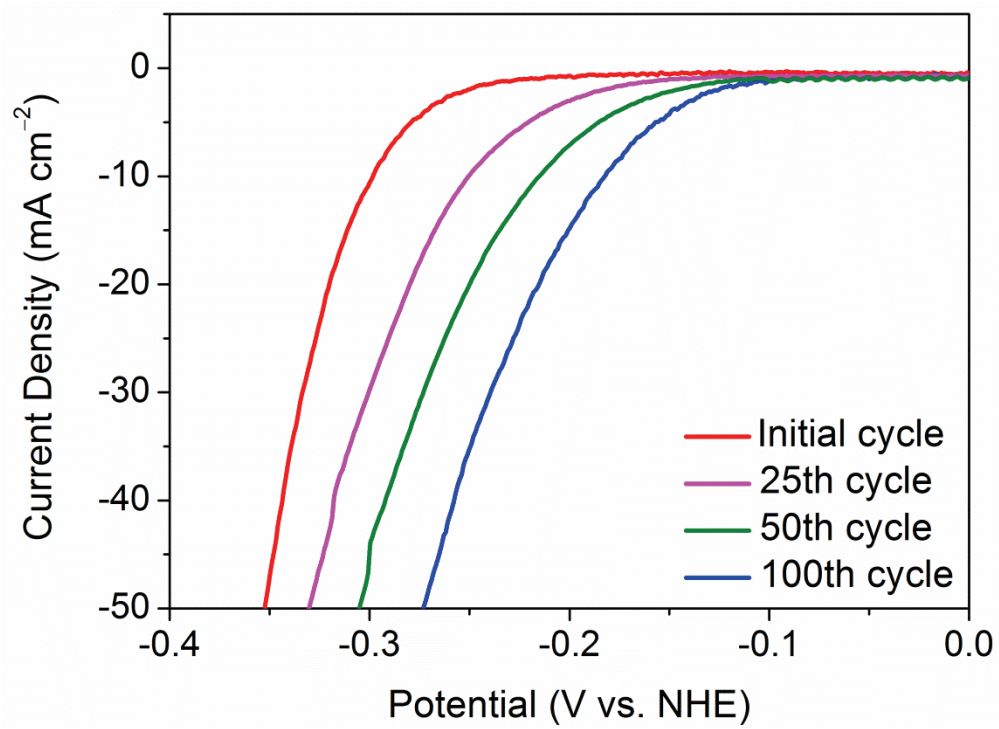

Figure 6-2: *Comparison of the current densities achieved by nanocrystalline 1T'-$MoTe_2$ after sweeping between the potential range of +0.2 V and –0.5 V (vs. NHE) for 25, 50 and 100 cycles in 1 M H_2SO_4.*

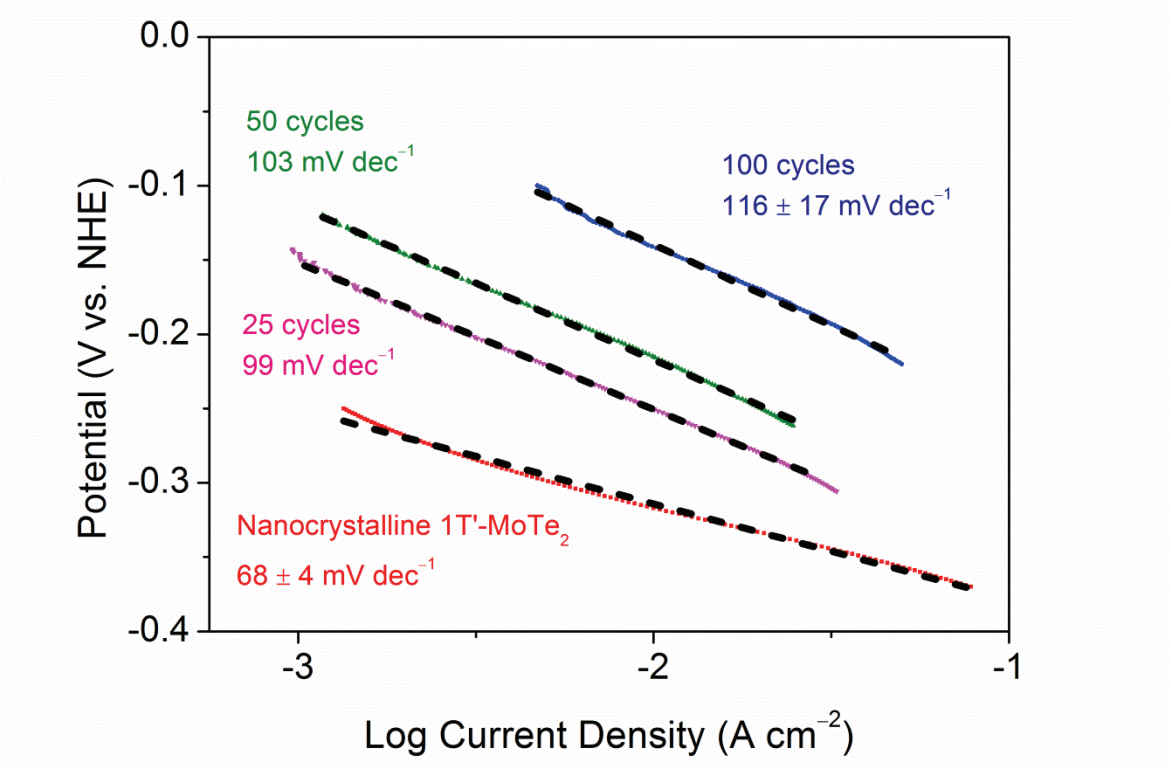

Figure 6-3: *Tafel plots and corresponding Tafel slopes of nanocrystalline 1T'-$MoTe_2$ before and after 25, 50 and 100 cycles between +0.2 V and –0.5 V (vs. NHE). Dashed lines are provided as a guide to the eye. All current densities have been corrected for resistance.*

Further evidence of a sufficient activation energy required to overcome the limiting electrochemical processes is provided by narrowing the potential range at which the catalyst is swept. Narrowing the applied potential range to between +0.2 V and –0.4 V (vs. NHE) results in the material becoming only partially activated after 100 cycles, *i.e.* far more than 100 cycles would be required in order to reach the improved overpotential of 178 mV. Figure 6-4 shows the overpotential improvement of nanocrystalline 1T'-$MoTe_2$ after 100 cycles when the potential range is narrowed (+0.2 V and –0.4 V (vs. NHE)) compared with that of the optimum cycling range (+0.2 V and –0.5 V (vs. NHE)). Therefore, this study concludes that the overpotential improvement is gradual since the speed of activation is controlled by the choice of experimental parameters, with potential range and number of cycles being the determining factors.

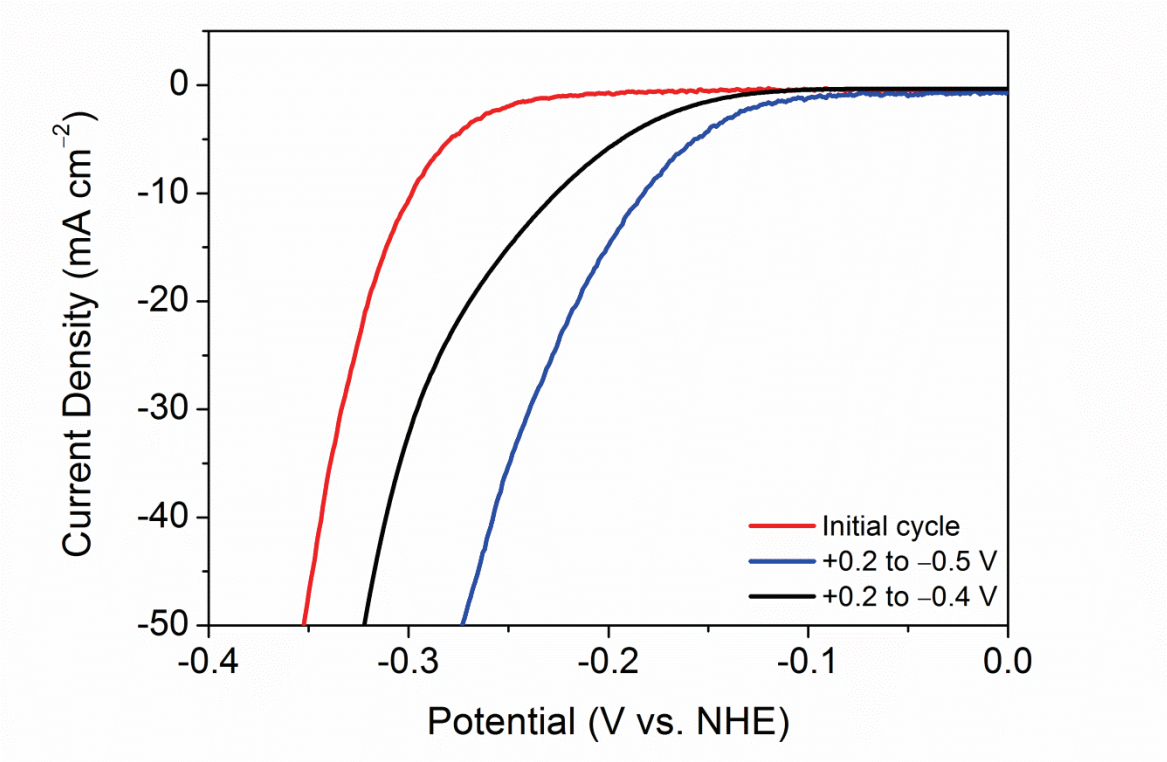

Figure 6-4: *Comparison of the current densities achieved by nanocrystalline 1T'-$MoTe_2$ after cycling the potential 100 times between +0.2 V and –0.5 V (blue); and +0.2 V and –0.4 V (black) (vs. NHE) in 1 M H_2SO_4.*

6.3.2. *In Operando* Studies

6.3.2.1. *In Operando* Raman Cell

Continuing with the theory of electron doping by hydrogen adsorption, attempts were made to study the activation method by *in operando* Raman spectroscopy. To do this, an *in situ* Raman cell was required. The cell was fabricated using materials available in the lab, and is depicted in Figure 6-5. The cell consisted of a screw cap with an aperture, fitted with a septum. In order to prevent any contamination and / or degradation of the screw cap in the 1 M H_2SO_4 electrolyte, the thread of a concentrated sulfuric acid bottle was cut to size to precisely fit within the walls of the cap. The glassy carbon working electrode and platinum counter electrodes were pierced through the septum in the up-turned position. The reference electrode was then positioned accordingly. Sulfuric acid was filled to a level at which the catalyst is covered by a thin layer of electrolyte. Using this experimental set up, the position of the working electrode remains fixed. In this way, the *in operando* activation of nanocrystalline 1T'-$MoTe_2$ can be studied by Raman spectroscopy.

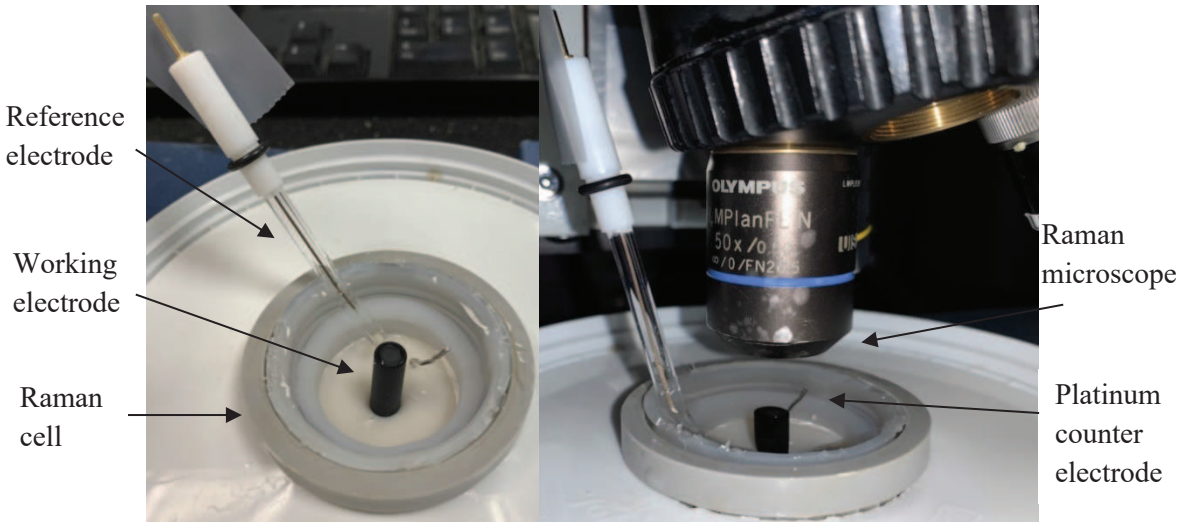

Figure 6-5: *Fabricated in operando Raman cell consisting of a screw cap with aperture to fit a septum. Glassy carbon is used as the working electrode and platinum wire as the counter, both of which are up-turned and pierced through the septum. 3 M Ag/AgCl is used as the reference and 1 M H_2SO_4 is the electrolyte.*

In operando Raman measurements were performed in 1 M H_2SO_4 with a catalyst deposited glassy carbon working electrode, 3 M Ag/AgCl reference electrode and Pt wire counter electrode. The Raman cell was fixed in position and the sample area was focused prior to electrochemical measurements. Each measurement was taken with a 1% filter, a 100 μm aperture hole, and run for 5 seconds with 5 repeats. In this way, a clear A_g mode corresponding to 1T'-$MoTe_2$ was observed each time without any degradation into Te.

The potential range was swept between +0.2 V and –0.4 V (vs. NHE) in order to avoid the generation of an excessive amount of bubbles at the catalyst surface, which may hinder the measurement. The potential was swept for 100 cycles, and the Raman spectra were collected during the 1st, 20th, 40th, 60th, 80, and 100th cycle. Figure 6-6 shows the corresponding Raman spectra, focusing on the A_g peak at 161 cm^{-1}. During the first 40 cycles, the intensity of this A_g peak increases, however, by the 60th cycle, a noticeable shift in peak position is observed. The A_g mode blue-shifts from ~161 cm^{-1} to ~163 cm^{-1}. This peak shift is maintained for the remainder of the activation process. The intensity of the peak, however, decreases as the number of cycles approaches 100. It is possible that this difference in intensity is the result of hydrogen bubbles forming on the electrode surface, which may affect the focus of the Raman microscope on the catalyst sample.

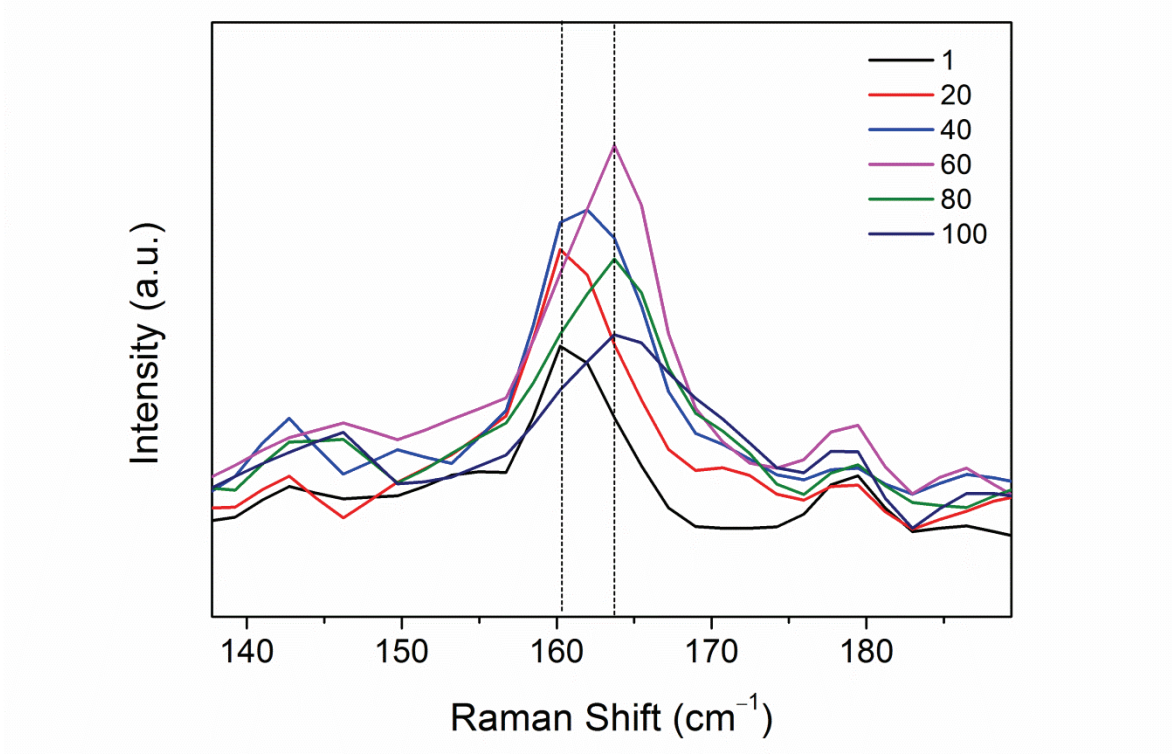

Figure 6-6: *Raman spectra of nanocrystalline 1T'-$MoTe_2$ in 1 M H_2SO_4 obtained during 100 CV cycles. The spectra shown were obtained during the 1st, 20th, 40th, 60th, 80th and 100th cycle. The electrode was fixed in position throughout the measurement ensuring the same sample spot was measured each time. Dashed lines are provided as a guide to the eye.*

Further, by examining the 1st and 100th cycle only (Figure 6-7), while there is a noticeable shift in the A_g mode at ~161 cm^{-1}, the B_g mode ~107 cm^{-1} remains intact. This finding is similar to that observed in a study by Li *et al.*[3] who investigated the Raman spectra of MoS_2 before and after electrochemical cycling. The authors claim that protons intercalate into the interlayer space of MoS_2 by electrochemically polarising the electrode at reductive potentials. The authors noted that the A_{1g} Raman peak blue-shifts by ~0.5 cm^{-1}, while the position of the E^1_{2g} peak remains intact. This was attributed to p-doping to MoS_2 as a result of proton intercalation, and was observed during *ex-situ* measurements.[3]

However, the authors also note a slight shift in the PXRD pattern after cycling to a lower angle, thus signalling a lattice expansion. Nevertheless, as discussed above, no internal standard was used and therefore the shift may be misleading. Moreover, Raman spectroscopy was performed *ex-situ*, indicating that the protons remain intercalated for a significant period of time. This is in contrast to nanocrystalline 1T'-$MoTe_2$ studied here as neither shift in PXRD nor Raman peak position is observed *ex-situ*. Due to the reversible

nature of the nanocrystalline 1T'-$MoTe_2$ activation, the shift in Raman peak has only been observed *in operando*. This therefore implies that the activation of MoS_2, as reported by Li *et al.*,[3] is not reversible, and may therefore operate *via* a different activation mechanism to that of 1T'-$MoTe_2$.

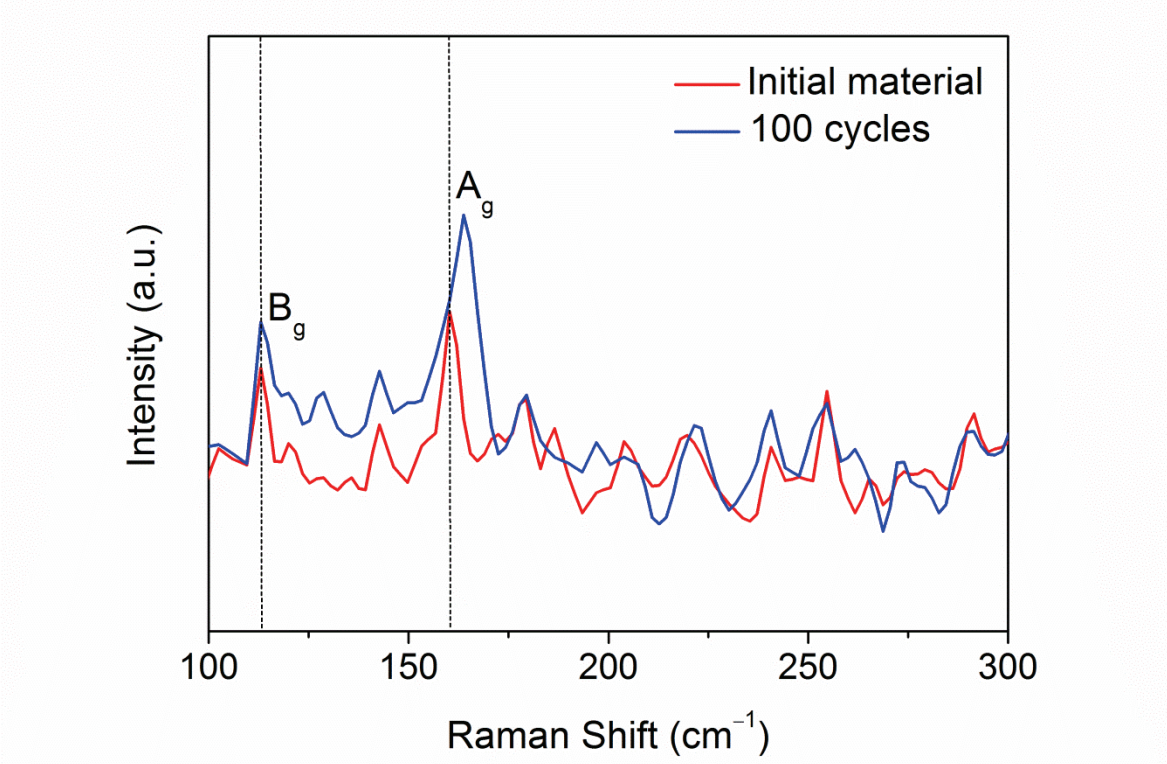

Figure 6-7: *Raman spectra of nanocrystalline 1T'-$MoTe_2$ in 1 M H_2SO_4 obtained using the in operando set up. The initial material (red) is shown in comparison with the spectra of that obtained during the 100th CV cycle (blue). The electrode was fixed in position throughout the measurement ensuring the same sample spot was measured each time. Dashed lines are provided as a guide to the eye.*

6.3.2.2. *In Operando* EXAFS

In order to elucidate any changes in structure during the electrochemical activation of nanocrystalline 1T'-$MoTe_2$, 'real time' experiments are essential. As discussed in Chapter 5, no changes in structure, morphology or composition are observed *ex-situ*, which is in line with the reversible nature of the activation mechanism. Therefore, as DFT calculations indicate that hydrogen adsorption on the 1T'-$MoTe_2$ is the cause of activation, *in operando* studies are imperative to gain further insight into any structural changes that may occur during the HER. Accordingly, *in operando* EXAFS studies were carried out at Diamond Light Source, with the aim of monitoring any changes to the Mo-Te bond during the

electrochemical reaction. To do this, nanocrystalline 1T'-$MoTe_2$ had to be incorporated into the electrochemical cell depicted in Figure 6-8. The *in operando* cell requires a permeable working electrode substrate to allow the electrolyte to reach the catalyst surface, *i.e.* the catalyst is not in direct contact with the electrolyte. The working electrode is then placed in the window to be aligned with the beam, all the while maintaining contact with the electrolyte. As such, glassy carbon is an inappropriate working electrode substrate.

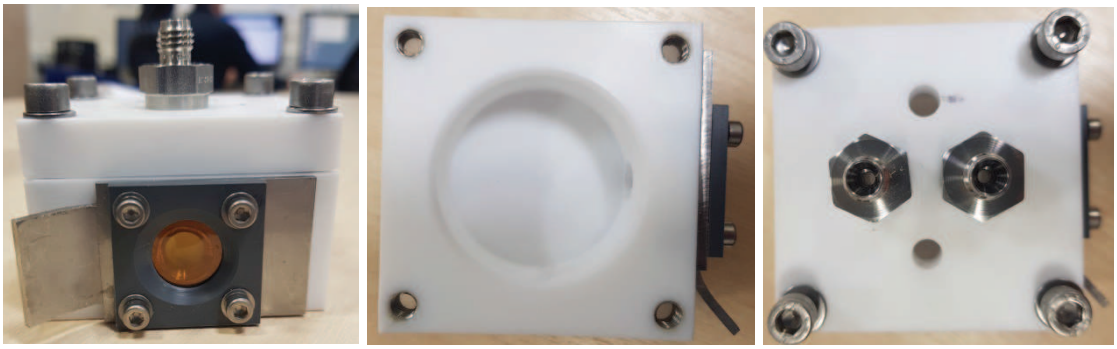

Figure 6-8: *In operando electrochemical cell available at Diamond Light Source. Front view of cell illustrating window used for positioning electrode to be in contact with solution and attached to electrical contact (left); inside view of the reservoir for electrolyte (middle) and top view showing holes for insertion of reference and counter electrodes (right).*

Instead, efforts were turned towards the use of carbon paper as the working electrode substrate. Carbon paper was chosen due to its permeable nature, which would allow for the H_2SO_4 electrolyte to pass through the paper and be in contact with the catalyst surface, which faces outward of the cell towards the beam. However, this required the method of catalyst deposition on the electrode surface to be altered. Drop-casting and dip-coating were deemed unacceptable due to the inconsistent distribution of catalyst on the carbon paper surface. Rather, the catalyst ink was deposited by painting the ink on the surface of carbon paper layer by layer.

Firstly, to determine whether carbon paper would be a viable substrate, initial tests were conducted with a catalyst ink which was prepared in an identical manner to that of glassy carbon (10 mg catalyst, 1 mL H_2O / ethanol and 80 µL Nafion™).The ink was then painted on to a 14 cm^2 sheet of carbon paper, with each layer being dried on a hot plate, as illustrated in Figure 6-9, until the entire quantity of ink was applied. The catalyst coated carbon paper was then cut into 1 cm^2 pieces, which could then be used as electrodes for the HER.

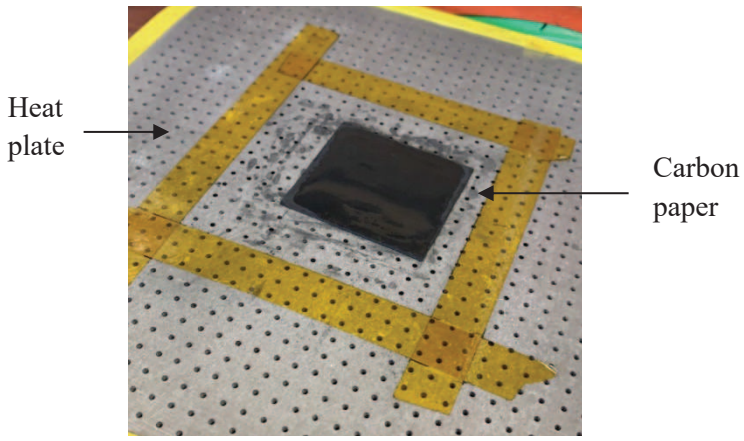

Figure 6-9: *Image of the painting procedure used to coat carbon paper with nanocrystalline 1T'-$MoTe_2$.*

Before carrying out catalytic tests using the electrochemical cell, initial reactions were completed using a typical experimental set-up, analogous to glassy carbon. In this way, the effect of changing substrate could be investigated. As such, cyclic voltammetry was employed to compare the current densities achieved when nanocrystalline 1T'-$MoTe_2$ was deposited on both carbon paper and glassy carbon electrodes. The catalyst was found to remain intact during CV, however Figure 6-10 shows that the current densities of the catalyst coated carbon paper electrode are much lower than that of the glassy carbon electrode. This was initially attributed to the difference in catalyst loading, hence the currents were normalised to the mass of catalyst rather than geometric surface area. For example, the mass of catalyst on glassy carbon with a surface area of 0.071 cm^2 was calculated to be 0.28 mg, while for 1 cm^2 carbon paper a mass of 0.7 mg was applied. Figure 6-11 shows that the currents achieved by both electrodes are more agreeable once this normalisation is applied. Hence, the catalyst ink was scaled up so that the loading of 1T'-$MoTe_2$ on carbon paper was identical to that on glassy carbon, *i.e.* 3.94 mg cm^{-2}.

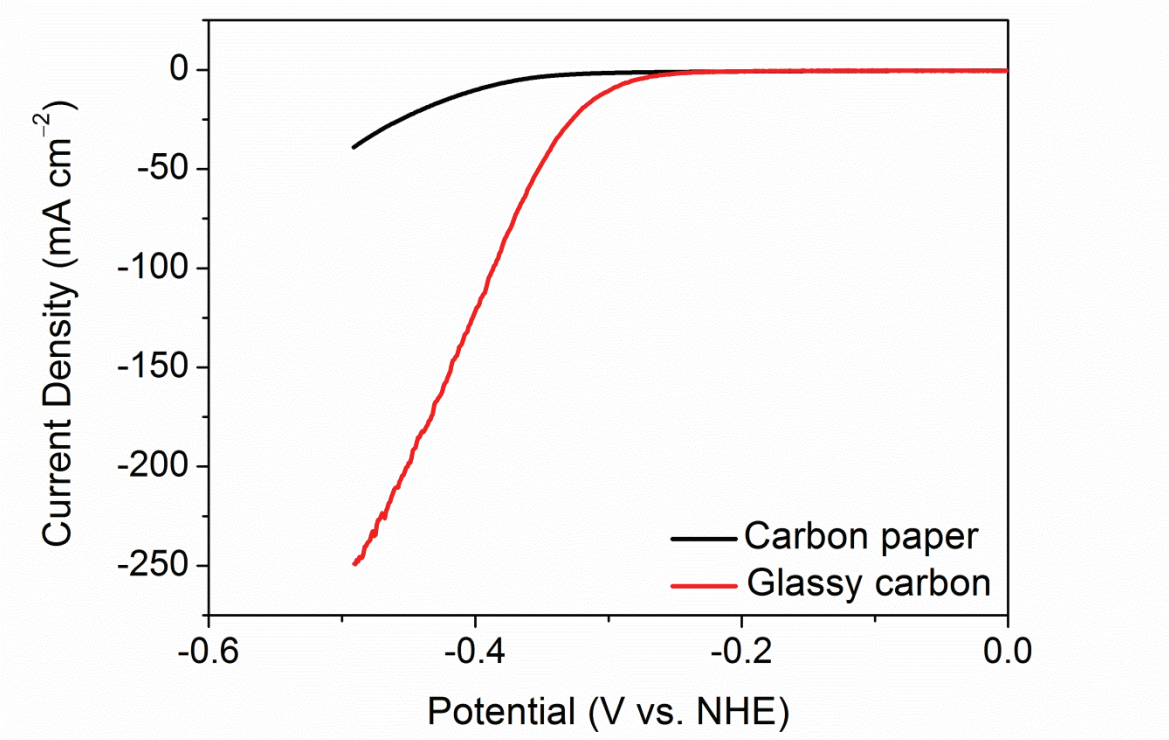

Figure 6-10: *Comparison of the current densities obtained by nanocrystalline 1T'-$MoTe_2$ on carbon paper (0.7 mg cm^{-2}) and on glassy carbon (loading: 3.94 mg cm^{-2}) in 1 M H_2SO_4.*

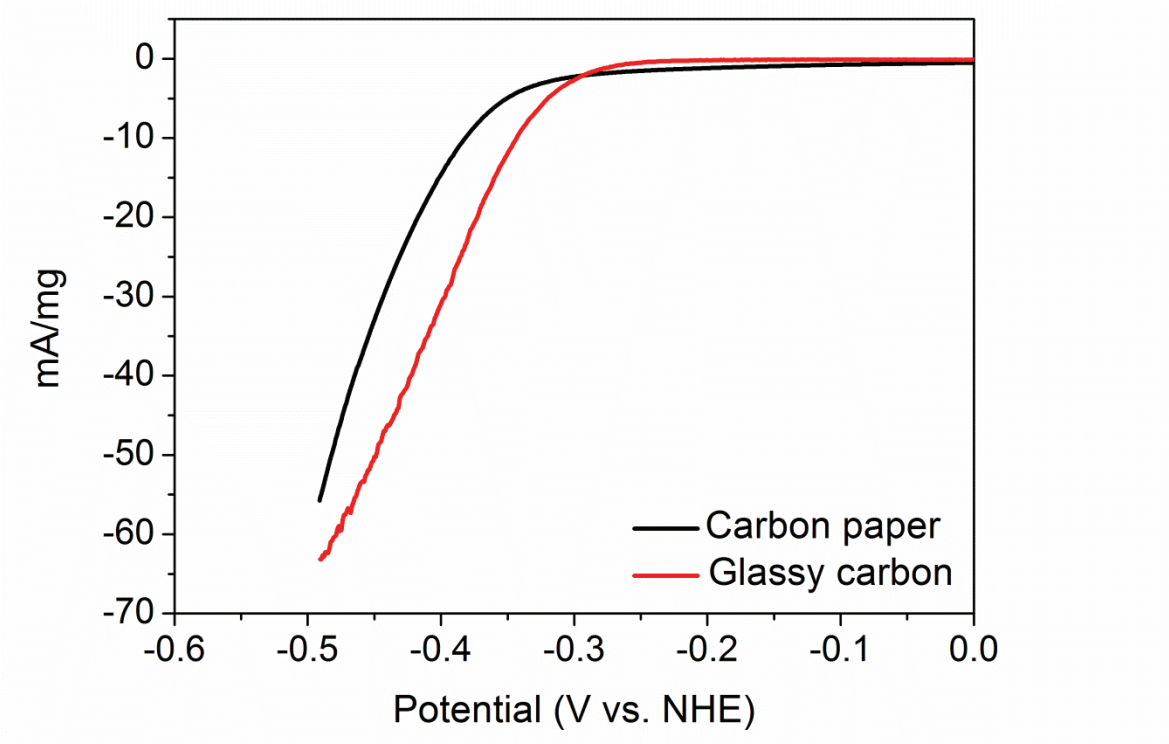

Figure 6-11: *Comparison of the currents normalised to mass of catalyst achieved by catalyst-deposited glassy carbon and carbon paper working electrodes.*

As both glassy carbon and carbon paper substrates have a catalyst loading of 3.94 mg cm^{-2}, a similar catalytic activity would be expected. However, from Figure 6-12, it is clear that, while the increased loading on carbon paper results in an increased current density (compared to Figure 6-10), the carbon paper substrate still shows an inferior performance to the glassy carbon substrate. This is most likely due to the differing surface morphologies of the carbon substrates, with the carbon paper being much more porous than the glassy carbon. This therefore demonstrates the limit of comparing catalysts to their geometric current densities. As suggested by Voiry *et al.*,[12] the electrocatalytic activities of HER electrocatalysts should ideally be normalised to their electrochemically active surface area (ECSA). Only in this way can the true intrinsic activities of HER catalysts be reliably compared.

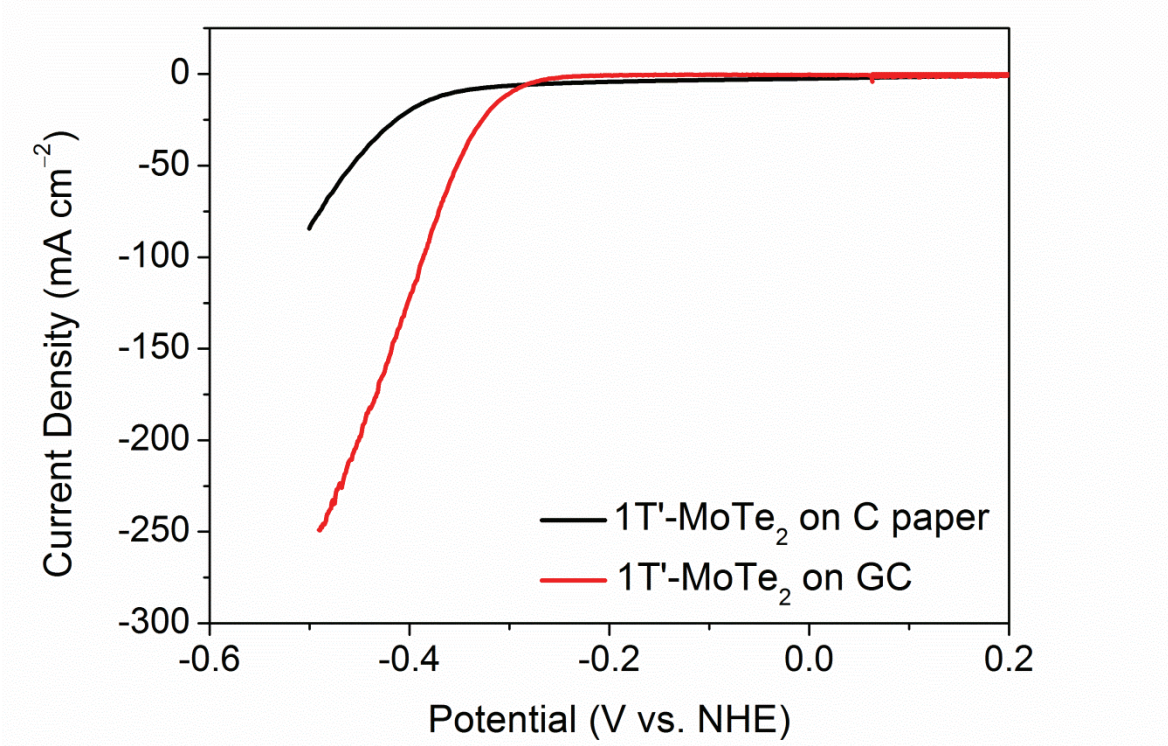

Figure 6-12: *Comparison of the current densities achieved by catalyst-deposited glassy carbon and carbon paper electrodes with an identical catalyst loading of 3.4 mg* cm^{-2}.

Comparison of the capacitance currents at various scan rates allows for the calculation of the double layer capacitance, which can then be used to estimate the ECSA.[13] The ECSA is directly proportional to C_{DL}, hence the ECSA values are qualitatively calculated rather than quantitatively.[14] Accordingly, the double layer capacitance values were calculated for both nanocrystalline 1T'-$MoTe_2$ deposited on glassy carbon and carbon paper substrates. Figure 6-13 shows the C_{DL} value of 1T'-$MoTe_2$/carbon paper to be approximately four times that

of 1T'-$MoTe_2$/glassy carbon. Consequently, the ECSA of 1T'-$MoTe_2$/carbon paper is greater than that of 1T'-$MoTe_2$/glassy carbon by a factor of four also.

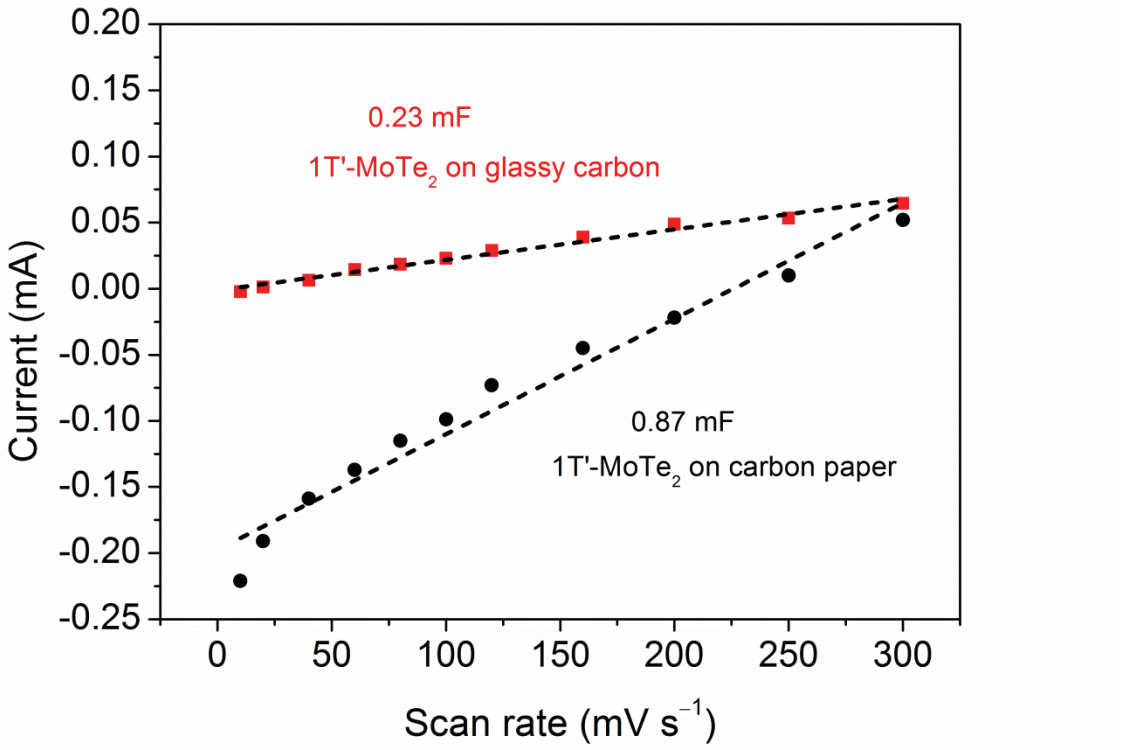

Figure 6-13: *Currents obtained by the catalyst-deposited glassy carbon and carbon paper electrodes plotted against scan rates. The capacitance currents were measured at 150 mV (vs. NHE).*

Now, assuming an ECSA of a flat surface to be $C_{DL(Ref)}$ = 40 µF cm^{-2}, as reported by Jaramillo *et al.*, the ECSA of both catalyst coated carbon electrodes can be calculated as:[15,16]

$$ECSA = \frac{C_{DL}}{C_{DL(Ref)}}$$

As such, the ECSA of nanocrystalline 1T'-$MoTe_2$ on glassy carbon and carbon paper can be calculated as 5.75 cm^2 and 21.75 cm^2, respectively. Normalising the obtained current to the ECSA values rather than geometric surface area presents a similar activity for both electrodes (Figure 6-14). Hence, by this method, the activities of both electrodes were found to be essentially identical regardless of the substrate.

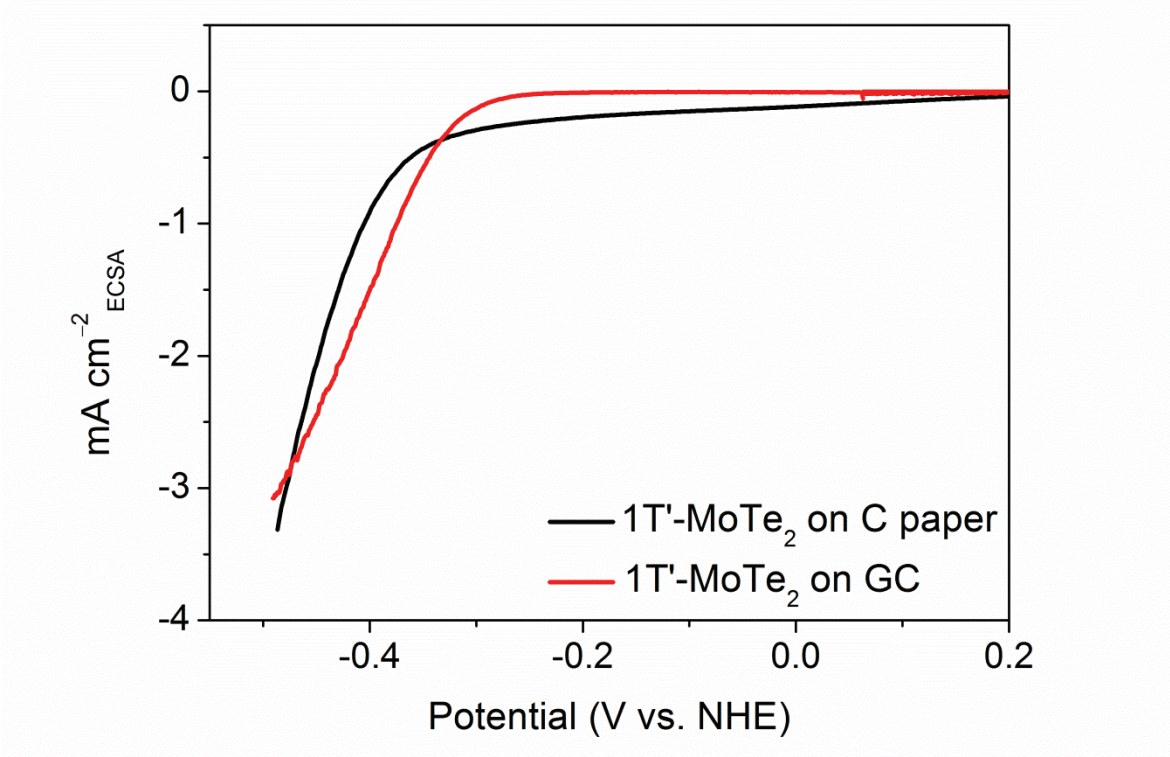

Figure 6-14: *Comparison of the current densities per electrochemically active surface area (ECSA) for nanocrystalline 1T'-$MoTe_2$ on glassy carbon and carbon paper.*

However, activating nanocrystalline 1T'-$MoTe_2$ becomes increasingly difficult with this larger surface area leading to an increase in electrochemical processes such as diffusion limitations and double layer formation. This then means that a larger energy barrier needs to be overcome in order for the activation to take place; hence the carbon paper electrode needs to be swept to higher potentials. In an attempt to activate $MoTe_2$ on carbon paper, the potential range was increased until the geometric current density of carbon paper was in line with that obtained on glassy carbon, and it was found that an electrochemical activation does indeed take place (Figure 6-15). After 100 cycles between +0.2 V and –0.65 V (vs. NHE) the overpotential improved from 350 mV to 260 mV. Thus, it is possible to activate $MoTe_2$ on a carbon paper substrate, but the parameters need to be optimised in order to achieve the improved overpotential of 180 mV.

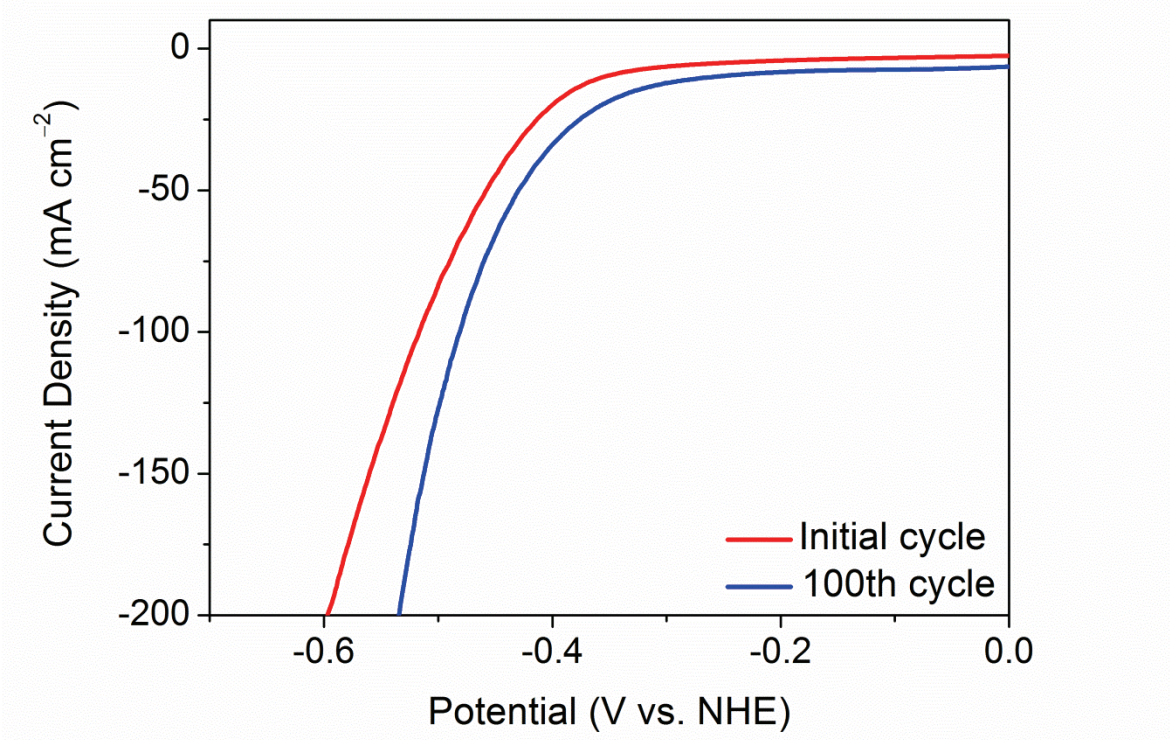

Figure 6-15: *Comparison of the current densities achieved by 1T'-$MoTe_2$ on carbon paper substrate before and after 100 cycles between +0.2 V and –0.65 V (vs. NHE) in 1 M H_2SO_4.*

Next, electrocatalytic tests were performed with the catalyst-deposited carbon paper loaded into the electrochemical cell (as depicted above in Figure 6-8). Notably, the current densities achieved dropped substantially when the catalyst-painted side of the carbon paper was facing outside the cell (*i.e.* not in direct contact with the electrolyte). This was attributed to the requirement of the electrolyte to diffuse through the carbon paper and hence overcome additional resistance. A comparison of the polarisation curves obtained with the catalyst-painted side facing inwards towards the electrolyte and outwards towards the beam are shown in Figure 6-16.

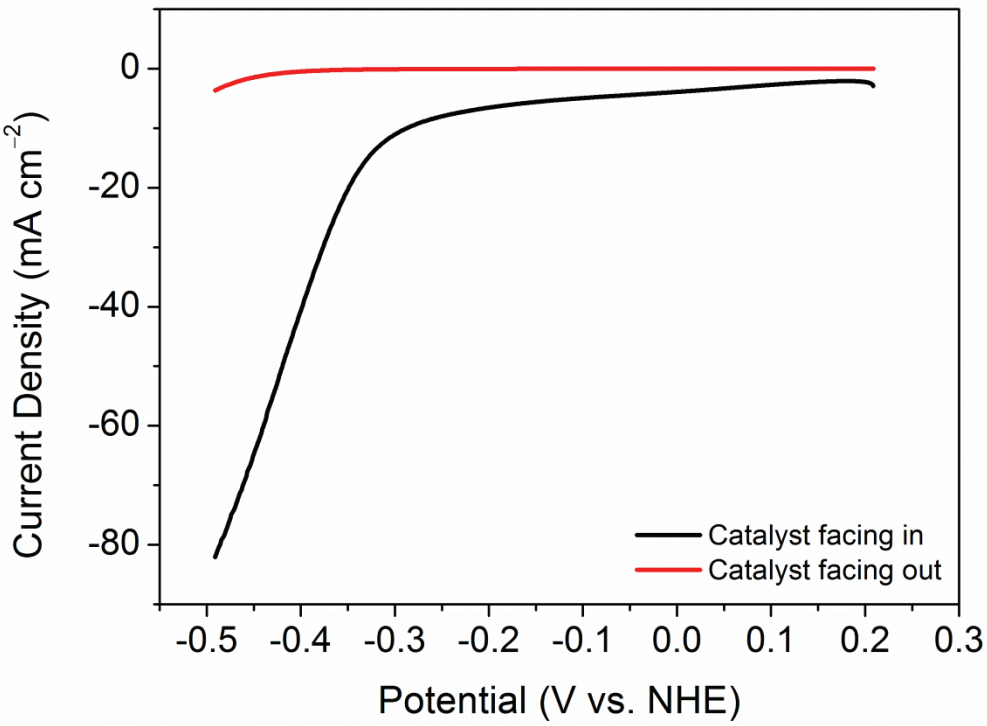

Figure 6-16: *Comparison of the current densities achieved when the catalyst-deposited carbon paper is loaded into the electrochemical cell facing inwards (in direct contact with electrolyte) and when the catalyst is facing outwards (not in direct contact with the electrolyte).*

Due to these lower current densities being achieved during cyclic voltammetry, chronoamperometry was applied with a constant potential of –320 mV (vs. NHE) for extended periods of time. Figure 6-17 shows a representative chronoamperometry profile of the catalyst-painted carbon paper (facing outwards) at –320 mV (vs. NHE) in comparison to that of bare carbon paper. As can be seen in Figure 6-17, the current density of bare carbon paper remains relatively stable, while that of the catalyst-painted electrode gradually improves with time. Additionally, CV performed directly after extended-time electrolysis shows that enhancement of the current densities are achieved (Figure 6-18). It should be noted that the bare carbon paper shows a slight improvement in current density; however this is considered to be minor when compared to that of the catalyst-painted electrode. Hence, it was concluded that the activation procedure could be investigated using the electrochemical cell provided by Diamond Light Source.

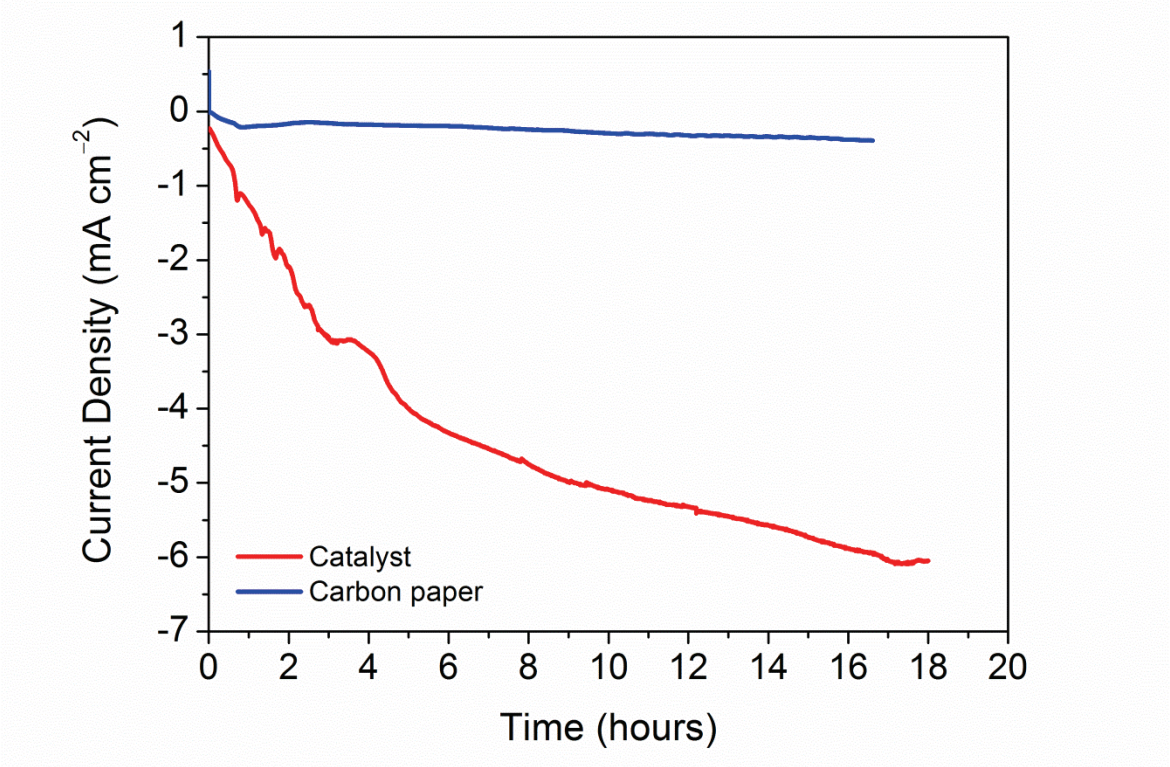

Figure 6-17: *Chronoamperometry profile of nanocrystalline 1T'-$MoTe_2$ painted on carbon paper vs. bare carbon paper. A constant voltage of –320 mV (vs. NHE) was applied in 1 M H_2SO_4. The catalyst was loaded into the electrochemical cell with the catalyst-painted side facing outwards.*

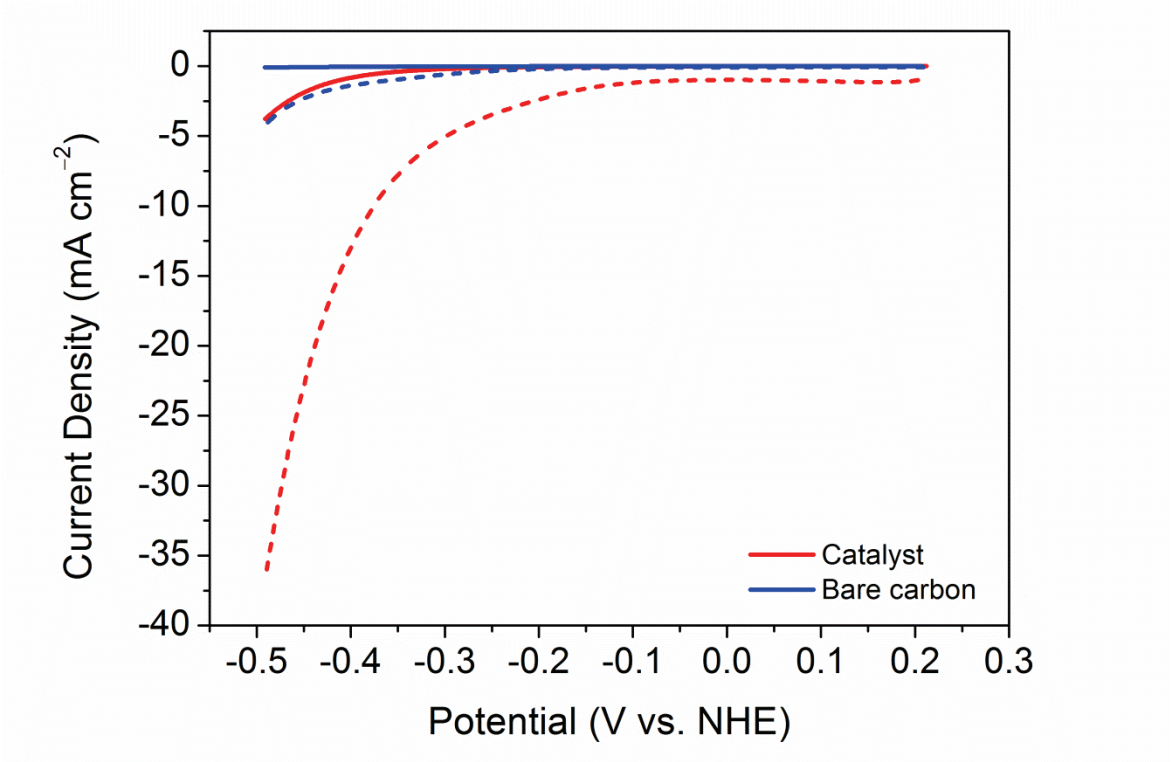

Figure 6-18: *Comparison of the current densities achieved by the catalyst on carbon paper and bare carbon paper before (solid lines) and after (dashed lines) electrolysis at a constant potential of –320 mV (vs. NHE) for 18 hours in 1 M H_2SO_4. The catalyst was loaded into the electrochemical cell with the catalyst-painted side facing outwards.*

Despite the electrochemical cycling of nanocrystalline 1T'-$MoTe_2$ deposited on carbon paper requiring higher energy inputs than glassy carbon in order for the activation to occur, the process of the activation remains the same, *i.e.* cycling under reductive potentials results in a lower potential required for a given current density. Therefore, it is reasonable to assume that any changes to the Mo-Te bond length that may occur on the catalyst-deposited glassy carbon electrode would also occur on the catalyst-painted carbon paper electrode. Thus, *in operando* EXAFS could be studied using this new electrode in the electrochemical cell as described above. *In operando* EXAFS measurements were performed at Diamond Light Source Ltd in an identical experimental set up described above.

Figure 6-19 shows a representative comparison of the EXAFS data collected both before and during the *in operando* electrochemical studies. Both spectra resemble the literature spectra of MoS_2, with the main edge at 20006 eV and a sharp feature at 20015 eV, which are consistent with the Mo^{4+} oxidation state. All *in operando* spectra were identical to the representative spectrum shown in Figure 6-19, regardless of the potential applied or length of electrolysis time, thus indicating that no changes to the Mo-Te bond length occurred. This result was surprising; however, it is possible that the low current densities achieved by the

use of carbon paper in the electrochemical cell were insufficient to induce any observable changes to the Mo-Te bond. Thus, in order to investigate the *in operando* activation further, alternative techniques such as *in operando* XPS would be required.

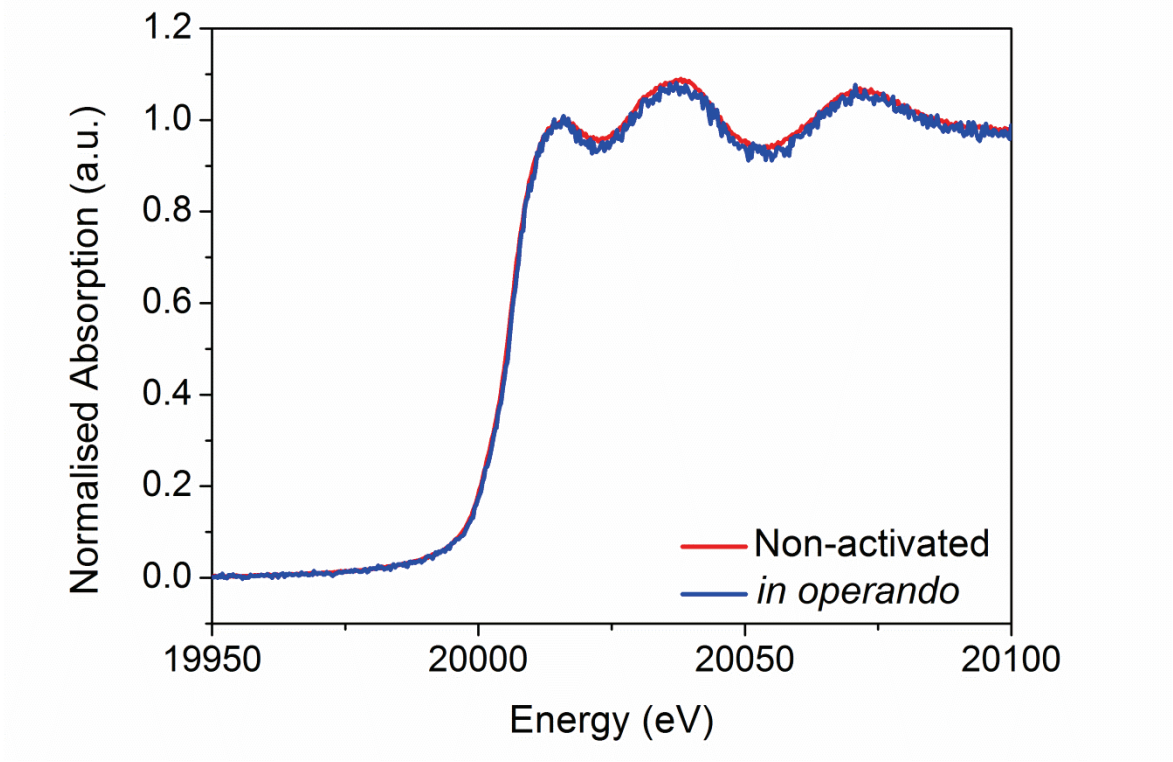

Figure 6-19: *Comparison of the EXAFS data collected for nanocrystalline 1T'-$MoTe_2$ obtained before activation and during in operando electrochemical studies.*

6.3.2.3. Revisiting *In Operando* Raman

With the catalyst-painted carbon paper electrode still in mind, the *in operando* Raman set up was revisited. To accommodate this new carbon paper working electrode, a new *in operando* Raman cell was required. Using the electrochemical cell available at Diamond Light Source for *in operando* EXAFS as the basis, a new cell was designed with the window for the working electrode moved from the side of the cell to the top surface. In this way, the electrode could be placed directly under the Raman microscope. This new *in operando* Raman cell was 3D printed and constructed as illustrated in Figure 6-20. Copper foil was used as the electrical contact for the working electrode and also acted as a holder to keep the carbon paper in position. The reference and counter electrodes were inserted through two holes on the top surface of the cell and the electrolyte was filled into the reservoir in the bottom compartment, as before. The H_2SO_4 electrolyte was filled to a level that was in contact with the catalyst-painted carbon paper, with the catalyst side facing the Raman microscope.

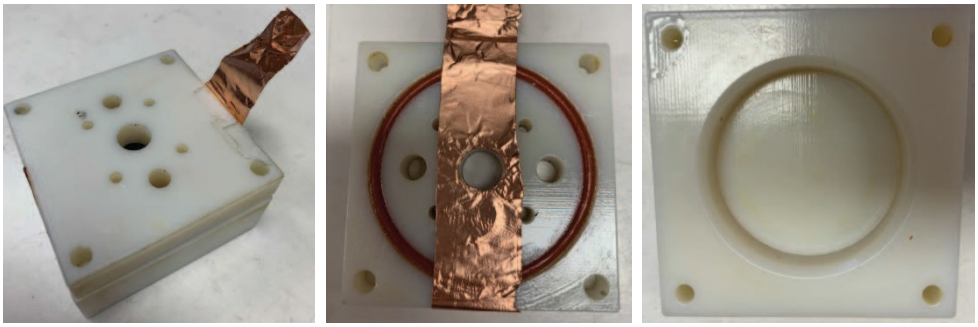

Figure 6-20: *3D printed in operando Raman cell (left); inside view of the lid, illustrating the copper foil electrical contact (middle) and inside view of the bottom compartment which contains a well for the electrolyte.*

Contrary to the result obtained with the glassy carbon electrode set up, no shift of the A_g Raman peak at ~161 cm^{-1} was observed using this new *in operando* cell which incorporates the carbon paper substrate (Figure 6-21). This, coupled with the *in operando* EXAFS result, perhaps suggests that the scaling of the catalyst from the glassy carbon electrode to carbon paper affected the activation process. Despite an activation being observed electrochemically, the extent to which the material is activated may be too low to be observed. Thus, in order to investigate the *in operando* electrochemical activation of 1T'-$MoTe_2$ further, additional studies are required for the preparation of the working electrode substrate. For example, it is likely that the porous nature of the carbon paper has an inhibiting effect on the catalytic activity, as seen previously when performing CV, as lower current

densities were obtained than on glassy carbon. Additionally, the positioning of the carbon paper, which requires indirect contact between the catalyst and electrolyte, may be an issue, as the current densities were found to substantially drop (see above). Thus, studies into the *in operando* activation of nanocrystalline 1T'-$MoTe_2$ are currently limited.

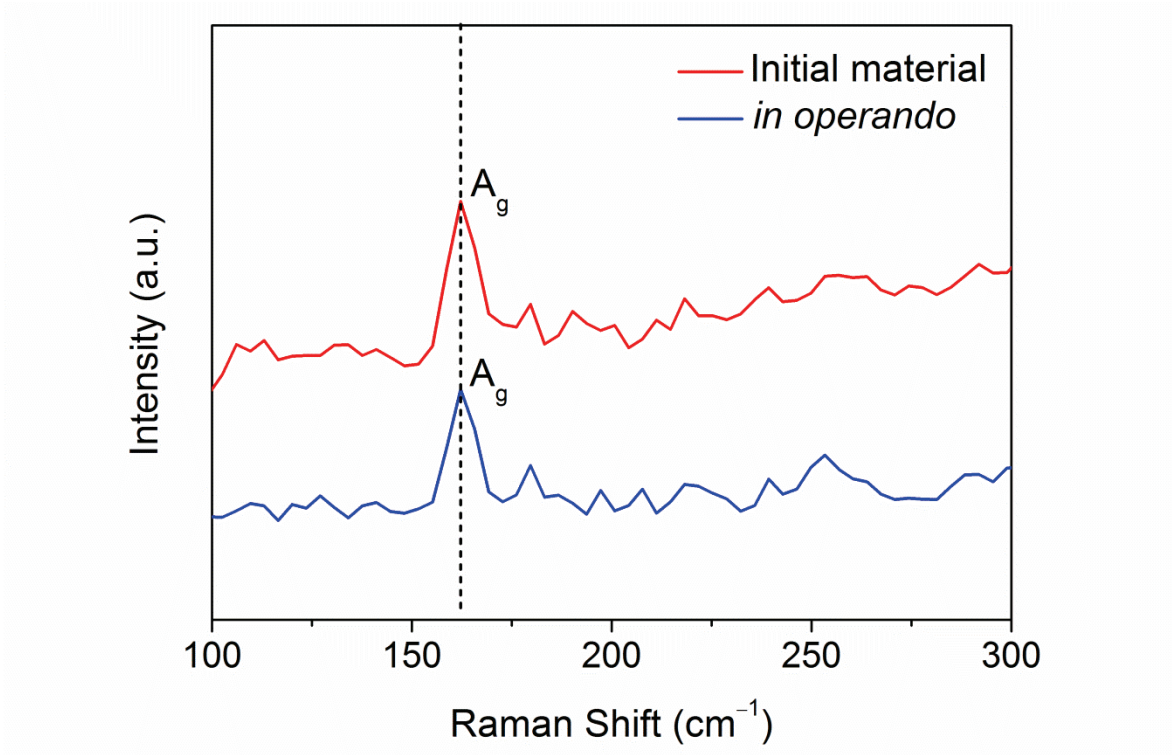

Figure 6-21: *Representative Raman spectra of nanocrystalline 1T'-$MoTe_2$ in 1 M H_2SO_4 obtained using the in operando set up which incorporated the catalyst-painted carbon paper working electrode. The initial material (red) is shown in comparison with the spectra of that obtained during the in operando measurements (blue). The electrode was fixed in position throughout the measurement ensuring the same sample spot was measured each time. The dashed line is provided as a guide to the eye.*

6.3.3. Alternative Routes of Activation

6.3.3.1. Removal of Surface Oxides

As discussed in Chapter 3, the $MoTe_2$ samples require an initial oxide layer removal before each measurement due to the presence of surface oxides. These surface oxides were evidenced by XPS, and are commonly observed in TMDC electrocatalysts. Thus, one may argue that the activation of nanocrystalline 1T'-$MoTe_2$ is due to the gradual removal of oxide species from the catalyst surface. Nanocrystalline 1T'-$MoTe_2$ may be initially oxidised, and when subjected to cathodic bias the surface oxides may be reduced and removed from the surface, thus revealing the true catalytic material. With this idea in mind, XPS studies were repeated under inert atmosphere in an attempt to observe any changes in oxidation state after cycling in 1 M H_2SO_4. Firstly, Figure 6-22 shows that bubbling nitrogen through the electrolyte during the cycling procedure has no effect on the activation of nanocrystalline 1T'-$MoTe_2$, with identical overpotentials being obtained within experimental error.

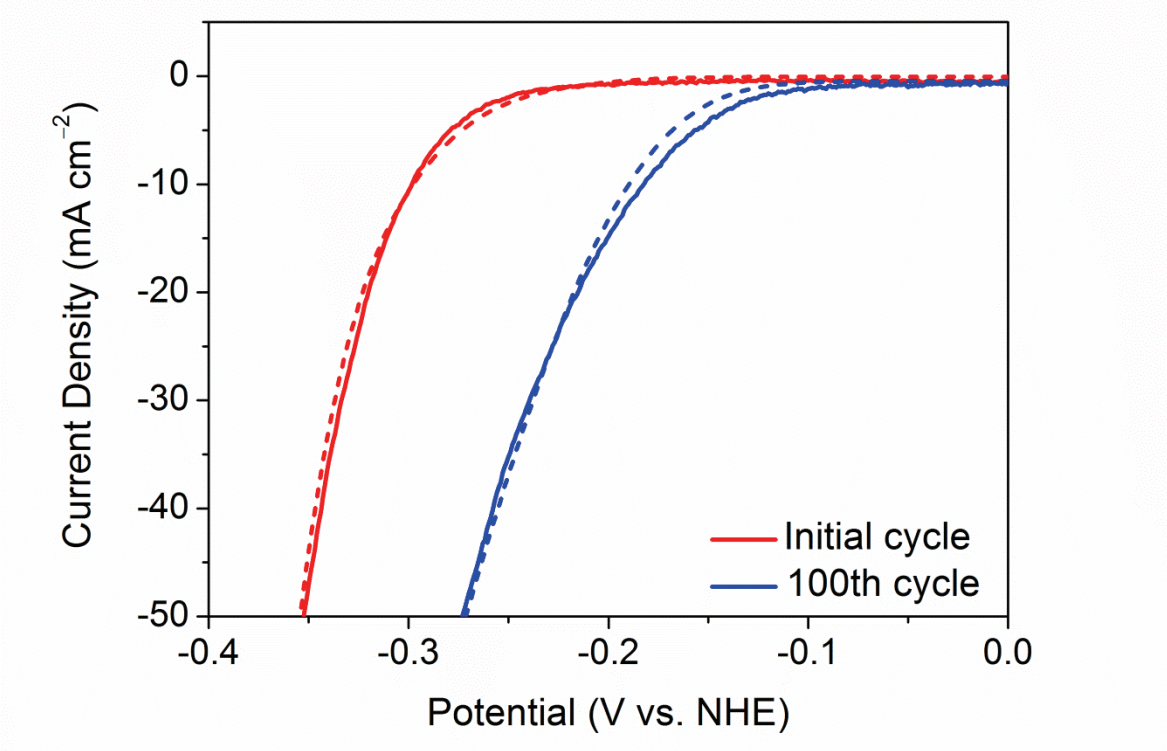

Figure 6-22: *Comparison of the current densities achieved by nanocrystalline 1T'-$MoTe_2$ before and after 100 cycles in 1 M H_2SO_4 under ambient conditions (solid lines) and when handled under inert atmosphere (dashed lines).*

Two electrodes were thus prepared for XPS studies under inert atmosphere in order to rule out the effect of oxygen as the reason for the enhanced catalytic activity at the EPSRC

National Facility for XPS. Two nanocrystalline 1T'-$MoTe_2$ samples were prepared on glassy carbon electrodes, with one being measured before activation and the other after 100 cycles in the potential range of +0.2 V and –0.5 V (vs. NHE). In both cases, the electrochemical cell, electrolyte and catalyst were degassed and maintained under a nitrogen atmosphere during the reaction. Before activation, the sample was immersed in 1 M H_2SO_4 and cycled 4 times, with the overpotential at $j = -10$ mA cm^{-2} reaching 320 mV. The second sample was cycled 100 times and the improved overpotential of 178 mV at $j = -10$ mA cm^{-2} was obtained, analogous to experiments in ambient conditions. Both electrodes were immediately transferred under nitrogen to the glovebox, packed and sent for XPS studies, thus ensuring measurement in inert atmosphere. The high resolution 3d Mo and 3d Te XPS spectra (Figure 6-23 and Figure 6-24) show a minor oxygen content is present in both non-activated and activated samples, as evidenced by the broad shoulder. Most interestingly, the shoulder is more prominent in the activated sample, thus suggesting that the removal of oxide species is not the underlying cause of the electrocatalytic enhancement. The peak shifts are within the resolution error of the instrument (0.1 eV) and are therefore unlikely to be due to any substantial changes in oxidation state. From this perspective, it is highly improbable that the reduction of surface oxides is the cause of the activation.

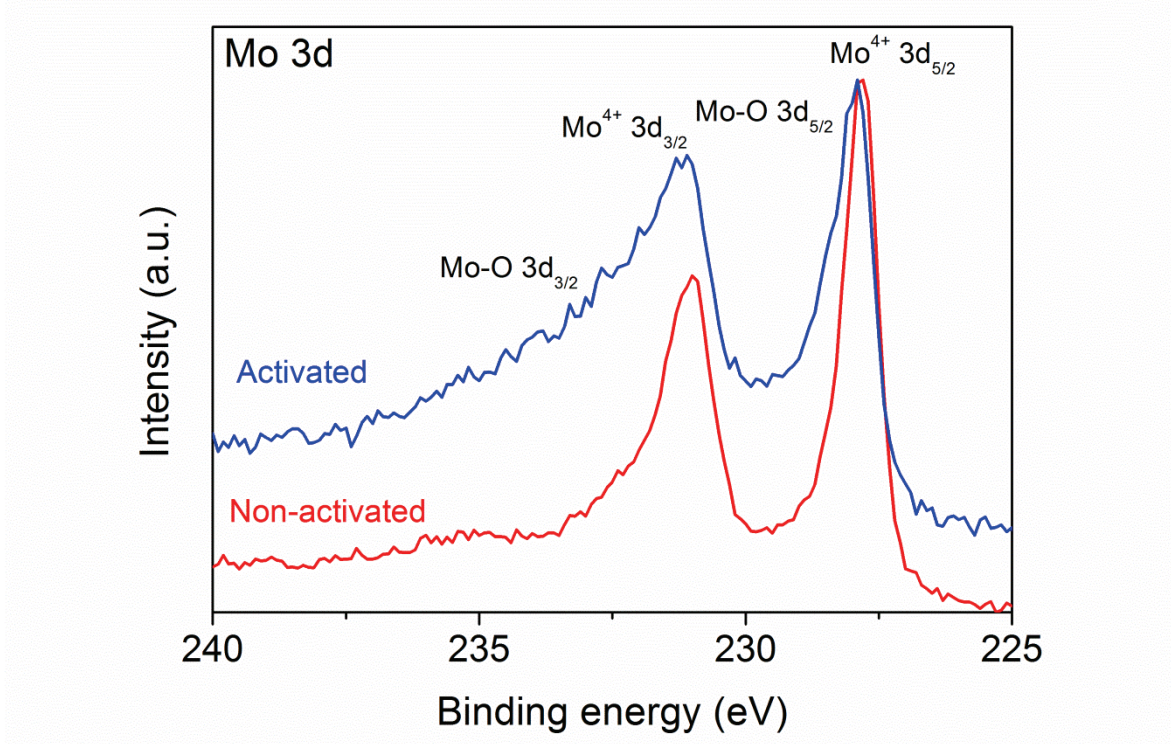

Figure 6-23: *3d Mo XPS spectra of activated (after 100 cycles) and non-activated nanocrystalline 1T'-$MoTe_2$ under inert conditions.*

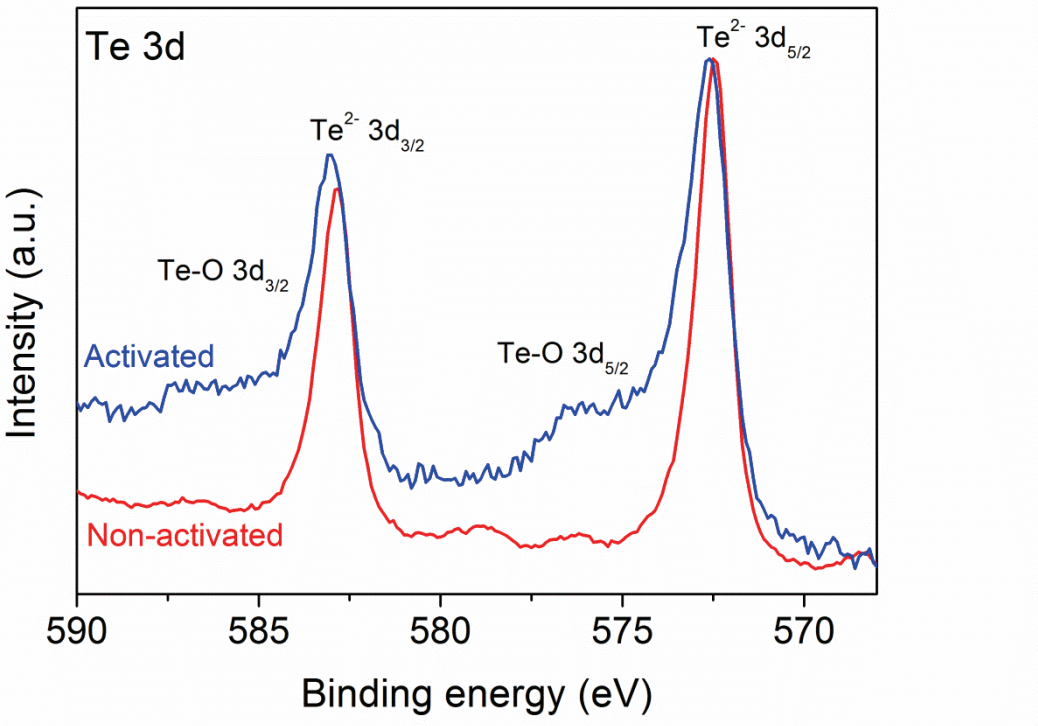

Figure 6-24: *3d Te XPS spectra of activated (after 100 cycles) and non-activated nanocrystalline 1T'-$MoTe_2$ under inert conditions.*

6.3.3.2. Role of Edges vs. Basal Plane

In the same vein, one may argue that the proposed activation of the basal plane may also be valid for the edge sites. Therefore, the possibility of the edge sites being the cause of the activation was further investigated. As such, this section seeks to distinguish the role of each active site.

It has been well established that the edge sites are more easily oxidised than the basal plane, therefore it is possible to differentiate between peaks which correspond to the oxidation of each site.[17] Following a procedure by Bonde *et al.*,[18] nanocrystalline 1T'-$MoTe_2$ was cycled at anodic potentials under a constant flow of nitrogen between the potential range of +1.05 V and –0.35 V (vs. NHE) (Figure 6-25). Close examination of the anodic sweep allowed for the identification of two distinct peaks which correspond to the oxidation of the edges (minor peak, maximum at +0.65 V (vs. NHE)) and the oxidation of the basal plane (major peak, maximum at +0.9 V (vs. NHE)). Also, it should be noted that an additional reduction wave (other than proton reduction) is observed at –0.24 V (vs. NHE). This reduction wave is attributed to the removal of the oxide layer during the initial CV cycle, as discussed in Chapter 3.

Thus, it is possible to oxidise the edge sites and observe their effect (or lack of) on the catalytic activity. If the catalytic activity of nanocrystalline 1T'-$MoTe_2$ were to deplete, or remain stable after 100 cycles, this would confirm that the edges contribute to the activation. On the other hand, if the activation were to proceed as normal, we could confidently attribute the catalytic enhancement to be due solely to the basal plane. Accordingly, nanocrystalline 1T'-$MoTe_2$ was cycled between +1.05 V and –0.35 V (vs. NHE). As can be seen in Figure 6-25, by cycling to such anodic potentials both the edge sites and the basal plane are oxidised, resulting in a loss of catalytic activity and deactivation of the material.

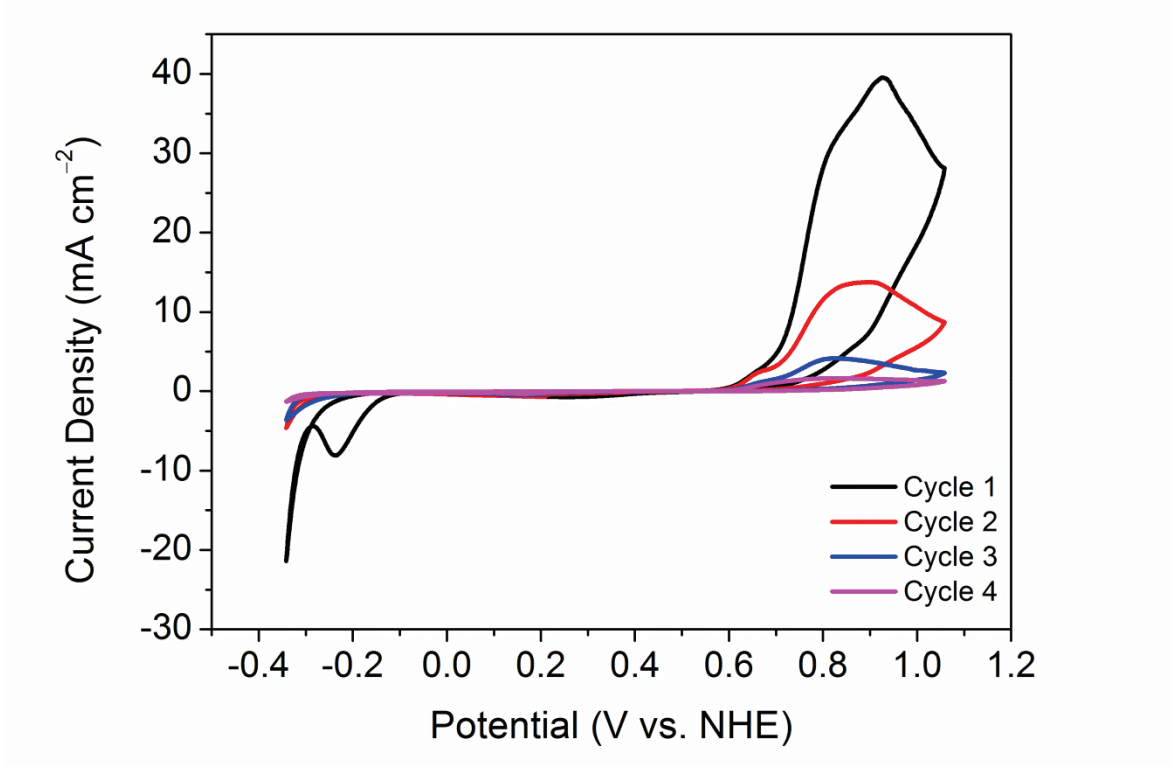

Figure 6-25: *Cyclic voltammogram of the oxidation and consequent deactivation of nanocrystalline 1T'-$MoTe_2$ in 1 M H_2SO_4 under a nitrogen atmosphere with a scan rate of 10 mV s^{-1}. During the first anodic sweep, two oxidations occur followed by a decrease in current density at cathodic potentials indicating catalyst deactivation.*

Subsequently, narrowing the potential range to +0.65 V and –0.40 V (vs. NHE), so that only the edge sites are oxidised, ensures the basal plane remains intact, thus allowing for its effect on the catalytic activity to be analysed. Cycling nanocrystalline 1T'-$MoTe_2$ 100 times within this potential range results in an identical overpotential improvement, as seen before (Figure 6-26). Thus, since the oxidation of the edges has no effect on the catalytic enhancement, it is unlikely that they are involved in the activation of nanocrystalline 1T'-$MoTe_2$. This then indicates that the basal plane is responsible for the activation of nanocrystalline 1T'-$MoTe_2$.

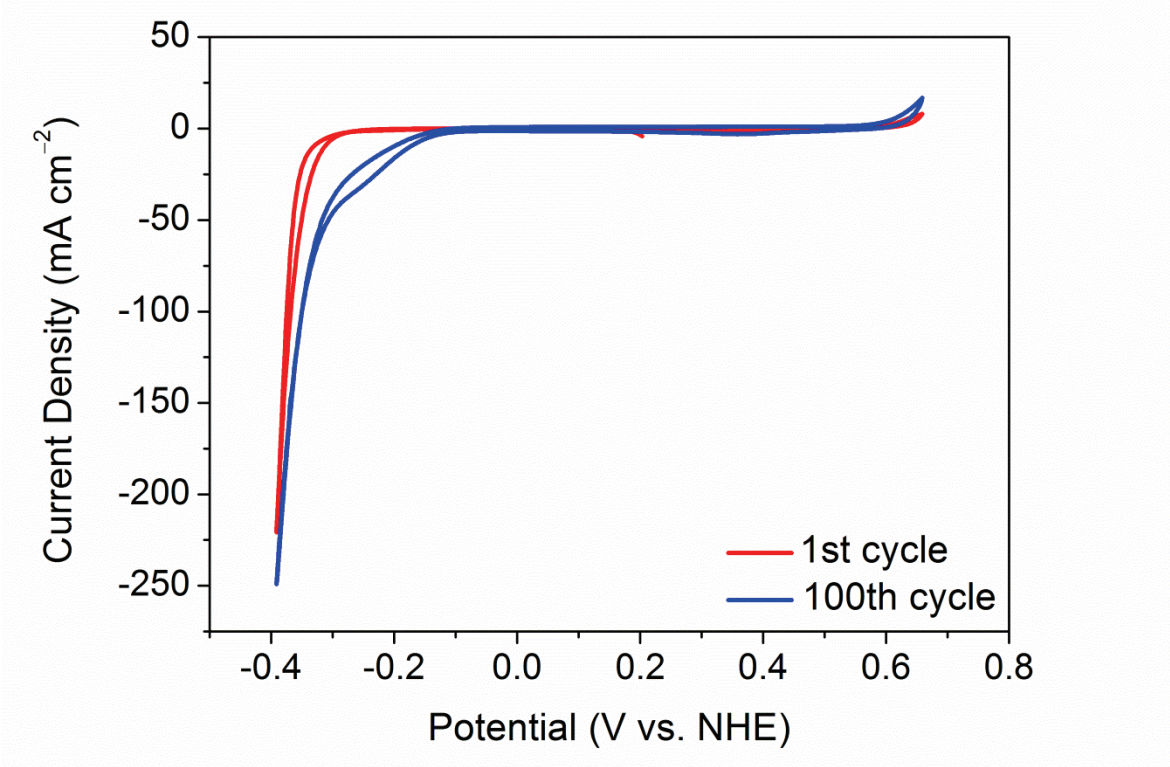

Figure 6-26: *Cyclic voltammogram of nanocrystalline 1T'-$MoTe_2$ before and after 100 cycles whereby the edges sites are oxidized. Measurements were performed in 1 M H_2SO_4 under a nitrogen atmosphere with a scan rate of 100 mV s^{-1}.*

6.3.3.3. Nanocrystalline variant of 2H-$MoTe_2$

As discussed in Chapter 4, the greater surface area of nanocrystalline 1T'-$MoTe_2$ results in a greater number of edge sites. Despite the basal plane widely being accepted as the main active site in metallic TMDCs,[19–22] few studies have disputed this and dedicate the enhanced performance to the abundance of edge sites.[23,24] With the activity of the edge sites in mind, a low temperature variant of 2H-$MoTe_2$ was synthesised at 500 °C by reannealing nanocrystalline 1T'-$MoTe_2$ for a total of 72 hours. This prolonged reaction time ensured the complete formation from 1T'-$MoTe_2$ to 2H-$MoTe_2$ and is evidenced by PXRD (Figure 6-27). For ease of comparison, this low temperature variant of 2H-$MoTe_2$ will also be named *nanocrystalline* 2H-$MoTe_2$. Analogous to 1T'-$MoTe_2$, crystalline 2H-$MoTe_2$ consists of plate-like microcrystals while nanocrystalline 2H-$MoTe_2$ is more disordered and possesses many more edge sites. See Figure 6-28 for a comparison of the crystalline and nanocrystalline 2H-$MoTe_2$ morphologies.

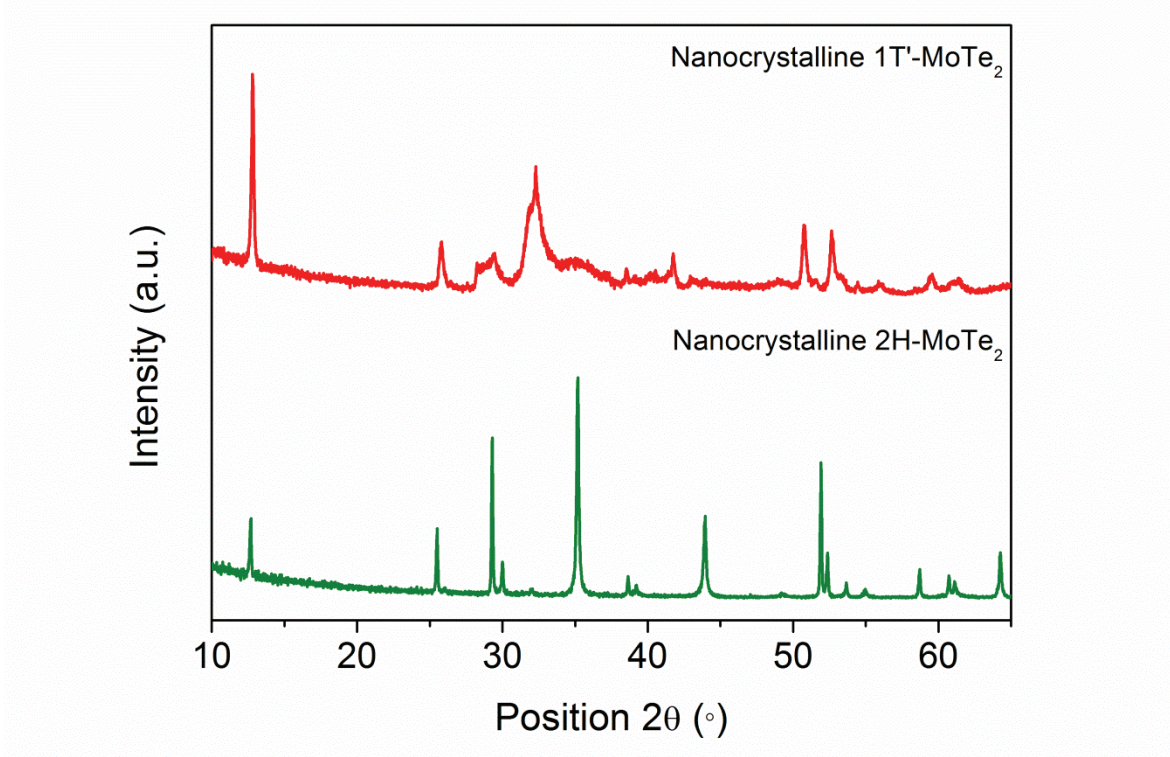

Figure 6-27: *PXRD patterns of nanocrystalline 1T'-$MoTe_2$ (top) and nanocrystalline 2H-$MoTe_2$ (bottom).*

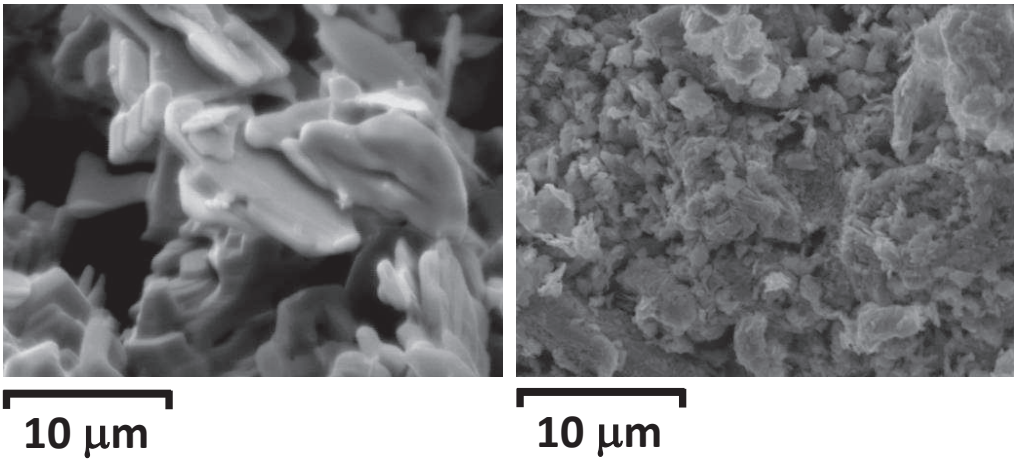

Figure 6-28: *Sample morphologies of crystalline 2H-$MoTe_2$ (left) and nanocrystalline 2H-$MoTe_2$ (right).*

For semiconducting TMDCs, *i.e.* 2H-MoS_2, 2H-$MoTe_2$, *etc*., the edge sites are catalytically active whereas the basal plane is inert.[25] Thus, many studies have focussed on optimizing the edge to basal plane ratio in order to maximize catalytic activity.[6,26,27] Therefore, it is unsurprising that nanocrystalline 2H-$MoTe_2$ requires a significantly lower overpotential for $j = -10$ mA cm^{-2} than its crystalline counterpart. By lowering the reaction temperature and increasing the number of edge sites, the overpotential at $j = -10$ mA cm^{-2} improves from

650 mV to 405 mV (Figure 6-29). This is in close agreement with the overpotential of 380 mV obtained by Luxa *et al*. by chemical exfoliation of 2H-$MoTe_2$ *via* Li intercalation.[28] In this study, the authors reported no such phase transition from 2H to 1T'-$MoTe_2$, therefore the improved catalytic activity was reported to be due to the increase in number of edge sites. For the 2H-phase, it is widely acknowledged that the edge sites are active and the basal plane is inert, therefore the substantial difference in electrocatalytic performance between nanocrystalline and crystalline materials is expected due to the increased number of edges.

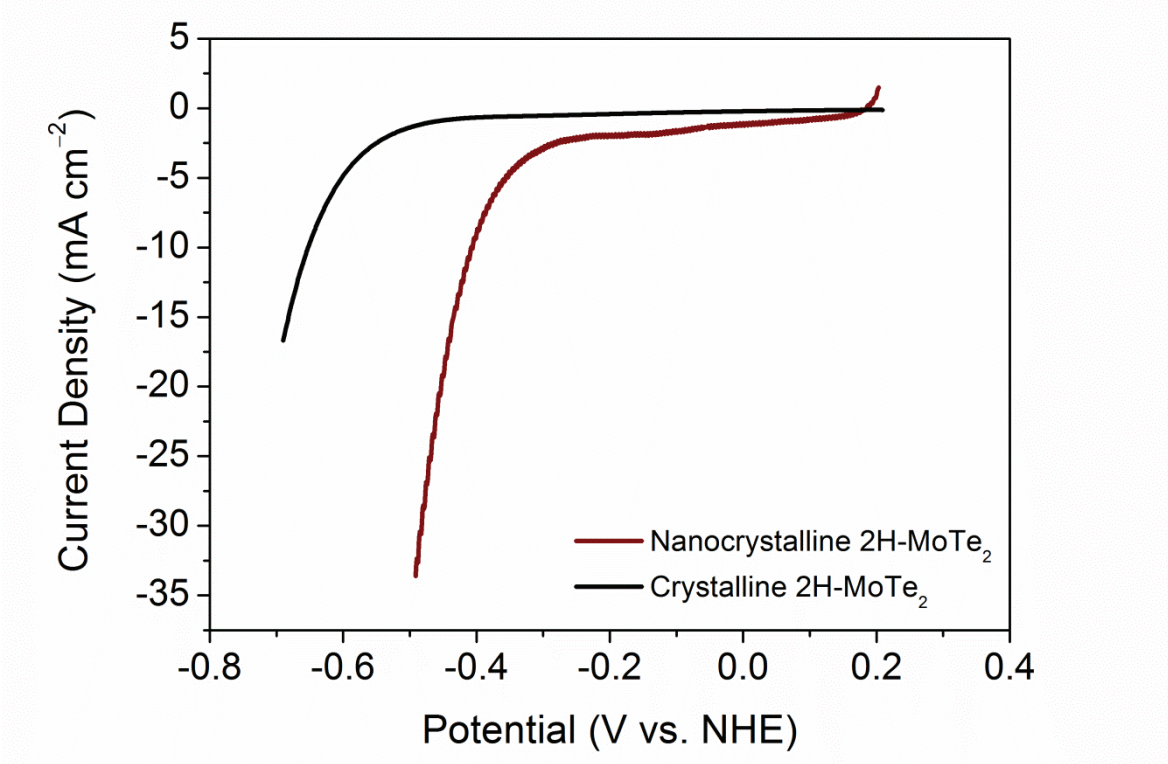

Figure 6-29: *Comparison of the current densities achieved by crystalline and nanocrystalline 2H-$MoTe_2$ catalysts in 1 M H_2SO_4. Catalysts were prepared on a glassy carbon working electrode as described in the experimental section. Carbon felt and 3 M Ag/AgCl were used as the counter and reference electrodes, respectively.*

Contrastingly, upon transitioning from crystalline to nanocrystalline 1T'-$MoTe_2$, although a similar increase in the number of edge sites is observed, only a small decrease in overpotential is observed (360 mV for crystalline vs. 320 mV for nanocrystalline 1T'-$MoTe_2$). This minor improvement in overpotential further evidences that the edges are not the source of the electrocatalytic enhancement. If the improved overpotential were due to the increased number of edges, then the initial cycle would display an overpotential of 178 mV, rather than improving gradually, as is observed. Additionally, despite the increased number of edge sites, nanocrystalline 1T'-$MoTe_2$ shows no such activation (Figure 6-30)

analogous to its crystalline counterpart. This further implies that the activation is electronic in origin. Evidently, while the edges are seen to be the active sites for the 2H-phase, these results suggest that they are not the main active site for the 1T'-phase, and hence the electrocatalytic activation is attributed to the basal plane.

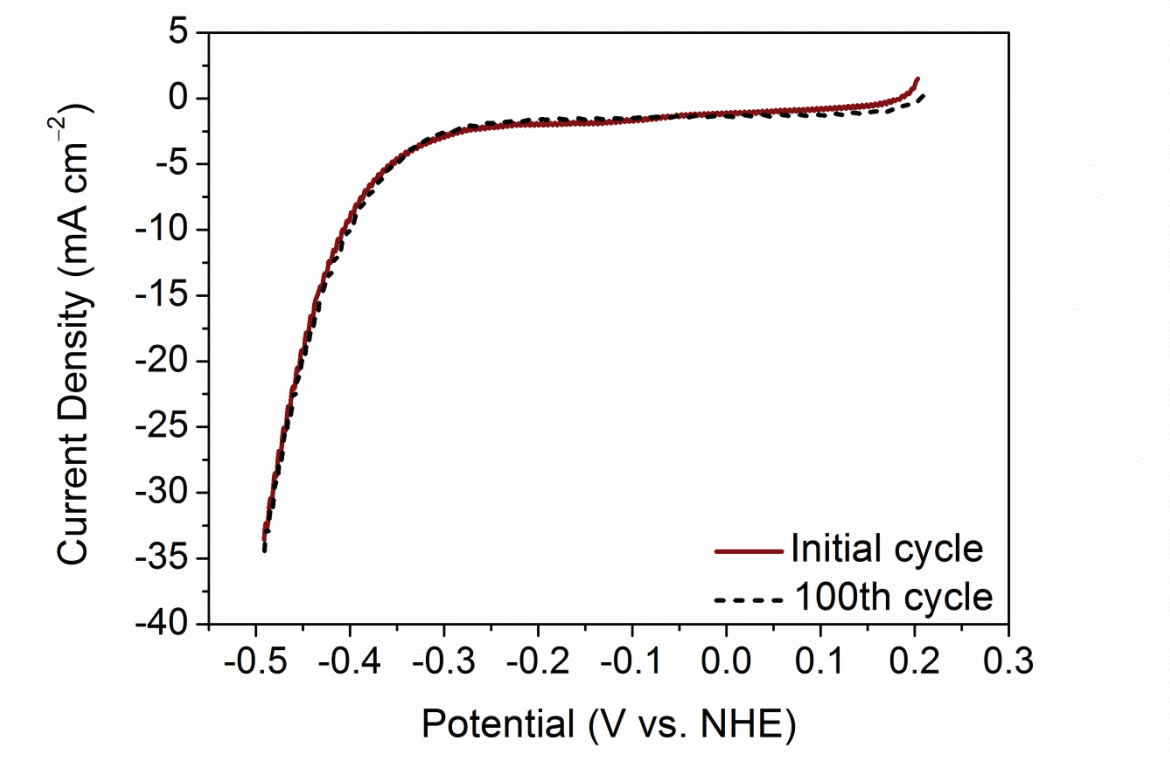

Figure 6-30: *Comparison of the current densities achieved by nanocrystalline 2H-$MoTe_2$ before and after 100 cycles in 1 M H_2SO_4. Catalysts were prepared on a glassy carbon working electrode as described in the experimental section. Carbon felt and 3 M Ag/AgCl were used as the counter and reference electrodes, respectively.*

6.4. Conclusions

To summarise, this chapter has been dedicated to gaining further insight into the gradual improvement in activation mechanism. Rather than the improved overpotential of 178 mV being observed immediately as a result of electron doping, the overpotential can be seen to reduce as the cycle number increases. This was attributed to limiting electrochemical processes which must be overcome in order for the activation to take place, thus the activation is dependent on the applied voltage. Likewise, the pulsing nature of cyclic voltammetry allows for the use of highly reducing potentials, which would otherwise result in the loss of contact between the catalyst and the electrolyte. The speed of activation can therefore be tuned by altering the potential range and number of cycles at which the potential is swept.

In operando Raman spectroscopy of nanocrystalline 1T'-$MoTe_2$ deposited on glassy carbon revealed a shift in Raman peak, which may be due to the intercalation of protons between the layers of $MoTe_2$. However, when scaling up the electrode to carbon paper, no such Raman shift was observed. Additionally, *in operando* EXAFS studies on catalyst-painted carbon paper revealed no changes in the Mo-Te bond length. Therefore, further optimisation of the working electrode substrate is required in order to fully understand the activation mechanism by *in operando* methods. Nonetheless, the scaling up from glassy carbon to carbon paper revealed the limits of substrate morphology for HER electrocatalysts.

Removing oxide species was excluded as being the reason for the gradual improvement by XPS, which showed that surface oxides remain both before and after activation. Finally, the argument of edge sites vs. the basal plane was settled, as the activity of nanocrystalline 1T'-$MoTe_2$ was completely lost by oxidising the basal plane, whereas oxidising the edge sites had no effect on the catalytic performance. As a result, the activation of nanocrystalline 1T'-$MoTe_2$ is believed to occur on the basal plane, with electron doping due to hydrogen adsorption being the most plausible activation mechanism.

6.5. References

1. Liu, Y., Wu, J., Hackenberg, K. P., Zhang, J., Wang, Y. M., Yang, Y., Keyshar, K., Gu, J., Ogitsu, T., Vajtai, R., Lou, J., Ajayan, P. M., Wood, B. C. & Yakobson, B. I. Self-optimizing, highly surface-active layered metal dichalcogenide catalysts for hydrogen evolution. *Nat. Energy* **2** (2017)

2. McGlynn, J. C., Dankwort, T., Kienle, L., Bandeira, N. A. G., Fraser, J. P., Gibson, E. K., Cascallana-Matías, Kamarás, K., Symes, M. D., Miras, H. N. & Ganin, A. Y. The rapid electrochemical activation of $MoTe_2$ for the hydrogen evolution reaction. *Nat. Commun.* **10**, 4916 (2019).

3. Li, G., Zhang, D., Yu, Y., Huang, S., Yang, W. & Cao, L. Activating MoS_2 for pH-Universal Hydrogen Evolution Catalysis. *J. Am. Chem. Soc.* **139**, 16194-16200 (2017).

4. Yu, Y., Huang, S-Y., Li, Y., Steinmann, S. N., Yang, W. & Cao, L. Layer-Dependent Electrocatalysis of MoS_2 for Hydrogen Evolution. *Nano Lett.* **14**, 553–558 (2014).

5. Vrubel, H. & Hu, X. Molybdenum Boride and Carbide Catalyze Hydrogen Evolution in both Acidic and Basic Solutions. *Angew. Chem. Int. Ed.* **51**, 12703-12706 (2012).

6. Merki, D., Fierro, S., Vrubel, H. & Hu, X. Amorphous molybdenum sulfide films as catalysts for electrochemical hydrogen production in water. *Chem. Sci.* **2**, 1262 (2011).

7. Vrubel, H., Merki, D. & Hu, X. Hydrogen evolution catalyzed by MoS_3 and MoS_2 particles. *Energy Environ. Sci.* **5**, 6136-6144 (2012).

8. Li, Y., Yu, Y., Huang, Y., Nielsen, R. A., Goddard, W. A., Li, Y. & Cao, L. Engineering the Composition and Crystallinity of Molybdenum Sulfide for High-Performance Electrocatalytic Hydrogen Evolution. *ACS Catal.* **5**, 448–455 (2015).

9. Mirabelli, G., McGeough, C., Schmidt, M., McCarthy, E. K., Monaghan, S., Povey, I. M., McCarthy, M., Gity, F., Nagle, R., Hughes, G., Cafolla, A., Hurley, P. K. & Duffy, R. Air sensitivity of MoS_2, $MoSe_2$, $MoTe_2$, HfS_2, and $HfSe_2$. *J. Appl. Phys.* **120**, 125102 (2016).

10. Chen, B., Sahin, H., Suslu, A., Ding, L., Bertoni, M. I., Peeters, F. M. & Tongay, S.

Environmental Changes in $MoTe_2$ Excitonic Dynamics by Defects-Activated Molecular Interaction. *ACS Nano* **9**, 5326–5332 (2015).

11. Seok, J., Lee, J-H., Bae, D., Ji, B., Son, Y-W., Lee, Y. H., Yang, H. & Cho, S. Hybrid catalyst with monoclinic $MoTe_2$ and platinum for efficient hydrogen evolution. *APL Mater.* **7**, (2019).

12. Voiry, D., Chhowalla, M., Gogotsi, Y., Kotov, N. A., Li, Y., Penner, R. M. Schaak, R. E. & Weiss, P. S. Best Practices for Reporting Electrocatalytic Performance of Nanomaterials. *ACS Nano* **12**, 9635–9638 (2018).

13. Trasatti, S. & Petrii, O. A. Real surface area measurements in electrochemistry. *Pure Appl. Chem.* **63**, 711–734 (1991).

14. McCrory, C. C. L., Jung, S., Peters, J. C. & Jaramillo, T. F. Benchmarking Heterogeneous Electrocatalysts for the Oxygen Evolution Reaction. *J. Am. Chem. Soc.* 135, 16977-16987 (2013).

15. Clark, E. L., Resasco, J., Landers, A., Lin, J., Chung, L-T., Walton, A., Hahn, C., Jaramillo, T. F. & Bell, A. T. Standards and Protocols for Data Acquisition and Reporting for Studies of the Electrochemical Reduction of Carbon Dioxide. *ACS Catal.* **8**, 6560–6570 (2018).

16. McCrory, C. C. L. *et al.* Benchmarking Hydrogen Evolving Reaction and Oxygen Evolving Reaction Electrocatalysts for Solar Water Splitting Devices. *J. Am. Chem. Soc.* **137**, 4347–4357 (2015).

17. Kautek, W. & Gerischer, H. Anisotropic photocorrosion of n-type MoS_2 $MoSe_2$, and WSe_2 single crystal surfaces: the role 0f cleavage steps, line and screw dislocations. *Surf. Sci.* **119**, 46–60 (1982).

18. Bonde, J., Moses, P. G., Jaramillo, T. F., Nørskov, J. K. & Chorkendorff, I. Hydrogen evolution on nano-particulate transition metal sulfides. *Faraday Discuss.* **140**, 219-231 (2008).

19. Voiry, D., Salehi, M., Silva, R., Fujita, T., Chen, M., Asefa, T., Shenoy, V. B., Eda, G. & Chhowalla, M. Conducting MoS_2 Nanosheets as Catalysts for Hydrogen Evolution Reaction. *Nano Lett.* **13**, 6222-6227 (2013).

20. Yang, T., Bao, Y., Xiao, W., Zhou, J., Ding, J., Feng, Y. P., Loh, K. P., Yang, M. &

Wang, S. J. Hydrogen Evolution Catalyzed by a Molybdenum Sulfide Two-Dimensional Structure with Active Basal Planes. *ACS Appl. Mater. Interfaces* **10**, 22042–22049 (2018).

21. Seok, J., Lee, J-H., Cho, S., Ji, B., Won Kim, H., Kwon, M., Kim, D., Kim, Y-M., Ho Oh, S., Wng Kim, S., Hee Lee, Y., Son, Y-W. & Yang, H. Active hydrogen evolution through lattice distortion in metallic $MoTe_2$. *2D Mater.* **4**, 25061 (2017).

22. Lukowski, M. A., Daniel, A. S., Meng, F., Forticaux, A., Li, L. & Jin, S. Enhanced Hydrogen Evolution Catalysis from Chemically Exfoliated Metallic MoS_2 Nanosheets. *J. Am. Chem. Soc.* **135**, 10274-10277 (2013

23. Zhuang, P., Sun, Y., Dong, P., Smith, W., Sun, Z., Ge, Y., Pei, Y., Cao, Z., Ajayan, P. M., Shen, J. & Ye, M. Revisiting the Role of Active Sites for Hydrogen Evolution Reaction through Precise Defect Adjusting. *Adv. Funct. Mater.* **29**, 1901290 (2019).

24. Zhang, J., Wu, J., Guo, H., Chen, W., Yuan, J., Martinez, U., Gupta, G., Mohite, A., Ajayan, P. M. & Lou, J. Unveiling Active Sites for the Hydrogen Evolution Reaction on Monolayer MoS_2. *Adv. Mater.* **29**, 1701955 (2017).

25. Jaramillo, T. F., Jørgensen, K. P., Bonde, J., Nielsen, J. H., Horch, S. & Chrokendorff, I. Identification of Active Edge Sites for Electrochemical H_2 Evolution from MoS_2 Nanocatalysts. *Science* **317**, 100–102 (2007).

26. Hinnemann, B., Georg Moses, P., Bonde, J., Jørgensen, K. P., Nielsen, J. H., Horch, S., Chorkendorff, I. & Nørskov, J. K. Biomimetic Hydrogen Evolution: MoS_2 Nanoparticles as Catalyst for Hydrogen Evolution. *J. Am. Chem. Soc.* **127**, 5308–5309 (2005).

27. Laursen, A. B., Kegnæs, S., Dahl, S. & Chorkendorff, I. Molybdenum sulfides - efficient and viable materials for electro- and photoelectrocatalytic hydrogen evolution. *Energy Environ. Sci.* **5**, 5577–5591 (2012).

28. Luxa, J., Vosecky, P., Mazánek, V., Sedmidubsky, D., Pumera, M., Lazar, P. & Sofer, Z. Layered Transition-Metal Ditellurides in Electrocatalytic Applications - Contrasting Properties. *ACS Catal.* **7**, 5706–5716 (2017).

7. Conclusions and Outlook

The work described in this thesis has provided a logical insight into the electrocatalytic activity of $MoTe_2$. Applying a solid-state approach to the synthesis of $MoTe_2$ allowed for the synthesis of both semiconducting 2H- and metallic 1T'-$MoTe_2$ in the bulk form. In doing so, the morphology can be preserved between each polymorph, thus allowing for any changes in catalytic activity associated with the effect of nanostructuring to be excluded. Since the polymorphs of $MoTe_2$ can be synthesised simply by altering the reaction temperature, the need for chemical exfoliation *via* lithium intercalation is excluded, thus no additional reactant species are introduced into the material. Therefore, unlike MoS_2, the catalytic activity can be investigated reliably and the effect of transitioning between polymorphs accurately determined. As a result, the emergence of catalytic activity was attributed solely to the metallic character associated with the formation of the 1T'-phase. The emergence of metallic character benefits catalytic activity due to the more efficient reaction kinetics associated with the reduced charge transfer resistance. Additionally, gas chromatography confirmed that the reductive current is associated with the reduction of protons to hydrogen, with a full Faradaic Efficiency being achieved. This study has therefore highlighted the importance of material design for catalytic activity, which may well be applicable to the entire TMDC electrocatalyst family.

Following this discussion on polymorphic control of $MoTe_2$, attention was shifted to the metallic 1T'-$MoTe_2$ material exclusively, with focus being given to the effect of surface area on catalytic activity. The first chapter was centred on bulk crystalline $MoTe_2$, with large plate-like microcrystals being exhibited. The subsequent chapter presented a new nanocrystalline variant of this metallic material, which was obtained simply by lowering the reaction temperature. Due to the surprising synthesis of the metallic phase, in tandem with its more disordered nature, extensive characterisation was performed to ensure that the low temperature material was indeed phase pure monoclinic 1T'-$MoTe_2$. Upon confirming the identical coordination geometry of $\{MoTe_6\}$ distorted octahedra, the sole difference between the crystalline and nanocrystalline materials was deemed to be the surface area. This then led to a reliable investigation of the effect of surface area on the catalytic activity. Electrochemical measurements showed that, at low current densities, *i.e.* $j = -10$ mA cm^{-2}, the overpotential for both crystalline and nanocrystalline materials were similar in value, with 360 mV and 320 mV being required, respectively. However, as the potential is swept to more reductive values, the current densities reached by the nanocrystalline phase are far

greater than that of the crystalline. Since the same catalyst loading per geometric surface area was applied for both electrodes, the increased activity of the nanocrystalline material was credited to being a result of the greater surface area. This was also corroborated by the ECSA, which indicates a greater number of active sites are available for nanocrystalline 1T'-$MoTe_2$ than for crystalline 1T'-$MoTe_2$. Additionally, EIS shows that the charge transfer kinetics are more efficient for the nanocrystalline phase, which is a direct result of the increased contact between the catalyst surface and electrolyte.

Perhaps the most interesting observation in this thesis is the reversible activation mechanism of nanocrystalline 1T'-$MoTe_2$. Reported as the first of its kind, nanocrystalline 1T'-$MoTe_2$ experiences a positive shift in overpotential at $j = -10$ mA cm^{-2} from 320 ± 12 mV to 178 ± 8 mV after 100 cycles between the potential range of +0.2 V and –0.5 V (vs. NHE). This remarkably improved overpotential remains consistently for at least 1000 cycles, until such point that the cathodic bias is removed. Upon doing so, the overpotential reverts back to its original value, highlighting the reversible nature of the activation mechanism. The reversibility of this process itself is evidence that no *ex-situ* structural, morphological or compositional changes are the reason behind the activation. Nonetheless, extensive characterisation was carried out on the material before and after activation, with the material remaining intact.

Rather, the enhancement is proposed to occur *via* an electrochemical activation, by which hydrogen adsorbed on to the surface of the catalyst plays an important role. Continuous reductive potential cycling was found to result in enhanced charge transfer kinetics, all the while maintaining an identical ECSA as the non-activated material. Computational studies indicate that the activation is electronic in nature, which is corroborated by the lack of activation in the semiconducting 2H-$MoTe_2$ material when subjected to reductive potential cycling. DFT calculations indicate that as the HER progresses, a Peierls-type lattice distortion is induced, which is driven by hydrogen adsorption and consequently electron doping. Further, the adsorption of hydrogen was proposed to occur on Te α-sites, with the energy of hydrogen adsorption becoming more favourable on the neighbouring site once initial H adsorption occurs.

Further exploration into the activation mechanism was achieved by monitoring the gradual improvement in overpotential. The slow cathodic response initially casts doubt on the proposed activation *via* electron doping. However, considering limiting electrochemical processes such as diffusion limitations and double layer formation associated with the bulk

freestanding nature of the material, the gradual nature becomes apparent. An activation energy is therefore required in order for the catalytic enhancement to occur, with the speed of activation being controlled by the applied potential. The sweeping nature of cyclic voltammetry effectively pulses the material at high energy inputs, thus allowing for the catalyst to maintain contact with the electrode substrate. The compromise, however, is the speed of activation; therefore more cycles are required for lower energy inputs.

Due to the reversible nature of the activation mechanism, no structural changes could be observed *ex-situ*, therefore attention was turned to *in operando* measurements. The bottleneck of this study, however, is the scaling up of the working electrode. Attempts were made to paint the catalyst ink on to a carbon paper substrate. However, problems arose due to the requirement of carbon paper as the working electrode substrate for *in operando* electrochemical cells. Due to the high surface area of the carbon paper, the applied parameters were deemed insufficient at activating the material to an extent which could be observed by *in operando* techniques. Therefore, in order to pursue a further understanding of the electrochemical activation mechanism, a method of scaling the working electrode needs to be optimised. Until such point, *in operando* measurements cannot be accurately performed.

The exclusion of alternative activation mechanisms brings this thesis to a close. One may argue that the improvement in overpotential may be due to the gradual removal of surface oxides with continued cycling. This argument was eliminated by performing XPS analysis under inert conditions, which show that surface oxides remain before and after cycling. Lastly, the edge site vs. basal plane dispute was revisited. By completely oxidising the basal plane, the electrocatalytic activity of nanocrystalline 1T'-$MoTe_2$ was lost. In contrast, oxidising the edge sites did not obstruct the activation, with an identical overpotential improvement being achieved. Therefore, in the case of nanocrystalline 1T'-$MoTe_2$, this study proves that the activation occurs on the basal plane.

This thesis has explored the origins of catalytic activity in $MoTe_2$, beginning with the control of polymorphism to identify the key role of coordination geometry in TMDC electrocatalysts. Upon identifying the enhanced activity being a result solely of the emergence of metallicity in the 1T'-$MoTe_2$ phase, the effect of surface area was investigated. Comparison of crystalline and nanocrystalline variants of 1T'-$MoTe_2$ expressed the importance of surface morphology when designing HER electrocatalysts, with the nanocrystalline material exhibiting enhanced charge transfer kinetics due to the increased contact between catalyst surface and electrolyte. Upon investigating the electrocatalytic

activity of nanocrystalline 1T'-$MoTe_2$, the remarkable phenomenon of electrochemical activation was observed. Further, nanocrystalline 1T'-$MoTe_2$ undergoes a reversible activation mechanism, which is the first of its kind to be reported. This thesis was therefore dedicated to understanding the origins of the activation, with its roots found to be electronic in nature. Electron doping as a result of hydrogen adsorption on the Te α-sites was found to be the most plausible activation mechanism, however, without reliable *in operando* measurements this cannot be confidently confirmed. Nevertheless, the elimination of alternative scenarios proves the theory of electron doping to be the most plausible. Thus, this work has provided thorough insight into the origins of electrocatalytic activity in $MoTe_2$, with its findings most likely being relevant to other TMDC HER electrocatalysts.